# Characterizing, Testing and Modeling Of Highly Sensing Smart Spacer Fluids, Smart Cement And Smart Orthopedic Cast Materials For Multiple Applications

by
Sai Anudeep Reddy Maddi

A dissertation submitted to the Civil Engineering Department,
Cullen College of Engineering
in partial fulfillment of the requirements for the degree of

Doctor of Philosophy

in Civil Engineering

Chair of Committee: Dr. Cumaraswamy Vipulanandan

Committee Member: Dr. Yi-Lung Mo

Committee Member: Dr. Hong-Yi Li

Committee Member: Dr. George K. Wong

Committee Member: Dr. Chandra Mohan

University of Houston
May 2020

# ACKNOWLEDGEMENTS

This study would not have been possible without valuable assistances of several individuals throughout my research. First, I would like to express my sincere gratitude to my advisor, Dr. C. Vipulanandan, for his valuable guidance, encouragement and kindness throughout my study. I would like to extend my appreciation to Dr. Yi-Lung Mo, Dr. Hong-Yi Li, Dr. Chandra Mohan and Dr. George K. Wong for serving in my dissertation committee and taking time for exchanging valuable suggestions.

I also wish to acknowledge my friends in the GEM group for their help and companionship throughout my research.

Special thanks go to my family for their understanding, unconditional help, endless patience, and encouragement without which it would have been a difficult task.

The financial support provided by the CIGMAT and THC-IT at the University of Houston is gratefully acknowledged.

# ABSTRACT

The main focus of this study was to make the fluids and cementitious materials highly sensing to be used for real time monitoring of changes during the installation and entire service life. For optimizing the well cementing, it is important to develop technology to monitor drilling and cementing operation in real time during the well installation to minimize operation delays, failures and ensure safety.

In this study, the effects of pressure, temperature and magnetic field strength on the electrical resistivity and rheological properties of a sensing smart spacer fluid modified with iron oxide nanoparticles (nano$Fe_2O_3$) were investigated. The spacer fluid rheology was modelled using Bingham-plastic model, Herschel Bulkley model and Vipulanandan model. The electrical resistivity was used as sensing parameter to monitor the percentage of oil cleaning efficiency of the spacer fluid. In this spacer fluid study, the axial flow of the spacer fluid in the annulus was investigated analytically. The shear stresses, velocity profiles, strain profiles and pressure gradients were predicted using the Bingham- Plastic model and were compared to the new rheological model, Vipulanandan model.

In this study, the potential of using the smart cement in installation of oil well was tested for real time monitoring using large laboratory models and a field model for a period of 6 years. The laboratory oil well models of 10 ft. deep and the field model of 40 ft. deep were instrumented and monitored for changes in electrical resistivity, curing and stresses over period of 5 years (2000 days). The piezoresistivity of the smart cement response was related to the casing pressure using a nonlinear relationship. The experimental results were also modeled using the artificial neural network (ANN) models, finite element models and compared to the Vipulanandan models.

Plaster is the traditional cementious material used for orthopedic casting in the medical industry with need for real time monitoring of setting, strength gain and performance. In this study, electrical measurements are used to monitor and characterize the condition of the cast material in

real time. The Orthopedic casting material was modified with conductive filler to make it sensitive and has been tested under various mechanical loadings, temperature and water seepage conditions.

# TABLE OF CONTENTS

# LIST OF TABLES

# LIST OF FIGURES

# CHAPTER 1 INTRODUCTION

## 1.1 General

Real time monitoring the performance of materials used in oil and gas wells construction, infrastructure and medical industry is gaining importance over time. With the industrialization and growth of population around the world, the demand for oil and gas is increasing with millions of production wells in service around the world. With the increasing pressure, the oil and gas industry is now forced to drill to greater depths reaching about 30,000 ft (Gaddy, 1998; Al-Sarraf et al., 1997). The advancements in the field of drilling enabled oil and gas industry to expand to many inaccessible areas around the world. In the construction of an oil well first, a wellbore is drilled, and a metal casing is placed inside of it. Spacer Fluid is pushed inside through the casing out into the annulus for cleaning the casing of any drilling fluids residue. Spacer fluids have been primarily developed to separate the cement slurry from the drilling fluid because of contamination of the cement affecting the cementing operation and long-term stability of the cemented wells (Theron et al., 2002; Sarap et al., 2009; Maserati et al., 2010; Olowolagba et al., 2011). Incompatibility in the fluids can cause significant increase in the viscosity, and thus hydraulic resistance inside the wellbore. Efficient displacement and effective removal of the drilling fluids and associated residues from the wellbore prior to the completion of a well is critical for optimized hydrocarbon recovery (Quintero et al., 2008).

The next step in oil well drilling is the cementing. In this, cement is poured in and flows up, reinforcing the space between the wellbore and the casing. This cement reinforcement is critical to the integrity of the well. Over $40 billion in damages, 4 million barrels of oil spilled into the Gulf of Mexico, and 11 Workers were killed with the 2010 Oil Spill (Pallardy, 2010). One of the main contributing factors that caused this event was the cementing, which did not set properly in the oil well (Pallardy, 2010).

As deepwater exploration and production of the oil and gas expands around the world, there are unique challenges in well construction beginning at the seafloor. Also preventing the loss of fluids to the formations and proper well cementing have become critical issues in well construction to ensure wellbore integrity because of varying downhole conditions (Labibzadeh et al., 2010; Eoff et al., 2009; Ravi et al., 2007; Gill et al., 2005; Fuller et al., 2002). Moreover, the environmental friendliness of the cements is a critical issue that is becoming increasingly important (Durand et al., 1995; Thaemlitz et al., 1999; Dom et al., 2007). Lack of cement returns may compromise the casing support and excess cement returns cause problems with flow and control lines (Ravi et al., 2007; Gill et al., 2005; Fuller et al., 2002). Hence there is a need for monitoring the cementing operation in real time. At present there is no technology available to monitor the cementing operation real time from the time of placement through the entire service life of the borehole. Also, there is no reliable method to determine the length of the competent cement supporting the casing.

Vipulanandan et al., (2014) have developed smart cement with real time monitoring ability. They have used electrical resistivity as the sensing property to quantify changes in the cement due to pressures, temperatures, contaminations, corrosion and cracking.

The medical industry currently uses many cementitious materials for therapy and there is very little understanding on the mechanical behavior of these materials (Parmar et al., 2014). There is been an extensive need for developing monitoring systems for casting materials used in orthopedic surgery. This enables the medical staff to accurately access the healing process and patient condition during an orthopedic injury.

## 1.2 Problem Statement

During the installation of oil and gas production wells, it is critical to have a successful cementing operation (Steven, 2013). The quality of the cementing job strongly depends on the cleaning efficiency of the spacer fluid in removing not only the drilling fluid with the cuttings but

also the filter cakes during the drilling operation. Based on the depth applications, different types of spacer fluids are used in the oil gas industry. Optimization of spacer formulation based on material properties such as density, rheology and cleaning efficiency as the variables is required. The cleaning efficiency of spacer fluids currently cannot be obtained in the field and hence needs more reliable methods for real time detection. New parameters have to be investigated to quantify the cleaning efficiency and its performance in the field.

Cementing operation during oil well installation is important to provide effective inter-zonal isolation and protect casing string from fluid formation. It will serve the production of oil economically and safely over the well's lifetime. Real time monitoring of the cementing is necessary to prevent failures in the oil wells.

Several nondestructive methods have been used by researchers to monitor and characterize the behavior of cementitious materials, such as impact-echo, pulse-echo, ultrasonic pulse velocity, wave reflection, resonant frequency, acoustic emission and microwave adsorption methods (Panzera et al., 2011). Use of these methods has two major drawbacks. Firstly, these methods only give snapshot of the data and do not provide any kind of real time monitoring. Secondly, implementation of all these techniques require temporary stopping of the well operations. Recently, nondestructive real time monitoring system with monitoring the cement sheath from outside the casing using instrumentation was developed by using electrical resistivity measurements (Vipulanandan et al., 2015).

The well cement was monitored using cement bond logs and ultrasonic cement evaluation (Spoerker et al., 2002). Cement bond logs can give a reasonable estimate of bonding and a semi-quantitative idea of presence or absence of larger cement channels but will not certify pressure or fluid isolation of a zone. Cement bond logs have been proven to miss a percentage of smaller channels in cement, even under ideal conditions (Hill, 1990). Bond logs have failed to show bond in many wells that proved to be well isolated in a differential pressure test. Error within the

application and interpretation of cement bond logs has resulted in numerous workovers to repair cement that was not faulty, resulting in higher costs and a decrease in the well integrity by unnecessary perforating and attempts to block using squeeze cement (George, 2012).

The smart cement can be used for real-time monitoring while it sustains its structural properties. Electrical resistivity has been considered as a monitoring parameter since it is a material property, which is sensitive to the changes inside the material, during setting and hardening (McCarter et al., 1990).

There is emerging interest in characterizing and determination of performance properties of cements under various conditions. Some modifications such as introducing additives can be done to improve the physical and sensing properties of oil well cement. Preparation of smart cement material sensitive to stresses, temperatures, cracks, contaminations enables us to monitor the changes in the material with high accuracy over long period of time. Hence, it is important to optimize the composition of the materials and also experimentally characterize these materials.

Plaster is the traditional material used for medical casting. It is considered the most versatile of the splinting materials, is completely moldable and can withstand considerable forces (Stephanie et al., 2011). One of the important downsides of this cast could be its hardening via an exothermic process. In some cases, these exothermic processes can cause temperatures to rise to dangerous levels that can risk thermal injury. Other disadvantages include high water permeability and setting times. A rather large concern regarding the use of cast material is to assess the injury beneath cast. There are common complications that could occur due to poor plastering techniques. Currently there is no technique to access the actual condition of casting in real time. Some risks can be minimized with correct Casting Monitoring Technique.

## 1.3 Objectives

The overall objective was to develop and characterize highly sensing smart spacer fluid with nano$Fe_2O_3$ for in–situ sensing and property modifications, smart cement and smart orthopedic cast material using the electrical resistivity and piezoresistive behavior under application of different stresses. The specific objectives are as follows:

(i) Design spacer fluid with higher cleaning efficiency (>95%) of oil-based drilling fluid contamination using iron nanoparticles and investigate the effects of magnetic field and temperature on the sensing and rheology property modifications.

(ii) Characterize the curing and piezoresistive behavior of smart cement with in large and field model environment for 2000 days of curing under effect of stresses, temperature and water seepage.

(iii) Develop and characterize the smart orthopedic casting material using electrical resistivity under effect of compression, tensile and bending stresses.

## 1.4 Organization

This dissertation is organized into seven chapters. Chapter 1 is the introduction to this research study, which presents the research problem that was the focus of this study, in a detailed manner. Chapter 2 summarizes background and literature review related to the spacer fluids, smart cementitious materials and orthopedic casts. In Chapter 3, materials used for preparing the spacer, cement and orthopedic cast samples and experimental procedures are broadly discussed. It also provides the necessary theory and information about the testing methods used and modeling of curing and piezoresistivity. Chapter 4 provides the characterization of smart spacer fluid. Rheological, piezoresistive and cleaning efficiency properties are discussed in correlation to electrical resistivity. Chapter 5 provides the characterization of smart foam cement. Thermal, Rheological, Piezoresistive, Fluid loss properties are discussed in correlation to electrical resistivity. Chapter 5 also discusses about the lab and field implementation models of smart cement,

their installation and monitoring for curing period of 2000 days. This chapter also provides results of pressure testing, temperature testing and water seepage tests performed on the oil well models in laboratory and field. The experimental data is also analytically modelled using Vipulanandan models and ANN models. Chapter 6 discusses the characterization of orthopedic cast material for curing, piezoresistive properties. Chapter 7 includes modeling of fluid flow of spacer fluids using different rheological models for shear stresses, shear strain rates and velocity profiles. This chapter also contains finite element modeling of cement sheath in oil wells and orthopedic casts material under application of internal stresses.

Finally, major findings of this research with some recommendations for future work have been summarized in Chapter 9.

.

# CHAPTER 2 BACKGROUND AND LITERATURE REVIEW

## 2.1 Introduction

The main purpose of this chapter is to provide a review on the topics that are closely related to the proposed study. This chapter summarizes the background to the past research on spacer fluids, oil well cementing and orthopedic casts. Also, reviews on the self-health monitoring materials, impedance measurement and piezoresistive materials are discussed.

## 2.2 Oil and Gas Well Drilling and Cementing

The Oil and gas industry has emerged as one of the most powerful branches of world economy. More than four billion metric ton of oil is produced around the world annually. The United States is the largest producer, generating over 12 percent of the world's total oil production. The United States likely surpassed Russia and Saudi Arabia to become the world's largest crude oil producer earlier in 2018 with production close to 12 million barrels per day (Dunn et al., 2018). The global oil consumption is experiencing ever increasing demand with an increase from 70 million barrels a day in 2000 to 95 million barrels a day in 2015. This increase is leading to increase of deep-water explorations with about 272 wells in 2014 and 169 wells in 2015 (Lesley et. al., 2014). Cementing of these oil wells at higher depth is leaving new challenges. It is attributed that about 60% of the oil and gas failures a result of poor cementing job. One of such consequence is the recent BP Oil spill in 2010. $40 Billion in damages, 4 Million barrels of oil spilled into the Gulf of Mexico, and 11 Workers killed (Pallardy, 2010) with the 2010 BP Oil Spill. One of the main contributing factors that caused this event was the cement, which did not set properly in the BP's oil wells. All these incidents magnify the importance for the improvement of cementing operations and its monitoring. Oil well cementing is defined as the process of placing of the cement in the annulus between casing and well bore. This oil well cementing is part of process of preparing the well for further drilling, production or abandonment.

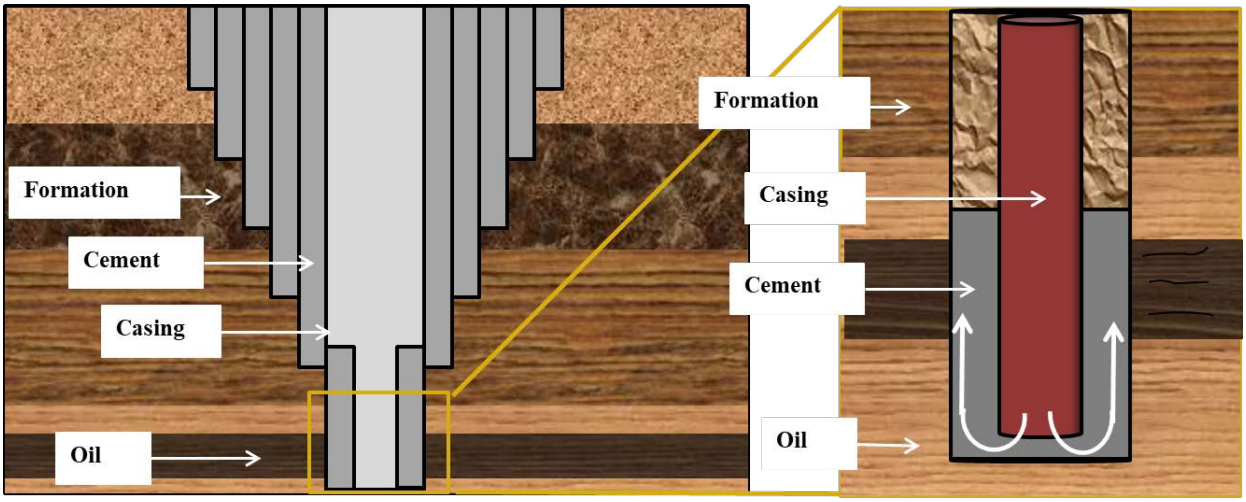


**Figure 2-1:Oil well Cementing.**

The cementing is generally used for number of uses, mainly serving as protection and sealing for the wellbore. Most commonly, cementing is used to permanently shut off water penetration into the well. Additionally, cementing is used to seal a lost circulation zone, or an area where there is a reduction or absence of flow within the well. In directional drilling, cementing is used to plug an existing well, in order to run a directional well from that point. Also, cementing is used to plug a well to abandon it.

Cementing is performed when the cement slurry is deployed into the well via pumps, displacing the drilling fluids still located within the well, and replacing them with cement (Figure 2-1). The cement slurry flows to the bottom of the wellbore through the casing and then flows up. From there it fills in the space between the casing and the actual wellbore and hardens. This cement reinforcement is critical for the integrity of the well. This creates a seal so that outside materials cannot enter the well flow, as well as permanently positions the casing in place. The creation and life of a well can be divided up into four stages: (a) Planning, (b) Drilling, (c) Completion, (d) Production.

**Drilling**

The well is created by drilling a hole 12 cm to 1 meter (5 in to 40 in) in diameter into the earth with a drilling rig. After the hole is drilled, sections of steel pipe (casing), slightly smaller in

diameter than the borehole, are placed in the hole. Drilling fluid, "mud", is pumped down the inside of the drill pipe and exits at the drill bit. The principal components of drilling fluid are usually water and clay, but it also typically contains a complex mixture of fluids, solids and chemicals that must be carefully tailored to provide the correct physical and chemical characteristics required to safely drill the well (Johannes, 2015). Particular functions of the drilling mud include cooling the bit, lifting rock cuttings to the surface, preventing destabilization of the rock in the wellbore walls and overcoming the pressure of fluids inside the rock so that these fluids do not enter the wellbore. Cement may be placed between the outside of the casing and the borehole known as the annulus. The casing provides structural integrity to the newly drilled wellbore, in addition to isolating potentially dangerous high-pressure zones from each other and from the surface.

With these zones safely isolated and the formation protected by the casing, the well can be drilled deeper (into potentially more unstable and violent formations) with a smaller bit, and also cased with a smaller size casing. Modern wells often have two to five sets of subsequently smaller hole sizes drilled inside one another, each cemented with casing.

**Completion**

After drilling and casing the well, it must be 'completed'. Completion is the process in which the well is enabled to produce oil or gas.

In a cased-hole completion, small holes called perforations are made in the portion of the casing which passed through the production zone, to provide a path for the oil to flow from the surrounding rock into the production tubing.

**Production**

The production stage is the most important stage of a well's life; when the oil and gas are produced. By this time, the oil rigs and workover rigs used to drill and complete the well have moved off the wellbore, and the top is usually outfitted with a collection of valves called a Christmas tree or production tree. These valves regulate pressures, control flows, and allow access

to the wellbore in case further completion work is needed. From the outlet valve of the production tree, the flow can be connected to a distribution network of pipelines and tanks to supply the product to refineries, natural gas compressor stations, or oil export terminals.

As long as the pressure in the reservoir remains high enough, the production tree is all that is required to produce the well. If the pressure depletes and it is considered economically viable, an artificial lift method mentioned in the completions section can be employed.

The production stage is the most important stage of a well's life, when the oil and gas are produced. Enhanced recovery methods such as water flooding, steam flooding, or $CO_2$ flooding may be used to increase reservoir pressure and provide a "sweep" effect to push hydrocarbons out of the reservoir (Zitha et al., 2011). Such methods require the use of injection wells (often chosen from old production wells in a carefully determined pattern) and are used when facing problems with reservoir pressure depletion, high oil viscosity, or can even be employed early in a field's life. In certain cases – depending on the reservoir's geomechanics – reservoir engineers may determine that ultimate recoverable oil may be increased by applying a water flooding strategy early in the field's development rather than later. Such enhanced recovery techniques are often called "tertiary recovery." The Oil well cannot be monitored for leaks and other structural damages occurring in the cement during its lifetime (Syed, 2017).

## 2.3 Spacer Fluids

Spacer fluids have been primarily developed to separate the cement slurry from the drilling fluid because of contamination of the cement affecting the cementing operation and long-term stability of the cemented wells. The most common types of spacer fluids include water-based spacers and oil based spacer fluids (Carney, 1974). Incompatibility in the fluids can cause significant increase in the viscosity, and thus hydraulic resistance inside the wellbore. Efficient displacement and effective removal of the drilling fluids and associated residues from the wellbore prior to the completion of a well is critical for optimized hydrocarbon recovery (Quintero et al.,

2008). There are several benefits in using drilling mud in drilling operations but there are concerns about potential contamination of the spacer and cement (Vipulanandan and Amani, 2015). Also, cements are sensitive to drilling fluid contaminations and therefore even a thin layer of drilling fluid could prevent the cement from bonding to the formation and the casing. Effective displacement of the synthetic or oil based drilling mud is extremely important in order to minimize non-productive time (NPT), reduce waste volume, to prevent cement failures and to reduce the risk of completion tool complications (Quintero et al., 2012).

Selecting the proper spacer fluid is typically important and is dependent on the chemistry of the drilling fluid, its composition and conditions of the well. Spacer fluids play a crucial role in proper cementing job by complete displacement of the drilling mud and removal of the filter cake developed along the formation. Various types of spacer systems are available in the oil and gas industry, but they may not be suitable for changing conditions with depth. The spacer design can be changed according to different conditions including geological condition of the well; however, it should be designed for a specific density, mud system, cement system and rheology. Generally, a spacer fluid is composed of the following components. (1) Water/Oil as the base fluid of spacer system; (2) Weighting materials to increase the density of the spacer system; (3) Rheological modification agent or polymers and (4) A proper surfactant Package. Using these components in the spacer fluid makes the spacer density and rheological properties fall in between the density and rheological profile of drilling fluid and cement (Zanten et al., 2011)

During recent years the operators are to explore and produce from increasingly more difficult environments. Fluid displacements in offshore environments require spacer fluids to perform more than one operation effectively at low and high temperatures encountered in the well. In each of these cases there have to be a novel design to adjust for different conditions. Use of nanoparticles in spacer system can provide enhancements in rheological, thermal, mechanical, magnetic and optical profiles. Nanoparticles with noticeable alterations in the optical, magnetic

field strength and electrical properties are excellent tools for the development of sensors and the formation of imaging contrast (Ramanan, 2015). Since the nanoparticles are extremely small in size, nanoparticles are preferred to be used in the oil and gas industry as their abrasive forces are negligible with less kinetic energy impact. The nanoparticles are added to the mud in small amount, with the concentration of the order of 1%. Nano-based drilling muds could be the fluid of choice in conducting drilling operations in sensitive environments to protect other natural resources. Recent studies have shown that when nanomaterials are added to the drilling muds it can be used as a sensing material downhole for temperature and pressure (Vipulanandan and Mohammed, 2017). Nanotechnology is increasingly being deployed in hydraulic fracturing of conventional and unconventional wells. Most of the proposed applications of nanotechnology in the oil field can be classified into the following areas of sensing or imaging, enhanced oil recovery, gas mobility control, drilling, and completion and produced fluid treatment.

## 2.4 Oil well Cements

### 2.4.1 Application of oil well cement

Oil well cement is used in the production and exploration of oil and gas onshore as well as deep water offshore wells. According to World Oil Well Cement Market Forecast 2024 by CemWeek Research, the current consumption of cementitious materials in the US is around 3200 million tons and is expected to reach 4000 million tons by 2024 at an annual growth rate of 6.5%. A typical well can be thousands of meters deep, less than a meter wide, and is constructed by using a metal casing surrounded by a special cement slurry mix that fills the annulus between the outer face of the tubing and the wall formation of the hole. Lafarge North America's oil well cement provides a base ingredient in the slurry mix that is pumped into the interior metal section of the well and forced back toward the surface from the base of the borehole filling the annulus. Oil well cement slurries are designed for a multitude of purposes from the establishment of the well's safety

and structural integrity during drilling to the isolation of the zone of interest and the production of oil and gas upon completion.

The following are the objectives of cementing an oil well: Provide zonal isolation, hydraulic seal, protect casing from corrosion, provide structural support for the casing, protect resources around the well (Steven, 2013). The API Technical Report 1PER15K-1 Protocol for Verification and Validation of High-Pressure High-Temperature Equipment defines a high-pressure well as having pressure greater than 15,000 psi [103 MPa]; a well that has temperatures above 350Â°F [177°C] is considered high temperature. Given the complexity of the application and its extreme conditions of temperature and pressure, oil well cement must be carefully designed to meet demanding requirements such as predictable thickening time (set time), high sulfate resistance, high durability, fluid loss control, consistency, low viscosity, low free fluid, and strength. Unlike surface construction, oil well completion is much less tolerant to errors. The application of oil well cement depends of each of the factors which are used to carefully modify the cement.

The following are some of the factors affecting the cementing, the type of cement used and its composition. Geomechanics, Geology and pressure and temperature are considered of utmost importance (Dinesh et al., 2018). The presence of in- situ stresses along the borehole considerably affect the cement and its cementing. So, the slurries must be designed to withstand the in- situ stresses allowing least chance for its modification downhole. The variation of pressure and temperature over the life of the well leads to effect the zonal isolation. The expansion and contraction lead to damage of cement sheath, thus depleting the structural integrity. So, the cements are generally prepared to withstand pressure and temperature cycles. The type of geology is one of the most important factors dictating the type of cement to be used (Dinesh et al., 2018). Presence of intolerant formation demands the use of light weight slurries to prevent lost circulation and formation damage. Manufacturing most suitable for a given oil well is one of the challenges of cementing.

**Cements Used in Oil Well Industry**

Depending on the well bore depths, downhole pressure and temperatures, the following type of cements are employed.

API Classification of Oil Well Cements. (API Spec. 10A)

Class A -- Available only in ordinary, O, grade (similar to ASTM Spec. C150, Type I)

Class B -- Available in both MSR and HSR grades (similar to ASTM Spec. C150, Type II)

Class C -- Available in ordinary, O, MSR, and HSR grades (similar to ASTM Spec. C150, Type III)

Class G – This product is intended for use as a basic well cement. Available in MSR and HSR grades. Intended for use from surface to 2438m and its range of use can be extended from lowest to highest temperatures.

Class H -- I This product is intended for use as a basic well cement. Available in MSR and HSR grades. Intended for use from surface to 2438m and its range of use can be extended from lowest to highest temperatures. High density slurries of upto 1.98g/cc.

### 2.4.2 Improving Cementing and Monitoring

With some of the reported failures and growing interest in environmental and economic concerns in the oil and gas industry, integrity of the cement sheath is of major importance (Vipulanandan et al., 2014). Due to the Hazards and the number of unsuccessful events, researchers are reviewing on the feasibility of monitoring of the installation process and as well as the cement during its lifetime. Cement reinforcement between piping and earth is a standard for all downhole operations in the oil and gas industry, including drilling, fracking, and natural gas storage. And when this cement fails, the environmental consequences can be severe. The oil well operators are required to monitor their wells to prevent the occurring of disasters.

Today, this is achieved through a process called wireline testing which was developed in the 1970's and has been the industry standard for downhole monitoring ever since. The general type of wireline testing includes Cement Bond logs, Sonic and ultrasonic logs and Triple Combo.

However, the wireline testing has two fundamental problems. First, to get well data using wireline testing, operators have to drop measurement tools into a well. But to do this, they must temporarily shut down that well. This costs millions of dollars over the lifetime of an operation because they aren't producing in that time. The second problem is that it can only provide data while those tools are dropped in the well. So, once they take the tools out and start producing again, operators no longer have any idea how the cement is doing. In other words, they can't really monitor their well, they can only check in on it.

Real time monitoring of the cement during its installation and through the life of the well is hence gaining importance. The structural integrity of the civil infrastructure is essential for the safety, productivity and quality over the life of the well (Chung et al., 2003). Thus, there is need for monitoring damage nondestructively, so that timely repair of the oil wells takes place. Real time monitoring gives information on the time, load condition or other conditions at which damage occurs, thereby facilitating the evaluation of the cause of the damage.

### 2.4.3 Structural Health Monitoring Materials

The damage in cement-based materials is most commonly studied by destructive mechanical testing; however, there is an increasing interest in nondestructive testing of materials. Electrical resistivity measurement has been used by many researchers to characterize the cement concrete and in other applications (Azhari et al., 2012; Chung et al., 2003; Wei et al., 2008).Concrete is a poor electrical conductor and hence it requires the presence of conductive particle or fibers that are added to attain stable and accurate conductive properties (Naik et al., 2010). The design formulation of conductive cements is based on the "Electrical Percolation" principle by which the cement matrix conductivity increases with increasing conductive particles

and reaches a critical value. The commonly used additives for making cement matrix conductive include carbon fibers, steel fibers, carbon black, coke breeze, ferrous compound, high carbon fly ash and other materials (Garas et al., 2003; Chung et al., 2003; Vipulanandan et al.,2014; Naik et al., 2010; Wei et al., 2008) . From the recent studies, it was observed that about 60% use carbon fibers as their conductive particles. The cement matrix with electrically conductive properties makes it smart material that has important applications in self health monitoring systems. The fibers enhance the damage sensing ability of the cement matrix.

The conventional methods of measuring the electrical resistivity of cementitious materials can be categorized into direct current (DC) methods and alternating current (AC) methods, where of both electrodes are needed for the measurements (Vipulananadan et al., 2014). The DC methods can be categorized into two or four probe methods. About 60% of the researchers use DC four probe method. The use of AC two probes was limited to very few researchers. The number of studies on electrical characterization of foam cement was very limited (Sugama et al., 2004) and was only to extent of impedance characterization. Some of the recent studies aimed at microstructural evolution in hydrating cement-based material systems using non-contact electrical resistivity methods (Wei et al., 2008). Use of electrical resistivity measurements for sensitivity has been proven advantageous at microscopic level. The presence of electrically conductive fibers in the cement-based materials is necessary for the piezoresistivity to be sufficient in magnitude and in reversibility.

A material is said to be piezoresistive if resistivity of that material changes under applied stress. Piezoresistivity has been proven to be a good sensing property in the literature (Carmona et al., 1987; Vipulanandan et al., 2015). It can be used to sensing of stress/strain, damage and thermoelectric properties and monitor health of the structure and more. Development and characterization of piezoresistive smart structural materials led a new path to study on Piezoresistive Structural Sensors (PRSS). The researchers have studied electrical resistivity with

curing time, changes in electrical resistivity with loading, fiber content and impedance characterization under electrical characterization of cement-based materials. (Wei et al., 2012; Chung et al., 2003; Vipulanandan et al., 2004 & 2015).

The number of studies on electrical characterization of foam cement was very limited (Sugama et al., 2004) and was only to extent of impedance characterization.

**Table 2-1:Summary of Electrical Characterization of Cementitious Materials.**

| Reference | Main constituents | Fiber & content | Water/ cement ratio | Electrical measurement | Important parameters studied | Remarks |
|---|---|---|---|---|---|---|
| Vipulanandan, et al. (2015) | Class H Oil well cement, Conductive Filler | Conductive filler 0.1% | 0.38,0.44 and 0.54 | AC two probe in frequency range 20 Hz to 300 kHz | Piezoresistivity, Rheological modeling, Compressive Strength vs resistivity measurement | (1). AC Impedance Method<br>(2) 2 Probe Method<br>(3) Resistivity – p-q model, Rheology – Hyperbolic modeling |
| Changguo, et al. (2015) | Portland Cement, Fly Ash, Agar pad | No Fiber | 0.45 | Copper Electrodes, DC, two probe | The effect of curing on strength and resistivity. | (1). DC Method<br>(2) 2 Probe Method<br>(3). No Modeling |
| Wei, et al. (2012) | Portland cement | N/A | 0.4 | Non-Contact Electrical Resistivity measurement. | Effect of strength on the initial resistivity, Compressive strength prediction from resistivity value. | (1). AC Impedance method<br>(2) Non-contact resistivity measurement.<br>(3) Resistivity modeling |
| Naik, et al. (2010) | Portland Cement Type I | High Carbon Fly ash, Pan Type carbon Fibers 0.03% to 0.5% | 0.4 | Copper electrodes, AC Two probe, Frequency 120, 1000Hz. | Effect of Fiber on strength, Resistivity Vs Curing | (1). AC Impedance method<br>(2) Two Probe Method.<br>(3) Resistivity modeling, Carbon Fiber optimization |

**Table 2-1:Summary of Electrical Characterization of Cementitious Materials. (continued)**

| Reference | Main constituents | Fiber & content | Water/ cement ratio | Electrical measurement | Important parameters studied | Remarks |
|---|---|---|---|---|---|---|
| Vipulanandan & Sett (2004) | Polyester resin, sand | Short carbon fiber, 6 % | N/A | 2 probe method with DC used | Tensile properties were studied. | (1). DC Method<br>(2) 2 Probe Method<br>(3) Resistivity – p-q model |
| Chung et al. (2003) | Portland cement, carbon fiber, fine and coarse aggregates | Carbon fiber-2% | 0.47 | DC 4 Probe Method | Fractional changes in resistance with curing age and fatigue loading. | (1). DC Method<br>(2) 4 Probe Method<br>(3). No Modeling |
| Garas (2003) | Ordinary Portland cement type I/II, aggregate | PAN based chopped carbon fiber, 6 % by weight | 0.5, 1.0 | DC, 2 probe | Electrical Resistivity, Pulse Velocity, and Compressive Properties | (1). DC Method<br>(2) 2 Probe<br>(3)Relation between electrical resistivity and young's modulus |
| **Remarks** | Portland cement – 70%<br>Class H and polymers – 30% | Carbon Fibers-60%<br>High Carbon Fly ash -15%<br>Other -25% | 0.38 to 1 | AC two probe-25%<br>DC two probe-60%<br>Non-Contact 15% | Electrical Resistivity Changes with Strength, Loading, curing, fiber content. | (1). AC and DC Methods.<br>(2) 2 probe, 4 probe and non-contact methods.<br>(3). Resistivity modeling, young's modulus modeling |

### 2.4.4 Smart Cement

Primary energy consumption continues to accelerate globally despite several years of slow economic growth. With increased consumption, production of oil continues to grow surpassing record level of 90 million barrels per day worldwide. Not only does the oil industry need to produce more to meet ever increasing demand, it also needs to overcome existing well production declines. All active wells ultimately decline in production as resources are tapped, though there is an opportunity for technology to slow or in some cases even temporarily reverse those decline rates. In addition, as existing wells decline, more and more new wells need to be drilled to keep up with demand. This is leading to exploration of oil at very large depths where the formations are very weak, fragile with lost circulation zones. Hence the need for cement monitoring system during its installation and the life of the well are the driving factors for the study.

Use of smart cement ensures us to

- Safe Installation: The installation process of the cement sheath can be monitored continuous and this gives the scope for monitoring the quality of cementing during the installation process.
- Monitor Cement Profile: The smart cement technology enables us to know exactly the level of the cement and the drilling muds which helps in monitoring any formation failures. The cement sheath can be monitored as it is curing over its lifetime. This enables us to monitor or detect any failures or changes in the cement.
- Monitor Cement Quality: The quality of the cement can be monitored using resistivity measurements. The effect of fracturing or any mechanical operations on cement can be identified.
- Monitor the Cement sheath bonding: The bond between cement and casing is critical for zonal isolation. Smart cement technology helps us monitor the integrity of the well by monitoring the bond.

- Monitor the Stresses: Smart cement monitors both the physical and thermal stresses coming on to the oil well system and notifies the possible damage that can occur in the well in advance to provide scope for repair and reconstruction.
- Prevent Failures like Macondo, 2010: Enhanced smart monitoring system can help prevent accidents as it is the most sensitive technology available to monitor the stresses.

Figure 2-2 and Figure 2-3 show the typical stress-strain and piezoresistive behavior of the neat cement and smart cement. Cement generally fails at 0.2% strain (Praveen, 2014). Monitoring this low strain needed very accurate measurements of the data which is not easy.

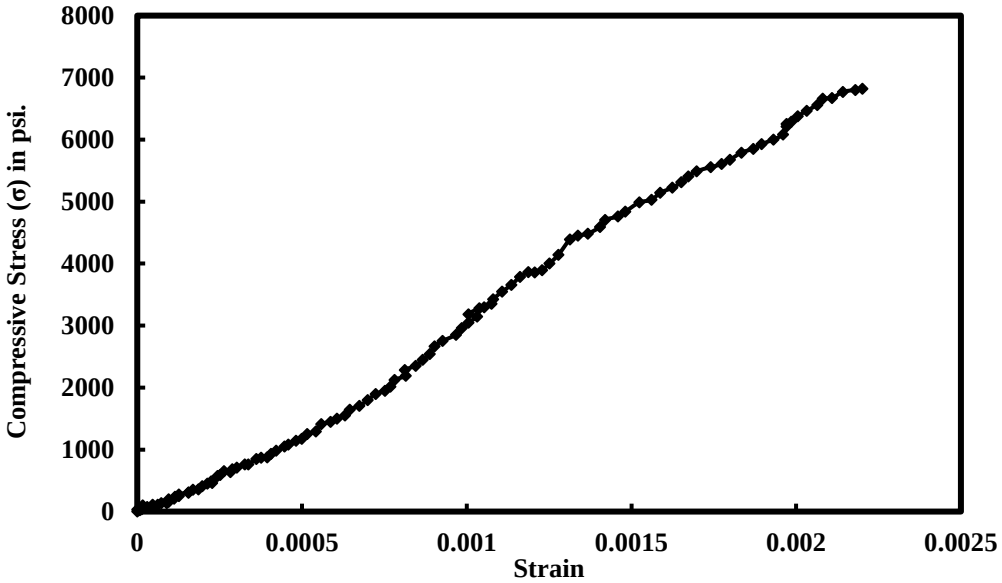


**Figure 2-2:Typical Stress Strain Behavior of Cement Composite.**

(Data from: Praveen, 2014)

The smart cement technology can monitor the changes in the cement at very high magnification of about 2500 times after one day curing (Vipulanandan et al., 2014). The main property of interest is piezoresistivity, the change in the resistivity of the cement with the application of the stress. Also, the rheological properties were not affected by the addition of conductive filler (Vipulanandan et al., 2014).

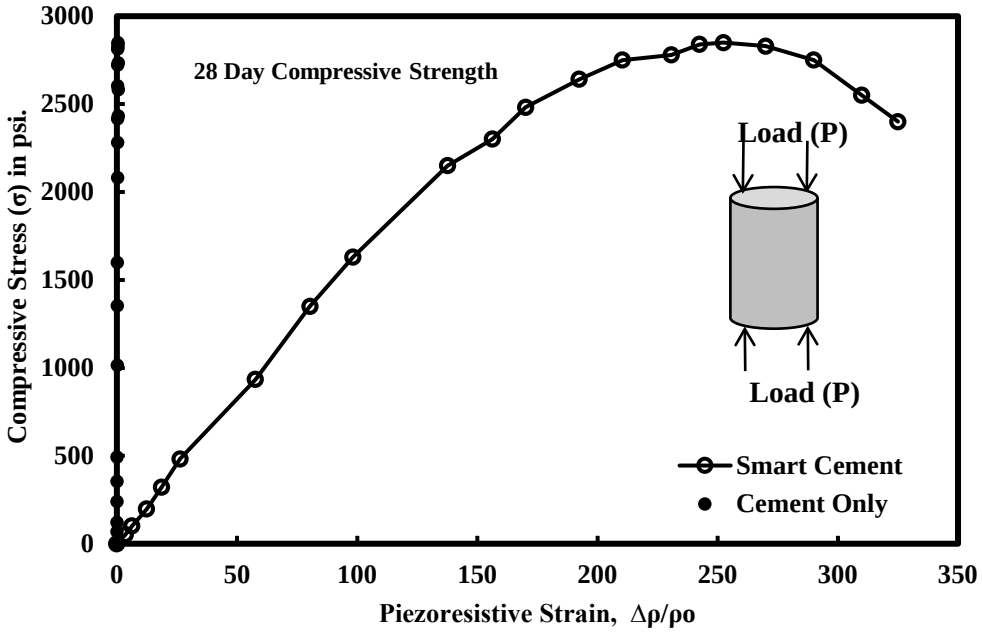


**Figure 2-3:Typical Piezoresistive Behavior of Cement Composite.**

(Data from: Vipulanandan et al., 2014)

## 2.5 Need for Artificial Intelligence

With the advancement of various technologies, there is a need to integrate them for more efficient field applications for real-time monitoring, minimizing failures and safety issues. Use of artificial intelligent (AI) in various applications with multiple variables are becoming popular. Cementing the oil wells have been used for over 200 years cementing failures during installation and other stages of operations have been clearly identified as some of the safety issues that have resulted in various types of delays in the cementing operations and oil production and also has been the cause for some of the major disasters around the world. For successful oil well cementing operations, it is essential to monitor it real-time because of the varying environmental and geological conditions with depth and also performance of the cement sheath after hardening during the entire service life.

Artificial Intelligence (AI), otherwise known as machine learning or computational intelligence, is the science and engineering aimed at creating intelligent tools, devices and machines. Its application in solving complex problems and case-based complications in various field applications has become more and more popular and acceptable over time (Opeyemi et al., 2016). AI techniques are developed and deployed worldwide in a myriad of applications as a result of its symbolic reasoning, explanation capabilities, potential and flexibility (Demrican et al., 2011). Most of the artificial intelligence techniques or tools have shown tremendous potential for generating accurate analysis and results from large historical databases, the kind of data an individual may find extremely difficult for conventional modelling and analysis processes (Shahab 2000). AI is currently employed in various sections of oil and gas Industry, from selection of drill bits to well bore risk analysis. In recent years, there has been a drastic increase in the application of AI in petroleum industry due to presence of digital data and case studies. AI can provide real time prediction in oil and gas industry from selection, monitoring, diagnosing, predicting and optimizing, thus leading to better production efficiency and profitability. (Opeyemi et al., 2016)

## 2.6 Artificial Intelligence

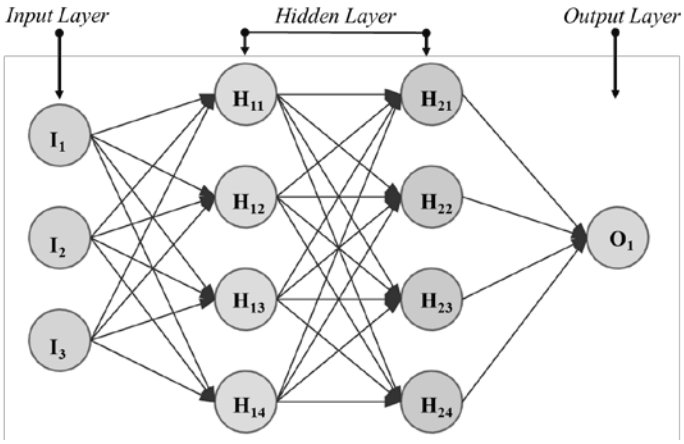


**Figure 2-4:Artificial Intelligent (AI) with Integrated Artificial Neural Networks (ANN).**

An artificial neural network (ANN) is a computational numerical model which is based on, at some level, brain like learning as opposed to traditional computing which is based on

programming. The model consists of interconnected groups of artificial neurons, which simulate the structure of the brain to store and use experience, and processes information using a connectionist approach (Figure 2-4). Artificial neural network is an adaptive system which trains itself (changes its structure) during the learning phase based on the information flowing through the network.

The researchers who have studied neural networks aimed to model the fundamental cell of the living brain: neuron. The recognized US pioneers who first introduced the concept of artificial neural network were neurophysiologist Warren McCulloch and the logician Walter Pitts in 1943. They developed a simple model of variable resistors and summing amplifiers that represent the variable synaptic connections or weights which link neurons together and the operation of the neuron body, respectively. The popularity of neural network increased in 1962 with the introduction of 'perceptron' by Frank Rosenblatt who used the term to refer to a system which recognized images using the McCulloch and Pitts model (Alexander 1990).

Artificial Intelligence (AI) can be defined as a collection of new analytical algorithms and tools that attempts to imitate and predict situations. These Artificial intelligence techniques exhibit an ability to learn and deal with new situations. Artificial neural networks, evolutionary programming and fuzzy logic are among the paradigms that are classified as Artificial Intelligence (Sadiq et al., 2000). The main root principles of AI include reasoning, knowledge, planning, learning, communication, perception and ability to manipulate objects (Bhattacharyya, 2011).

### 2.6.1 Artificial Neural Networks (ANN)

Neural Network research was first published by McCulloh and Pitts in 1943 (Hubbert et al., 1957). The artificial neural network is a numerical model that mimics the functional aspects of neural network in human brain system (Behnood et al., 2018). It consists of many artificial neurons interconnected where each of them gives a single output (Y) induced from all inputs (Xi) (Hammoudi et al., 2019). The predictive capability of artificial neural networks comes from the

ability to learn and adapt to new situations in which additional data becomes available. In an artificial neural network, a training set comprising of input and output data is entered and the neural network algorithms attempt to map the process by which inputs become outputs (Sadiq et al., 2000). ANN is a multilayer perceptron (MLP) including three layers (Fig. 1). The first layer (input layer) consists of neurons representing the independent variables (inputs Xi), the second one is the hidden layer (Hi, f(Hi)), and the last one is the ANN responses (output layer, representing AI). The number of neurons required in the hidden layer is determined in a way to minimize both prediction error and number of neurons.

The general forms of the equations are as

$$Hj = \sum WijXi + bj \tag{2-1}$$

where Xi represent the inputs (Figure 2-4, neurons I) and subscript i represents the inputs (I and summation 1 to n). The Wij is the weighing matrix for each input term Xi connecting it to the hidden term Hj, the bj is the bias input function.

Using Sigmoid as the transfer function f(Hj) is represented as

$$f(H_j) = 1 + \frac{1}{1 + e^{-H_j}}. \tag{2-2}$$

Two accurate neural network algorithms are Back Propagation Neural Networks (BPNN) and Generalized Regression Neural Networks (GRNN). The following are the summaries on these algorithms.

**Back Propagation Neural Networks (BPNN)**

BPNN are the most widely used type of artificial neural networks (Sadiq et al., 2000). BPNN consists of an input layer that is propagated through the network with set of weights to have a predicted output. BPNN is set with an objective to adjust the set of weights so that the difference between output prediction and required output is reduced.

**Generalized Regression Neural Networks (GRNN)**

The generalized regression neural network (GRNN) is a feedforward neural network based on non-linear regression theory consisting of three or more layers: the input layer (one layer), the pattern layer with the summation layer (one or more layers), and the output layer. While the neurons in the first three layers are fully connected, each output neurons are connected only to some processing units in the summation layer. The individual pattern units compute their activation using a radial basis function (bj), which is typically the Gaussian kernel function (Sadiq et al., 2000). The training of the GRNN is quite different from the training used for the BPNN. It is completed after presentation of each input-output vector pair from the training set to the GRNN input layer only once. What this means is that both the centers of the radial basis functions of the pattern units and the weights in connections of the pattern units and the processing units in the summation layer are assigned simultaneously.

### 2.6.2 Development of Neural Network and Design

The data used in this study were obtained from set of laboratory and field scale studies on smart cement. The obtained data comprises of electrical resistance, piezoresistive strain data from lab for 28 days and field for a period of 4.5 years. Database preparation for training of neural network represents very important in neural network modelling. The suggested neural network model does not consider weather and temperature factors. Neural network architecture with different hidden layers was used to predict laboratory and field measurements. Attempts were made to use hidden layers from one to four to obtain a good fit to the data. BPNN architecture with 4 hidden layers exhibited better correlation to laboratory and field measurements. The coefficient of determination ($R^2$) and root mean-square-error (RMSE) were used to evaluate the statistical significance of the ANN models.

## 2.7 Plaster of Paris

Plaster of Paris has been the most commonly available material used both for immobilization of acute lesions and mobilization splinting. When a bone fragments, it is important to keep the healing bone confined within a hard-durable casing. This protection is usually provided by the use of a cast (Teresa et al., 2007).

The mechanical failure of plasters used for medical purposes has been shown to be due to tensile stresses which are generated by bending (Lewry et al., 1994). Knowledge of the materials properties and handling techniques is of great importance when constructing orthoses and prostheses (Parmar et al., 2014).

### 2.7.1 History of Plaster of Paris

Plaster of Paris takes its name from Paris, France, where it was first widely used chemically, surgically and in construction works (Browner et al., 2008). Plaster of Paris is produced by removing the impurities from the mined gypsum and then heating it under controlled conditions to reduce the amount of water of crystallization (Szostakowski, et al., 2017). Plaster of Paris was well known as a building material for many centuries before it was introduced as casting material. Egyptians as well as Romans used it for plastering walls however not more is known on plaster use after the end of Roman occupation. In modern day England, it was widely excavated in Roman coffins discovered in York, and on the walls in the military barracks of the Second Augustian Legion excavated at Caerleon in Monmouthshire. In mediaeval times gypsum was used only for alabaster statuary. There are various accounts describing the origin for the name plaster of Paris. One account mentions King Henry III who visited Paris in 1254 and was so impressed by fine white walls that he introduced similar plastering in England where it became known as plaster of Paris.

Plaster of Paris ($2CaSO_4.H_2O$) is calcium sulphate with water. It is prepared by heating gypsum ($CaSO_4.2H_2O$) at 120°C to allow partial dehydration. When mixed with water, it gives out

heat and quickly sets to a hard-porous mass within 5 to 15 minutes. The first step is called the setting stage with a slight expansion in volume. The second stage is the hardening stage.

Stage 1: Plaster of Paris formation (Heating at 120 °C)

$$2(CaSO_4 \cdot 2H_2O) \xrightarrow{\Delta} 2\ (CaSO_4 \cdot \tfrac{1}{2}\ H_2O) + 3\ H_2O \qquad (2\text{-}3)$$

Stage 2: Casting

$$(CaSO_4 \cdot \tfrac{1}{2}\ H_2O) + 3\ H_2O \rightarrow 2\ (CaSO_4.2H_2O) + \text{Heat} \qquad (2\text{-}4)$$

**2.7.2 Casting**

Its first documented medical use dates back to 1852 when A. Mathyson, a Dutch Army Surgeon, rubbed powdered plaster into cotton bandages to form splints. The first use of plaster of Paris as a cast for injured limbs took place through a technique known as *plâtre coulé* that became popular in Europe at the beginning of 19$^{th}$ century. This technique involved pouring plaster of Paris around injured limbs encased in a wooden construct (Szostakowski, et al., 2017). Due to the weight of the construct, the patient was largely confined to bed during the period of fracture healing. This disadvantage was highlighted by Seutin, but this remained a relatively popular technique in Europe with some surgeons using it for lower limbs only and some using it for both upper and lower. Starched and albuminated bandages were also used as a casting method. In 1839, Lafargue of St. Emilion used fresh warm starch paste mixed with plaster of Paris powder applied to layers of linen strips (Browner et al., 2008). That dressing had the advantage of hardening much quicker, reducing setting time down to six hours. The Dutch military surgeon Anthonius Mathijsen while working at the military hospital in Haarlem discovered that bandages soaked in water and plaster of Paris were becoming hard within minutes providing sufficient casting for injured limbs. He published his monograph in 1852 in a medical magazine called *Repertorium*. His plaster bandage was based on the principles of Seutin, who 10 years earlier introduced starched bandages known as *bandage amidonnee* . In his paper entitled "*New Method for Application of Plaster-of-Paris Bandage*", Mathijsen highlighted many disadvantages of Seutin's dressings including lack of self-adjustment

to the changing conditions of the limb, long duration of days needed for the casing to become sufficiently solid, carton splints shrinking and becoming shorter when they dried off adversely affecting fractures, and in cases of suppuration or with small children urinating, dressing becoming soft and loosen. Mathijsen's bandages consisted of strips of coarse cotton cloth with finely powdered plaster rubbed in. This method of preparation was used until 1950.

Early plaster bandages used at hospitals were made by nursing staff. They were usually freshly made from plaster powder kept in air tight containers that was applied on to the woven bandage or strips of cloths. Care was required while soaking dry bandage in water to prevent the plaster coming off the bandages and dissolving in water. In the early 1930's, the first commercially manufactured bandages were available in Germany. They were made by spreading plaster mixed with minute quantities of volatile liquids on soft cloth.

### 2.7.3 Application of Plaster Cast

Application of plaster of Paris requires good knowledge of anatomy and pathology that we are aiming to treat. It must be applied with a great care that is also need in its supervision afterwards. The perfect plaster dressing must retain the limb under all conditions in the desired position with complete comfort. It must be strong yet light, effective in use but easily removed when no longer required.

Prior to casting, any skin lesions or soft tissue injuries must be carefully noted (Szostakowski, et al., 2017). It is important to observe and document neurovascular status of the extremity, and this needs to be repeated following application of plaster. Patients with neuropathy or neurologic deficits are at greater risk for skin problems with abnormal sensation under the plaster. It is crucial that plaster bandages are rolled on to the limb and not pulled. Figure of eight turns, creases and ridges have to be avoided. Rubbing and massaging plaster bandages during application helps to bond layers together creating stronger and lighter casts. Plaster bandages should be soaked in tepid or slightly warm water. Plaster sets quicker with warm water compared with cold water.

The faster the material sets the greater heat produces and the greater the risk of burns. Fast setting plasters have increased risk of thermal injury. There is a risk if casts are allowed to dry resting on pillow. Temperature elevations could be related to the plaster being dipped too briefly and the water being squeezed too aggressively out of the plaster. The water helps release heat, and if there is not enough, the plaster gets hotter (Szostakowski, et al., 2017).

### 2.7.4 Need for Cast Monitoring

There are complications and risks associated with the use of Plaster of Paris casts. Below are some of the complications.

**Deep Vein Thrombosis (DVT)**

Deep vein thrombosis (DVT) occurs when a blood clot (thrombus) forms in one or more of the deep veins in your body, usually in your legs. Deep vein thrombosis can cause leg pain or swelling, but also can occur with no symptoms.

**Compartment Syndrome**

Compartment syndrome is a painful condition that occurs when pressure within the muscles builds to dangerous levels. This pressure can decrease blood flow, which prevents nourishment and oxygen from reaching nerve and muscle cells (Figure 2-5).

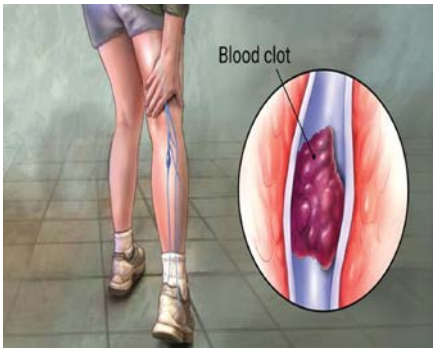


**Figure 2-5:Compartment Syndrome.**

**Soft Tissue Swelling**

Soft tissue swelling associated with the fractured limb will usually subside within 48 hours from the injury leaving the cast loose. This may lead to displacement of well positioned or reduced

fracture, and the reapplication of a new well-fitted cast may be needed. This is more likely to be an issue with unstable fractures (Stress).

**Pressure Sores**

Pressure sores are areas of damaged skin caused by staying in one position for too long. Plaster pressure sores can occur as a result of poor plastering technique associated with inadequate skeletal protection or failure to trim the extremities of the cast correctly (Szostakowski, et al., 2017) (High Temperatures).

**Venous Congestion**

Swelling or blue discoloration of the extremities suggests impaired venous return due to tightness of the plaster. The blue discoloration of venous congestion must be differentiated from bruising (High Stresses).

There are several other complications that relate to long periods of immobilization and include joint stiffness, muscle atrophy, cartilage degradation, ligament weakening, and osteoporosis. Some risks can be minimized with correct Casting Monitoring Technique.

### 2.7.5 Important Factors for Plaster of Paris Cast Monitoring

**Setting Time:**

Although setting takes only a few minutes, drying may take many hours – roughly 36 hours for an arm cast, 48-60 hours for a leg cast and up to 7 days for a hip spica, especially if the atmosphere is moist and cool. Monitoring the setting time of the cast essentially could reduce the wait time for patients (Parmar, et al., 2014).

**Temperature:**

If a bandage is immersed in cold water the initial set will be delayed and thus “working time” lengthened. However, if a very rapid set is required soaking the bandage in warm water will accelerate the rate of reaction. The temperatures beneath the cast could rise to dangerous levels causing thermal injuries due to the exothermic reaction occurring curing setting. The standard range

of temperatures below the cast during setting vary from 31 to 47 °C (Franklin et al., 2013). Monitoring this temperature prevents the cases of thermal injuries and also contributes to quicker healing of the injuries.

**Strength:**

The cast strength is depending on upon the thickness of plaster and the shape of the cast which follows the contours of the affected limb. However, excess plaster will also increase weight and bulk and heat product. Therefore, these different factors must be weighed against each other. Plaster also is permeable and absorbs water losing strength. Monitoring the cast strength could contribute to better immobilization process. Splitting tensile strength of the casting varied from 14 to 42 psi (Parmar et al., 2014). Also monitoring the stresses developed under the cast due to bulging or other reasons alerts the patients before it is turning into an injury. Therefor Plaster of Paris cast must be monitored for pressures, temperature and contaminations to have efficient immobilization and improve the speed of recovery.

## 2.8 Summary

Based on the literature review related to spacer fluid, oil well cement and orthopedic casting material characterization, methods of monitoring the fluid and solid cementitious materials, the following can be summarized:

1. Spacer fluids are characterized by using rheological properties and cleaning efficiency tests were performed to quantify the performance of spacer fluids by various researchers. Electrical characterization of spacer fluids has never been done and very limited literature exists in this space.
2. Various conductive fillers have been studied for enhancing the pressure sensing ability of cement composites. In general, conductive fillers have been used in cementitious and polymeric composites by researchers to make the material more conductive.
3. Electrical resistivity is identified as the best parameter to monitor the behavior of cement composites. Many researchers have characterized using the DC method with four electrodes. Very few researchers tried the AC two probe method of characterization.
4. There are very few papers characterizing the cement using electrical methods.
5. Safety is a major issue during the operation of oil wells as a poor cementing job could result in major accident. Introduction of various secondary additives to the cementitious material in addition to conductive fillers improves the sensing ability and mechanical properties as well.
6. Orthopedic casts in the medical industry are generally tested to improve performance. Real time monitoring techniques are not currently employed for quantifying the performance of the cast material and the encased conditions (temperature, moisture, mechanical stresses).

# CHAPTER 3 MATERIALS AND METHODS

## Introduction

In this chapter, preparation of different types of materials and testing methods used in this study are summarized. Materials of interest are smart cement and smart foam cement. Sample preparation, in- situ treatment methods, thermal property analysis, compression test, method of electrical resistivity measurement, rheological property measurements and the curing conditions are discussed.

## 3.1 Materials

### 3.1.1 UH Biosurfactant

The biosurfactant is produced from waste oil with acclimated bacteria in continuously stirred batch reactor (Harendra et al., 2008; Vipulanandan et al., 2000). The critical micelle concentration (CMC) for this biosurfactant is 0.5 g/L and the surface tension reduces to 30 dynes/cm. The biosurfactant is water soluble and based on Fourier Transform Infra Read (FTIR) spectroscopy analyses both carboxyl (COO-) and hydroxide (OH-) groups were identified in the biosurfactant.

### 3.1.2 Diesel Oil

Diesel oil, representing the oil-based drilling fluid, with a density of 5.6 ppg was used for the cleaning efficiency test. The resistivity of the Oil was greater than 1000 Ωm.

### 3.1.3 Cement

To study the effect of smart cement, the class H oil well cement was used.

### 3.1.4 Smart Cement

Commercially available oil well cement (Class H cement) was modified with conductive fillers to make it a piezoresistive material. The Cement was modified by adding about 0.04% of conductive filler (CF), by weight, and the water to cement ratio was 0.38.

## 3.2 Methods of Testing

### 3.2.1 Spacer Fluid Preparation

The spacer fluid was prepared by using water as the base fluid. Rheology modifiers such as Guargum up to 1% and UH biosurfactant up to 0.4% were added. Also up to 3% KCl was added with the weighting agent lead nitrate ($Pb(NO_3)_2$). KCl was first mixed with water and was mixed thoroughly till it completely dissolved. Then rheology modifier Guargum was added followed with the UH Bio-surfactant and mixed until uniform solution is obtained. This uniform mixture was then mixed with the weighting agent to obtain the spacer fluid. Also, Nano Iron was added to the spacer fluid to enhance the performance with pressure, temperature and magnetic field. Also, the fluid was characterized with electrical resistivity and density measurements at each stage of mixing.

**Density**

The density plays a major role in providing the needed hydrostatic pressure in the wellbore. Density of the spacer fluid with and without Nano Iron was measured immediately after mixing using the standard mud balance cup.

**Electrical Resistivity**

Two different instruments were used to measure the electrical resistivity of the spacer fluid. The instruments were calibrated using standard salt solution.

**(a) *Conductivity Probe***

A commercially available conductivity probe was used to measure the conductivity (inverse of electrical resistivity) of the fluids. The conductivity measuring range was from 0.1μS/cm to 1000 mS/cm, representing a resistivity of 1,000 Ω-m to 0.1 Ω-m, respectively.

**(b) *Digital Resistivity Meter***

The digital resistivity meter measured the resistivity of fluids, slurries, and semi-solids with resistivities in the range of 0.01Ω-m to 400 Ω-m.

**HPHT Testing**

The spacer fluid was tested up to of 500 psi pressure. The change in the bulk resistivity of the material was measured and modelled using Vipulanandan model.

**Rheological Properties**

Rheological properties determine the pumpability and cleaning capability of spacer. The rheology tests for smart spacer fluid with different contents of Nanoiron (nano$Fe_2O_3$) at temperature of 25°C to 75°C and magnetic fields of 0 to 0.6T were tested using a viscometer in the speed range of 0.3 to 600 rpm (shear strain rate of 0.5 $s^{-1}$ to 1024 $s^{-1}$) and related shear stresses were recorded. The speed accuracy of this device was 0.001 rpm. The temperature of the spacer was controlled to an accuracy of ±2˚C. The viscometer was calibrated using several standard solutions. All the rheological tests were performed after 10 minutes of mixing of the spacer solutions. The viscometer was calibrated using several standard solutions.

**Cleaning efficiency test**

The cleaning efficiency test was performed on the spacer fluid to quantify the ability of the spacer to clean the diesel oil representing the oil-based drilling fluid. For this test the following procedure was followed. Initially the viscometer cup and the spindle were cleaned and dried. The dry weight of the spindle was measured ($W_1$). The viscometer cup was filled with diesel oil and ran the spindle for 10 minutes at 100 rpm. After 10 minutes, the viscometer spindle was weighed again with the contamination ($W_2$). Then the spacer fluid was placed in the cup and the spindle was rotated again for 10 minutes at 100 rpm. Then the viscometer spindle was weighted again (W3). Also, the change in the resistivity of the cleaning spacer fluid was measured.

**3.2.2 Cement Mixing Procedure**

Smart cement with a water- to-cement ratio of 0.38 was used in this study. The cement slurries were prepared using hand mixing followed by mixing using a high-shear blender type mixer with bottom driven blades. First, measured amount of mixing water was poured into the container.

Then little amount of conductive fillers was added to the water and then a little amount of cement was mixed to the mixture. Then little by little cement and conductive fillers were gradually added to the container and mixed for about 1 minute so that it could be properly dispersed in the mixing water. Final mixing was done with blender at a low speed for about 4 to 5 minutes to ensure homogeneity. Then the slurry was mixed for about 5 minutes till a uniform consistency has been obtained. A metal spatula was used to recover material sticking to the wall of the mixing container during final mixing. Mixing was done at room temperature of 23±2 °C.

**Cement Specimen Preparation**

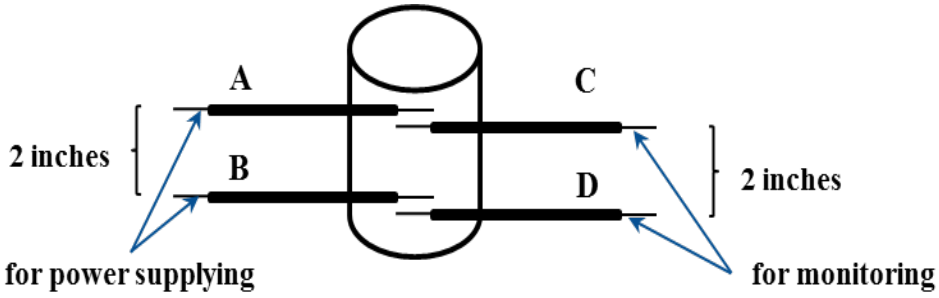


**Figure 3-1:Specimen for Electrical Properties Measurement.**

After mixing, cement specimens were prepared using cylindrical molds with a diameter of 2 inches and a height of 4 inches. Four conductive wires were placed in all the molds (Figure 3-1). The vertical distances between the two wires of the specimens were kept the same. All specimens were capped to minimize moisture loss and were cured up to the day of testing for quantifying the piezoresistivity. In order to have consistent results, at least three specimens were prepared for each type of mix.

**Density**

The density plays a major role in providing the needed hydrostatic pressure in the wellbore. Density of the spacer fluid with and without Nano iron was measured immediately after mixing using the standard mud balance cup.

**Thermal Property Test**

Volumetric specific heat capacity ($C_v$) for the cement composite during hydration at room temperature was tested using the KD2 Pro thermal property meter (Decagon Devices) with and without different additives. An SH-1 sensor (a 30 mm dual needle) was used after the setting of the cement composite to test the $C_v$ of the composite which was used to calculate the heat generated during cement hydration. The range of thermal conductivities measured by the analyzer was from 0.02 to 2 W/mK. The operating environment for the device was 0 to 50°C.

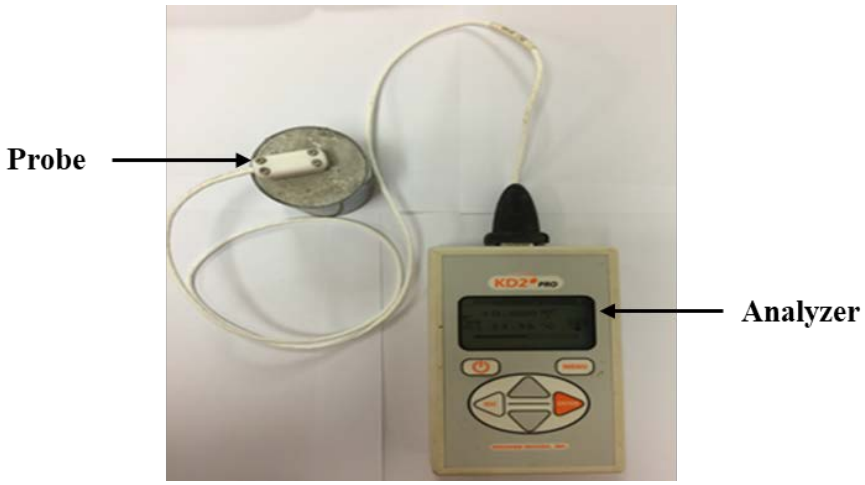


**Figure 3-2:KD2 Pro Thermal Properties Analyzer.**

**Electrical Resistivity**

Identifying the sensing parameter for the cement-based material is vital. After numerous studies by Vipulanandan et al., (2004, 2013 and 2014), electrical resistivity (ρ) was selected as the sensing property for cement-based materials. Resistivity and change in resistivity were used to quantify the sensing properties of the cement.

**Resistivity of Cement Slurry**

Two different instruments were used for resistivity measurements of cement slurries. The digital resistivity meter measured the resistivity directly and the other device, conductivity meter measured the conductivity of the cement slurry and later resistivity was calculated.

**Digital Resistivity meter**

Digital resistivity meter (used in the oil industry) was used measure the resistivity of fluids, slurries and semi-solids directly. Resistivity meter measures resistivity in the range of 0.01 Ω·m to 400 Ω·m. Suction bulb was used to fill the slurry into the Lucite cell. Slurry was filled and discharged several times before the final fill to avoid air bubble in the sample. Then the sample cell was reattached onto the conductive pins on the meter and reading was taken.

**Conductivity Meter**

Commercially available conductivity probe was used to measure the conductivity (inverse of resistivity) of the fluids. In the case of cement, this meter was used during the initial curing of the cement. The conductivity measuring range is from 0.1 µS/cm to 1000 mS/cm, representing a resistivity of 10,000 Ω·m to 0.1 Ω·m. Conductivity meter was first calibrated using standard solution with a known value of conductivity. After calibration, the device was double checked with another standard solution for consistency. The conductivity probe and the digital electrical resistivity device were calibrated using standard solution of sodium chloride (NaCl).


**Figure 3-3:(a) Digital Resistivity Meter and (b) Conductivity Probe.**

**Resistivity of Hardened Cement**

Measuring the resistivity of the hardened cement was a challenge due to the limitation of devices. Also calculating the resistivity from measurable parameters was also a challenge because of the uncertainty in actual conductive path of the current inside the specimen. Therefore, electrical

resistance was measured using LCR meter for hardened cement and during the curing time. To minimize the contact resistances, the resistance was measured at 300 kHz using two- probe method. The idealized circuits for measuring the impedance are shown in Figure 3-4.

The resistance measured at 300 kHz using the two-probe method was correlated to the resistivity (measured using the digital resistivity device) to determine the K factor (Eqn. 3-1) for a time period of initial five hours of curing. This K factor was used to determine the resistivity of the cement with the curing time.

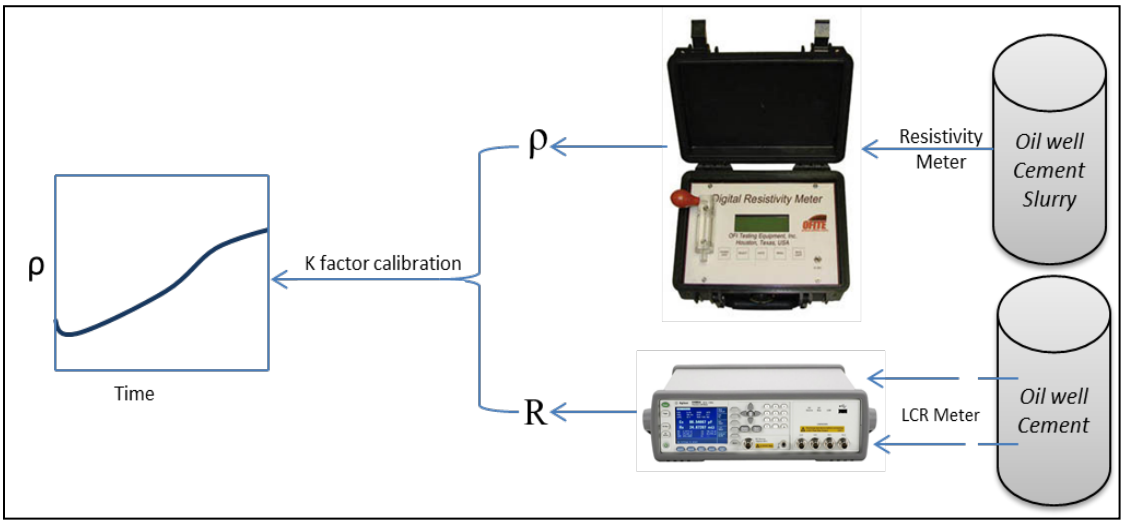


**Figure 3-4:Resistance Measurement Technique (Heidari, 2014).**

Each specimen was calibrated to obtain the electrical resistivity ($\rho$, Ω·m) from the measured electrical resistance ($R$, Ω) based on

$$\rho = \frac{R}{K + GR}, \tag{3-1}$$

where K & G are model constants.

**Compression Test**

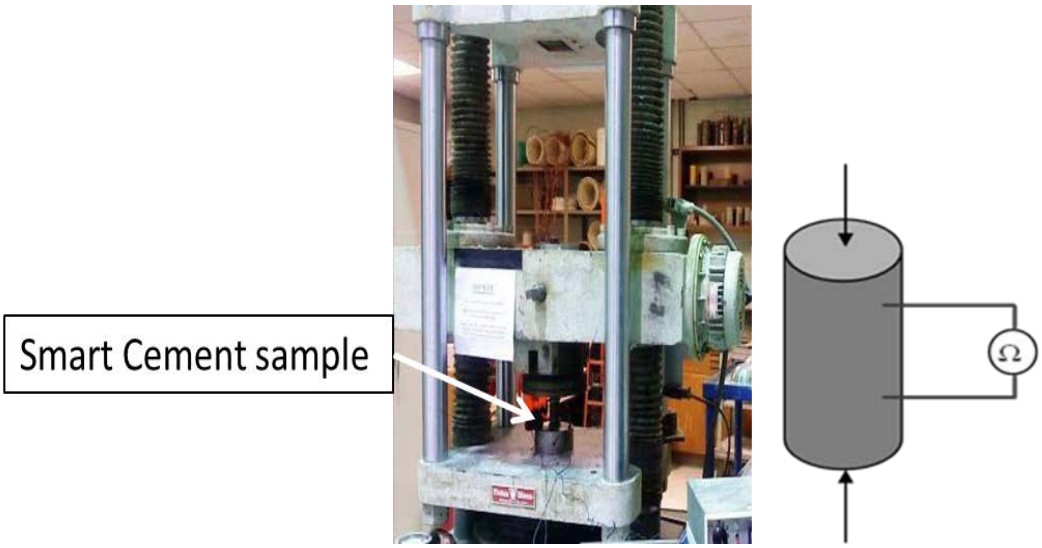


**Figure 3-5:Standard Compression Test.**

The cylindrical specimens (50 mm dia.*100 mm height) were capped and tested at a predetermined controlled displacement rate. Compression tests were performed on cement samples after 1 day and 28 days of curing using a hydraulic compression machine.

**Piezoresistivity Test**

Piezoresistivity describes the change in the electrical resistivity of a material under stress. In this study both cement slurry and solidified cement will be tested and characterized. Since oil well cement serves as pressure-bearing part of the oil and gas wells in real applications, the piezoresistivity of smart cement (stress – resistivity relationship) with different foam contents were investigated under compressive loading at different curing times. During the compression test, electrical resistance was measured in the direction of the applied stress. To eliminate the polarization effect, AC resistance measurements were made using an LCR meter at frequency of 300 kHz (Vipulanandan et al., 2013).

**Rheological test**


**Figure 3-6:Rheological test.**

The rheology tests for smart cement with different foam contents at temperature of 25°C were tested using a viscometer in the speed range of 0.3 to 600 rpm (shear strain rate of 0.5 $s^{-1}$ to 1024 $s^{-1}$). The speed accuracy of this device was 0.001 rpm. The temperature of the slurry was controlled to an accuracy of ±2˚C. The viscometer was calibrated using several standard solutions. All the rheological tests were performed after 10 minutes of mixing of the cement slurries.

### 3.2.3 Smart Orthopedic Cast Material Preparation

Commercially available Plaster of Paris (POP) was used for characterizing the cast material. The Plaster of Paris was modified with conductive fillers to make it a piezoresistive material. The POP was modified by adding 0.05% of conductive filler (CF), by weight of the plaster of Paris. The water to plaster ratio used was 0.5. The Plaster of Paris slurries were prepared using hand mixing by adding POP in stages into the water. After mixing, POP specimens were prepared using cylindrical hollow molds. The Cylindrical hollow molds have internal diameter of 0.79-inch, outer diameter of 2 inches and a height of 4 inches.

**Compression and Tensile Test**

The compression and tensile tests were performed using universal compression testing machine. The compression tests were performed according to ASTM C39 while for tensile test, the procedure of Brazilian tensile testing (splitting tensioning test) was used according to ASTM C496.

**Bending Test**

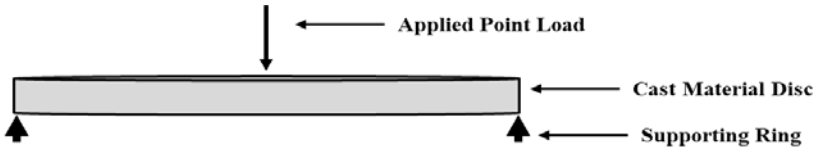


**Figure 3-7:Bending Test Sample Setup**

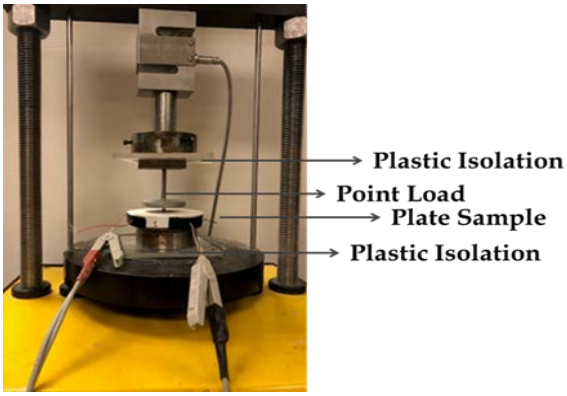


**Figure 3-8:Bending Test Apparatus.**

**Figure 3-9:Electrical Resistance Measurement Apparatus.**

POP specimens were prepared using cylindrical molds and circular plates. The Cylindrical molds are 2 inches in diameter and a height of 4 inches. Circular plates of 3.65 inch diameter with thickness of 0.047 inch and 0.032 inch were also prepared for bending test. This test was performed on plate specimen using point load at the center with compression testing machine. The point load was recorded with the change in resistivity of the POP material using the LCR meter as shown in Figure 3-7, Figure 3-8 & Figure 3-9.

## 3.3 Modeling

### 3.3.1 Theory and Concepts

It was very critical to identify the sensing properties for the cement and drilling mud that can be used to monitor the performance. After years of studies and based on the current study on oil well cements and drilling muds, electrical resistivity (ρ) was selected as the sensing property for cements (Vipulanandan et al., 2005, 2012). Hence two parameters (resistivity and change in resistivity) were used to quantify the sensing properties as

$$R = \rho (L/A) = \rho K, \quad (3\text{-}2)$$

where,

R = electrical resistance,

L = Linear distance between measuring points,

A = effective cross-sectional area,

K = Calibration parameter is determined based on the resistance measurement method.

Normalized change in resistivity with the changing conditions can be represented as

$$\Delta\rho/\rho = \Delta R/R. \quad (3\text{-}3)$$

The modified cement materials represented in terms of resistivity (ρ) to changes (composition, curing and stress) has been quantified to evaluate the sensitivity of the selected parameter.

### 3.3.2 Impedance Model

*Equivalent Circuit.*

It is important to identify the most appropriate equivalent circuit to represent the electrical properties of a material to characterize its performace with time. There are many difficulties associated with choosing a correct equivalent circuit. It was necessary to somehow link the different elements in the circuit to different regions in the impedance data of the corresponding sample. Given the difficulties and uncertainties in establishing this link, researchers tend to take a pragmatic approach and adopt a circuit which they believe to be most appropriate from their knowledge of the expected behavior of the material under study, and demonstrate that the results are consistant with the circuit used.

In this study, different possible equivalent circuits were analyzed to find an appropriate equivalent circuit to represent smart cement and drilling mud.

*Case 1: General Bulk Material –Capacitance and Resistance*

In the equivalent circuit for Case 1, the contacts were connected in series, and both the contacts and the bulk material were represented using a capacitor and a resistor connected in parallel (Figure 3-10).In the equivalent circuit for Case 1, $R_b$ and $C_b$ are resistance and capacitance of the bulk material, respectively; and $R_c$ and $C_c$ are resistance and capacitance of the contacts, respectively. Both contacts are represented with the same resistance ($R_c$) and capacitance ($C_c$), as they are identical. Total impedance of the equivalent circuit for Case 1 ($Z_1$) can be represented as

$$Z_1(\sigma) = \frac{R_b(\sigma)}{1+\omega^2 R_b^2 C_b^2} + \frac{2R_c(\sigma)}{1+\omega^2 R_c^2 C_c^2} - j\left\{\frac{2\omega R_c^2 C_c(\sigma)}{1+\omega^2 R_c^2 C_c^2} + \frac{\omega R_b^2 C_b(\sigma)}{1+\omega^2 R_b^2 C_b^2}\right\}, \quad (3\text{-}4)$$

where $\omega$ is the angular frequency of the applied signal. When the frequency of the applied signal is very low, $\omega \rightarrow 0$, $Z_1 = R_b + 2R_c$, and when it is very high, $\omega \rightarrow \infty$, $Z_1 = 0$.

*Case 2: Special Bulk Material - Resistance Only*

Case 2 is a special case of Case 1 in which the capacitance of the bulk material ($C_b$) is assumed to be negligible (Figure 3-11).

The total impedance of the equivalent circuit for Case 2 ($Z_2$) is

$$Z_2(\sigma) = R_b(\sigma) + \frac{2R_c(\sigma)}{1+\omega^2 R_c^2 C_c^2} - j\frac{2\omega R_c^2 C_c(\sigma)}{1+\omega^2 R_c^2 C_c^2}. \quad (3\text{-}5)$$

When the frequency of the applied signal is very low, $\omega \rightarrow 0$, $Z_2 = R_b + 2R_c$, and when it is very high, $\omega \rightarrow \infty$, $Z_2 = R_b$ (Figure 3-12).

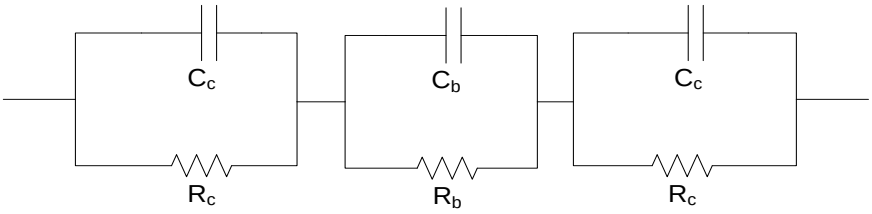


**Figure 3-10:Equivalent Circuit for Case 1.**

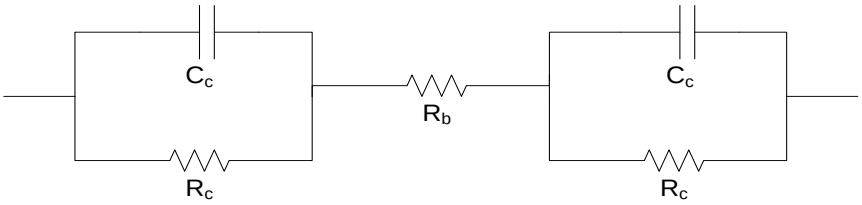


**Figure 3-11:Equivalent Circuit for Case 2.**

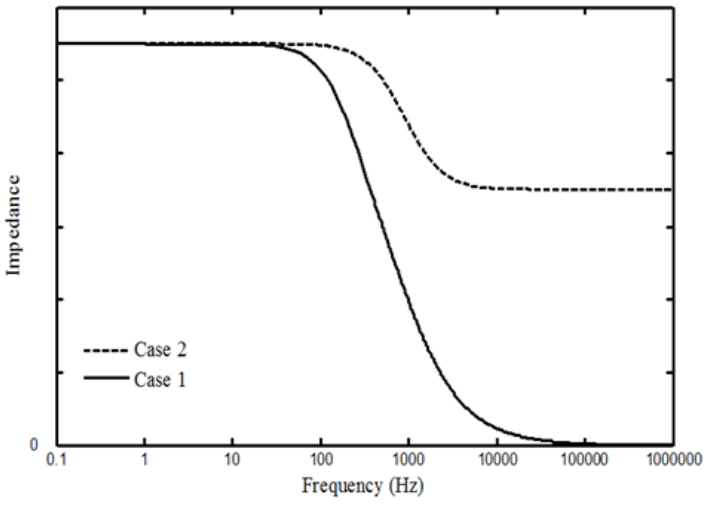


**Figure 3-12:Comparison of Typical Responses of Equivalent Circuits for Case 1 and Case 2.**

The shape of the curves shown in Figure 3-12 is very much influenced by material response and the two probe instruments used for monitoring. Testing of smart cement indicated that Case 2 represented their behavior and hence the bulk material properties can be represented by resistivity and characterized at a frequency of 300 kHz using the two probes.

### 3.3.3 Rheological Modeling

The cement slurry showed non-linear shear thinning behavior with a yield stress. Based on the test results, following conditions have to be satisfied for the model to represent the observed behavior.

Hence the conditions are as follows:

$\tau = \tau_o$ when $\dot{\gamma} = 0$,

$$\frac{d\tau}{d\dot{\gamma}} > 0, \tag{3-6}$$

$$\frac{d^2\tau}{d\dot{\gamma}^2} < 0, \tag{3-7}$$

and $\dot{\gamma} \to \infty \Rightarrow \tau = \tau^*$. (3-8)

The rheological models used for predicating the shear thinning behavior of spacer fluids, smart cement are shown below.

**Herschel-Bulkley model (1926)**

The Bingham plastic model includes both yield stress ($\tau_o$) and a limiting viscosity (μ) at finite shear rates, which the Power law model fails to consider. For a nonlinear flow relationship shear-thinning or shear thickening behavior may be observed and the assumption of constant plastic viscosity is not valid. The Herschel-Bulkley (Eqn. 3-9) model defines a fluid with three parameters and can be represented mathematically as

$$\tau = \tau_{o1} + k * (\dot{\gamma})^n, \tag{3-9}$$

where $\tau$, $\tau_{o1}$, $\dot{\gamma}$, k and n represent the shear stress, yield stress, shear strain rate, correction

parameter and flow behavior index respectively. For $\tau < \tau_o$ the material remains rigid. The model assumes that below the yield stress ($\tau_o$), the slurry behaves as a rigid solid, similar to the Bingham plastic model. For $\tau > \tau_o$ the material flows as a Power law fluid. The exponent n describes the shear thinning and shear thickening behavior. Slurries are considered as shear thinning when n <1 and shear thickening when n >1. A fluid becomes shear thinning when the apparent viscosity decreases with the increase in shear strain rate.

Hence the model should satisfy the following conditions (Eqns. (3-6), (3-7) and (3-8)).

Applying the conditions, we have

$$\frac{d\tau}{d\dot{\gamma}} = k*n*\dot{\gamma}^{(n-1)} > 0 \Rightarrow k*n > 0 \quad (3\text{-}10)$$

and $\frac{d^2\tau}{d\dot{\gamma}^2} = k*n(n-1)*\dot{\gamma}^{(n-2)} \Rightarrow \mathrm{k}*\mathrm{n}*(\mathrm{n}-1) < 0.$ (3-11)

One condition when both Eqn (3-10) and Eqn. (3-11) will be satisfied is as follows:

$0 < n < 1$ and $k_1 > 0$.

From the Eqn. (3-9),

when $\dot{\gamma} \to \infty \Rightarrow \tau_{max.} = \infty$.

Hence Herschel-Bulkley model doesn't satisfy the upper limit condition for the shear stress limit.

**Vipulanandan Rheological model (2014)**

Hyperbolic relationship between shear stress and shear strain rate for the oil well cement slurry with different temperature was investigated (Vipulanandan and Mohammed 2014).

$$\tau - \tau_{o2} = \frac{\dot{\gamma}}{C + D*\dot{\gamma}}, \quad (3\text{-}12)$$

where $\tau$: shear stress (Pa); $\tau_{o2}$: yield stress (Pa); C (Pa. s)$^{-1}$ and D (Pa)$^{-1}$: are model parameters and $\dot{\gamma}$: shear strain rate (s$^{-1}$).

By applying the conditions from Eqns. (3-6), (3-7) and (3-8), we have

$\frac{d\tau}{d\dot{\gamma}} = \frac{(C + D\dot{\gamma}) - \dot{\gamma} * D}{(C + D\dot{\gamma})^2} = \frac{C}{(C + D\dot{\gamma})^2} > 0 \Rightarrow C > 0$ and

$\frac{d^2\tau}{d\dot{\gamma}^2} = \frac{-2CD}{(C + D\dot{\gamma})^3} < 0 \Rightarrow D > 0.$

Also when $\dot{\gamma} \to \infty \Rightarrow \tau_{\max} = \frac{1}{D} + \tau_{o2}.$ (3-13)

Hence this model has a limit on the maximum shear stress; the slurry will produce at relatively high rate of shear strains.

### 3.3.4 Cleaning Efficiency

The cleaning efficiency of the spacer is calculated using the following formula

$$\text{Cleaning efficiency}(\%) = \frac{W_3 - W_2}{W_2 - W_1} * 100, \quad (3\text{-}14)$$

where,

$W_1$ = Weight of the viscometer spindle before the test in gms,

$W_2$ = Weight of viscometer spindle with the contamination in gms and

$W_3$ = Weight of the viscometer spindle after the test in gms.

### 3.3.4 Vipulanandan Cleaning Efficiency model

The relation between maximum shear stress and cleaning efficiency for smart spacer fluid is given as

$$CE(\%) = \frac{\tau_{\max}}{E + F * \tau_{\max}}, \quad (3\text{-}15)$$

where CE (%) = Cleaning efficiency in percentage,

$\tau_{\max}$ = Maximum Shear Stress of the spacer fluid (Pa) and

E, F = Model parameters.

### 3.3.5 Resistivity - Cleaning Efficiency model

The relation between maximum shear stress and change in electrical resistivity for smart spacer fluid is given as

$$CE(\%) = C_o + \left(\frac{(\Delta\rho/\rho)}{G + H * (\Delta\rho/\rho)}\right), \quad (3\text{-}16)$$

where CE (%) = Cleaning efficiency in percentage,

$C_o$ = Cleaning efficiency with no resistivity change (%),

$\Delta\rho/\rho$ = Change in Resistivity of the spacer fluid (%) and

G, H = Model parameters.

### 3.3.6 Bentonite Contamination Model

The relationship between Bentonite Contamination and resistivity of the smart spacer fluid is given by the following equation

$$BC(\%) = \frac{\rho - \rho_o}{I + J(\rho - \rho_o)}, \tag{3-17}$$

where BC = Bentonite Contamination in percentage,

$\rho_o$ = Resistivity of the spacer fluid without oil (Ω-m), ($\rho \geq \rho_o$) and

I, J = Model parameters.

### 3.3.7 Electrical Resistivity model

To characterize the resistivity of the hardened cement, p-q model (Vipulanandan and Paul, 1990) can be used, which is defined as

$$\frac{1}{\rho(t)} = \left(\frac{1}{\rho_{min}}\right) \frac{\left(\frac{t+t_0}{t_{min}}\right)}{q_1 + (1 - p_1 - q_1) * \left(\frac{t+t_0}{t_{min}}\right) + p * \left(\frac{t+t_0}{t_{min}}\right)^{\frac{q_1+p_1}{p_1}}}, \tag{3-18}$$

where $\rho\ (t)$ is electrical resistivity that changes with the curing time (t), $\rho_{min}$ is minimum electrical resistivity, $t_{min}$ is time corresponding to minimum electrical resistivity, $p(t)$ and $q(t)$ are time dependent model parameters. $\rho_{min}$, $t_{min}$ and $t_0$ are time independent model parameters that will explain the changes occurred due to the addition of the materials to the cement slurry.

### 3.3.8 Piezoresistivity Model

Piezoresistivity shall be modeled using p-q model (Vipulanandan and Paul, 1990) which can be used as

$$\sigma = \frac{\sigma_{max} \times \left(\frac{\left(\frac{\Delta\rho}{\rho}\right)}{\left(\frac{\Delta\rho}{\rho}\right)_0}\right)}{q_2 + (1 - p_2 - q_2) \times \left(\frac{\left(\frac{\Delta\rho}{\rho}\right)}{\left(\frac{\Delta\rho}{\rho}\right)_0}\right) + p_2 \times \left(\frac{\left(\frac{\Delta\rho}{\rho}\right)}{\left(\frac{\Delta\rho}{\rho}\right)_0}\right)^{\left(\frac{p_2+q_2}{p_2}\right)}}, \tag{3 19}$$

where $\sigma_{max}$ is the maximum stress at failure, $(\Delta\rho/\rho)_0$ is the piezoresistivity of the hardened cement under the maximum stress, $(\Delta\rho/\rho)$ is the piezoresistivity at any stress $\sigma$ and $p_2$ and $q_2$ are experimentally fit parameters.

### 3.3.9 Artificial Neural Network Model

The excellent predictive capability of artificial neural networks comes from the ability to learn and adapt to new situations in which additional data becomes available. In an artificial neural network, a training set comprising of input and output data is entered and the neural network algorithms attempt to map the process by which inputs become outputs (Sadiq et al., 2000).

The following transfer functions were used for ANN prediction.

i) Sigmoid function given by

$$f(x) = 1/(1 + e^{-x}). \tag{3-20}$$

ii) Hyperbolic tangent function given by

$$\tanh(x) = (e^{-2x} - 1)/(e^{-2x} + 1). \tag{3-21}$$

ANN is a multilayer perceptron (MLP) including three layers. The first layer (input layer) consists of three neurons representing the same three independent variables, the second one is the hidden layer, and the last one is the ANN responses (output layer). The number of neurons required in the hidden layer is determined in a way to minimize both prediction error and number of neurons.

Two accurate neural network algorithms are Back Propagation Neural Networks (BPNN) and Generalized Regression Neural Networks (GRNN). The following is short review on these algorithms.

### 3.3.10 Fluid Loss Model

Fluid loss of the slurry shall be modeled using the following nonlinear equation given by

$$FL = \frac{t}{M + N * t}, \tag{3-22}$$

where $FL$ is the change in fluid loss in mL, $t$ is the time elapsed in minutes and M, N are model parameters.

### 3.3.11 Piezoresistivity Model for Cement Slurry

Piezoresistivity of the slurry shall be modeled using the following equation as

$$\frac{\Delta\rho}{\rho_o} = \frac{-p}{A + Bp}, \tag{3-23}$$

where $(\Delta\rho/\rho_o)$ is the change in bulk resistivity, $p$ is the pressure applied in MPa and A, B are model parameters.

### 3.3.12 Atmospheric Temperature Model

The following mathematical model was used to predict the average changes in the temperature along the time as

$$y - y_o = K * Sin(L(t - t_o)), \tag{3-24}$$

where K and L are model parameters, $y_o$= initial correction factor for average temperature, and $t_o$ = initial correction factor for the time.

### 3.3.13 Change in Resistivity - Temperature Model

Temperature inside orthopedic cast shall be modeled using the following equation as

$$T = T_o + \frac{\frac{\Delta\rho}{\rho_o}}{A + B\frac{\Delta\rho}{\rho_o}}, \tag{3-25}$$

where $(\Delta\rho/\rho_o)$ is the change in bulk resistivity, and $T_o$, A, B are model parameters.

## 3.4 Summary

The summary of experimental study is as follows.

1. For measuring the electrical resistance, AC measurements were performed from 20 Hz to 300 kHz using LCR meter and the behavior of material was characterized based on the impendence response.
2. Standard electrical resistivity meter and conductivity meter was used to determine the resistivity of different modified cement specimens.
3. Tinius Olsen, a hydraulic testing machine was used to test oil well cement specimens under compression in room temperature and pressure conditions.
4. Compressive, tensile and bending property analysis was performed for the cement with various compositions and different treatments. Electrical impedance was also measured while loading the specimen. Piezoresistive based sensitivity of various samples were evaluated based on test results.
5. Thermal properties of smart cement with and without additives were measured using the semi-adiabatic calorimeter and KD2 Pro thermal property meter.
6. Based on the modeling of the behavior, the proposed p-q model predicted the piezoresistive and curing behavior of behavior of both modified and unmodified smart cement.
7. The rheological, curing, piezoresistivity and artificial intelligence models will be used to predict the experimental results.

# CHAPTER 4 SMART SPACER FLUID

Spacer fluid applications require the materials to be multifunctional. Hence the spacer fluid must be modified or treated to enhance the different properties such as density, rheology, cleaning efficiency, resistivity and sensitivity. In this study, oil well spacer fluid was modified with nano$Fe_2O_3$ for in – situ sensing, property modifications and to investigate the effect of magnetic field and temperature on the sensing property.

## 4.1 Density

### 4.1.1 Spacer Fluid

The density of the spacer fluid was 8.46 ppg. With the addition of 0.5% and 1% nano$Fe_2O_3$ (based on total weight of the spacer fluid) increased the density to 8.51 and 8.55 ppg. The density was increased by 0.6% with addition of 0.5% nano$Fe_2O_3$. The density also increased by 1% with the addition of 1% nano$Fe_2O_3$.

### 4.1.2 Oil based and Water based Drilling Fluid

#### Diesel Oil

Diesel oil, representing the oil-based drilling fluid, with a density of 5.6 ppg was used for the cleaning efficiency test. The resistivity of the Oil was greater than 1000 Ω-m.

#### Water Based Drilling Fluid

The water-based drilling fluid is prepared by addition of 8% bentonite by weight of water. The density and resistivity of the drilling fluid was 8.2 ppg and 7 Ω-m.

## 4.2 Electrical Resistivity

The spacer fluids with and without nano$Fe_2O_3$ were subjected to a temperature in the range of 25 °C to 75 °C to investigate the change in electrical resistivity of the fluid.

**T = 25°C:** The resistivity of the smart spacer fluid increased with increase in the addition of nano$Fe_2O_3$ (Figure 4-1). The resistivity of the spacer fluid without and with 0.5% and 1%

nano$Fe_2O_3$ were 0.2 Ω-m, 0.202 Ω-m and 0.207 Ω-m. At 25 ℃ temperature, the increase in the electrical resistivity was 3.5%, with addition of 1% nano$Fe_2O_3$.

**T = 50℃:** The resistivity of the smart spacer fluid at 50 C increased linearly with addition of nano$Fe_2O_3$ content (Figure 4-1). The resistivity of the spacer fluid without, with 0.5% and 1% nano$Fe_2O_3$ were 0.182 Ω-m, 0.187 Ω-m and 0.193 Ω-m. At 50 ℃ temperature, the increase in the electrical resistivity was 6%, with addition of 1% nano$Fe_2O_3$.

**T = 75℃:** The resistivity of the smart spacer fluid increased with increase in the addition of nano$Fe_2O_3$ (Figure 4-1). The resistivity of the spacer fluid without, with 0.5% and 1% nano$Fe_2O_3$ were 0.169 Ω-m, 0.172 Ω-m and 0.176 Ω-m. At 75 ℃ temperature, the increase in the electrical resistivity was about 4%, with addition of 1% nano$Fe_2O_3$.

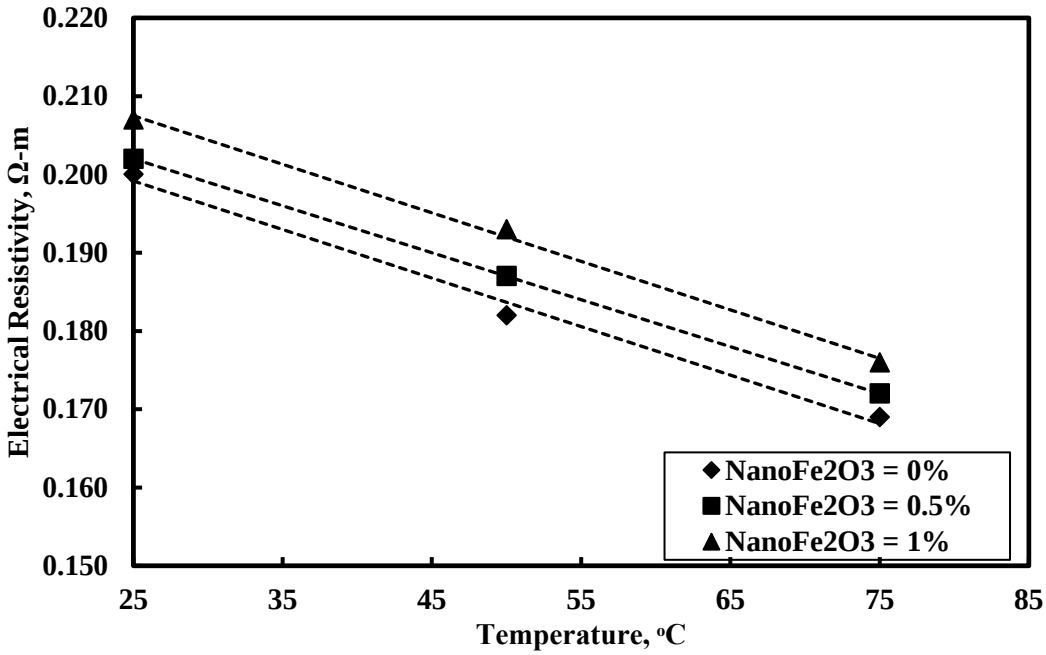


**Figure 4-1:Effect of temperature on electrical resistivity of spacer fluid with different nano$Fe_2O_3$ contents.**

The electrical resistivity of the smart spacer fluid decreased from 0.2 Ω-m to 0.169 Ω-m, a 15 % decrease with the increase in temperature from 25 to 75 °C.

## 4.3 Piezoresistivity

The smart spacer fluid with and without nano$Fe_2O_3$ were subjected to pressure up to 500 psi in the high pressure high temperature chamber (HPHT) to investigate the piezoresistive behavior.

**NanoFe$_2$O$_3$ = 0%:** The resistivity of the spacer fluid decreased nonlinearly with increase in the pressure (Figure 4-2). At 500 psi pressure the decrease in the resistivity was 0.7%, indicating low piezoresistivity characteristics of the spacer fluid.

**NanoFe$_2$O$_3$ = 0.5%:** The resistivity of the smart spacer fluid with 0.5% nano$Fe_2O_3$ decreased nonlinearly with increase in the pressure (Figure 4-2). At 500 psi pressure the decrease in resistivity was 4%, indicating the piezoresistivity characteristics of the smart spacer fluid.

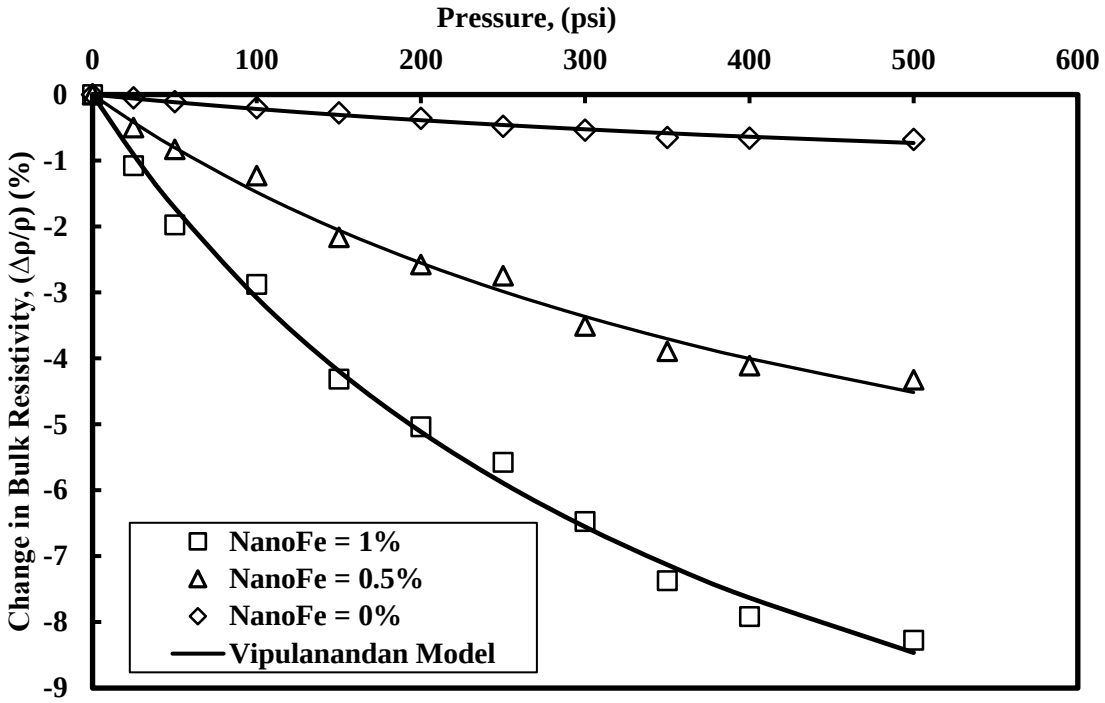


**Figure 4-2:Measured and Predicted Stress-Resistivity Relationship for the Smart Spacer Fluid with different nano$Fe_2O_3$ contents.**

**NanoFe$_2$O$_3$ = 1%:**The resistivity of the smart cement slurry with 1% nanoFe$_2$O$_3$ decreased nonlinearly with increase in the pressure (Figure 4-2).

At 500 psi pressure the decrease in resistivity was 8%, indicating the piezoresistivity characteristics of the smart spacer fluid.

## 4.4 Rheology

### 4.4.1 Effect of NanoFe$_2$O$_3$

Shear stress – shear strain rate relationships were predicted using the Vipulanandan rheological model and compared with the Bingham Plastic and Herschel Bulkley models, as shown in Figure 4-3.

**Bingham model (1919)**

The plastic viscosity (PV) and yield stress were determined using the Bingham plastic model. Increasing the nanoFe$_2$O$^3$ content in the spacer fluid increased the plastic viscosity and yield stress of the spacer fluid. The yield stress of the spacer fluid with 1% nanoFe$_2$O$_3$ increased from 12.34 Pa to19.52 Pa at 25 $^o$C as shown in Figure 4-3 and summarized in Table 4-1. The Plastic viscosity increased from 37 to 49 cP with addition of 1% nanoFe$_2$O$_3$ in the spacer fluid.

**Herschel-Bulkley model (1926)**

The root mean square of error (RMSE) for the Herschel Bulkley model varied between 1.34 to 2.3 Pa. The model parameter k for the spacer fluid at 25 $^o$C varied from 4.58 to 8.14 Pa.s$^n$ as summarized. The model parameter n was in the range of 0.29 to 0.33 (Table 4-1).

**Vipulanandan Rheological model (2014)**

The shear thinning behavior of the spacer fluid with and without nanoFe$_2$O$_3$ was modeled using the Vipulanandan rheological model up to a shear strain rate of 1024 s$^{-1}$ (600 rpm). Increasing the nanoFe$_2$O$_3$ content in the spacer fluid increased the yield stress of the spacer fluid. The yield stress of the spacer fluid increased from 3.94 Pa to 6.63 Pa when nano Fe$_2$O$_3$ was increased from 0% to 1% at 25 $^o$C as shown in figure 3. The $\tau_{max}$ for the spacer fluid increased from 49.4 Pa to 65.5

Pa, 33% increase at the temperature of 25 °C with 1% addition of nano$Fe_2O_3$ respectively as summarized. The root mean square of error was in range of 1.4 to 2.13 Pa (Table 4-1).

**Table 4-1:Rheological model parameters for the spacer fluids with different nano$Fe_2O_3$ contents.**

| | Bingham Plastic Model | | Hershel Bulkley Model | | | | Vipulanandan Model | | | | |
|---|---|---|---|---|---|---|---|---|---|---|---|
| Model Parameters | PV(cP) | Yield Stress (τ), Pa | n | k | τ (yield) | RMSE | A(Pa. s)$^{-1}$ | B (Pa)$^{-1}$ | τ (yield)(Pa) | τ (max)(Pa) | RMSE |
| NanoFe = 0% | 37 | 12.34 | 0.332 | 4.58 | 0 | 1.34 | 3.43 | 0.022 | 3.94 | 49.4 | 1.39 |
| NanoFe = 0.5% | 44 | 17.93 | 0.289 | 7.61 | 0 | 2.3 | 1.95 | 0.019 | 5.43 | 58.1 | 1.7 |
| NanoFe = 1% | 49 | 19.52 | 0.294 | 8.14 | 0 | 2.03 | 199 | 0.017 | 6.63 | 65.5 | 2.13 |

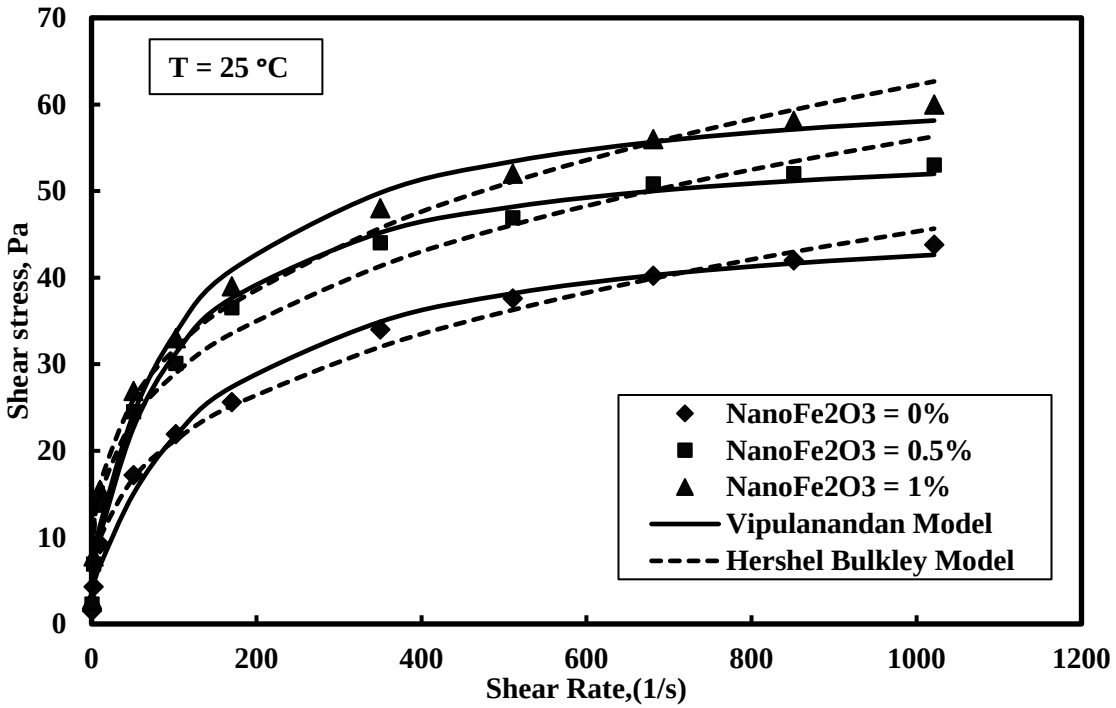


**Figure 4-3:Shear Stress- Shear Strain rate Relationship for Spacer Fluid different nano$Fe_2O_3$ contents.**

### 4.4.2 Effect of Temperature

***<u>NanoFe$_2$O$_3$ = 0%:</u>***

**Bingham model (1919)**

The spacer fluid without nano$Fe_2O_3$ showed decrease in rheological properties with the increase in temperature from 25 to 75 °C. The Plastics viscosity reduced from 37 to 30 cP, 19 % decrease and yield stress from 12.34 Pa to 10.06 Pa, 18.5% decrease as in Figure 4-4.

**Herschel-Bulkley model (1926)**

The model parameter k for the spacer fluid at 25 °C varied from 3.82 to 4.58 Pa.s$^n$ as summarized in Table 4-2. The model parameter n was in range of 0.32 to 0.34. The root mean square of error (RMSE) for the Herschel Bulkley model varied between 0.99 to 1.34 Pa.

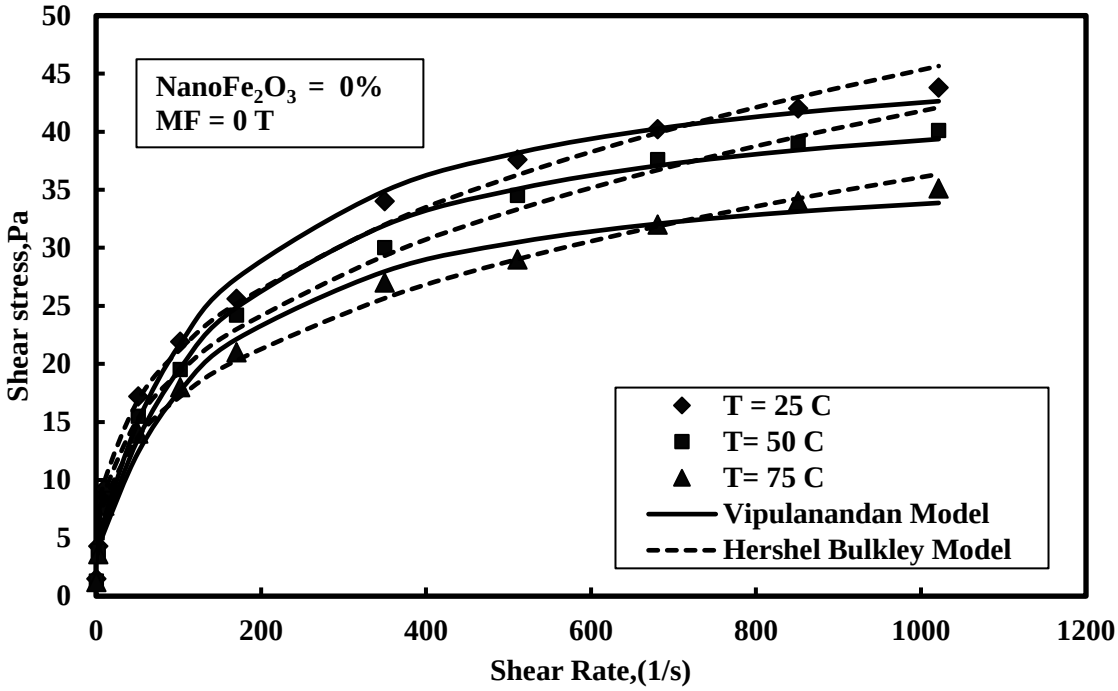


**Figure 4-4:Shear Stress- Shear Strain rate Relationship for Spacer Fluid without nanoFe$_2$O$_3$ at temperatures of 25 °C, 50 °C and 75 °C.**

**Table 4-2:Rheological model parameters for Spacer Fluid without nanoFe$_2$O$_3$ at temperatures of 25 °C, 50 °C and 75 °C.**

| Temperature | Bingham Plastic Model | | Hershel Bulkley Model | | | | Vipulanandan Model | | | | |
|---|---|---|---|---|---|---|---|---|---|---|---|
| Model Parameters | PV(cP) | Yield Stress (τ), Pa | n | k | τ (yield) | RMSE | A(Pa. s)$^{-1}$ | B (Pa)$^{-1}$ | τ (yield)(Pa) | τ (max)(Pa) | RMSE |
| NanoFe = 0%, T = 25 | 37 | 12.34 | 0.332 | 4.58 | 0 | 1.34 | 3.44 | 0.022 | 3.94 | 49.4 | 1.39 |
| NanoFe = 0%, T = 50 | 35 | 11.15 | 0.338 | 4.06 | 0 | 1.17 | 3.91 | 0.024 | 3.62 | 45.3 | 1.2 |
| NanoFe = 0%, T = 75 | 30 | 10.06 | 0.325 | 3.82 | 0 | 0.99 | 4.17 | 0.028 | 3.31 | 39.0 | 0.89 |

**Vipulanandan model (2014)**

The shear thinning behavior of spacer fluids without nanoFe$_2$O$_3$ at temperatures of 25 to 75 °C were tested and modeled using the Vipulanandan model up to a shear strain rate of 1024 s$^{-1}$ (600 rpm). The average yield stress for the spacer fluid at temperature of 25 °C was 3.94 Pa which

decreased with the increase in the temperature to 3.31 Pa at 75 °C, showing 16 % decrease. The $\tau_{max}$ for the spacer fluid decreased from 49.4 Pa to 39 Pa, 21% decrease with the increase in temperature from 25 to 75 °C. The root mean square of error was in range of 0.89 to 1.39 Pa. (Table 4-2).

***NanoFe$_2$O$_3$ = 0.5%:***

**Bingham model (1919)**

The smart spacer fluid with 0.5% nanoFe$_2$O$_3$ showed decrease in rheological properties with the increase in temperature from 25 to 75 °C similar to spacer without nanoFe$_2$O$_3$. The Plastics viscosity reduced from 43 to 41 cP, 4.6 % decrease and yield stress from 17.94 Pa to 13.4 Pa, 25.3% decrease as shown in Figure 4-5.

**Herschel-Bulkley model (1926)**

The root mean square of error (RMSE) for the Herschel Bulkley model varied between 1.99 to 2.4 Pa. The model parameter k for the spacer fluid at 25 °C varied from 4.99 to 7.61 Pa.s$^n$ as summarized in Table 3. The model parameter n was in the range of 0.29 to 0.33 (Table 4-3).

**Vipulanandan model (2014)**

The shear thinning behavior of spacer fluids with 0.5% nanoFe$_2$O$_3$ at temperatures of 25 to 75 °C were tested and modeled using the Vipulanandan model up to a shear strain rate of 1024 s$^{-1}$ (600 rpm).

**Table 4-3:Rheological model parameters for Spacer Fluid with 0.5% nanoFe$_2$O$_3$ at temperatures of 25 °C, 50 °C and 75 °C.**

| Temperature | Bingham Plastic Model | | Hershel Bulkley Model | | | | Vipulanandan Model | | | | |
|---|---|---|---|---|---|---|---|---|---|---|---|
| Model Parameters | PV(cP) | Yield Stress (τ), Pa | n | k | τ (yield) | RMSE | A(Pa. s)$^{-1}$ | B (Pa)$^{-1}$ | τ (yield)(Pa) | τ (max)(Pa) | RMSE |
| NanoFe = 0.5%, T = 25 C | 43 | 17.94 | 0.3 | 7.6 | 0 | 2.3 | 1.95 | 0.019 | 5.43 | 58.1 | 1.7 |
| NanoFe = 0.5%, T = 50 C | 42 | 16.1 | 0.3 | 6.6 | 0 | 2.4 | 2.03 | 0.02 | 3.96 | 54.0 | 1.5 |
| NanoFe = 0.5%, T = 75 C | 41 | 13.4 | 0.3 | 5 | 0 | 1.99 | 2.56 | 0.02 | 2.98 | 53.0 | 1.42 |

The average yield stress for the spacer fluid at temperature of 25 °C was 5.43 Pa which decreased with the increase in the temperature to 2.98 Pa at 75 °C, showing 45 % decrease. The $\tau_{max}$ for the spacer fluid decreased from 58.1 Pa to 53 Pa, 8.7% decrease with the increase in

temperature from 25 to 75 °C. The root mean square of error was in range of 1.42 to 1.7 Pa (Table 4-3).

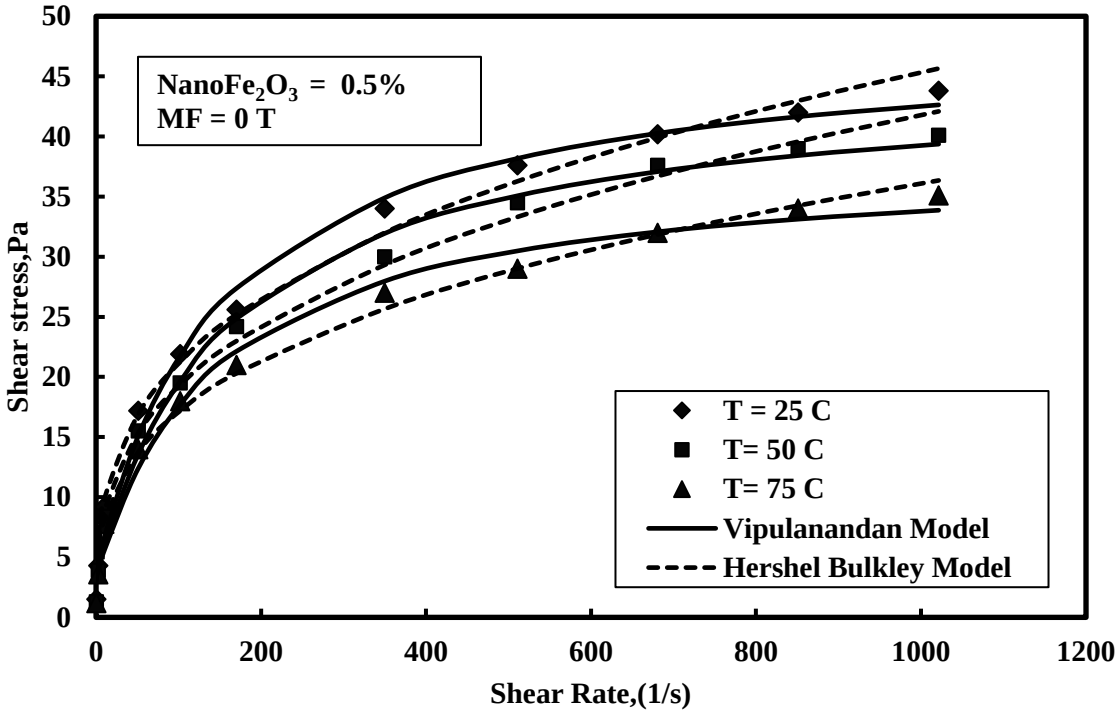


**Figure 4-5:Shear Stress- Shear Strain rate Relationship for Spacer Fluid with 0.5% nano$Fe_2O_3$ at temperatures of 25 ºC, 50 ºC and 75 ºC.**

***<u>NanoFe$_2$O$_3$ = 1%:</u>***

**Bingham model (1919)**

The smart spacer fluid with 1% nano$Fe_2O_3$ showed decrease in rheological properties with increase in temperature from 25 to 75 °C like spacer without nano$Fe_2O_3$. The Plastics viscosity reduced from 49 to 41.7 cP, 17 % decrease and yield stress from 19.52 Pa to 13 Pa, 33.4% decrease as in Figure 4-6.

**Herschel-Bulkley model (1926)**

The shear thinning behavior of spacer fluids with 1% nano$Fe_2O_3$ at temperatures of 25 to 75 °C were tested and modeled using the Herschel Berkley model up to a shear strain rate of 1024 $s^{-1}$ (600 rpm). The root mean square of error (RMSE) for the Herschel Bulkley model varied

between 1.86 to 2.4 Pa. The model parameter k for the spacer fluid at 25 °C varied from 4.78 to 8.15 Pa.s$^n$ as summarized in Table 4. The model parameter n was in the range of 0.29 to 0.33.

**Table 4-4:Rheological model parameters for Spacer Fluid with 1% nano$Fe_2O_3$ at temperatures of 25 °C, 50 °C and 75 °C.**

| Temperature | Bingham Plastic Model | | Hershel Bulkley Model | | | | Vipulanandan Model | | | | |
|---|---|---|---|---|---|---|---|---|---|---|---|
| Model Parameters | PV(cP) | Yield Stress (τ), Pa | n | k | τ (yield) | RMSE | A(Pa. s)$^{-1}$ | B (Pa)$^{-1}$ | τ (yield)(Pa) | τ (max)(Pa) | RMSE |
| NanoFe = 1%, T = 25 C | 49 | 19.52 | 0.295 | 8.15 | 0 | 2.03 | 2 | 0.0175 | 6.64 | 63.8 | 2.13 |
| NanoFe = 1%, T = 50 C | 42 | 16.11 | 0.303 | 6.55 | 0 | 2.4 | 2.46 | 0.018 | 4.79 | 60.3 | 2.35 |
| NanoFe = 1%, T = 75 C | 41.7 | 13.04 | 0.338 | 4.78 | 0 | 1.86 | 2.67 | 0.02 | 2.94 | 52.9 | 1.48 |

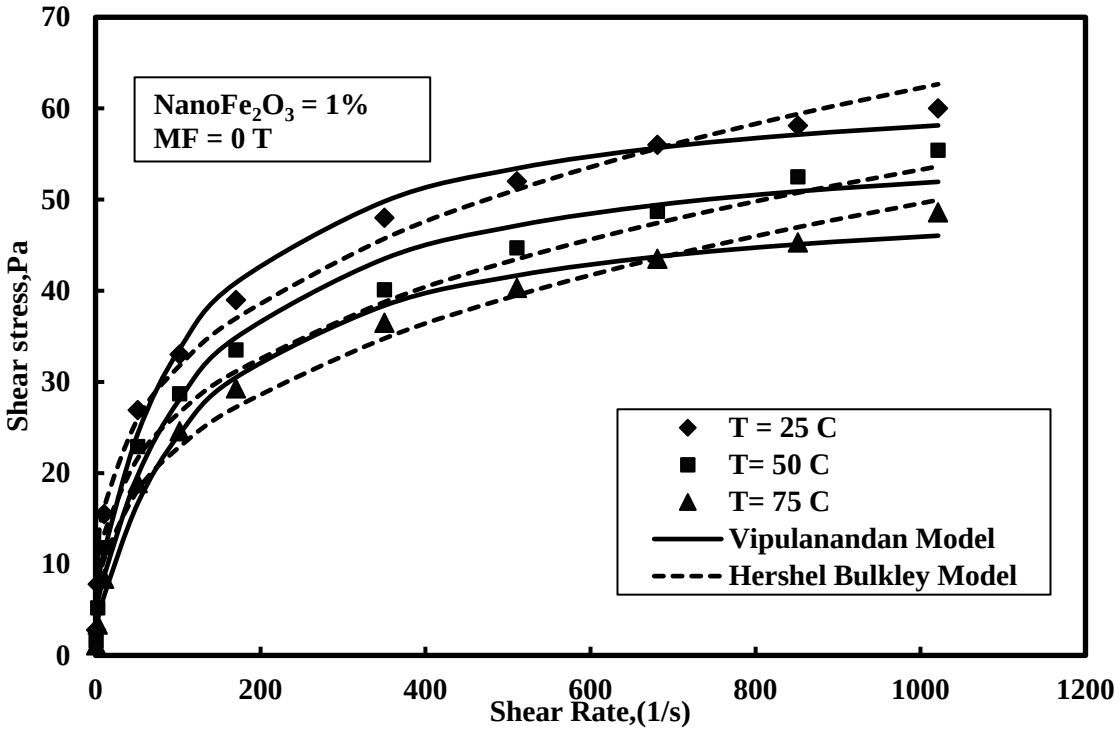


**Figure 4-6:Shear Stress- Shear Strain rate Relationship for Spacer Fluid with 1% nano$Fe_2O_3$ at temperatures of 25 °C, 50 °C and 75 °C.**

**Vipulanandan model (2014)**

The shear thinning behavior of spacer fluids with 1% nano$Fe_2O_3$ at temperatures of 25 to 75 °C were tested and modeled using the Vipulanandan model up to a shear strain rate of 1024 s$^{-1}$ (600 rpm). The average yield stress for the spacer fluid at temperature of 25 °C was 5.43 Pa which decreased with the increase in the temperature to 2.98 Pa at 75 °C, showing 45% decrease. The $\tau_{max}$

for the spacer fluid decreased from 58.1 Pa to 53 Pa, 8.7% decrease with the increase in temperature from 25 to 75 $^{o}$C. The root mean square of error was in range of 1.48 to 2.35 Pa. (Table 4-4).

### 4.4.3 Effect of Magnetic Field

***NanoFe$_2$O$_3$ = 0.5%:***

**Bingham model (1919)**

The spacer fluid with 0.5% nanoFe$_2$O$_3$ showed increase in rheological properties with the increase in the magnetic field from 0 to 0.6 T (Figure 4-7). The Plastics viscosity increased from 43 to 53 cP, a 23.2% increase and yield stress from 17.94 Pa to 21.8 Pa, a 21.5% increase.

**Herschel-Bulkley model (1926)**

The root mean square of error (RMSE) for the Herschel Bulkley model varied between 1.8 to 3.01 Pa. The model parameter k for the spacer fluid at 25 $^{o}$C varied from 7.6 to 9.19 Pa.s$^{n}$ as summarized. The model parameter n was in the range of 0.29 to 0.3 (Table 4-5).

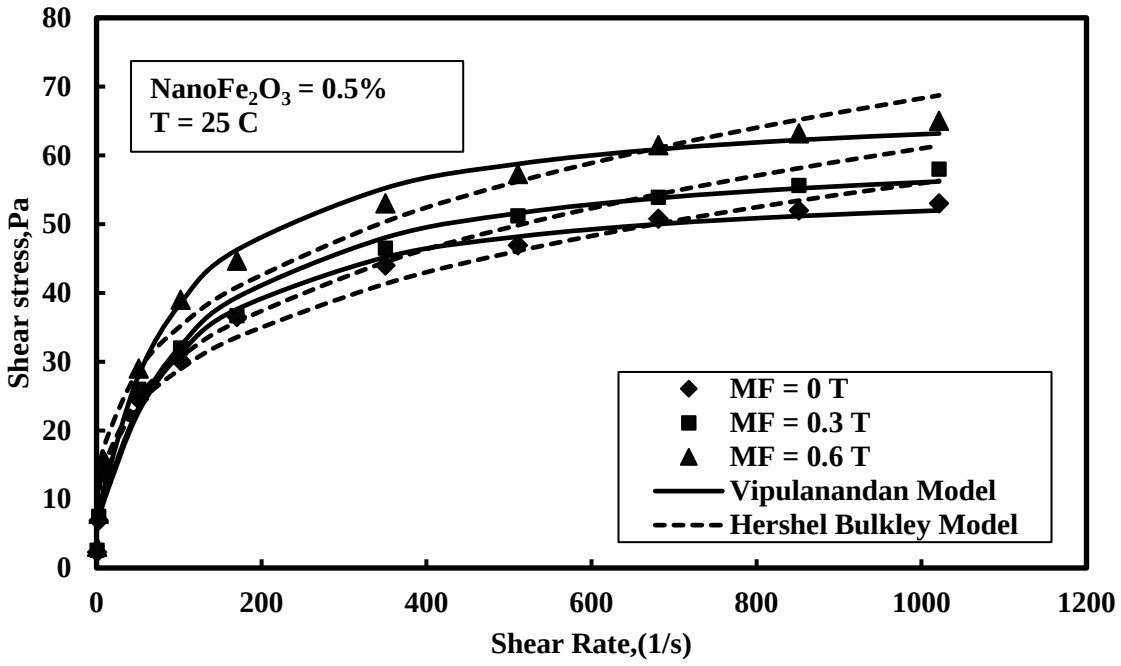


**Figure 4-7:Shear Stress- Shear Strain rate Relationship for Spacer Fluid with 0.5% nanoFe$_2$O$_3$ at temperatures of 25$^{o}$C under Magnetic Field Strengths of 0, 0.3T and 0.6 T.**

**Vipulanandan model (2014)**

Increasing the magnetic field strength from 0 T to 0.6 T, increased the yield stress from 5.43 to 5.95 Pa and $\tau_{max}$ from 58.1 to 68.5 Pa at room temperature. The maximum shear stress increased by 18% for increasing the magnetic field from 0 to 0.6 T as in figure 8. The root mean square of error was in range of 1.6 to 1.7 Pa. (Table 4-5).

**Table 4-5:Rheological model parameters for spacer fluid with 0.5% nano$Fe_2O_3$ at temperatures of 25 °C under Magnetic Field Strengths of 0, 0.3 T and 0.6 T.**

| Magnetic Field | Bingham Plastic Model | | Hershel Bulkley Model | | | | Vipulanandan Model | | | | |
|---|---|---|---|---|---|---|---|---|---|---|---|
| Model Parameters | PV(cP) | Yield Stress (τ), Pa | n | k | τ (yield) | RMSE | A(Pa. s)$^{-1}$ | B (Pa)$^{-1}$ | τ (yield)(Pa) | τ (max)(Pa) | RMSE |
| MF = 0 T | 43 | 17.94 | 0.29 | 7.61 | 0 | 2.3 | 1.95 | 0.019 | 5.43 | 58.1 | 1.7 |
| MF = 0.3 T | 42 | 16.1 | 0.3 | 7.6 | 0 | 1.8 | 2.09 | 0.018 | 6.35 | 61.9 | 1.6 |
| MF = 0.6 T | 53 | 21.8 | 0.29 | 9.19 | 0 | 3.01 | 1.5 | 0.016 | 5.95 | 68.5 | 1.74 |

***<u>NanoFe$_2$O$_3$ = 1%:</u>***

**Bingham model (1919)**

The spacer fluid with 1% nano$Fe_2O_3$ showed increase in rheological properties with the increase in the magnetic field from 0 to 0.6 T. The Plastics viscosity increased from 49 to 62 cP, a 26.5% increase and yield stress from 19.52 Pa to 24.4 Pa, a 25% increase (Figure 4-8 and Table 4-6).

**Herschel-Bulkley model (1926)**

The root mean square of error (RMSE) for the Herschel Bulkley model varied between 2 to 3.01 Pa. The model parameter k for the spacer fluid at 25 °C varied from 8.15 to 9.97 Pa.s$^n$ as summarized in Table 1. The model parameter n was in range of 0.29 to 0.3 (Figure 4-8).

**Vipulanandan model (2014)**

Increasing the magnetic field strength from 0 T to 0.6 T, increased the yield stress from 6.64 to 7.8 Pa and $\tau_{max}$ from 63.8 to 84.7 Pa at room temperature. The maximum shear stress increased by 32.7% for increasing the magnetic field from 0 to 0.6 T as in figure 9. The root mean square of error was in range of 2 to 2.2 Pa. (Table 4-6).

**Table 4-6:Rheological model parameters for spacer fluid with 1% nano$Fe_2O_3$ at temperatures of 25 °C under Magnetic Field Strengths of 0 , 0.3 T and 0.6 T.**

| Magnetic Field | Bingham Plastic Model | | Hershel Bulkley Model | | | | Vipulanandan Model | | | | |
|---|---|---|---|---|---|---|---|---|---|---|---|
| Model Parameters | PV(cP) | Yield Stress (τ), Pa | n | k | τ (yield) | RMSE | A(Pa. s)$^{-1}$ | B (Pa)$^{-1}$ | τ (yield)(Pa) | τ (max)(Pa) | RMSE |
| MF = 0 T | 49 | 19.52 | 0.3 | 8.15 | 0 | 2.03 | 2 | 0.0175 | 6.64 | 63.8 | 2.13 |
| MF = 0.3 T | 53 | 21.5 | 0.29 | 8.97 | 0 | 2.2 | 1.918 | 0.016 | 7.70 | 70.2 | 2.2 |
| MF = 0.6 T | 62 | 24.4 | 0.3 | 9.97 | 0 | 3.01 | 1.58 | 0.013 | 7.80 | 84.7 | 2.01 |

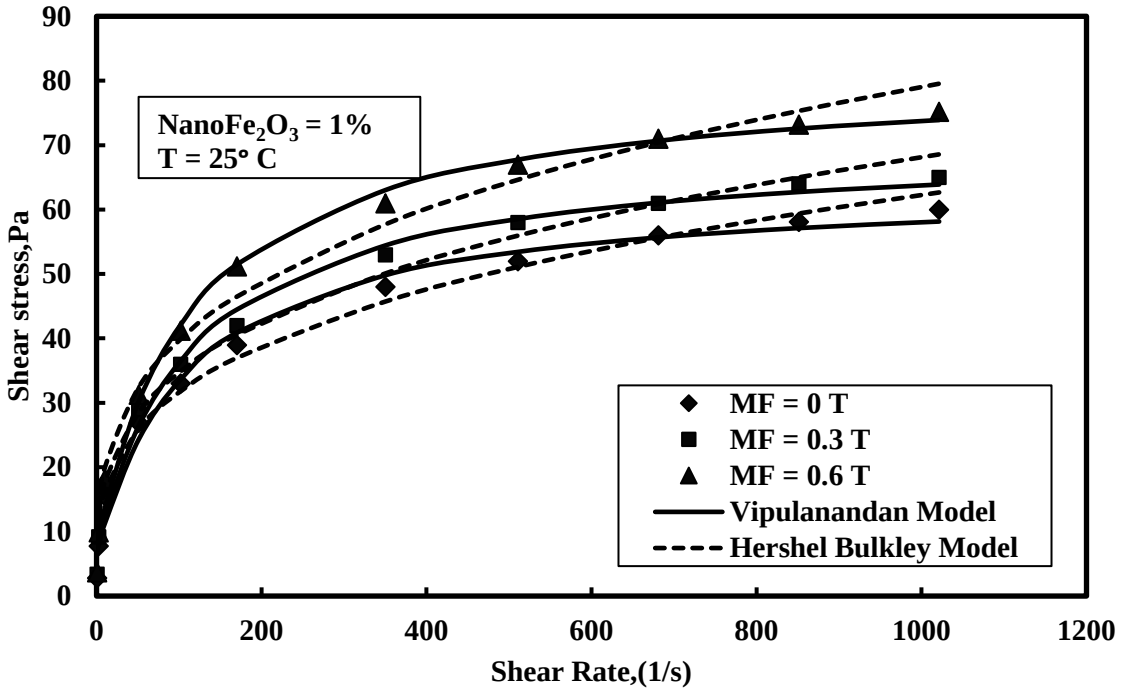


**Figure 4-8:Shear Stress- Shear Strain rate Relationship for Spacer Fluid with 1% nano$Fe_2O_3$ at temperatures of 25 °C under Magnetic Field Strengths of 0 , 0.3 T and 0.6 T.**

### 4.4.4 Effect of Bentonite Contamination

***Bentonite Contamination = 0.15%:***

**Bingham model (1919)**

The spacer fluid with 0.15% bentonite showed increase in rheological properties with the increase in nano$Fe_2O_3$ content at temperature of 25 °C. The Plastics viscosity increased from 39.7 to 55.2 cP, 40 % increase and yield stress from 10.3 Pa to 18.2 Pa, 76% increase as in Figure 4-9.

**Herschel-Bulkley model (1926)**

The root mean square of error (RMSE) for the Herschel Bulkley model varied between 1.08 to 3.38 Pa.

The model parameter k for the spacer fluid at 25 $^{o}$C varied from 3.32 to 6.9 Pa.s$^{n}$ as summarized in Table 4-7. The model parameter n was in range of 0.32 to 0.37.

**Vipulanandan model (2014)**

The shear thinning behavior of spacer fluids with different nano$Fe_2O_3$ contents and contaminated with 0.15% bentonite were tested and modeled using the Vipulanandan model up to a shear strain rate of 1024 $s^{-1}$ (600 rpm). The average yield stress for the spacer fluid without nano$Fe_2O_3$ was 2.91 Pa which increased with the increase in the addition of nano$Fe_2O_3$, showing 14 % increase. The $\tau_{max}$ for the spacer fluid increased from 50.5 Pa to 70 Pa, 38.6% increase with the increase in the addition of nano$Fe_2O_3$ at temperature of 25 °C. The root mean square of error was in range of 1.41 to 1.56 Pa. (Table 4-7)

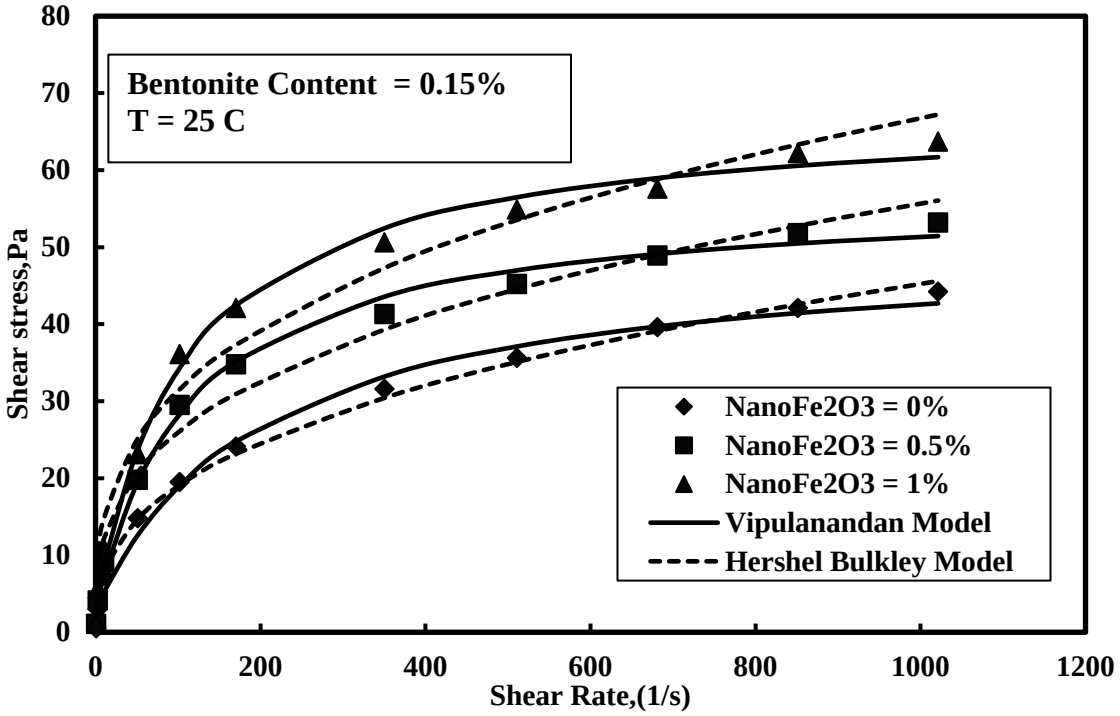


**Figure 4-9:Shear Stress- Shear Strain rate Relationship for Spacer Fluid with different nano$Fe_2O_3$ contents and 0.15 % bentonite contamination at temperature of 25 $^{o}$C.**

**Table 4-7:Bingham Plastic, Herchel-Bulkley and Hyperbolic Rheological model parameters for Spacer Fluid with different nano$Fe_2O_3$ contents and 0.15 % bentonite contamination at temperature of 25 °C.**

| | Bingham Plastic Model | | Hershel Bulkley Model | | | | Vipulanandan Model | | | | |
|---|---|---|---|---|---|---|---|---|---|---|---|
| Model Parameters | PV(cP) | Yield Stress (τ), Pa | n | k | τ (yield) | RMSE | C(Pa. s)$^{-1}$ | D (Pa)$^{-1}$ | τ (yield)(Pa) | τ (max)(Pa) | RMSE |
| NanoFe = 0% | 39.7 | 10.31 | 0.38 | 3.32 | 0 | 1.08 | 4.2 | 0.021 | 2.91 | 50.5 | 1.41 |
| NanoFe = 0.5% | 46.3 | 15.01 | 0.34 | 5.62 | 0 | 2.6 | 2.1 | 0.019 | 2.81 | 55.4 | 1.35 |
| NanoFe = 1% | 55.2 | 18.24 | 0.33 | 6.9 | 0 | 3.38 | 1.71 | 0.015 | 3.31 | 70.0 | 1.56 |

***Bentonite Contamination = 0.3%:***

**Bingham model (1919)**

The spacer fluid with 0.3% bentonite contamination showed increase in rheological properties with the increase in nano$Fe_2O_3$ content at temperature of 25 °C. The Plastics viscosity increased from 39.4 to 57.1 cP, 45 % increase and yield stress from 11.25 Pa to 20.26 Pa, 80% increase as in Table 4-8.

**Herschel-Bulkley model (1926)**

The root mean square of error (RMSE) for the Herschel Bulkley model varied between 1 to 3.98 Pa. The model parameter k for the spacer fluid at 25 °C varied from 3.84 to 7 Pa.s$^n$ as summarized in Table 4-8. The model parameter n was in range of 0.31 to 0.36 (Figure 4-10).

**Vipulanandan model (2014)**

The shear thinning behavior of spacer fluids with different nano$Fe_2O_3$ contents and contaminated with 0.3% bentonite were tested and modeled using the Vipulanandan model up to a shear strain rate of 1024 $s^{-1}$ (600 rpm). The average yield stress for the spacer fluid without nano$Fe_2O_3$ was 3.81 Pa which decreased with the increase in the addition of nano$Fe_2O_3$, showing 15 % decrease. The τmax for the spacer fluid increased from 51.4 Pa to 74.7 Pa, 45.3% increase with the increase in the addition of nano$Fe_2O_3$ at temperature of 25 °C. The root mean square of error was in range of 1.4 to 1.9 Pa (Table 4-8).

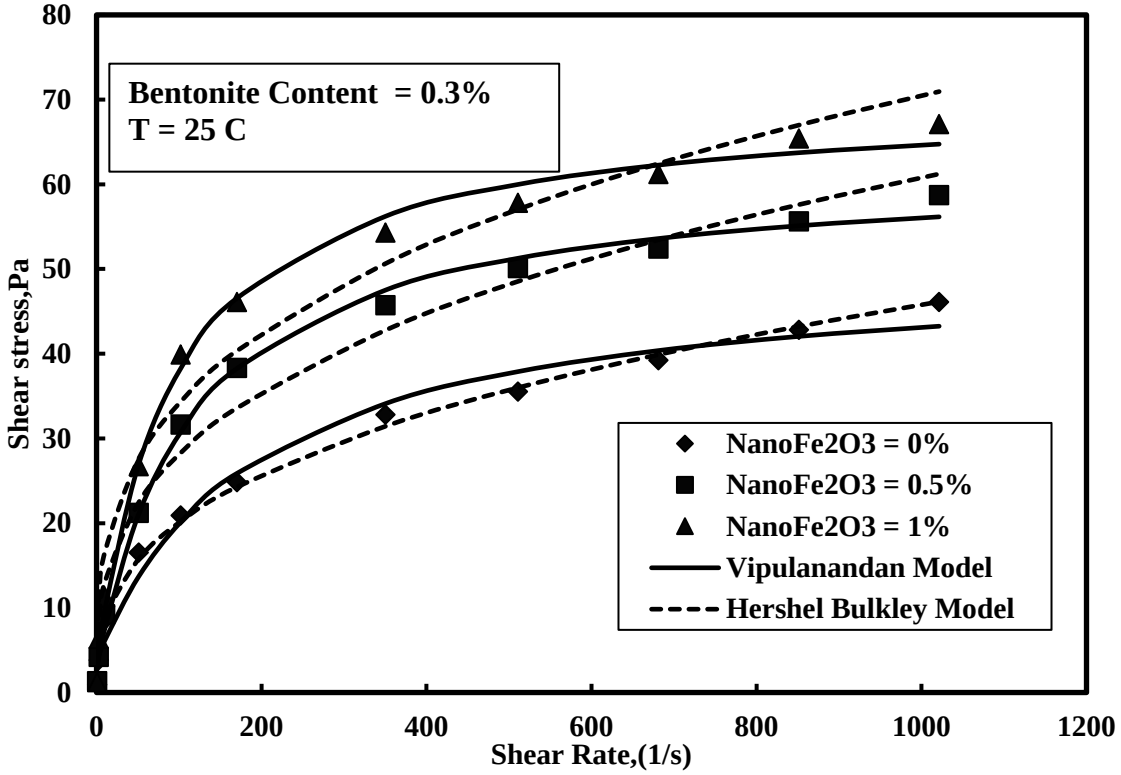


**Figure 4-10:Shear Stress- Shear Strain rate Relationship for Spacer Fluid with different nano$Fe_2O_3$ contents and 0.3% bentonite contamination at temperature of 25 °C.**

**Table 4-8:Bingham Plastic, Herchel-Bulkley and Hyperbolic Rheological model parameters for Spacer Fluid with different nano$Fe_2O_3$ contents and 0.3 % bentonite contamination at temperature of 25 °C.**

| | Bingham Plastic Model | | Hershel Bulkley Model | | | | Vipulanandan Model | | | | |
|---|---|---|---|---|---|---|---|---|---|---|---|
| Model Parameters | PV(cP) | Yield Stress (τ), Pa | n | k | τ (yield) | RMSE | C(Pa. s)$^{-1}$ | D (Pa)$^{-1}$ | τ (yield)(Pa) | τ (max)(Pa) | RMSE |
| NanoFe = 0% | 39.4 | 11.25 | 0.36 | 3.84 | 0 | 1 | 4.08 | 0.021 | 3.81 | 51.4 | 1.88 |
| NanoFe = 0.5% | 50.7 | 16.18 | 0.34 | 6 | 0 | 3.02 | 1.92 | 0.016 | 2.73 | 65.2 | 1.25 |
| NanoFe = 1% | 57.14 | 20.26 | 0.32 | 7.99 | 0 | 3.98 | 1.39 | 0.014 | 3.24 | 74.7 | 1.58 |

***Bentonite Contamination = 0.5%:***

**Bingham model (1919)**

The spacer fluid with 0.5% bentonite contamination showed increase in rheological properties with the increase in nano$Fe_2O_3$ content at temperature of 25 °C. The Plastics viscosity increased from 43.2 to 58.9 cP, 36% increase and yield stress from 13 Pa to 22.7 Pa, 75% increase as in Figure 4-11.

**Herschel-Bulkley model (1926)**

The root mean square of error (RMSE) for the Herschel Bulkley model varied between 1.34 to 3.33 Pa. The model parameter k for the spacer fluid at 25°C varied from 4.57 to 9.36 Pa.s$^n$ as summarized in Table 4-9. The model parameter n was in range of 0.3 to 0.35.

**Vipulanandan model (2014)**

The shear thinning behavior of spacer fluids with different nano$Fe_2O_3$ contents and contaminated with 0.5% bentonite were tested and modeled using the Vipulanandan model up to a shear strain rate of 1024 $s^{-1}$ (600 rpm).

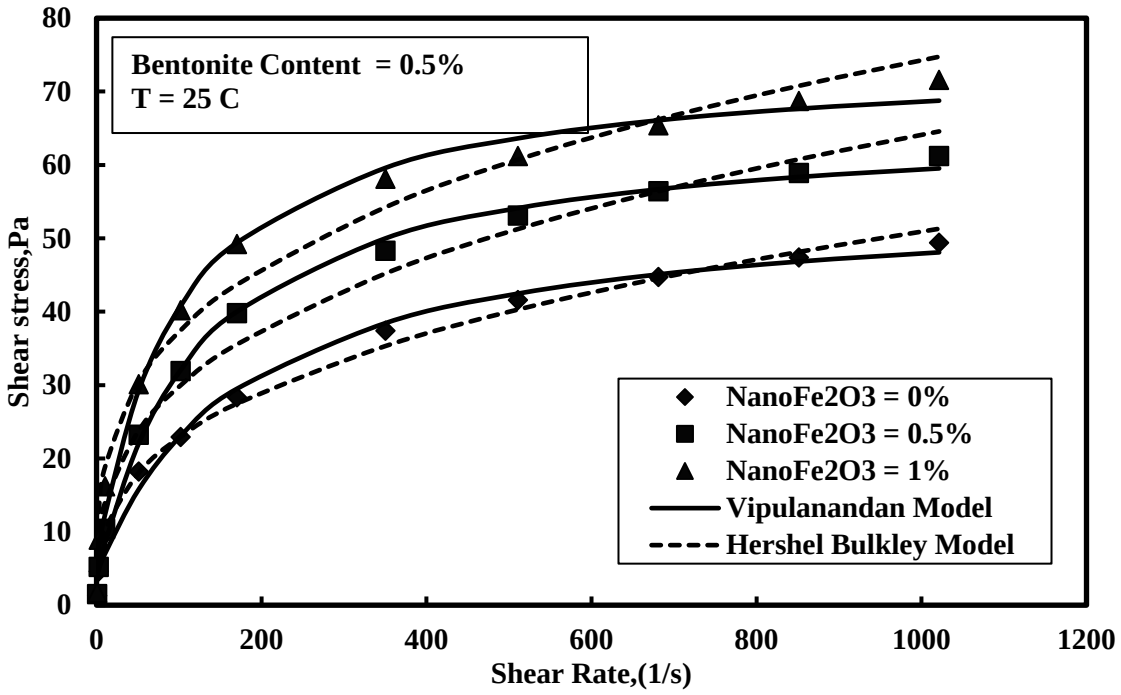


**Figure 4-11:Shear Stress- Shear Strain rate Relationship for Spacer Fluid with different nano$Fe_2O_3$ contents and 0.5 % bentonite contamination at temperature of 25 °C.**

The average yield stress for the spacer fluid without nano$Fe_2O_3$ was 4.18 Pa which increased with the increase in the addition of nano$Fe_2O_3$, showing 41 % increase. The $\tau_{max}$ for the spacer fluid increased from 56.8 Pa to 77.3 Pa, 36% increase with the increase in the addition of

nano$Fe_2O_3$ at temperature of 25 °C. The root mean square of error was in range of 1.2 to 2.1 Pa (Table 4-9).

**Table 4-9: Bingham Plastic, Herchel-Bulkley and Hyperbolic Rheological model parameters for Spacer Fluid with different nano$Fe_2O_3$ contents and 0.5 % bentonite contamination at temperature of 25 °C.**

| | Bingham Plastic Model | | Hershel Bulkley Model | | | | Vipulanandan Model | | | | |
|---|---|---|---|---|---|---|---|---|---|---|---|
| Model Parameters | PV(cP) | Yield Stress (τ), Pa | n | k | τ (yield) | RMSE | C(Pa. s)$^{-1}$ | D (Pa)$^{-1}$ | τ (yield)(Pa) | τ (max)(Pa) | RMSE |
| NanoFe = 0% | 43.2 | 13.02 | 0.35 | 4.57 | 0 | 1.34 | 3.41 | 0.019 | 4.18 | 56.8 | 1.52 |
| NanoFe = 0.5% | 53.3 | 17.26 | 0.33 | 6.42 | 0 | 2.83 | 1.96 | 0.015 | 3.61 | 70.3 | 1.23 |
| NanoFe = 1% | 58.9 | 22.74 | 0.3 | 9.36 | 0 | 3.33 | 1.44 | 0.014 | 5.89 | 77.3 | 2.16 |

## 4.5 Cleaning Efficiency

The cleaning efficiency test of the smart spacer fluid to effectively clean the bentonite drilling mud was performed as shown in Figure 4-12. The cleaning efficiency of the spacer fluid was 82.3% without the addition of nano$Fe_2O_3$. With the addition of nano$Fe_2O_3$ the cleaning efficiency increased from 82.3 to 98.5%, 16.2% increase in the efficiency (Figure 4-13).

**Figure 4-12: Cleaning efficiency test using Viscometer.**

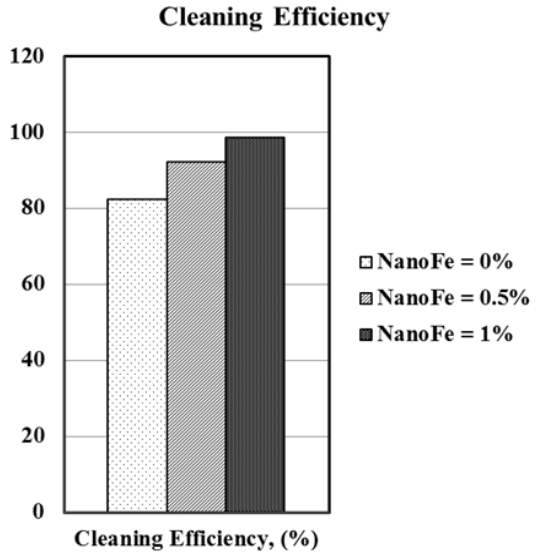


**Figure 4-13:Cleaning efficiency of Spacer Fluid with increasing NanoFe$_2$O$_3$ contents.**

### 4.5.1 Cleaning Efficiency & Maximum Shear Stress

The relation between maximum shear stress and cleaning efficiency for smart spacer fluid is given by Vipulanandan Cleaning Efficiency model (Eqn. 3-15). The model parameters E and F are 0.49 Pa/percent and 0.0025 /percent respectively for the cleaning efficiency model. The $R^2$ and RMSE for the model are 0.99 and 1.53%. The maximum shear stress ($\boldsymbol{\tau_{max}}$) of the smart spacer fluid indicated the better cleaning ability of spacer fluid with 1% nanoFe$_2$O$_3$ (Figure 4-14). The $\boldsymbol{\tau_{max}}$ increased from 49.4 to 65.5 Pa, a 32.5% increase with the addition of 1% nanoFe$_2$O$_3$ while similarly the cleaning efficiency increased from 82 to 99% (Table 4-1 & Table 4-10 ).

The main reason for the increased efficiency was having better rheological properties which produce higher shear stresses for cleaning and high surface to volume ratio of the nanoparticles. The maximum shear stress required to generate 100% cleaning efficiency was 65.5 Pa. The Nano Iron particles consists of magnetic iron oxide core surrounded by cross linked amphiphilic polymer poly-block-styrene (acrylic acid), possessing both hydrophilic acrylic and hydrophobic styrene groups which interact with hydrocarbons present in crude oils to enhance cleaning ability.

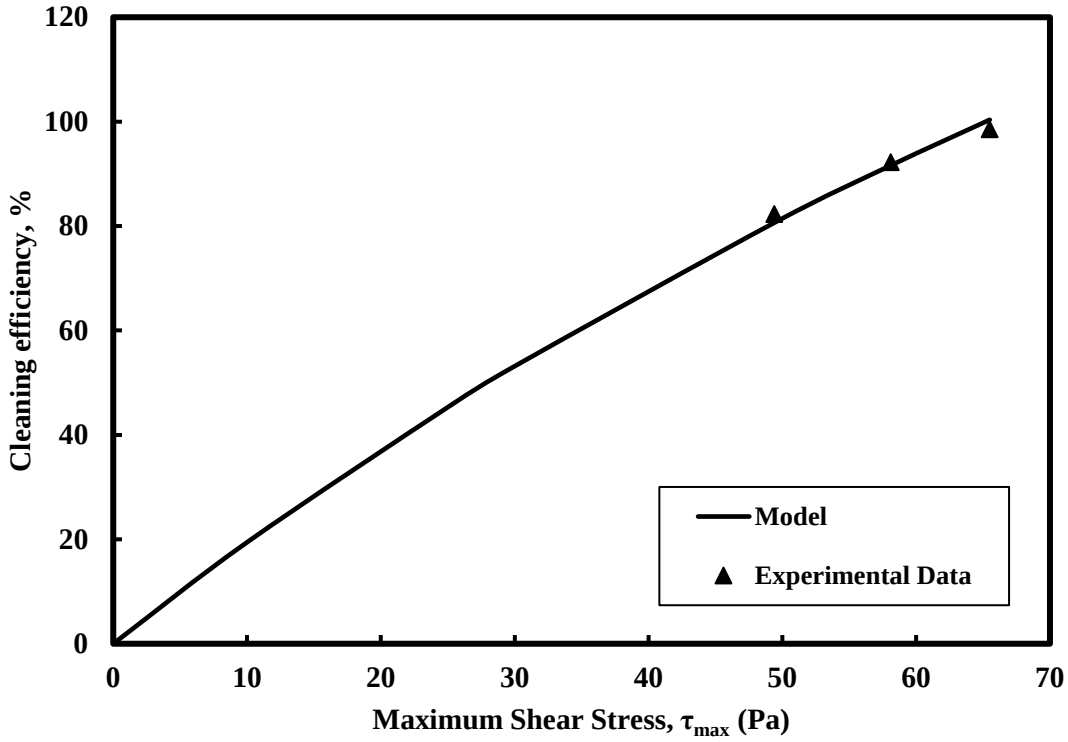


**Figure 4-14:Relation between maximum Shear Stress and cleaning efficiency of Spacer Fluid.**

### 4.5.2 Cleaning Efficiency & Change in Electrical Resistivity

The relation between cleaning efficiency and change in electrical resistivity for smart spacer fluid is given by Resistivity - Cleaning Efficiency model (Eqn. 3-16). The constant $C_o$ for the spacer fluid cleaning efficiency vs resistivity change model is 49.8 %. The model parameters G and H were 0.084 and 0.0156 /percent. The $R^2$ and RMSE for the model are 0.99 and 1.358%. Change in electrical resistivity of smart spacer fluid measured before and after the test correlated with the cleaning efficiency of the smart spacer fluid. The Electrical resistivity increased after the test with the contamination spacer fluids with bentonite. The smart spacer fluid with 1% nano$Fe_2O_3$ showed maximum change in the resistivity, 16% due increased cleaning and higher amount of bentonite contamination in the spacer fluid (Figure 4-15).

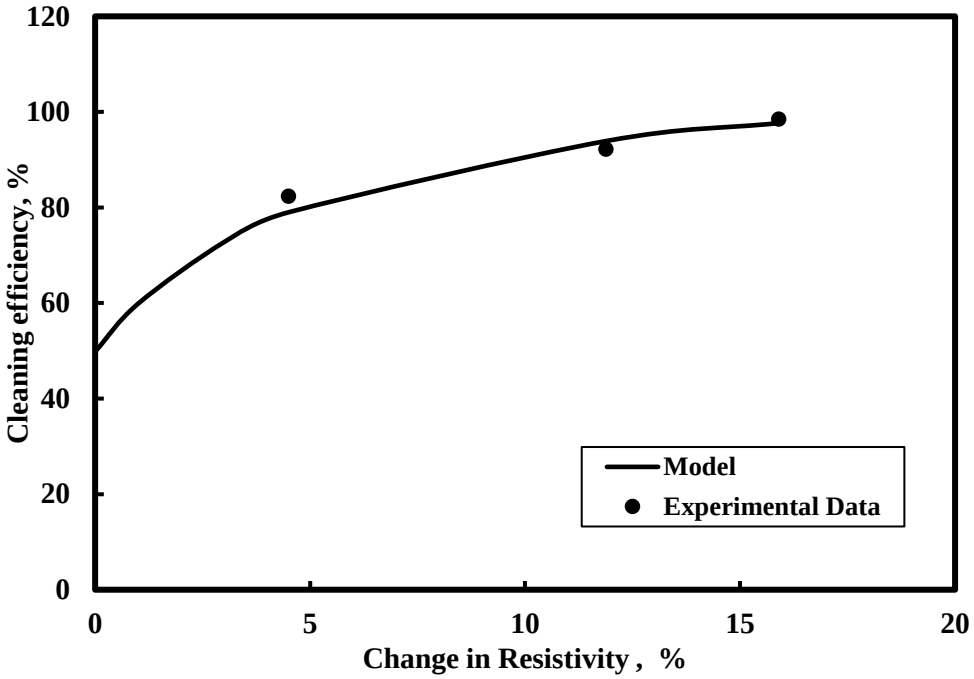


**Figure 4-15:Relation between change in resistivity and cleaning efficiency of the smart spacer fluid.**

## 4.6 Bentonite Contamination Prediction

The relationship between Bentonite Contamination and resistivity of the smart spacer fluid is given by the Bentonite contamination model (Eqn. 3-17). The model parameters I and J are equal to 0.053 Ω-m/percent and 0.43 /percent for the smart spacer fluid. The $R^2$ and RMSE for the model are 0.99 and 0.01%. The electrical resistivity parameter was sensitive to changes in the spacer in real time. The electrical resistivity was found to increase with the increase in the Bentonite content in the smart spacer fluid. The resistivity of spacer fluid increased from 0.2 Ω-m to 0.35 Ω-m with addition of about 1.5 % Bentonite content (Figure 12). From the Table 4-10, smart spacer fluid with 1% nano$Fe_2O_3$ showed a resistivity of 0.24 Ω-m after the cleaning efficiency test. The Bentonite Contamination in the spacer fluid is about 0.5% by weight of the smart spacer fluid (Figure 12). Electrical resistivity can be used as an indicator for the bentonite contamination and can also indicate the changes in the rheological properties in-situ.

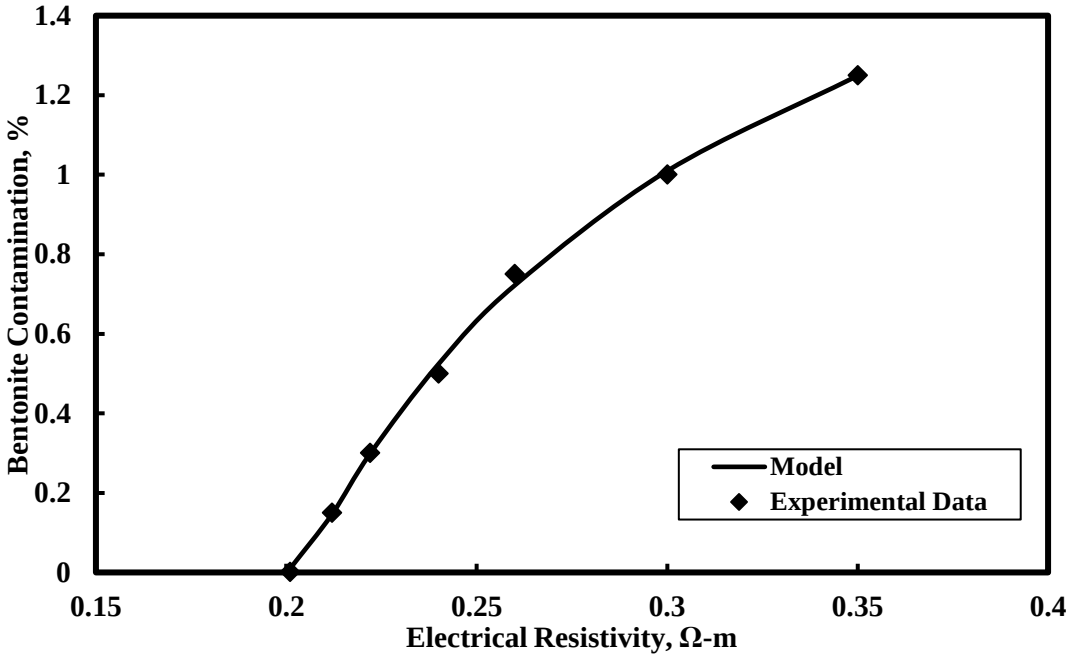


**Figure 4-16:Relation between the Resistivity of spacer fluid and bentonite content in the spacer fluid.**

**Table 4-10:Cleaning efficiency, Maximum Shear Stress and Resistivity changes during cleaning efficiency test for Spacer Fluid with different nano$Fe_2O_3$ contents.**

| Spacer | Cleaning Efficiency (%) | $\tau_{max}$ (Pa) | Resistivity (Ω-m) | | Resistivity Change (%) |
|---|---|---|---|---|---|
| | | | Before Test | After Test | |
| NanoFe = 0% | 82.3 | 49.4 | 0.2 | 0.209 | 4 |
| NanoFe = 0.5% | 92.2 | 58.1 | 0.202 | 0.226 | 12 |
| NanoFe = 1% | 98.5 | 65.5 | 0.207 | 0.24 | 16 |

## 4.7 Summary

In this study total of 240 samples were tested for rheological, cleaning efficiency and piezoresistivity behavior. In this study, effects of the magnetic field strengths, temperatures and bentonite contamination on the electrical resistivity and rheological properties of nano$Fe_2O_3$ modified spacer fluid were investigated. Also, the rheological properties were correlated to the electrical resistivity. Based on the experimental study and analytical modeling following conclusions are advanced:

1. The electrical resistivity of the spacer fluid decreased with increasing temperature and it was a good sensing parameter for real-time monitoring to predict the rheological properties of spacer fluid in the field.

2. The addition of nano$Fe_2O_3$ up to 1% modified the yield stress, shear thinning behavior, and ultimate shear stress limit of the spacer fluid. The amounts of changes in the properties were influenced by the temperature, nano$Fe_2O_3$ content, and magnetic field strength in the spacer fluid and have been quantified using a nonlinear model.

3. The smart spacer fluid with nano$Fe_2O_3$ when contaminated with bentonite showed better rheological properties compared to spacer fluid without nano$Fe_2O_3$.

4. Electrical resistivity of the spacer fluid can be implemented in the field to identify the level of contamination, cleaning efficiency and change in rheological properties in real time.

# CHAPTER 5 SMART CEMENT

## 5.1 Introduction

In order to simulate the field conditions, laboratory model and field model tests were performed. In this study, laboratory and field model wells were installed and cemented using the smart cement with enhanced piezoresistive properties. The laboratory and field model wells were designed, built and used to demonstrate the concept of real time monitoring of the flow of drilling mud, smart cement and hardening of the cement paste in place. The field test data was collected analyzed for a period of upto 5 years.

## 5.2 Laboratory Testing of Smart Cement

This section involves laboratory characterization of smart cement in both slurry and hardened state for a period of 28 days. The smart cement is characterized using electrical resistivity, electrical impedance, effect of curing conditions, compressive strength and piezoresistivity.

Commercially available oil well cement (Class H cement) was modified with conductive fillers to make it a piezoresistive material. The Cement was modified by adding about 0.04% of conductive filler (CF), by weight of cement, and the water to cement ratio was 0.38.

### 5.2.1 Density & Thermal Conductivity

The density of smart cement sample with a water to cement ratio was 1.94 g/cc or 16.2 ppg for a moisture control sample. The thermal conductivity of the cement slurry with a water-to-cement ratio of 0.38 was 0.802 W/mK.

### 5.2.2 K Value Characterization

The electrical resistance (R) of the smart cement sample was measured using LCR and the electrical resistivity ($\rho$) of the smart cement was measured using both digital resistivity meter and conductivity meter for 250 mins to calculate the K value at room temperature.

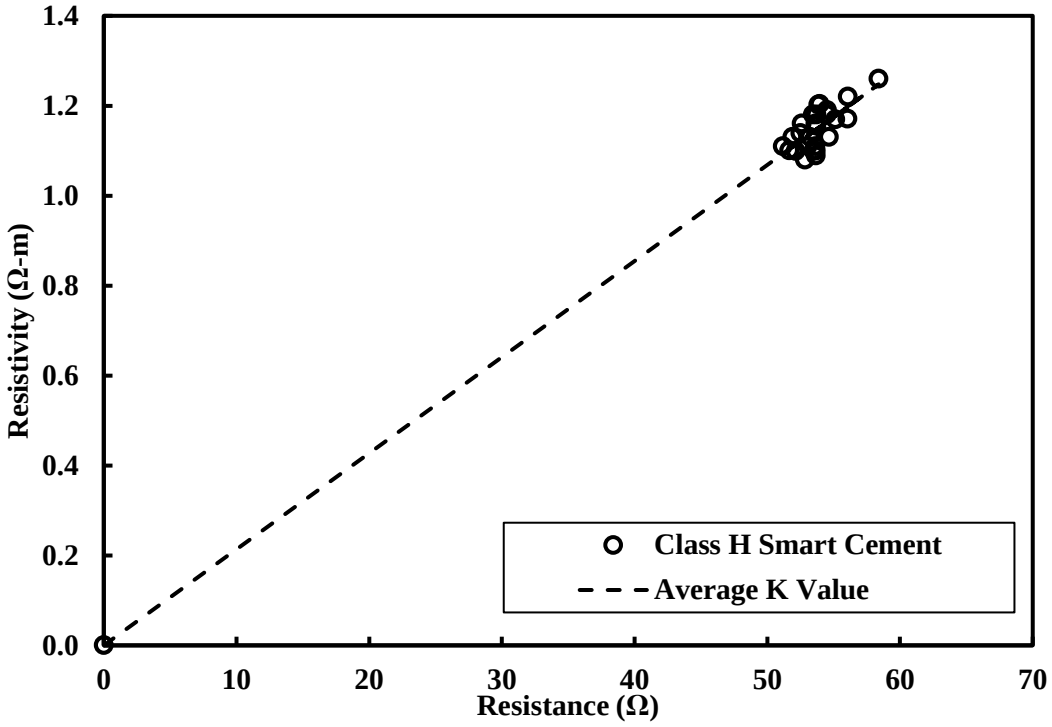


**Figure 5-1:Electrical Resistance vs Electrical Resistivity Plots for Smart Cement.**

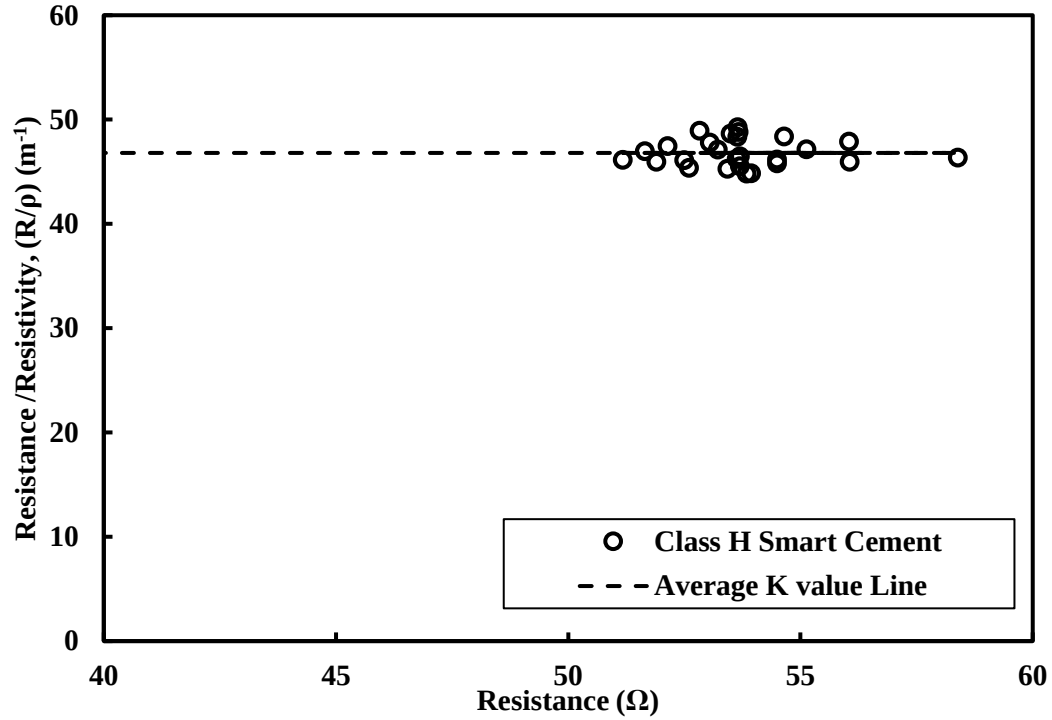


**Figure 5-2:Electrical Resistance/Electrical Resistivity (R/ρ) vs Electrical Resistivity plot for Smart Cement.**

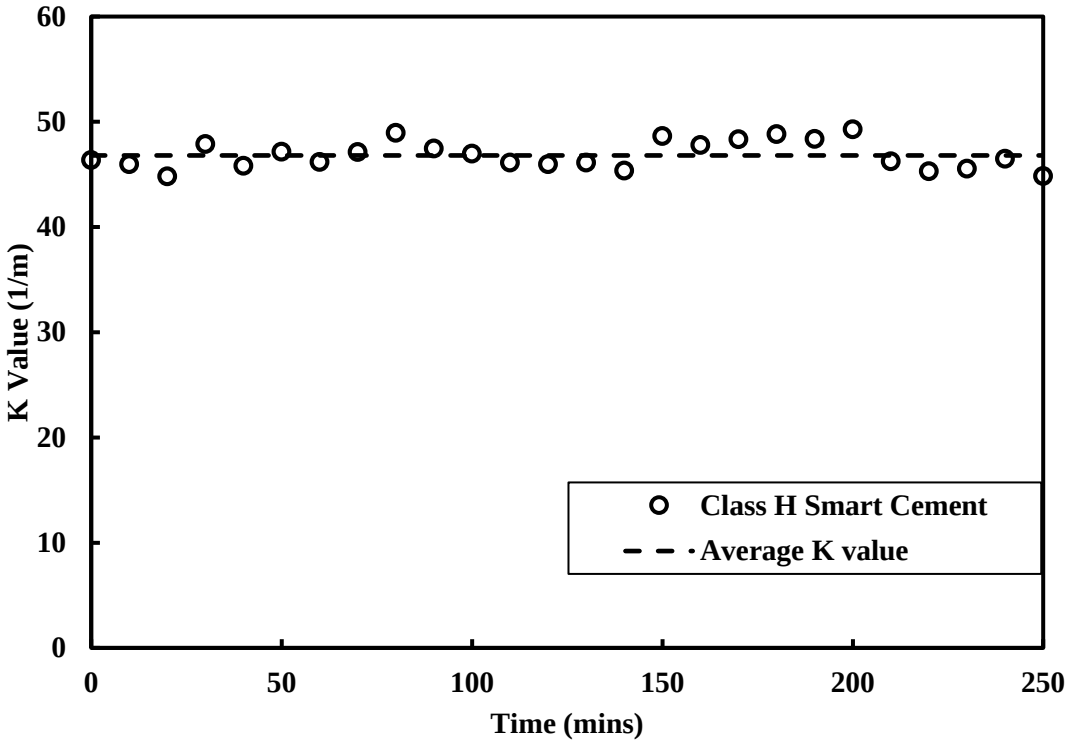


**Figure 5-3:K Value for Smart Cement for curing time of 250 minutes.**

The relation between electrical resistance, electrical resistivity and K value is given by

$$\rho = \frac{R}{K + GR}. \tag{5-1}$$

The constants K and G are 45.7 $m^{-1}$ and 0 (Figure 5-1). This showed that the electrical resistance and resistivity had linear relationship for smart cement. The electrical resistance and electrical resistivity increased with time under moisture control curing conditions. The average value of K was 46.6 $m^{-1}$ for a curing period of 250 mins and hence it is assumed to constant (Figure 5-3).

### 5.2.3 Impedance Vs Frequency Curves

Investigation of the impedance versus frequency relationship showed that the smart cement sample followed case 2 behavior as in Figure 3-12, indicating that the bulk material can be represented by resistance at high frequency impedance measurement. The following are the impedance curve for smart cement for a curing time of 1, 7 and 28 days (Figure 5-4).

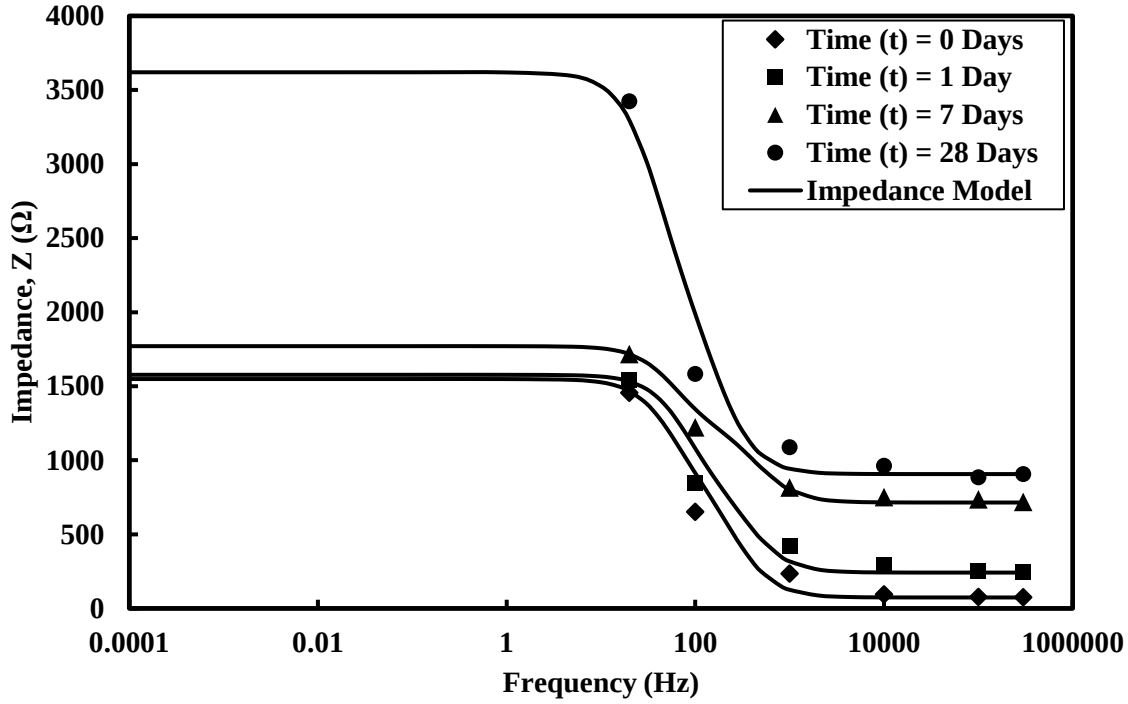


**Figure 5-4:Impedance vs frequency for smart cement for a curing time of 28 days.**

**5.2.4 Bulk Resistance, Contact Resistance and Capacitance**

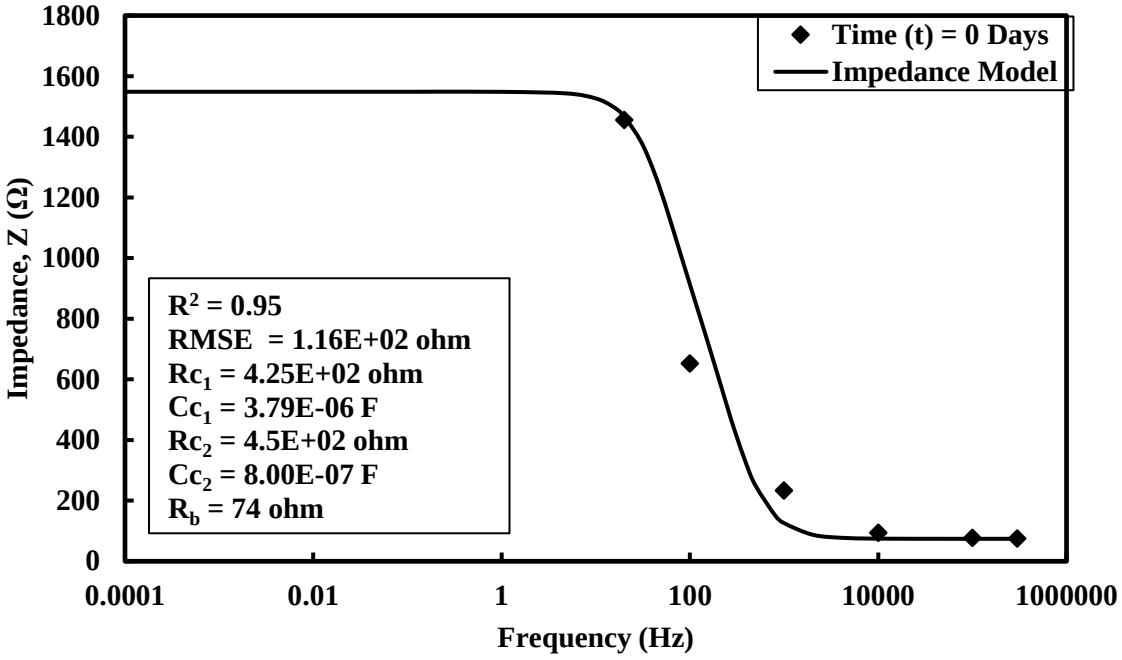


**Figure 5-5:Electrical Impedance for smart cement at time (t) = 0 Days.**

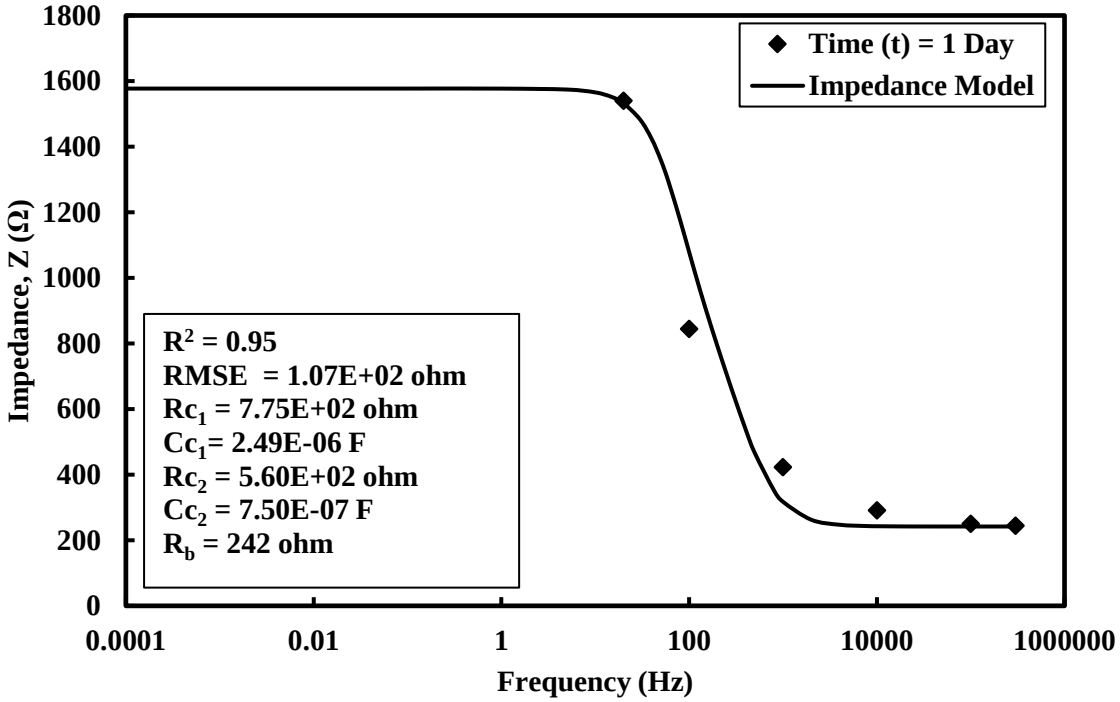


**Figure 5-6:Electrical Impedance for smart cement at time (t) = 1 Day.**

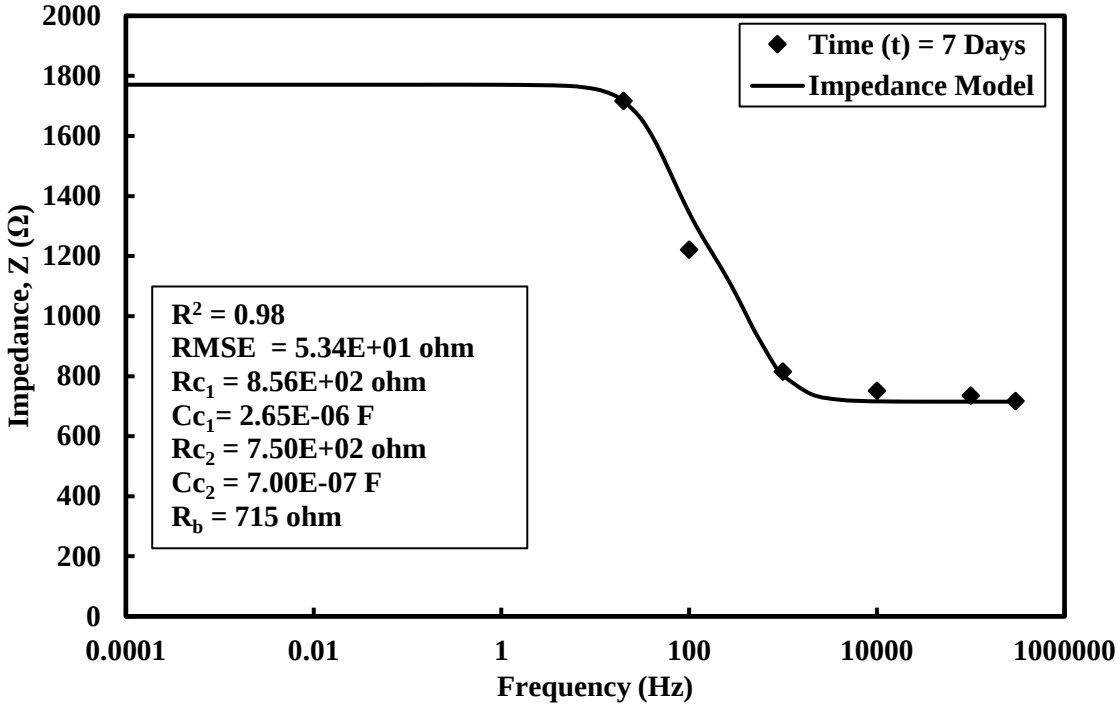


**Figure 5-7:Electrical Impedance for smart cement at time (t) = 7 Days.**

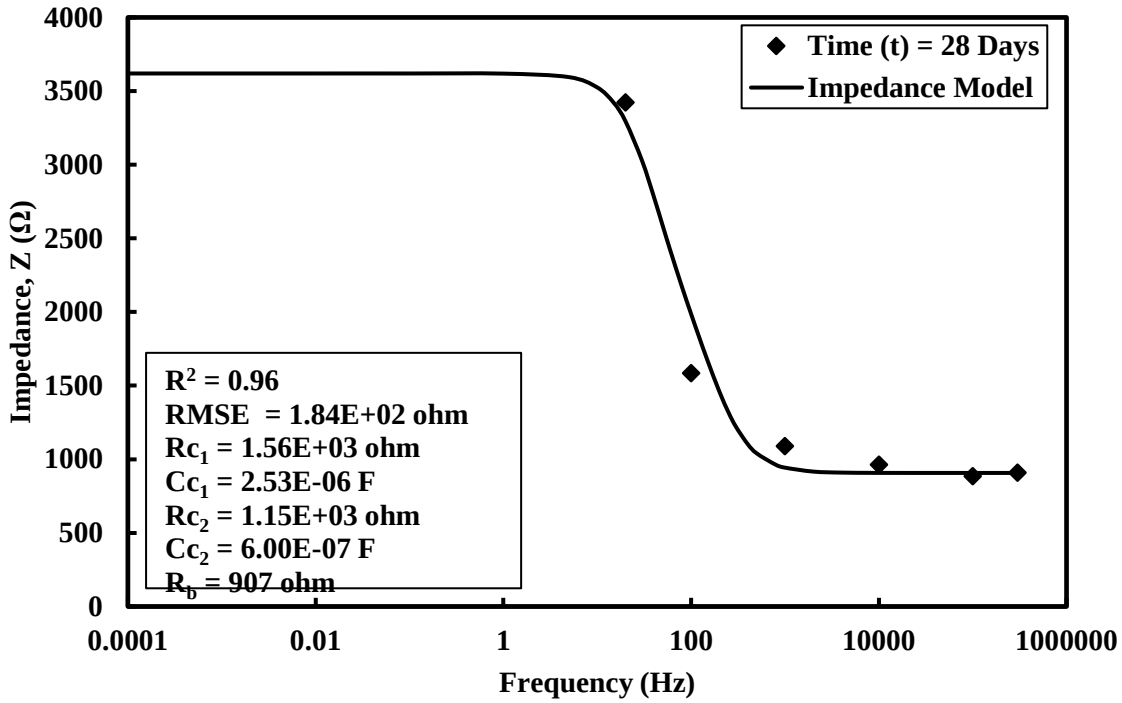


**Figure 5-8:Electrical Impedance for smart cement at time (t) = 28 Days.**

The contact resistances and capacitances for smart cement for curing time of 28 days are obtained using impedance model given by eqn. 3-5.

The Bulk resistance of the smart cement increased from 74 Ω to 907 Ω (Figure 5-5 & Figure 5-8), 1200% increase in 28 days when cured at room temperature of 25 °C. The contact resistance ($Rc_1$) increased from 425 Ω to 1560 Ω, 267% increase in 28 days of room temperature curing. The contact capacitance ($Cc_1$) varied from 3.79E-06 F to 2.53E-06 F, a 33% decrease over 28 days curing period. The electrical contact index ($Rc_1$*$Cc_1$) increased from 0.18E-02 Ω-F to 0.395E-02 Ω-F, a 43.6% increase during the 28 days of curing (Figure 5-9). Similarly, the contact resistance ($Rc_2$) increased from 450 Ω to 1150 Ω, 155% increase in 28 days of room temperature curing. The contact capacitance ($Cc_2$) varied from 8.00E-07 F to 6.00E-07 F, a 25% decrease over 28 days curing period. The electrical contact index ($Rc_2$*$Cc_2$) varied from 0.360E-03 Ω-F to 0.794E-03 Ω-F, a 120% increase during the 28 days of curing (Figure 5-9).

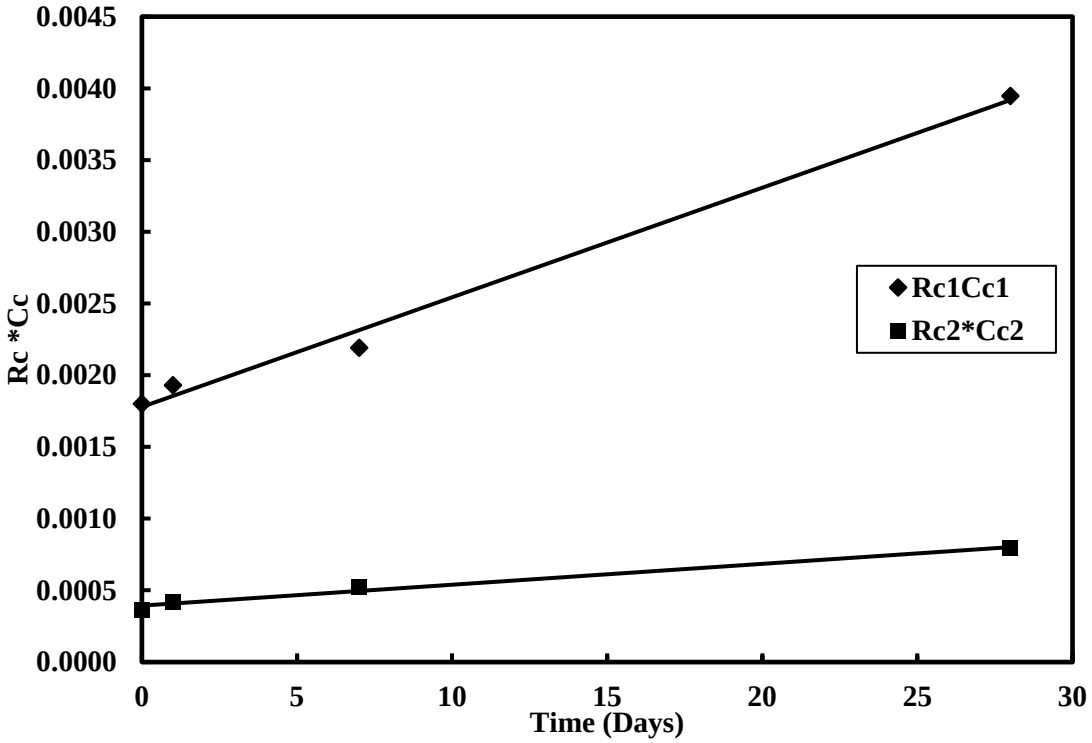


**Figure 5-9:Contact Resistance and Capacitance product variation over 28 days of time.**

### 5.2.5 Electrical Resistivity

**Curing of cement**

Initial resistivity was measured immediately after mixing the smart cement. Initial resistivity of the smart cement was 1.05 Ωm (Table 5-1). During the curing process under room condition (relative humidity of 50% and temperature of 72$^{o}$F (22$^{o}$C)), the resistivity rapidly changed with the time as shown in Figure 5-10. Hence, there are several parameters that can be used in monitoring the curing (hardening process) of the cement. The parameters are initial resistivity ($\rho_o$), minimum resistivity ($\rho_{min}$), time to reach the minimum resistivity ($t_{min}$) and resistivity after 24 hours of curing ($\rho_{24}$). After initial mixing, the electrical resistivity reduced to a minimum value ($\rho_{min}$), and then it gradually increased with time. Time to reach minimum resistivity, $t_{min}$, can be used as an index of speed of chemical reactions and cement set times. With the formation of resistive solid hydration products which block the conduction path, resistivity increased sharply with curing time. The following increase in electrical resistivity was caused by the formation of

large amounts of hydration products in the cement matrix. Finally, a relatively stable increase in trend was reached by the ions diffusion control of hydration process, and resistivity increased steadily with the curing time. The electrical resistivity was modeled using Vipulanandan electrical resistivity model (Eqn. 3-18) and artificial neural network model (Eqns. 3-20 & 3-21).

**Table 5-1:Electrical Resistivity Model parameters for smart cement in laboratory for 28 days of curing.**

| Cement Type | Initial Resistivity, $\rho_o$ (Ω-m) | $\rho_{min}$ (Ω-m) | $t_{min}$ (min) | $t_o$ (min) | $R^2$ | $p_1$ | $q_1$ |
|---|---|---|---|---|---|---|---|
| Smart Cement | 1.05 ± 0.03 | 0.96 ± 0.01 | 80 ± 5.0 | 110 | 0.99 | 0.61 | 0.38 |

**0.5 Day Curing**

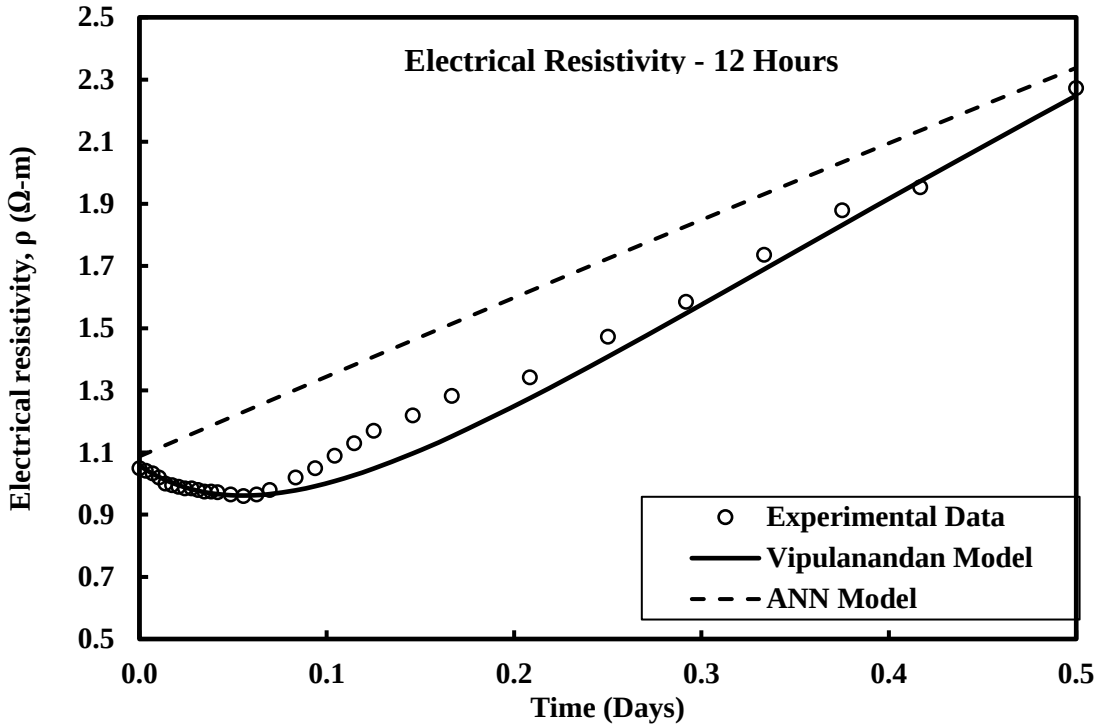


**Figure 5-10:Electrical Resistivity of Smart Cement in the Laboratory During 0.5 Day of Curing.**

The normal trend of the resistivity during the curing of cement is that the resistivity decreases up to a certain time ($t_{min}$) to reach the minimum resistivity ($\rho_{min}$) and then increases with time. The value of initial resistivity of smart cement was 1.05 Ω.m. immediately after mixing, which can be

used as a quality control measure in the field. The value of minimum resistivity was 0.96 Ω.m. and the time for minimum resistivity was 80 minutes after mixing (Figure 5-10). The resistivity after 0.5 day (12 hours) of curing was 2.27 Ω.m, more than doubled in resistivity compared to the initial resistivity. The resistivity after 12 hours (0.5 day) was over 116% compared to the initial resistivity. For training the AI models with one, two, three and four layers of ANN, total of 120 data were used with the GRNN approach. Based on the training results, four layer AI model was selected to do the predictions. Additional 30 data were used to predict the smart cement curing trend using the AI model and compare it to the Vipulanandan Curing Model. In predicting the new data, for the four layered AI model the coefficient of determination ($R^2$) was 0.61 and the RMSE (root mean square error) was 0.21 Ω.m. The AI model prediction is compared to the experimental data in Figure 5-10. The AI model over predicted the initial resistivity by 3% and also couldn't predict the minimum resistivity.

Vipulanandan Model parameters $p_1$ and $q_1$ were 0.61 and 0.38 (Table 5-1). This model predicted the curing trend very well including the minimum resistivity (Figure 5-10). The coefficient of determination ($R^2$) was 0.98 and the RMSE (root mean square error) was 0.05 Ω.m (Table 5-2).

**1 Day Curing**

The resistivity after 1 day (24 hours) of curing was 3.46 Ω.m, more than 230% increase compared to the initial resistivity. The resistivity after 24 hours (1 day) was over 50% higher compared to the resistivity after 12 hours (0.5 day). For training the AI models with one, two, three and four layers of ANN, total of 160 data were used with the GRNN approach. Based on the training results, four-layer AI model was selected to do the predictions. Additional 40 data were used to predict the smart cement curing trend using the AI model and compare it to the Vipulanandan Curing Model. In predicting the new data, for the four layered AI model the coefficient of determination ($R^2$) was 0.92 and the RMSE (root mean square error) was 0.19 Ω.m.

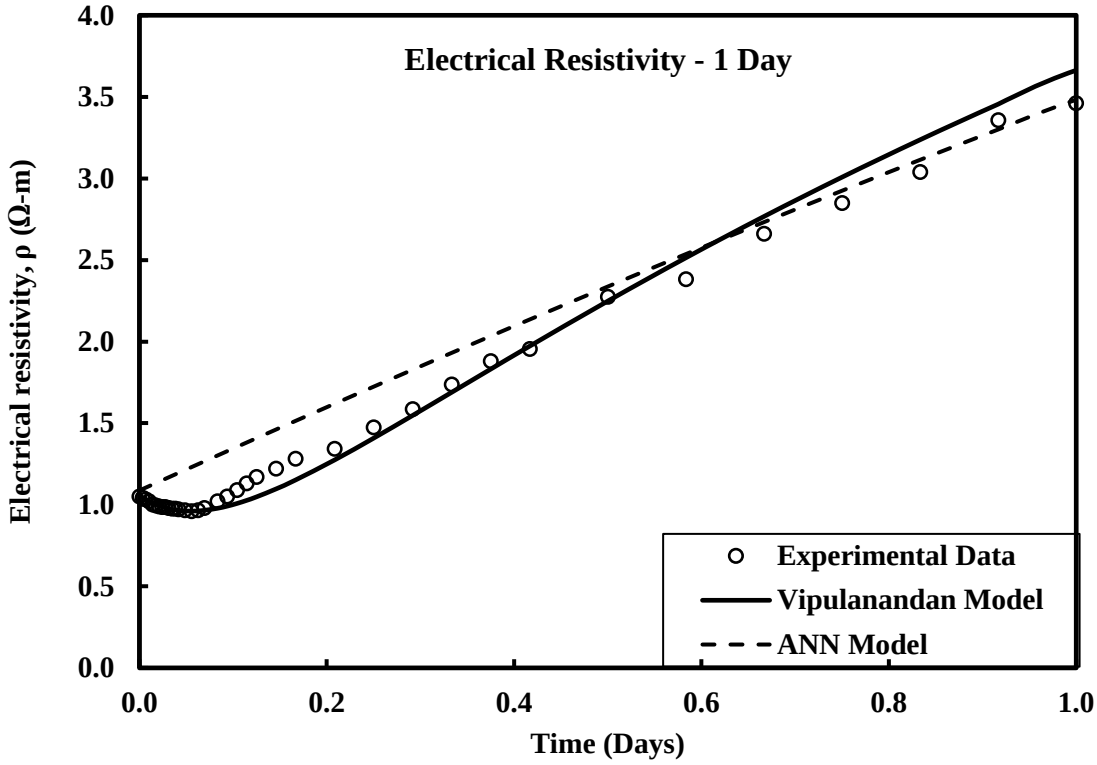


**Figure 5-11:Electrical Resistivity of Smart Cement in the Laboratory During 1 Day of Curing.**

The AI model prediction is compared to the experimental data in Figure 5-11. The AI model predicted the 24-hour resistivity very well. Vipulanandan Model parameters $p_1$ and $q_1$ were 0.61 and 0.38 (Table 5-1). This model predicted the curing trend very well including the minimum resistivity (Figure 5-11). The coefficient of determination ($R^2$) was 0.99 and the RMSE (root mean square error) was 0.08 Ω.m (Table 5-2).

**28 Days of Curing**

The resistivity after 28 days of curing was 14.54 Ω.m, more than 1285% increase compared to the initial resistivity. The resistivity after 28 days of curing was over 320% higher compared to the resistivity after 24 hours (1 day). This clearly indicates the sensitivity of resistivity to the cement curing.

For training the AI models with one, two, three and four layers of ANN, total of 180 data were used with the GRNN approach. Based on the training results, four-layer AI model was selected to do the predictions. Additional 45 data were used to predict the smart cement curing trend using the AI model and compare it to the Vipulanandan Curing Model. In predicting the new data, for the four layered AI model the coefficient of determination ($R^2$) was 0.99 and the RMSE (root mean square error) was 0.20 Ω.m. The AI model prediction is compared to the experimental data in Figure 5-12. The AI model predicted the 28 days of curing resistivity very well. Vipulanandan Model parameters $p_1$ and $q_1$ were 0.61 and 0.38 (Table 5-2). This model also predicted the curing trend very well (Figure 5-12). The coefficient of determination ($R^2$) was 0.99 and the RMSE (root mean square error) was 0.21 Ω.m (Table 5-2).

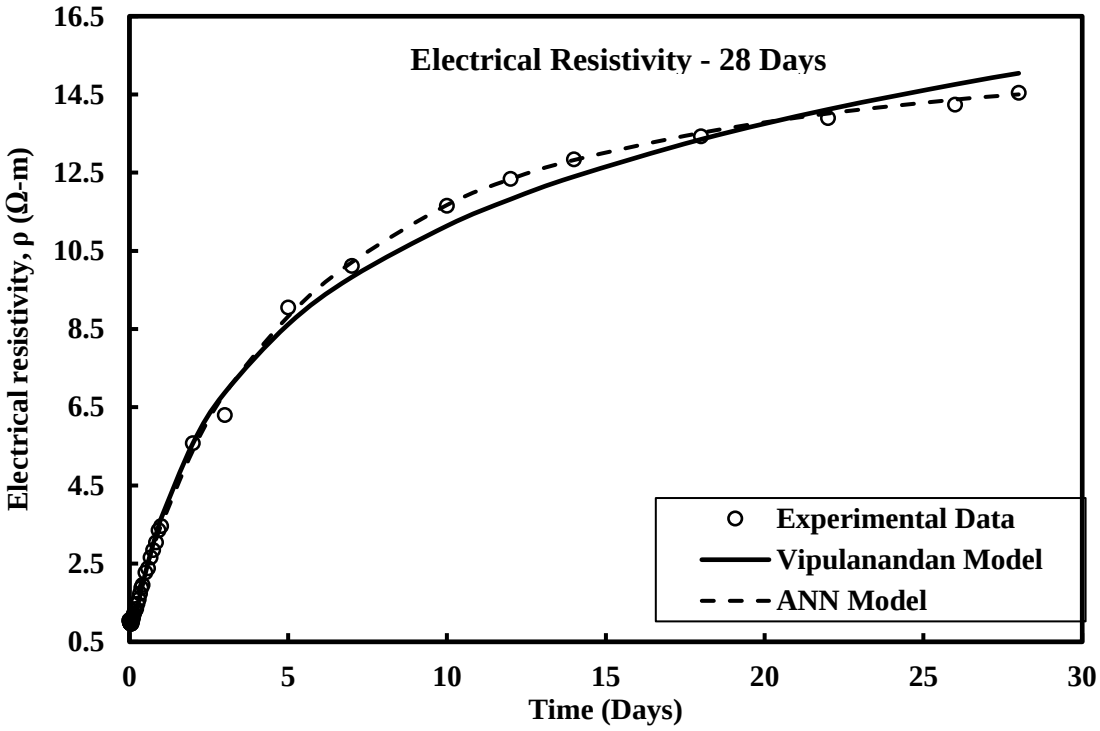


**Figure 5-12:Electrical Resistivity of Smart Cement in the Laboratory During 28 Days of Curing.**

**Table 5-2:Comparison of ANN Model and Vipulanandan Resistivity Model Predictions for Curing of Smart Cement.**

| | ANN Model | | Curing Model | |
|---|---|---|---|---|
| Time | $R^2$ | RMSE (Ω-m) | $R^2$ | RMSE (Ω-m) |
| T = 12 hours | 0.61 | 0.21 | 0.98 | 0.05 |
| T = 1 Day | 0.92 | 0.19 | 0.99 | 0.08 |
| T = 28 Days | 0.99 | 0.20 | 0.99 | 0.21 |

### 5.2.6 Fluid Loss

The total fluid loss from the cement slurry at pressure of 0.7 MPa (100 psi) with a water-to-cement ratio of 0.38 was 134 mL (Figure 5-13). Vipulanandan fluid loss model was used to predict the fluid loss with time (Vipulanandan et al., 2014). The root mean square error (RMSE) for Vipulanandan fluid loss model was 1.75 mL while for ANN model it was 13.3 mL (Figure 5-13). Without the foam, Vipulanandan fluid loss model better predicted the fluid loss based on the RMSE. With the addition of foam, the ANN model prediction was comparable to Vipulanandan model prediction.

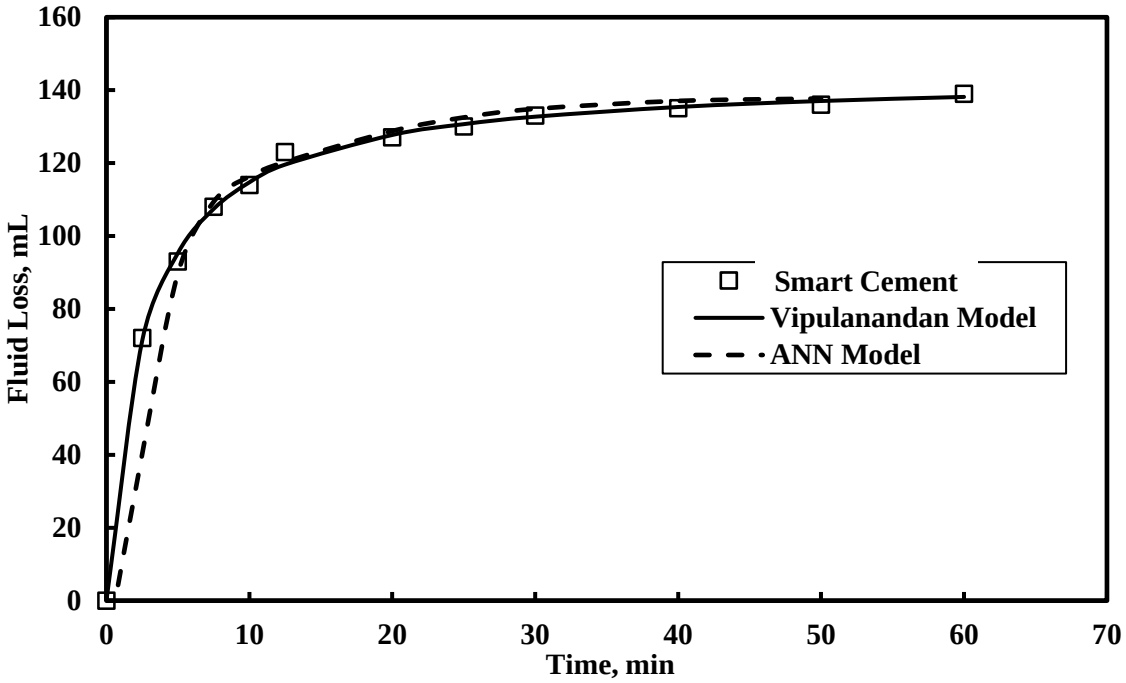


**Figure 5-13:Measured and Predicted Fluid Loss- Time Relationship for the Smart Cement.**

**Table 5-3:ANN and Fluid loss model parameters for smart cement slurry.**

| | ANN Model | | Fluid Loss Model | | | | |
|---|---|---|---|---|---|---|---|
| Model Parameters | $R^2$ | RMSE (mL) | E $(min.(mL)^{-1}$ | F $(mL)^{-1}$ | $(FL)_{max}$ (mL) | $R^2$ | RMSE (mL) |
| Smart Cement | 0.93 | 13.3 | 0.017 | 0.007 | 142.9 | 0.99 | 1.75 |

### 5.2.7 Rheology

Shear stress – shear strain rate relationships for smart foam cement were predicated using the Vipulanandan model and compared with ANN model as shown in Figure 5-14. Also, all the model parameters are summarized in Table 5-4 with root mean square error (RMSE) and coefficient of determination for all the predictions.

***Vipulanandan model (Vipulanandan et al., 2014)***

**Smart Cement**: The shear thinning behavior of smart cement slurry with w/c ratio of 0.38 at a temperature of 25$^o$C was tested and modeled using the Vipulanandan model (Eqn. (3-12)) up to a shear strain rate of 1024 $s^{-1}$ (600 rpm). The coefficient of determination ($R^2$) was 0.98 and the root mean square of error (RMSE) was 7.43 Pa as summarized in Table 5-4. The average yield stress ($\tau_{o1}$) for the cement slurry at temperature of 25$^o$C was 28 Pa. The model parameter C for the cement slurry with w/c ratio of 0.38 at 25$^o$C was 1.97 $Pa.s^{-1}$ as summarized in Table 5-4. The model parameter D for the cement slurry was 0.006 $Pa^{-1}$.

The root mean square of error (RMSE) was 13.34 Pa and coefficient of determination ($R^2$) was 0.94 for ANN model (Figure 5-14). Based on the RMSE, Vipulanandan model predicted better test results than ANN model.

**Table 5-4:ANN and Vipulanandan Rheological model parameters for smart cement slurry.**

| | ANN Model | | Vipulanandan Model | | | | |
|---|---|---|---|---|---|---|---|
| Model Parameters | $R^2$ | RMSE (Pa) | C$(Pa.\ s)^{-1}$ | D $(Pa)^{-1}$ | $\tau$ (yield)(Pa) | $\tau$ (max)(Pa) | RMSE (Pa) |
| Smart Cement | 0.94 | 13.34 | 1.97 | 0.0065 | 28.16 | 153.8 | 7.43 |

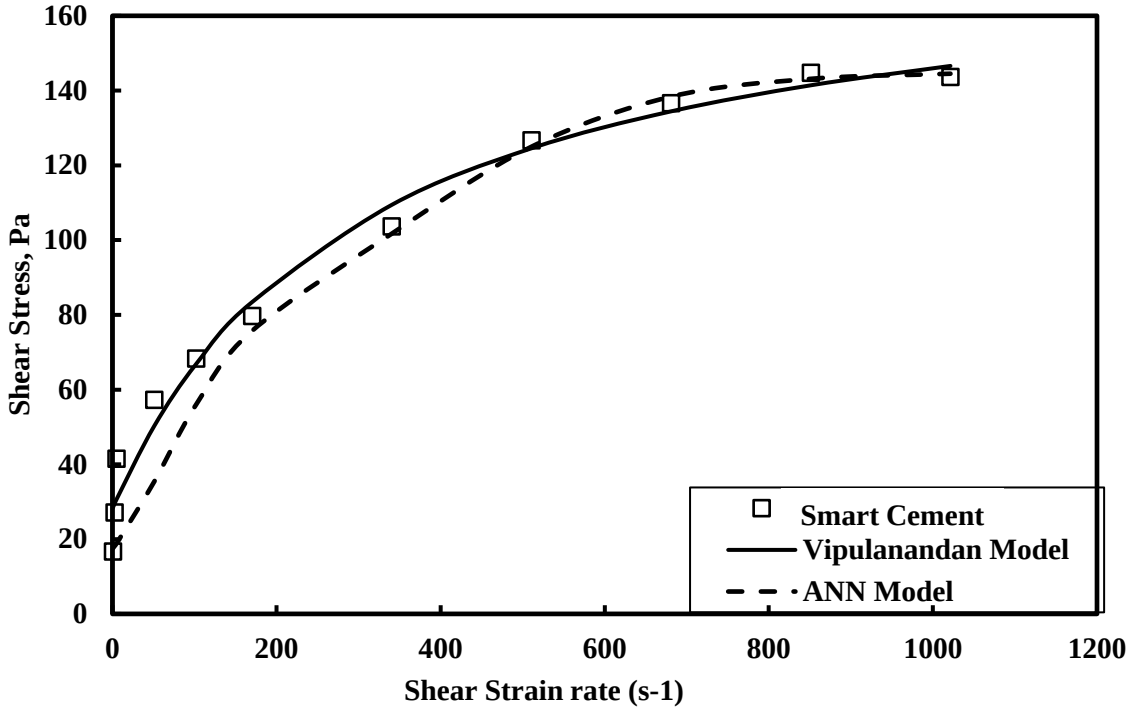


**Figure 5-14:Measured and Predicted Shear Stress-Shear Strain Rate Relationship for the Smart Cement.**

### 5.2.8 Piezoresistivity

**Slurry**

The smart cement slurry was subjected to pressure up to 4 MPa in the high-pressure high temperature chamber (HPHT) to investigate the piezoresistive behavior. The resistivity of the smart cement slurry decreased nonlinearly with increase in the pressure (Figure 5-15). At 4 MPa pressure the decrease in the resistivity was 8%, indicating the piezoresistivity characteristics of the smart cement slurry. The piezoresistivity per unit stress was 0.014%/psi for lab cement in slurry stage. The value of model parameters A, B are 20.26 MPa $(\%)^{-1}$ and 0.0875 $(\%)^{-1}$. The root mean square of error (RMSE) for piezoresistivity model was 0.457 % while it was 0.054 % for ANN model. Based on the RMSE, ANN model predicted better test results than piezoresistivity model (Table 5-5).

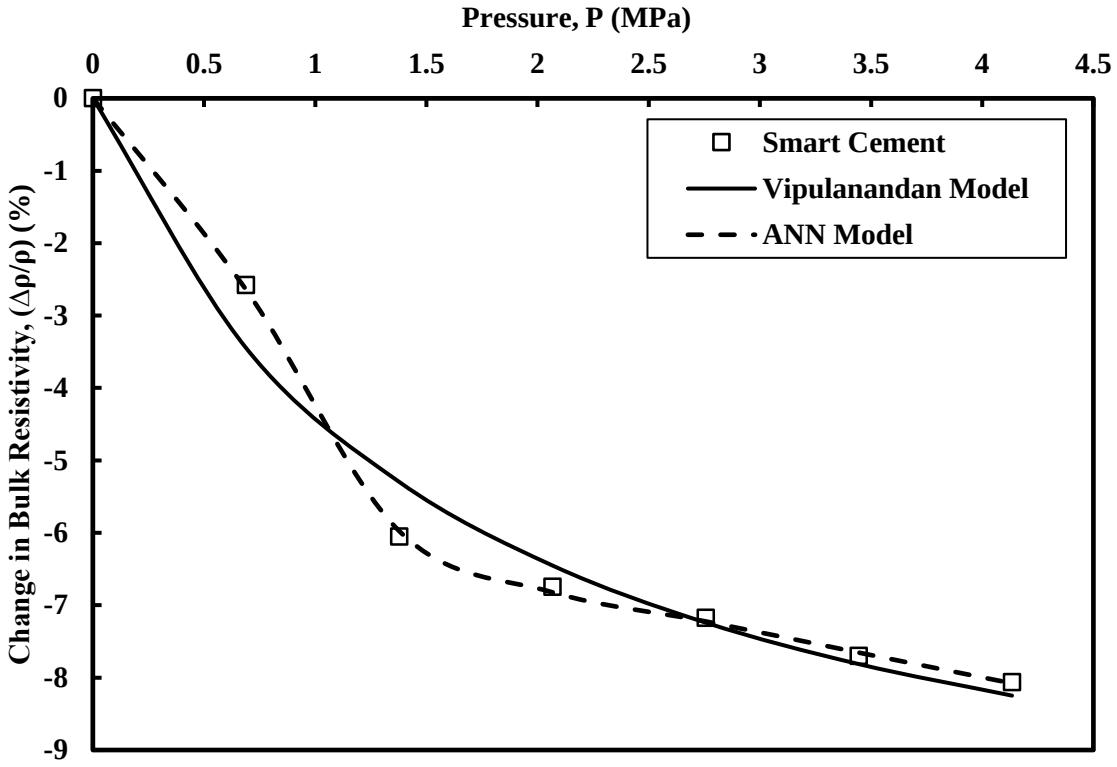


**Figure 5-15:Measured and Predicted Stress-Resistivity Relationship for the Smart Cement slurry after mixing.**

**Table 5-5:ANN and Vipulanandan piezoresistivity model parameters for smart cement slurry.**

| | ANN Model | | Piezoresistivity Model | | | | |
|---|---|---|---|---|---|---|---|
| Model Parameters | $R^2$ | RMSE (%) | A $(MPa.(\%)^{-1}$ | B $(\%)^{-1}$ | $(\Delta\rho/\rho)_{max}$ (%) | $R^2$ | RMSE (%) |
| Smart Cement | 0.99 | 0.054 | 20.26 | 0.0875 | 11.4 | 0.97 | 0.457 |

## Hardened cement

It is important to quantify the piezoresistive behavior of the smart cement. The specimens were cured under room condition and the stress- piezoresistive strain response was non-linear (Figure 5-16). The piezoresistive strain for smart cement sample was 343 % at a peak compressive stress of 1340 psi after 1 day of curing. Hence, the piezoresistivity per unit stress was 0.255%/psi in the lab samples after 1 day of curing. The piezoresistive strain for smart cement sample was 252 % at a peak compressive stress of 3450 psi after 28 days of curing. Hence, the piezoresistivity per unit stress was 0.073%/psi in the lab samples after 28 days of curing.

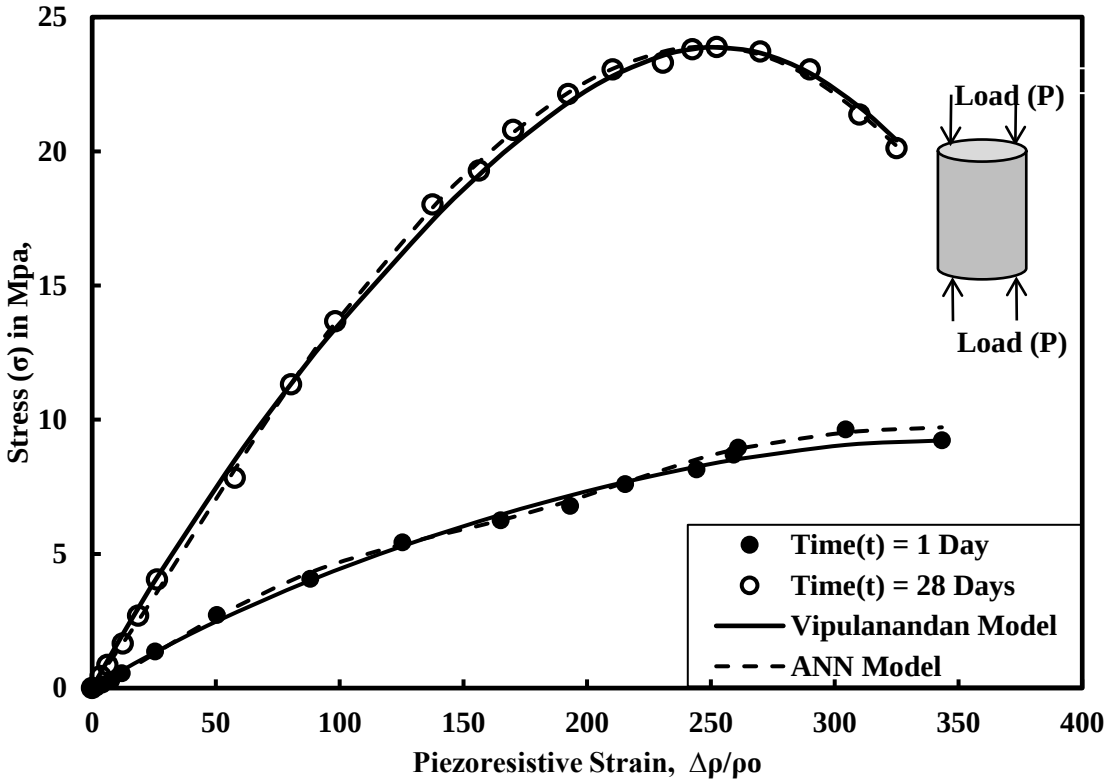


**Figure 5-16:Piezoresistive Behavior of Smart Cement for 28 days of curing.**

For training the AI models with one, two, three and four layers of ANN, total of 80 data were used with the GRNN approach. Based on the training results, four-layer AI model was selected to do the predictions. Additional 20 data were used to predict the smart cement piezoresistive behavior using the AI model and compare it to the Vipulanandan piezoresistive Model. In predicting the new data, for the four layered AI model the coefficient of determination ($R^2$) was 0.99 and the RMSE (root mean square error) was in the range of 0.18 to 0.195 MPa. The AI model prediction is compared to the experimental data in Figure 5-16.

Vipulanandan model parameter $p_2$ increased from 0.09 to 0.11 and $q_2$ increased from 0.48 to 0.56 over 28 day curing period (Table 5-6). This model also predicted piezoresistive behavior very well (Figure 5-16). The coefficient of determination ($R^2$) was 0.99 and the RMSE (root mean square error) varied from 0.23 to 0.3 MPa (Table 5-6). Both the AI model and Vipulanandan Piezoresistive Models predicted the behavior very well.

**Table 5-6: Correlation parameters for ANN model and Piezoresistivity model for smart cement for 28 days of curing.**

| | ANN Model | | Piezoresistivity Model | | | | |
|---|---|---|---|---|---|---|---|
| Time (Days) | $R^2$ | RMSE (MPa) | $p_2$ | $q_2$ | $\sigma c_{max}$ (MPa) | $R^2$ | RMSE (MPa) |
| 1 | 0.99 | 0.179 | 0.09 | 0.48 | 9.2 | 0.99 | 0.227 |
| 28 | 0.99 | 0.194 | 0.11 | 0.56 | 23.8 | 0.99 | 0.299 |

## 5.3 Lab Well Model

### 5.3.1 Instrumentation

The oil well in the field was replicated by a model in the lab with about 9ft height and 4in diameter steel pipe representing the casing. A PVC pipe of 9ft height and 8 in diameter was used to represent the bore hole (Figure 5-18). The gap between the PVC and the casing was cemented with smart class H oil well cement (added conductive fillers). The space between the casing and borehole was instrumented using steel angles which were used to monitor the installation and curing of cement for period of 5 years. Four angles with about 120 probes, 8 thermocouples and 9 strain gauges were used for monitoring. The probes were placed at about 6 inches vertical spacing from bottom to the top. Also, eight probes (A, B, C, D, E, F, G and H) were placed horizontally at each level (Figure 5-17).

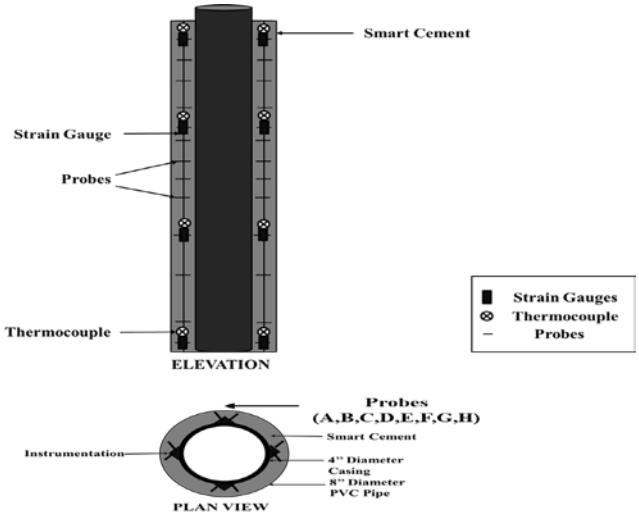


**Figure 5-17: Instrumentation Diagram of Lab Model well.**


**Figure 5-18:Lab Model Well.**

### 5.3.2 Calibration Parameter K Characterization

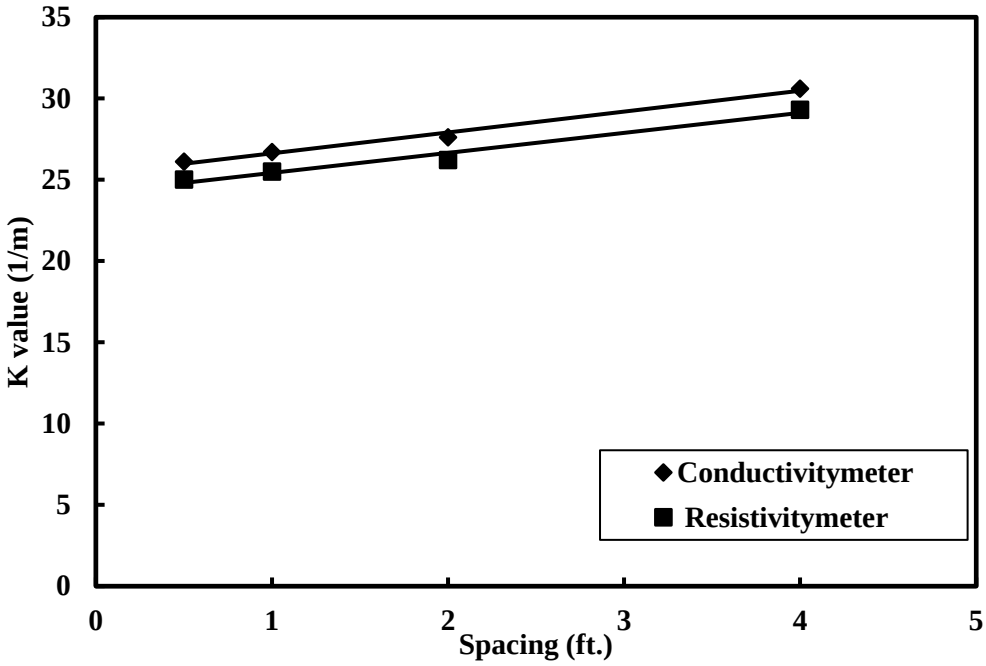


**Figure 5-19:Parameter K Vs Spacing for Lab model.**

The laboratory model angles were calibrated to obtain the parameter K for different spacing. The parameter K was computed for a spacing of 0.5 feet to about 4 feet. The parameter K

was found to increase with the increase in spacing as it was proportional to the resistance of the bulk material. The slope of the parameter K curve was close to 1.23 while the absolute parameter K varied from 25 to 30 (Figure 5-19). The parameter K showed a linear increasing trend with increase of the spacing. The parameter K was cross verified using both resistivity meter and conductivity meter. The parameter K computed with both resistivity meter and conductivity meter had close convergence.

### 5.3.3 Impedance Vs Frequency Curves

Investigation of the impedance versus frequency relationship showed that the smart cement lab model followed case 2 behavior as in Figure 3-12, indicating that the bulk material can be represented by resistance at high frequency impedance measurement. The following are the impedance curve for smart cement for a curing time of 1, 100, 1000 and 1900 days (Figure 5-20Figure 5-4).

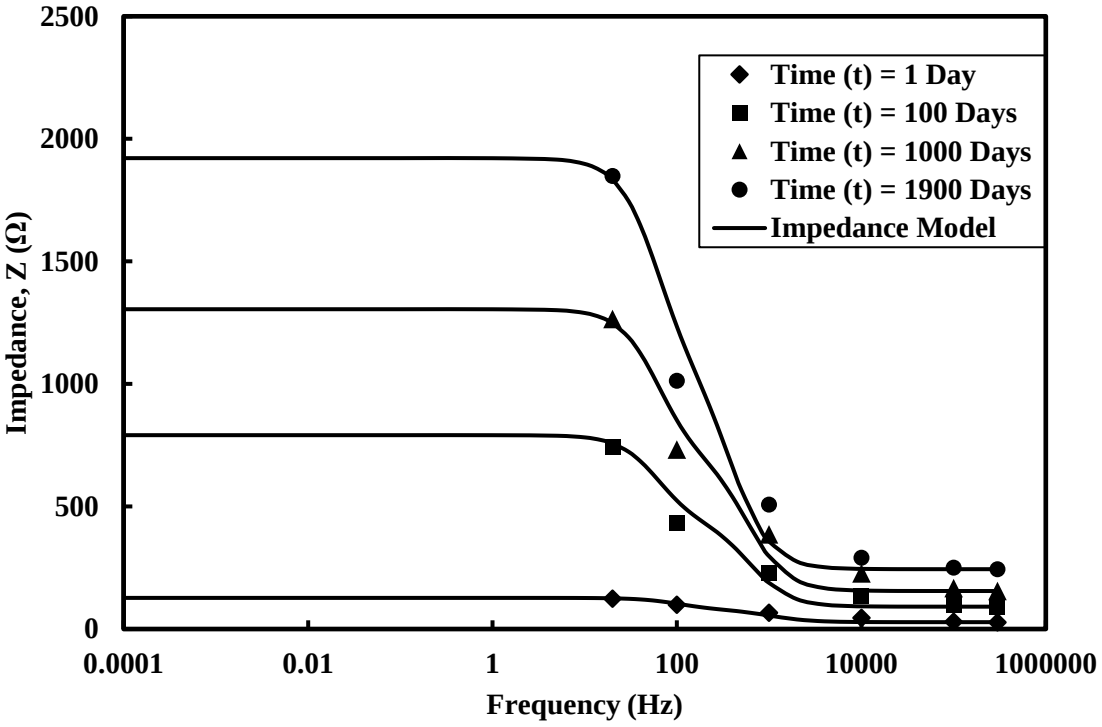


**Figure 5-20:Impedance vs frequency for smart cement for a curing time up to 1900 days.**

### 5.2.4 Bulk Resistance, Contact Resistance and Capacitance

The contact resistances and capacitances for smart cement for curing time of 1900 days are obtained using impedance model given by eqn. 3-5.

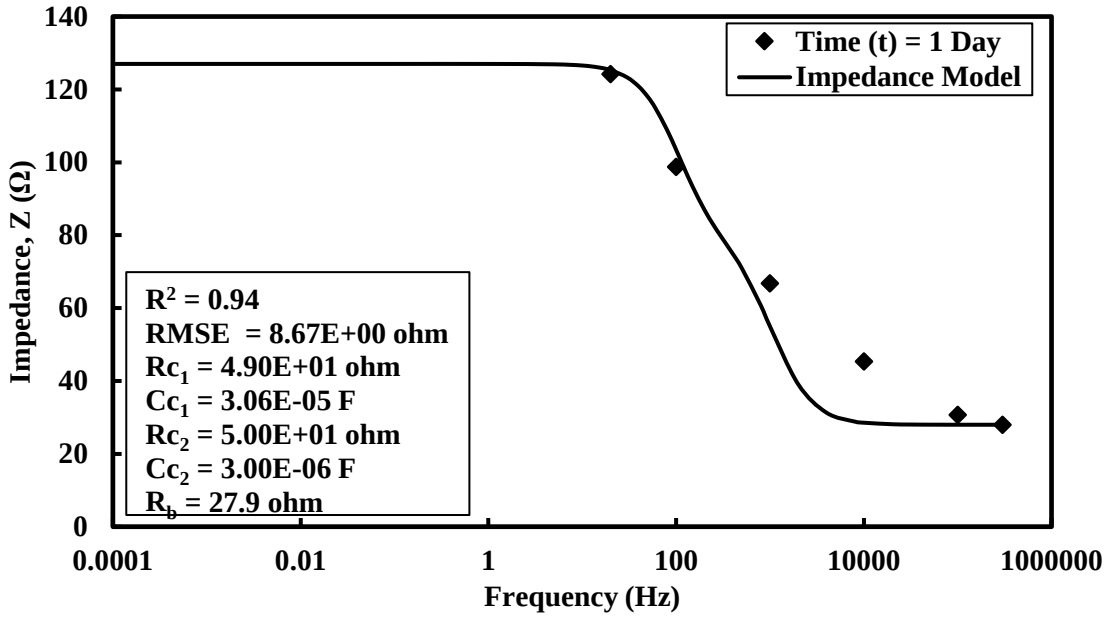


**Figure 5-21:Electrical Impedance for smart cement at time (t) = 1 Day.**

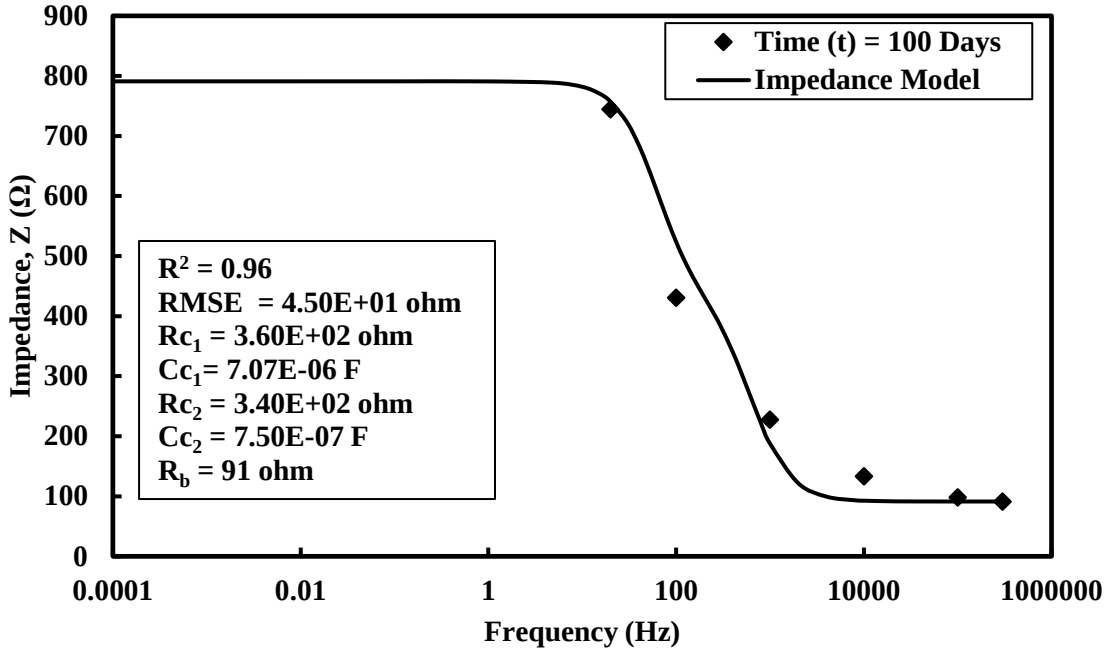


**Figure 5-22:Electrical Impedance for smart cement at time (t) = 100 Days.**

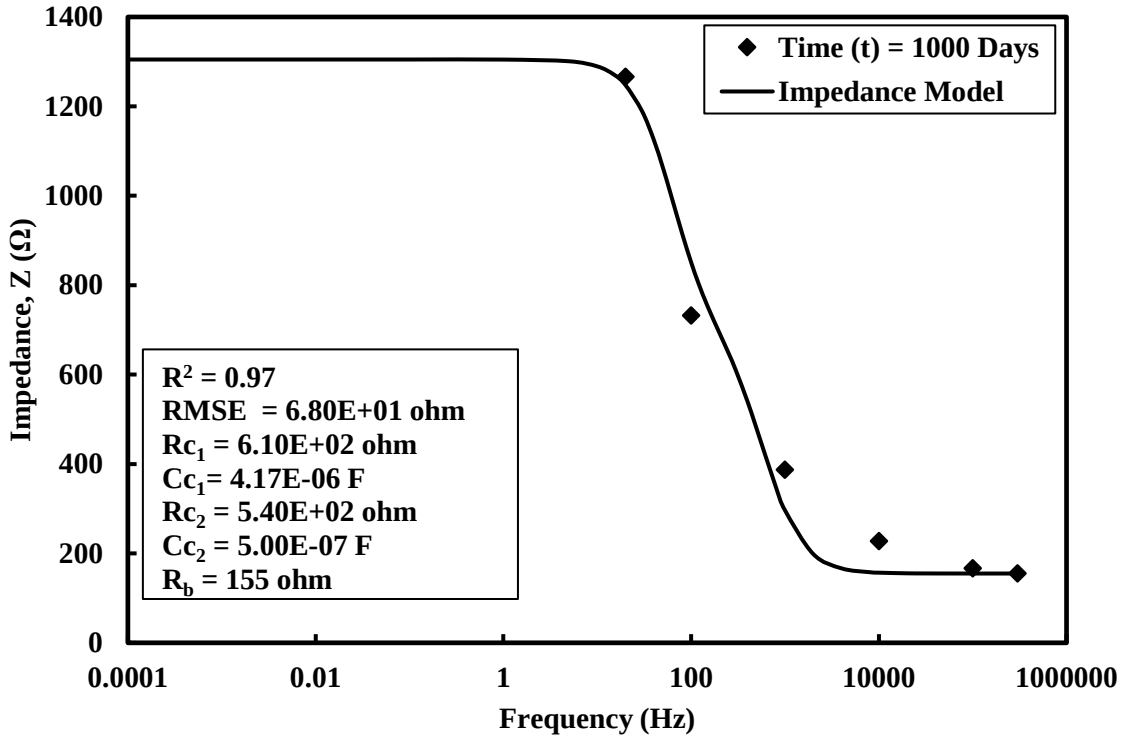


**Figure 5-23:Electrical Impedance for smart cement at time (t) = 1000 Days.**

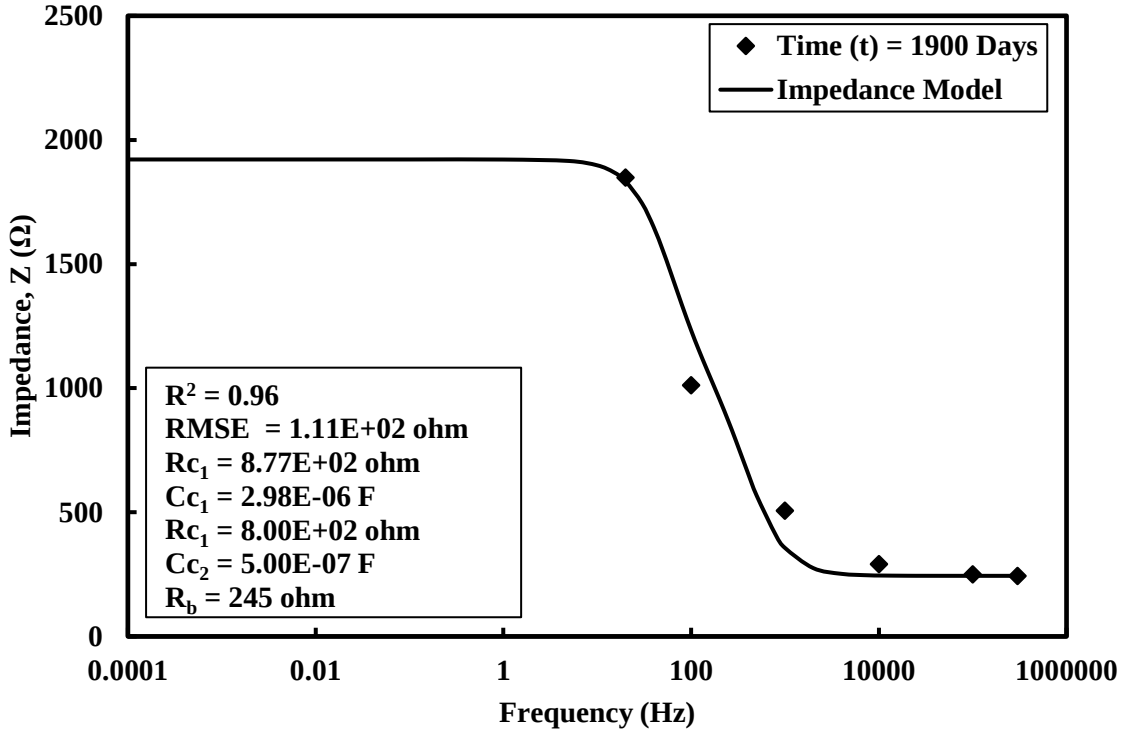


**Figure 5-24:Electrical Impedance for smart cement at time (t) = 1900 Days.**

The Bulk resistance of the smart cement increased from 25 Ω to 245 Ω (Figure 5-21 & Figure 5-24), 880% increase in 1900 days when cured at room temperature of 25 °C. The contact resistance ($Rc_1$) increased from 49 Ω to 877 Ω, 1680% increase in 1900 days of room temperature curing. The contact capacitance ($Cc_1$) varied from 3.06E-05 F to 2.98E-06 F, a 90% decrease over 1900 days curing period. The electrical contact index ($Rc_1$*$Cc_1$) increased from 0.15E-02 Ω-F to 0.261E-02 Ω-F, a 74% increase during 1900 days of curing (Figure 5-25).

Similarly, the contact resistance ($Rc_2$) increased from 50 Ω to 800 Ω, 1500% increase in 1900 days of room temperature curing. The contact capacitance ($Cc_2$) varied from 3.00E-06 F to 5.00E-07 F, a 83% decrease over 1900 days curing period. The electrical contact index ($Rc_2$*$Cc_2$) varied from 0.15E-03 Ω-F to 0.261E-03 Ω-F, a 74% increase during 1900 days of curing (Figure 5-25).

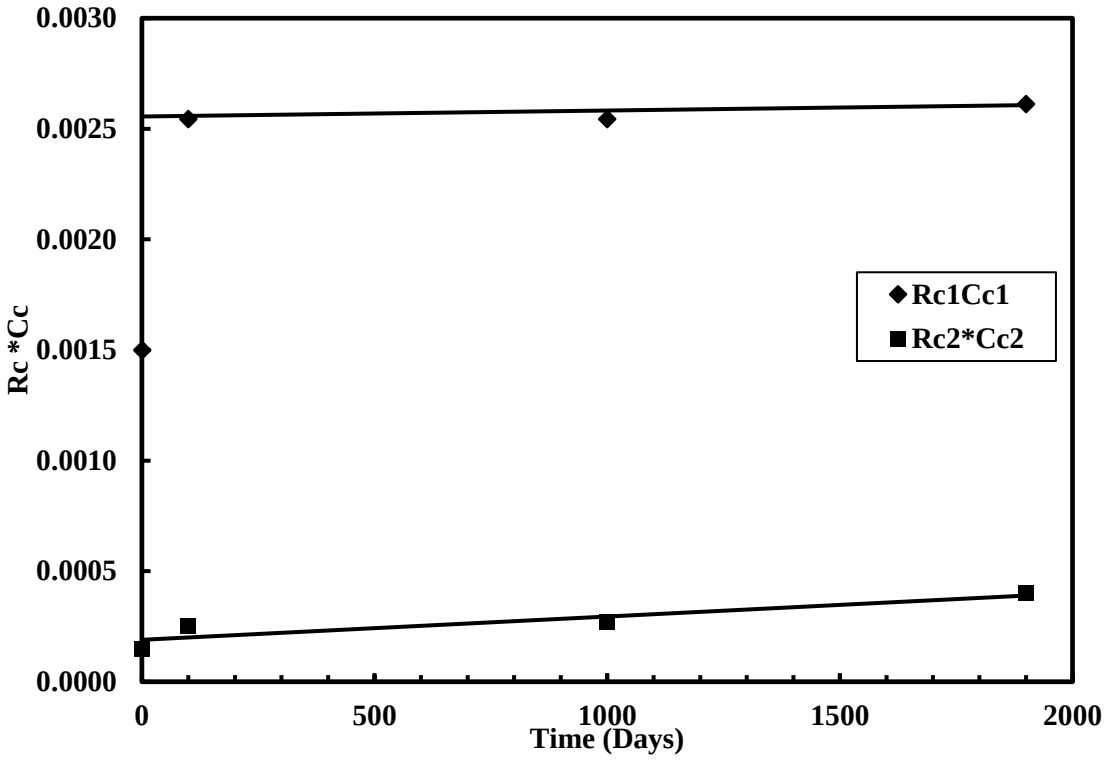


**Figure 5-25:Contact Resistance and Capacitance product variation over 1900 days of time.**

### 5.3.5 Cement Curing

The curing of the cement between the casing and PVC is monitored by measuring the resistance between the two probes. All the readings shown are vertical readings with angle A with a spacing of 6in. The levels from 1 to 10 are expected to cure under moist conditions while the levels 11- 14 are air cured. The bottom levels were experiencing surcharge load due to the self-weight of the cement. The resistance at all the levels was in the range of 17 to 25 Ω during the initial cementing of the model. The resistance value mainly depends on three factors namely resistivity changes due to stresses, curing conditions and temperature changes in the Lab. The resistance values experienced a change from 17 Ω to a maximum of about 321 Ω, a 17.8 times increase in about 1900 days (5.2 years) of curing (Figure 5-26). It was observed that the resistances were gradually increasing in value indicating the curing of the cement and its hardening with time.

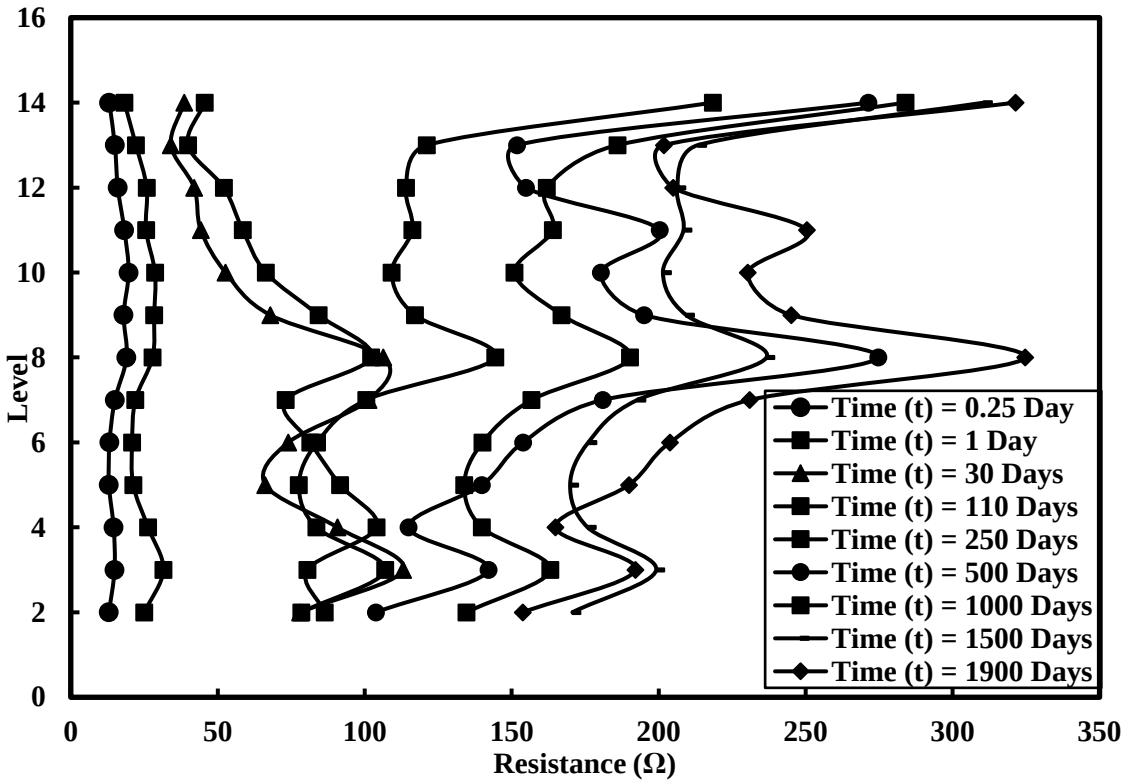


**Figure 5-26:Variation of vertical resistance with time in lab model.**

### 5.3.6 Electrical Resistance

The laboratory model was installed and cemented on November 23, 2014. Since then, the Laboratory model has been curing in room temperature of 22 °C for a period of 1900 days. During the room curing of the model, the top levels experienced maximum change in the resistance from about 17 Ω to 321 Ω in the level 13-14 (Figure 5-27). Similarly, the middle and bottom levels, 5- 6 and 2-3 experienced a change from about 25.3 Ω to 245 Ω and 23.6 Ω to 192 Ω. The top level experienced a maximum change of 17.8 times in electrical resistance due to air curing. The middle level showed a change of 8.7 times in electrical resistivity while the bottom levels had a change of 7.1 times. The middle and bottom levels showed approximately similar change in electrical resistance due to similar moist curing conditions.

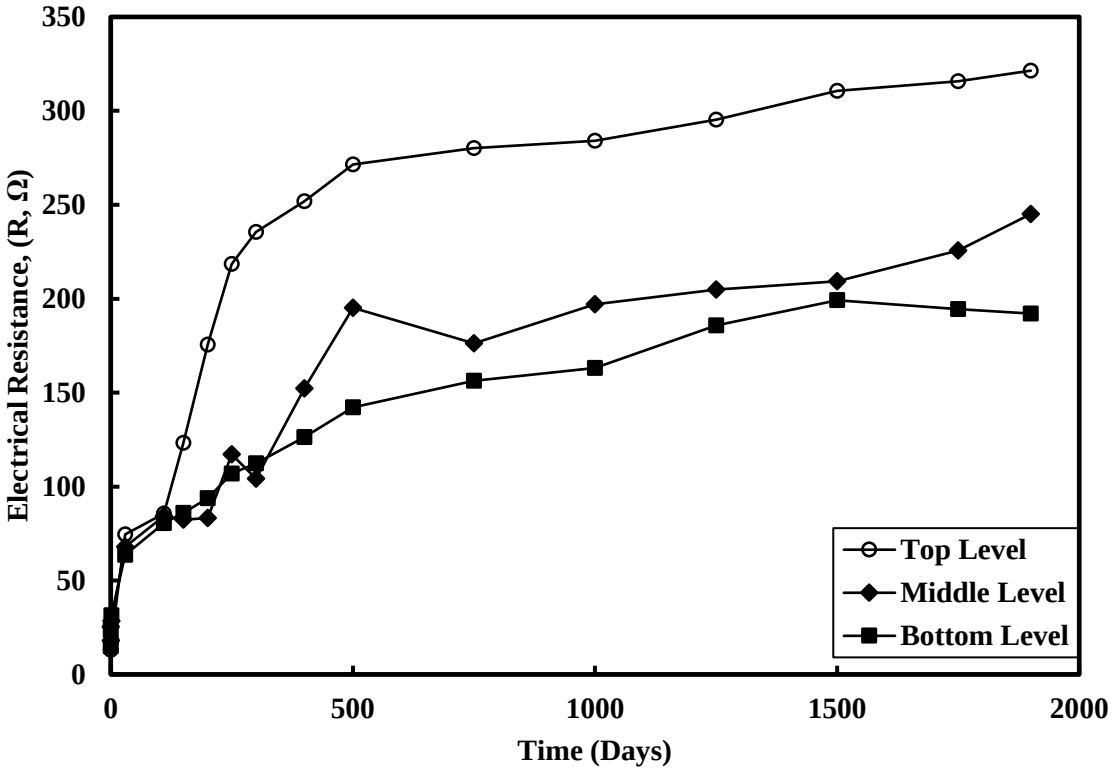


**Figure 5-27:Variation of Electrical Resistance in the Lab model at top, middle and bottom levels during a curing period of 1900 days.**

### 5.3.7 Electrical Resistivity of Lab Oil Well Model

***Top Level***

The value of initial resistivity of smart cement was 0.905 Ω.m. immediately after mixing. The electrical resistivity of smart cement was 17.1 Ω.m. after 5.2 years of curing (Figure 5-28). The time for minimum resistivity was 180 minutes after mixing (Table 5-7). Based on the preliminary analyses, AI model with four layers of ANN was selected to predict the resistivity change with time. Over 30 data was used perform the BPNN and predict the trend. Curing model parameters $p_1$ and $q_1$ were 0.71 and 0.28 respectively after 5.2 years of curing (Table 5-7). Also, the other curing model parameters are summarized in Table 5-7. The value of RMSE (root mean square error) for curing model was 1.81 Ω.m, while it was 0.81 Ω.m for the AI model. The value of $R^2$ for curing model was 0.99 while it was 0.99 for the AI model (Table 5-8). Thus, Vipulanandan curing model had comparatively equivalent prediction for long term compared to AI model.

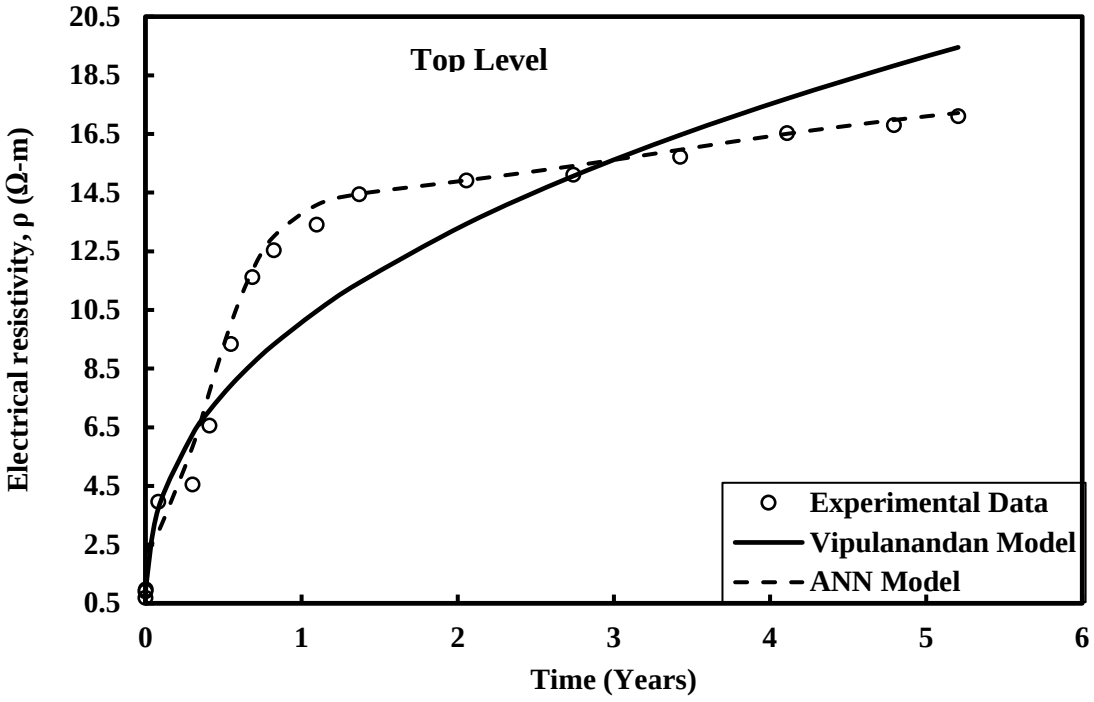


**Figure 5-28: Comparing the prediction of electrical resistivity at the top level using the AI model and Vipulanandan Curing model up to 5.2 years.**

***Middle Level***

The value of initial resistivity of smart cement was 0.905 Ω.m. immediately after mixing. The electrical resistivity of smart cement was 8.8 Ω.m. after 5.2 years of curing (Figure 5-29). The time for minimum resistivity was 180 minutes after mixing (Table 5-7). Based on the preliminary analyses, AI model with four layers of ANN was selected predict the resistivity change with time. Over 30 data was used perform the BPNN and predict the experimental trend. Curing Model parameters $p_1$ and $q_1$ were 0.4 and 0.15 respectively after 5.2 years of curing (Table 5-7). Also, the other curing model parameters are summarized in Table 5-7. The value of RMSE (root mean square error) for electrical resistivity model was 0.55 Ω.m while it was 0.407 Ω.m for AI model. The value of $R^2$ for electrical resistivity model was 0.99 while it was 0.99 for AI model (Table 5-8). Thus, Vipulanandan curing model had comparatively equivalent prediction for long term compared to AI model.

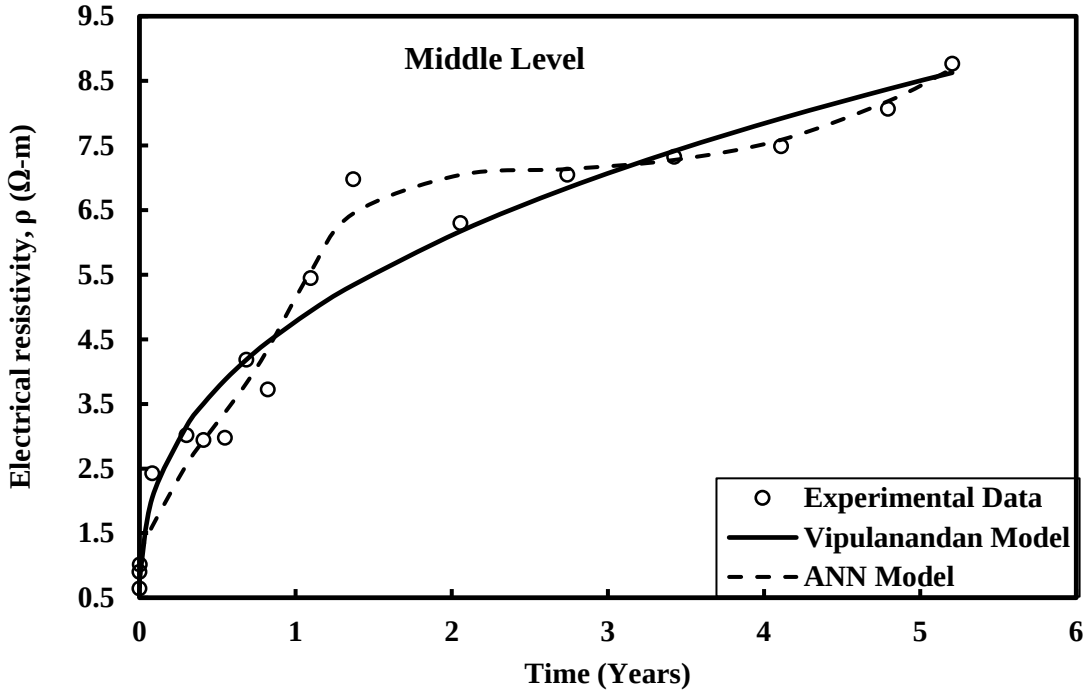


**Figure 5-29:Comparing the prediction of electrical resistivity at the middle level using the AI model and Vipulanandan Curing model up to 5.2 years.**

***Bottom Level***

The value of initial resistivity of smart cement was 0.907 Ω.m immediately after mixing. The electrical resistivity of smart cement was 7.4 Ω.m. after 5.2 years of curing (Figure 5-30). The time for minimum resistivity was 180 minutes after mixing (Table 5-7). Based on the preliminary analyses, AI model with four layers of ANN was selected predict the resistivity change with time. Over 30 data was used perform the BPNN and predict the experimental trend. Curing Model parameters $p_1$ and $q_1$ were 0.69 and 0.22 respectively after 5.2 years of curing (Table 5-7). Also, the other curing model parameters are summarized in Table 5-7. The value of RMSE (root mean square error) for electrical resistivity model was 0.24 Ω.m while it was 0.32 Ω.m for AI model. The value of $R^2$ for electrical resistivity model was 0.99 while it was 0.99 for AI model (Table 5-8). Thus, Vipulanandan curing model had comparatively better prediction for long term compared to the AI model.

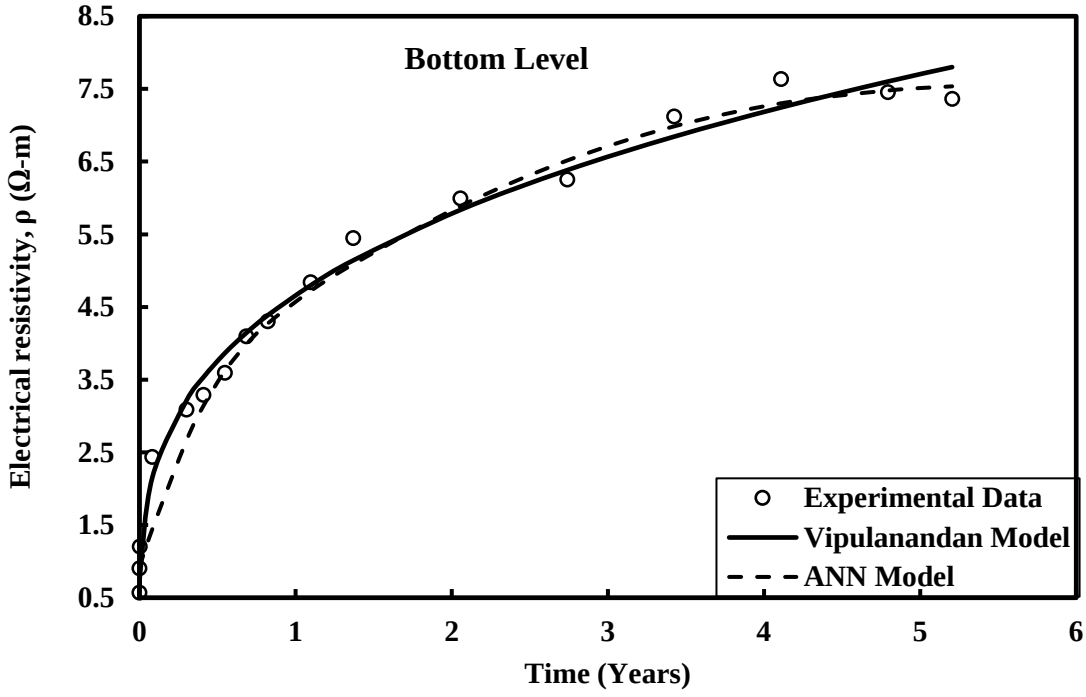


**Figure 5-30:Comparing the prediction of electrical resistivity at the bottom level using the AI Model and Vipulanandan Curing Model up to 5.2 years.**

**Table 5-7:Electrical resistivity model parameters for smart cement in lab for 5.2 years.**

| Level | Initial Resistivity, $\rho_o$ (Ω-m) | $\rho_{min}$ (Ω-m) | $t_{min}$ (min) | $t_o$ (min) | $p_1$ | $q_1$ |
|---|---|---|---|---|---|---|
| Top | 0.905 | 0.7 | 180 | 100 | 0.71 | 0.28 |
| Middle | 0.905 | 0.644 | 180 | 75 | 0.4 | 0.15 |
| Bottom | 0.907 | 0.571 | 180 | 34 | 0.69 | 0.22 |

**Table 5-8:Correlation parameters for ANN Model and Resistivity model for smart cement in lab field after 5.2 years.**

| | ANN Model | | Resistivity Model | |
|---|---|---|---|---|
| Level | $R^2$ | RMSE (Ω-m) | $R^2$ | RMSE (Ω-m) |
| Top | 0.99 | 0.81 | 0.99 | 1.81 |
| Middle | 0.99 | 0.407 | 0.99 | 0.55 |
| Bottom | 0.99 | 0.324 | 0.99 | 0.24 |

### 5.3.8 Pressure Test

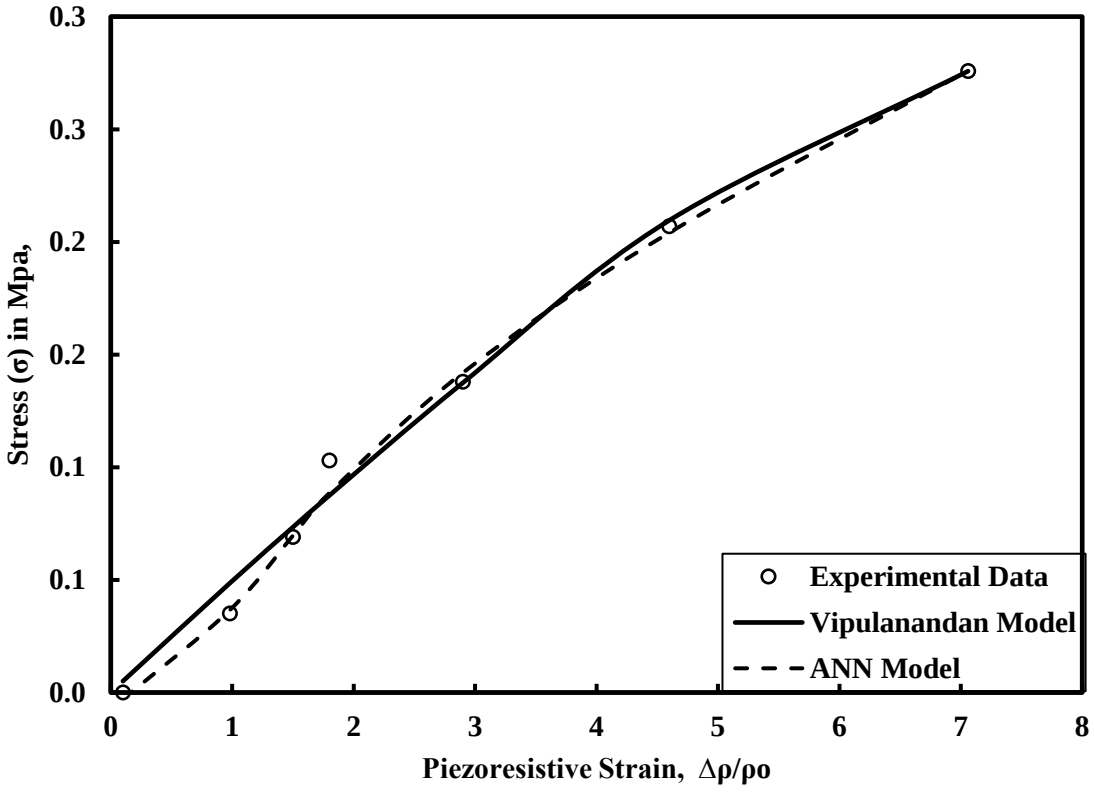


**Figure 5-31:Piezoresistive Strain for smart cement in the lab after 5.2 years of curing.**

**Table 5-9:Correlation parameters for ANN Model and piezoresistivity model for smart cement in lab after 5.2 years.**

| | ANN Model | | Piezoresistivity Model | |
|---|---|---|---|---|
| | $R^2$ | RMSE (MPa) | $R^2$ | RMSE (MPa) |
| Smart Cement Lab Model | 0.99 | 0.008 | 0.99 | 0.006 |

The pressure was applied inside the casing to measure the changes in the resistivity after curing period of 5.2 years. With the application of the 10-psi pressure, the resistivity was observed to increase reduce by about 1.5% at maximum and 1.2% on average throughout the model. With application of 20 psi pressure, the change of 2.9% at maximum was observed and 2.5% on an average. With application of 40 psi pressure, a maximum of 7.1% change was observed and 4.2% on an average throughout (Figure 5-31). The piezoresistivity per unit stress was 0.178%/psi for lab model after curing of 1900 days. These measurements show case that the model is most sensitive to pressure coming on to it. The decrease in the resistivity was due to the unloading effect of the load developed by deviatoric stress acting on the cement. The electrical resistivity was increase after application of higher pressure.

## 5.4 Field Model Well

In this study, polymer drilling fluid and smart cement were used.

- Polymer based drilling fluids are used to drill through reactive geological formation. Since this study the drilling was to be done through swelling soft montmorillonite clay, polymer drilling fluid was used. It is less reactive with the clay formations and controls the fluid loss into the formations. The density of the polymer drilling fluid was 8.7 ppg and the electrical resistivity was in the range of 2 Ω·m to 3 Ω·m.
- Cement slurry was prepared using a water-to-cement ratio of about 0.6, making the mixing and pumping easier in the field. The cement was modified with an addition of 0.075 percent conductive filler by total weight of the cement slurry. The initial resistivity of the cement slurry was in the range of 1.20 to 1.24 Ω·m. Total of 42 samples were collected for

characterizing the smart cement behavior. Commercially available conductivity probe and digital resistivity meters were used in deter-mining the resistivity of cement (Vipulanandan et al., 2014).

- Resistivity of smart cement: The LCR meter was used to measure the impendence (resistance, capacitance and inductance) in the frequency range of 20 Hz to 300 kHz. Based on the impedance (z) – frequency (f) response it was determined that the smart cement was a resistive material (Vipulanandan et al., 2013). Hence the resistance measured at 300 kHz using the two-probe method was correlated to the resistivity (measured using the digital resistivity device) to determine the K factor for a time period of initial five hours of curing. This K factor was used to determine the resistivity of the cement with the curing time.
- Piezoresistivity test: Piezoresistivity describes the change in electrical resistivity of a material under stress. Since oil well cement serves as pressure-bearing part of the oil and gas wells in real applications, the piezoresistivity of smart cement (stress – resistivity relationship) in these wells is obtained by application of pressure in the central casing for the lab model and in the aluminum pipes for the field model. To eliminate the polarization effect, AC resistance measurements were made using a LCR meter at frequency of 300 kHz (Vipulanandan et al., 2013).

### 5.4.1 Test Site and Soil Characterization

After careful reviewing, Energy Research Park (ERP) at University of Houston was selected to install the field well. The selected site had swelling clays with fluctuating moisture conditions (active zone) which represents nearly the toughest conditions encountered. The top 20 ft. of the soil was swelling clay soil with liquid limit over 50%. Based on the ASTM classification the soil was characterized as CH soil. The water table was 20 ft. below the ground and soil below the water table was also clay with less potential swelling and the liquid limit was below 40%. Based on ASTM classification, this soil was characterized as CL soil (Figure 5-32).

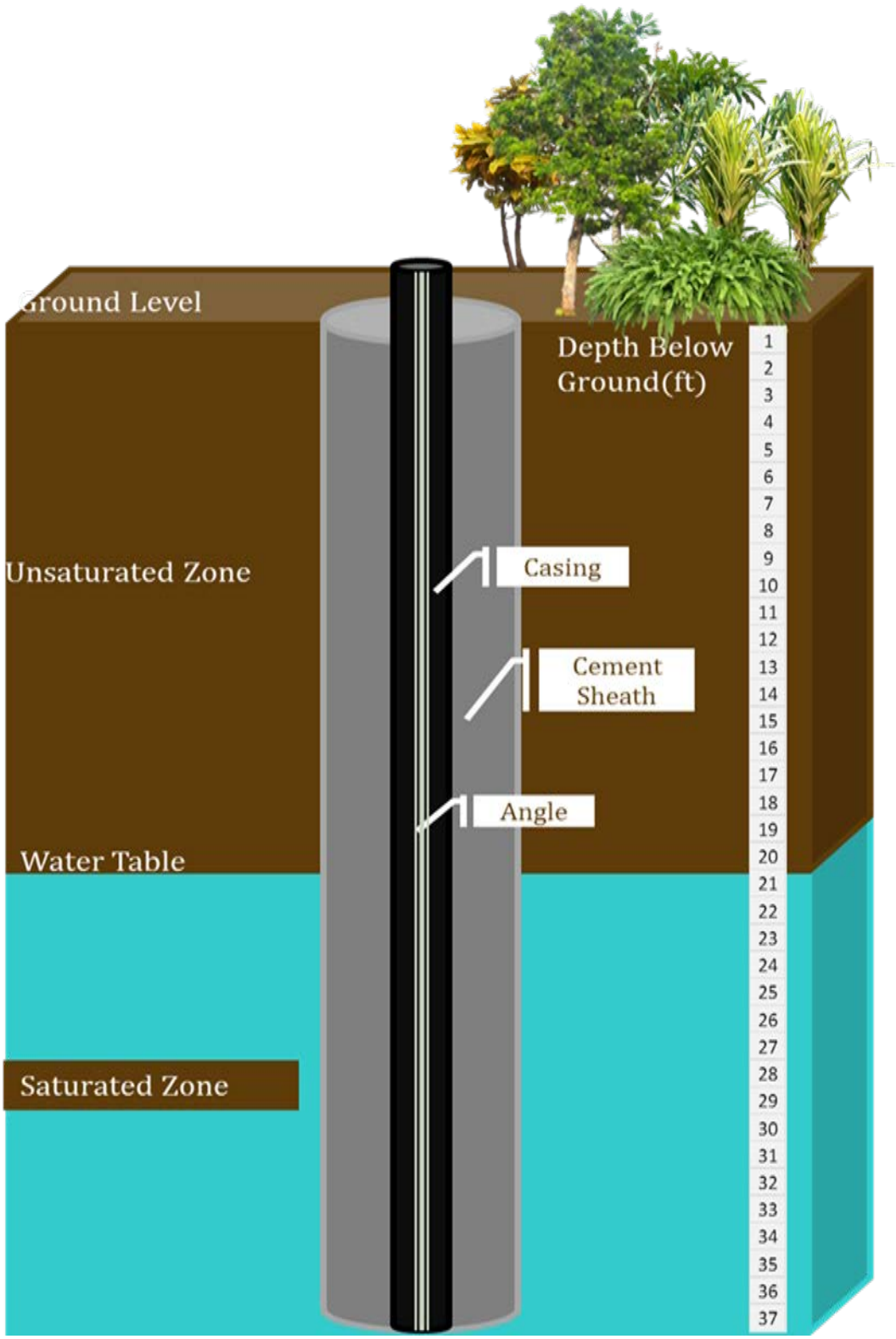


**Figure 5-32:Soil Profile around the Cemented Well.**


**Figure 5-33:Steel Casing with instrumentation and pressurizing tubes.**

The oil well in the field is replicated by a model with about 40ft height and $9_{5/8}$ in diameter representing the casing (Table 5-10). The gap between the formation and the casing is cemented with class A Portland cement with added conductive fillers in it. The casing is attached with steel angles which are used for the characterization of the bulk material (Figure 5-33). Arrangements are also made for observing the temperatures changes in the annulus and strain changes in the bulk material (Figure 5-34 & Table 5-11).

**Table 5-10:Instrumentation details of field model well.**

| | |
|---|---|
| Height of the model | 40 ft |
| Diameter of the Casing | 9 5/8 in |
| Number of Angles | 4 |
| Number of Angles instrumented | 3 |
| Number of Angles not instrumented | 1 |
| Naming of the Angles | |
| Angle | Sides |
| Angle 1 | Sides A, B |
| Angle 2 | Sides C, D |
| Angle 3 | Sides E, F |
| Ange 4 | Sides G, H |

**Table 5-11:Thermocouple and Strain gauges in the field model.**

| Thermocouples | | Strain Gauges | |
|---|---|---|---|
| Total number of thermocouples | 9 | Total number of Strain Gauges | 17 |
| Thermocouples on Angle 1 | 3 | Strain Gauges on Angle 1 | 6 |
| Thermocouples on Angle 2 | 3 | Strain Gauges on Angle 2 | 6 |
| Thermocouples on Angle 3 | 3 | Strain Gauges on Angle 3 | 5 |

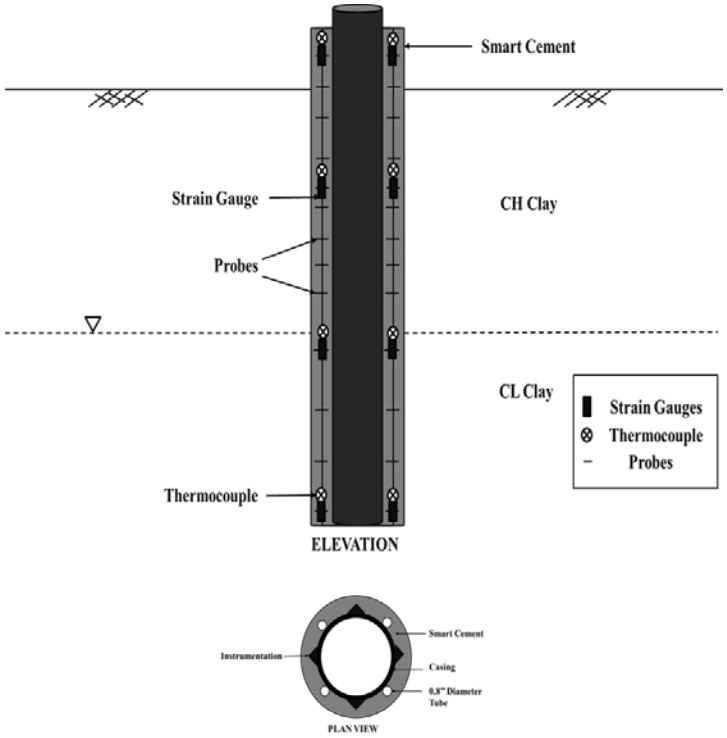


**Figure 5-34:Profile of Strain gauges, thermocouples and resistivity probes in the model.**

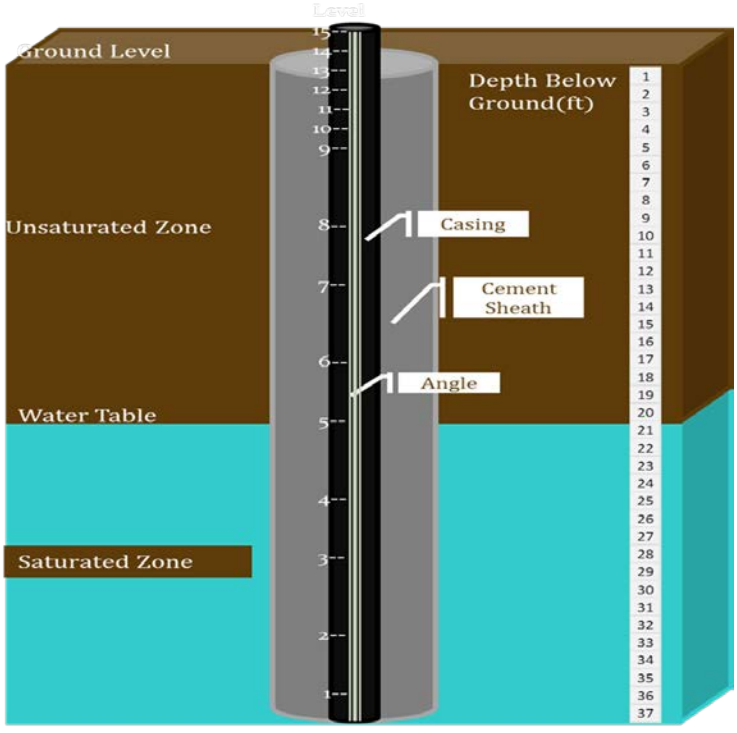


**Figure 5-35:The Spacing of the Probes in vertical direction.**

The spacing at the bottom of the angles was 4ft which was reduced to 2 in the following levels followed by 1ft and 0.5ft (Figure 5-35). A commercial company familiar with the drilling and cementing wells in an urban setting was selected to install the field well. A very large drilling truck with drilling with 14 in diameter drill was used to drill the hole and place the 9 5/8 in diameter standard steel casing. The total length of the casing was 42 feet and needed pieces (including well head and needed connections to lift the casing) were welded together to make a single unit. Initial 15 feet was drilled without any drilling fluid. Polymer based drilling fluid was used to drill the rest of the borehole. After completing the drilling, the casing and the instrumentation units were centered and lowered into the borehole. Initial resistivity of vertical probes was measured in the air which was about 1000 Ω. The casing and the instrumentations were lowered into the borehole and the cement was pumped from the bottom of the borehole and was driving the drilling mud up the borehole. Monitoring of the resistance between the probes, temperature and strains (strain gauges) was performed. All the levels except 14 and 15 were cemented showing that the depth of the well was close to 37ft (Figure 5-35). The Parameter K was determined for all the spacing's during calibration.

**Table 5-12:List of Operations performed during the installation.**

| **List of Operations** | | |
|---|---|---|
| Operation | Date | Time |
| Drilling Bore Hole | 5/1/2015 | 10:15 AM |
| Instrumentation of the Casing | 5/1/2015 | 11:00 AM |
| Placement of the Casing | 5/1/2015 | 1:15 PM |
| Pumping of the Drilling Mud | 5/1/2015 | 1:25 PM |
| Start of Cementing | 5/1/2015 | 2:15 PM |
| End of Cementing | 5/1/2015 | 2:30 PM |
| Top cementing of Bleed water | 5/1/2015 | 4:00 PM |
| Compaction around the Model | 5/4/2015 | 10:15 AM |
| Cementing to the top layers | 5/4/2015 | 10:30 AM |

The List of operations performed during the installation process are listed in Table 5-12.

The operations performed include borehole drilling (Figure 5-36), placement of the casing (Figure 5-37), pumping of drilling mud, and then followed by cementing.


**Figure 5-36:Drilling of the bore hole in site.**


**Figure 5-37:Installation of the casing in the bore hole.**

### 5.4.2 Calibration Parameter K Characterization

The field model angles were calibrated to obtain the parameter K for different spacing. The parameter K was computed for a spacing of 0.5 feet to about 4 feet. The parameter K was found to increase with the increase in spacing as it was proportional to resistance of the bulk material. The field model was found to replicate the lab model in several ways during the calibration. Firstly, the initial resistances were found to have closest match. The parameter K when compared with the spacing was found to have close convergence. The parameter K had increasing trend for both the fields and lab models. The slope of the parameter K for both the field and lab model were close enough in the range of 1.2 and 5 (Figure 5-38).

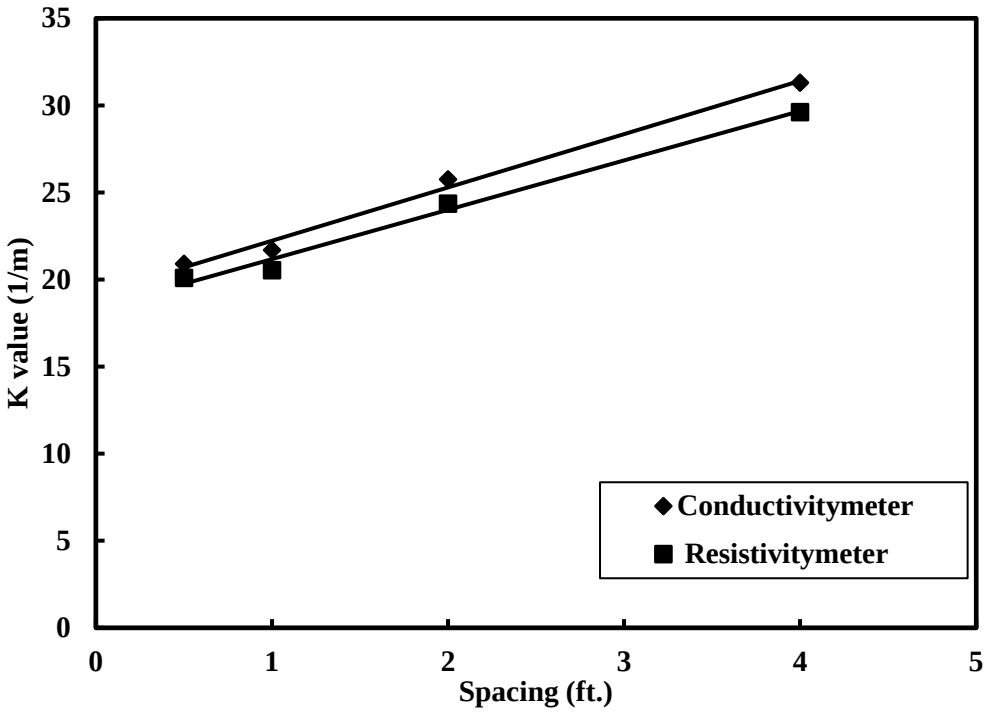


**Figure 5-38:Parameter K Vs Spacing for Field model.**

The parameter K had increasing trend with parameter K of around 20 $m^{-1}$ for 6 inch spacing for the lab model while the parameter K was 30 $m^{-1}$ for 48 inch spacing in the field model (Figure 5-38).

### 5.4.3 Installation

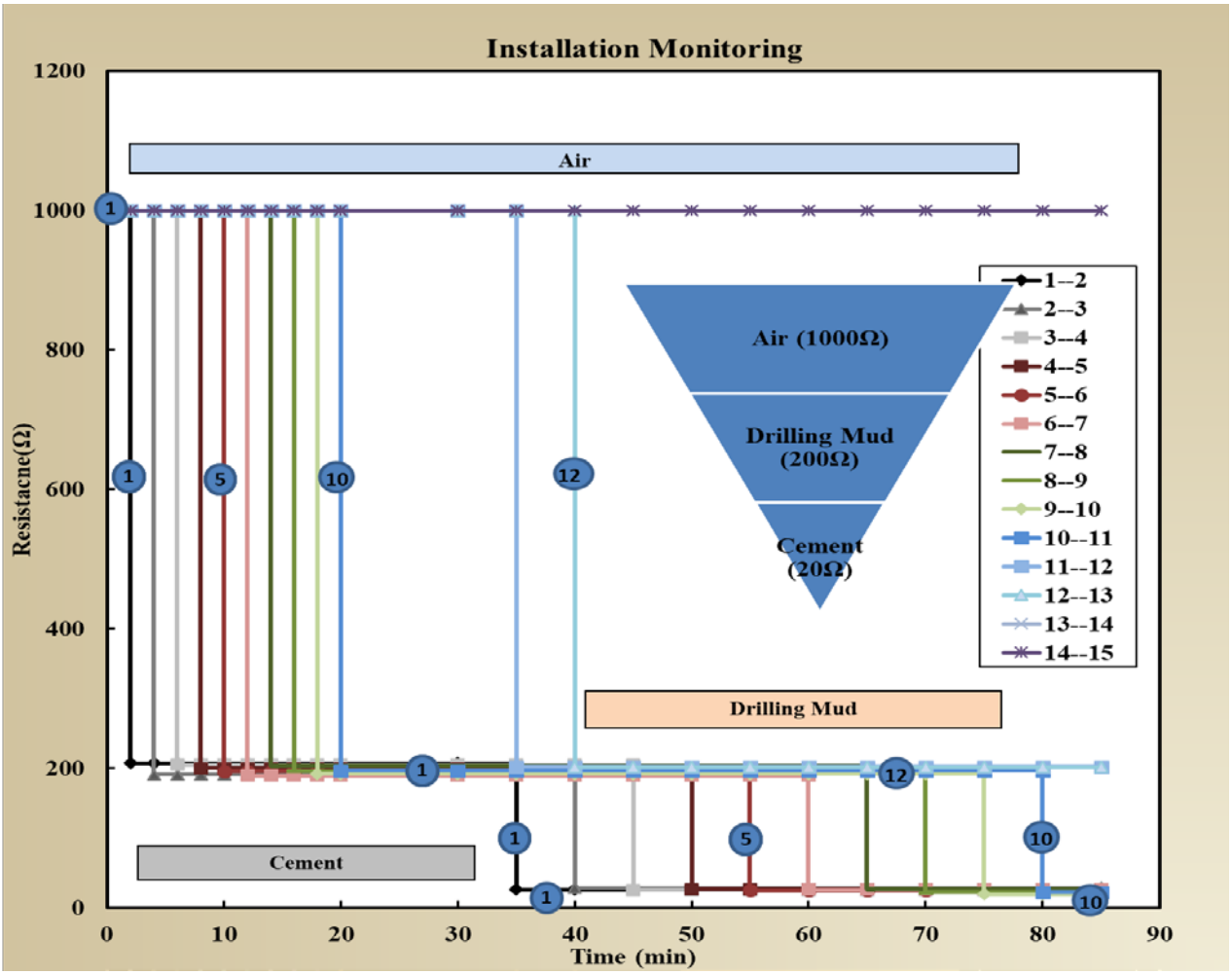


**Figure 5-39:Vertical resistances changes with time during installation.**

Installation Process involves instrumentation of the angles to the casing and lowering the casing. This operation was followed by pumping of drilling mud into the gap to be cemented. Then commercially available cement with conductive fillers was used to cement the spacing between the casing and the formation. By measuring the resistances between the wires, the material between the probes can be monitored. This method gave the flexibility to know where the drilling mud is located and how much more is needed to pump. The method is an effective way to monitor the cementing procedure.

The installation process (Figure 5-39) represents the operations performed during the installation with time. It can be seen that initially the resistances at all the levels was high reading about 1000 Ω which is due to the presence of only air in between the wires. The start of the drilling mud pumping is set as time zero. It can be seen that as the drilling mud is pumped, it starts filling up the levels gradually one by one dropping their resistances to 200 Ω. The drilling mud was pumped for time of about 35 minutes until it reaches the top level in formation which is 12-13. After this the cementing of the well was initiated. As the cementing was done, the levels get filled with cement indicating a drop in the resistances clearly showing that the cement had reached that level.

As the cementing started, the resistance at the level 1-2 first dropped to 20 Ω followed by 2-3 and so on. The cementing operation was stopped when the cement reached level 10-11 as it was the topmost level. This monitoring method enables us to know the level at which drilling mud, or the cement is located. The same method is been used to monitor the performance of the well and also its piezoresistive behavior. The electrical resistance changes observed during the placement of the drilling fluid and cement was very similar to the laboratory model test.

### 5.3.3 Impedance Vs Frequency Curves

Investigation of the impedance versus frequency relationship showed that the smart cement field model followed case 2 behavior as in Figure 3-12, indicating that the bulk material can be represented by resistance at high frequency impedance measurement. The following are the impedance curve for smart cement for a curing time of 1, 100, 1000 and 1600 days (Figure 5-40).

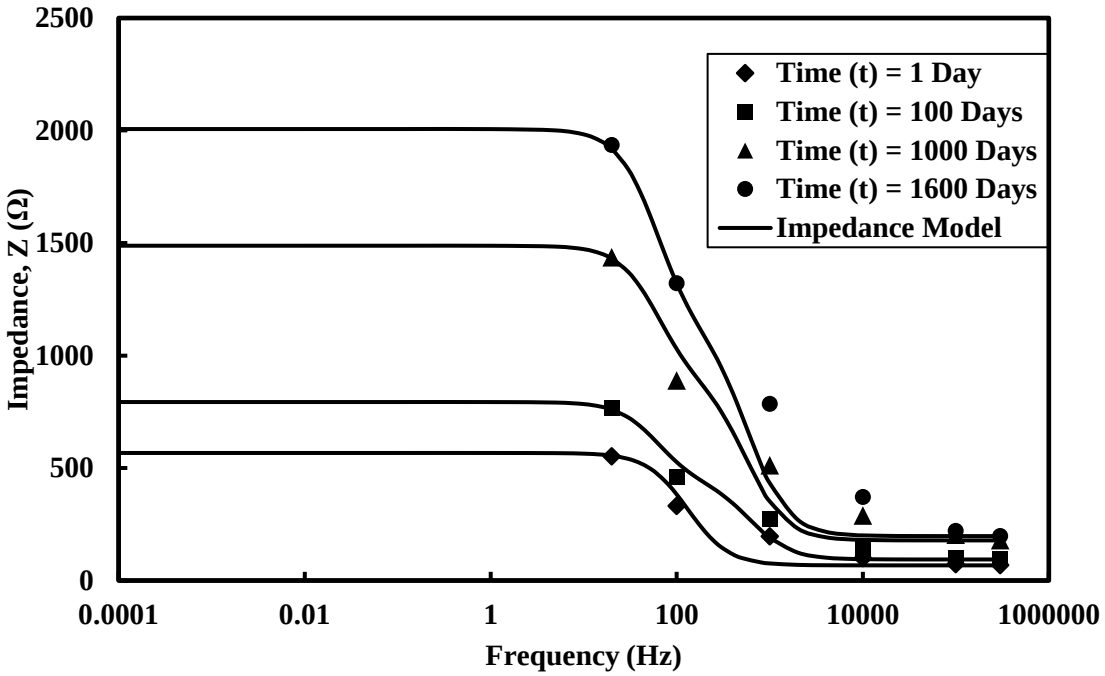


**Figure 5-40:Impedance vs frequency for smart cement for a curing time of 1600 days.**

### 5.2.4 Bulk Resistance, Contact Resistance and Capacitance

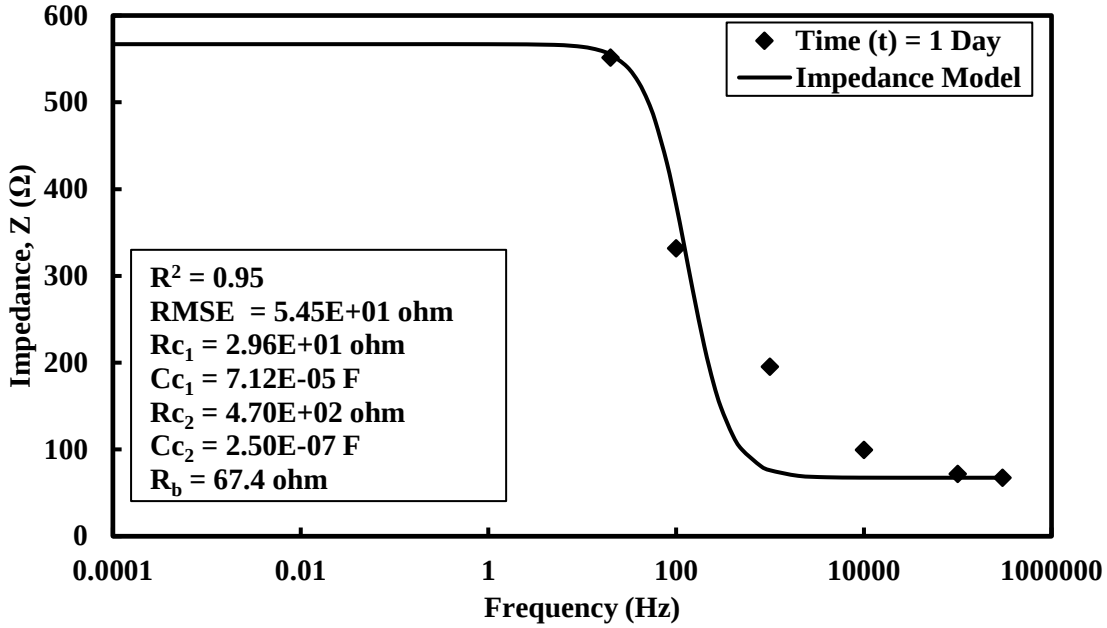


**Figure 5-41:Electrical Impedance for smart cement at time (t) = 1 Day.**

The contact resistances and capacitances for smart cement for curing time of 1600 days are obtained using impedance model given by eqn. 3-5.

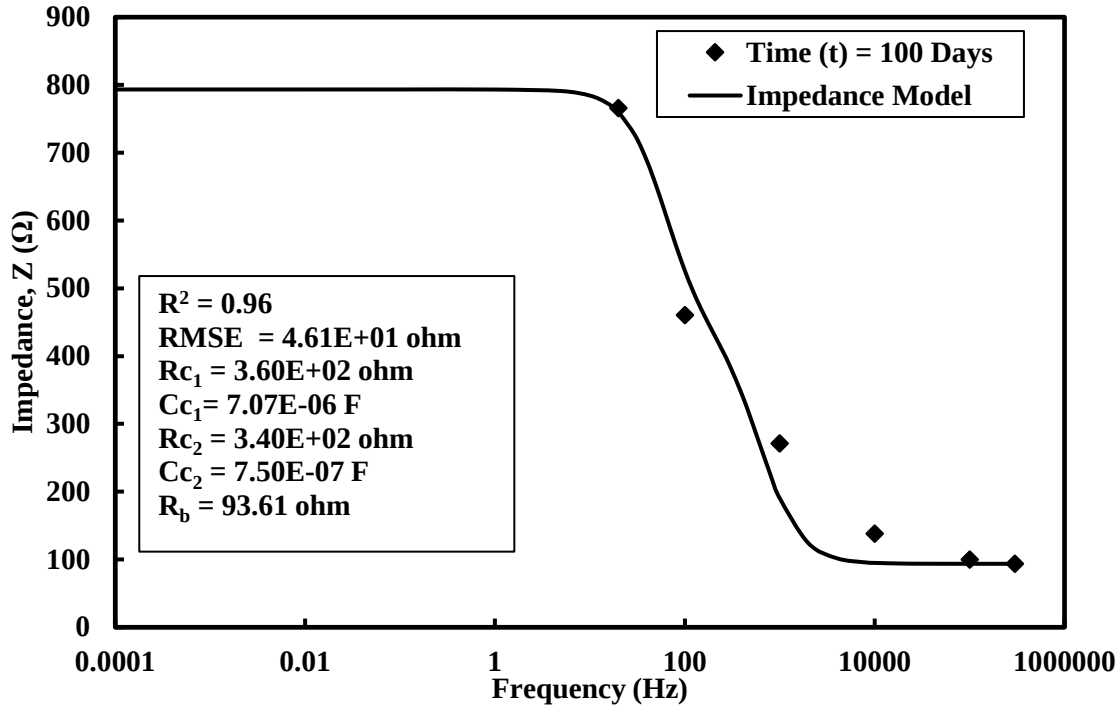


**Figure 5-42:Electrical Impedance for smart cement at time (t) = 100 Days.**

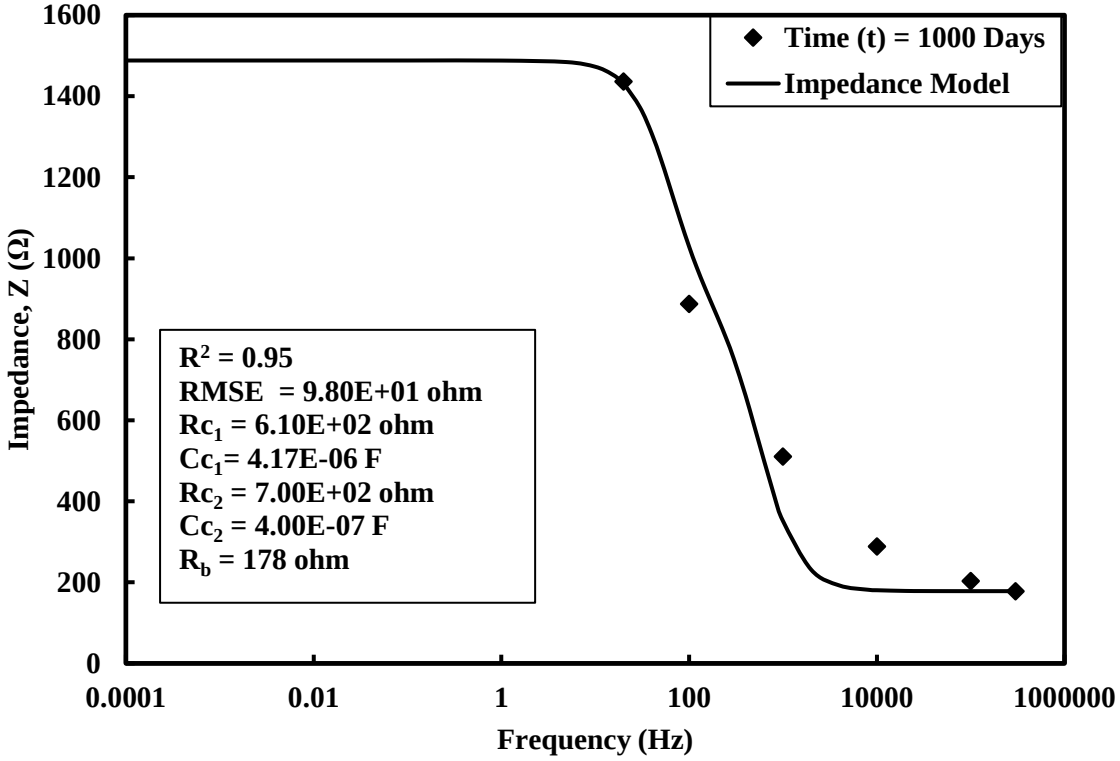


**Figure 5-43:Electrical Impedance for smart cement at time (t) = 1000 Days.**

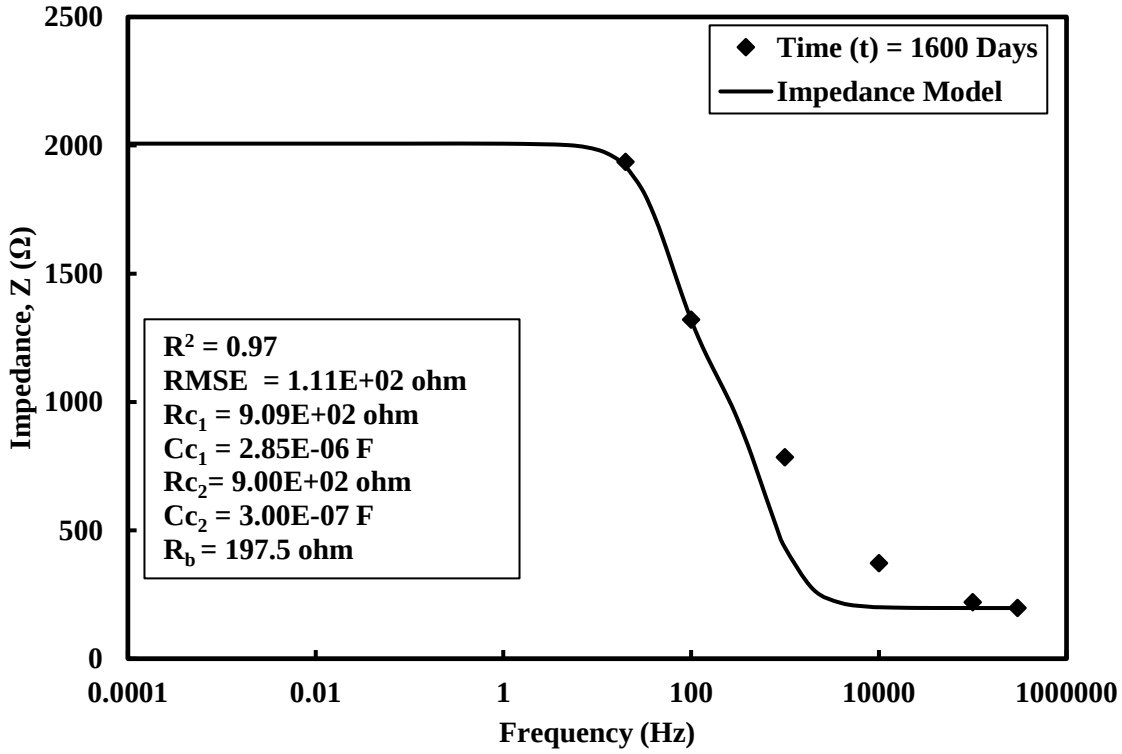


**Figure 5-44:Electrical Impedance for smart cement at time (t) = 1600 Days.**

The Bulk resistance of the smart cement increased from 20 Ω to 197.5 Ω (Figure 5-21 & Figure 5-24), 887% increase in 1600 days when cured at field. The contact resistance ($Rc_1$) increased from 29.6 Ω to 909 Ω, 2970% increase in 1600 days of field curing. The contact capacitance ($Cc_1$) varied from 7.12E-05 F to 2.85E-06 F, a 96% decrease over 1600 days curing period. The electrical contact index ($Rc_1$*$Cc_1$ – product of contact resistance and contact capacitance) varied from 0.21E-02 Ω-F to 0.261E-02 Ω-F, a 24% increase during 1600 days of curing (Figure 5-45).

Similarly, the contact resistance ($Rc_2$) increased from 470 Ω to 900 Ω, 91% increase in 1600 days of field curing. The contact capacitance ($Cc_2$) varied from 2.50E-07 F to 3.00E-07 F, a 20% increase over 1600 days curing period. The electrical contact index ($Rc_2$*$Cc_2$ - product of contact resistance and contact capacitance) varied from 0.11E-03 Ω-F to 0.3E-03 Ω-F, a 200% increase during 1600 days of curing (Figure 5-45).

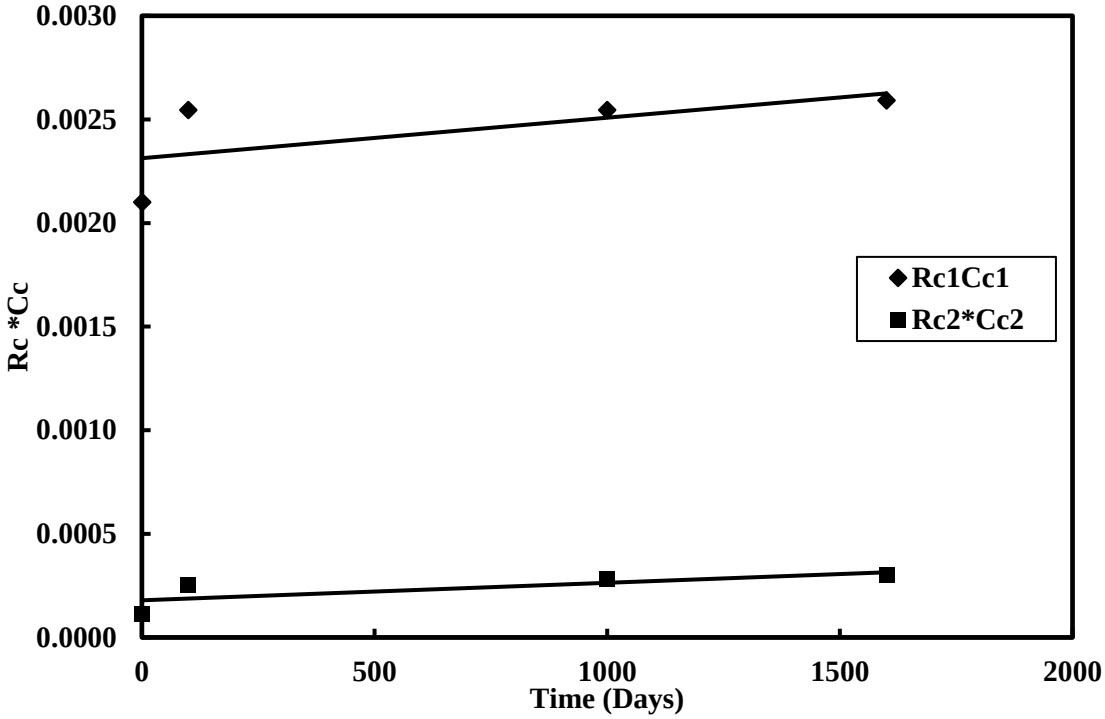


**Figure 5-45:Contact Resistance and Capacitance product variation over 1600 days of time.**

### 5.2.5 Environmental Factors – (Temperature and Rainfall)

The behavior of smart cement in the field was affected by the outside environmental factors such as temperature, rainfall, stress, water table and swelling soft clay. In this study ANN model was compared with the Temperature model and cumulative rainfall model (Eqn. 3-24) to predict the changes in temperature and rainfall over the past five years from 2015 to 2019.

**Temperature**

The average monthly atmospheric temperature fluctuated between 85 $^{o}$F to 48 $^{o}$F from 2015 to 2020 (Figure 5-46). For training the AI models with one, two, three and four layers of ANN, total of 60 data were used with the BPNN approach. Based on the training results, four-layer AI model was selected to do the predictions. AI model was compared it to the Vipulanandan temperature Model. In predicting the temperature data, using the four-layered AI model the coefficient of determination ($R^2$) was 0.94 and the RMSE (root mean square error) was 2.75 $^{o}$F. The AI model prediction is compared to the experimental data in Figure 5-46.

Vipulanandan Temperature Model parameters K, L, $t_o$ and $y_o$ are 15.4 $^oF$, 1, 71.1 year and 2.09$^oF$ respectively. The coefficient of determination ($R^2$) was 0.91 and the RMSE (root mean square error) was 3.48 $^oF$ (Table 5-13). Both the AI model and Vipulanandan Temperature Models predicted the temperatures well (Figure 5-46).

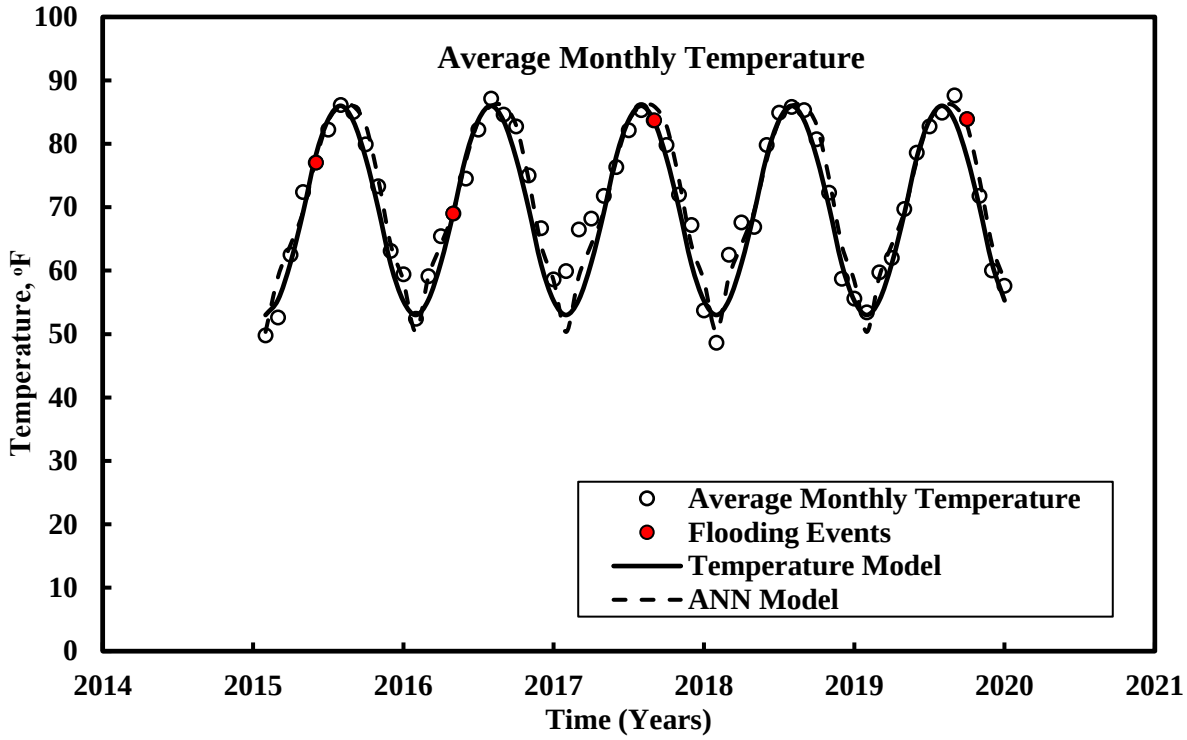


**Figure 5-46:Comparing the Average Monthly Temperature from Year 2015 to 2020 with the Model Predictions.**

**Rainfall**

The cumulative annual rainfall varied from 51 to 80 inches from 2015 to 2020. The four flooding events during this period as shown in Figure 5-46 (years 2015, 2016, 2017 and 2019). For training the AI models with one, two, three and four layers of ANN, total of 60 data were used with the BPNN approach. Based on the training results, four-layer AI model was selected to do the predictions. AI model was compared it to the Vipulanandan Rainfall Model. In predicting the temperature data, using the four-layered AI model the coefficient of determination ($R^2$) was 0.86

and the RMSE (root mean square error) was 9.22 inches. The AI model prediction is compared to the experimental data in Figure 5-47.

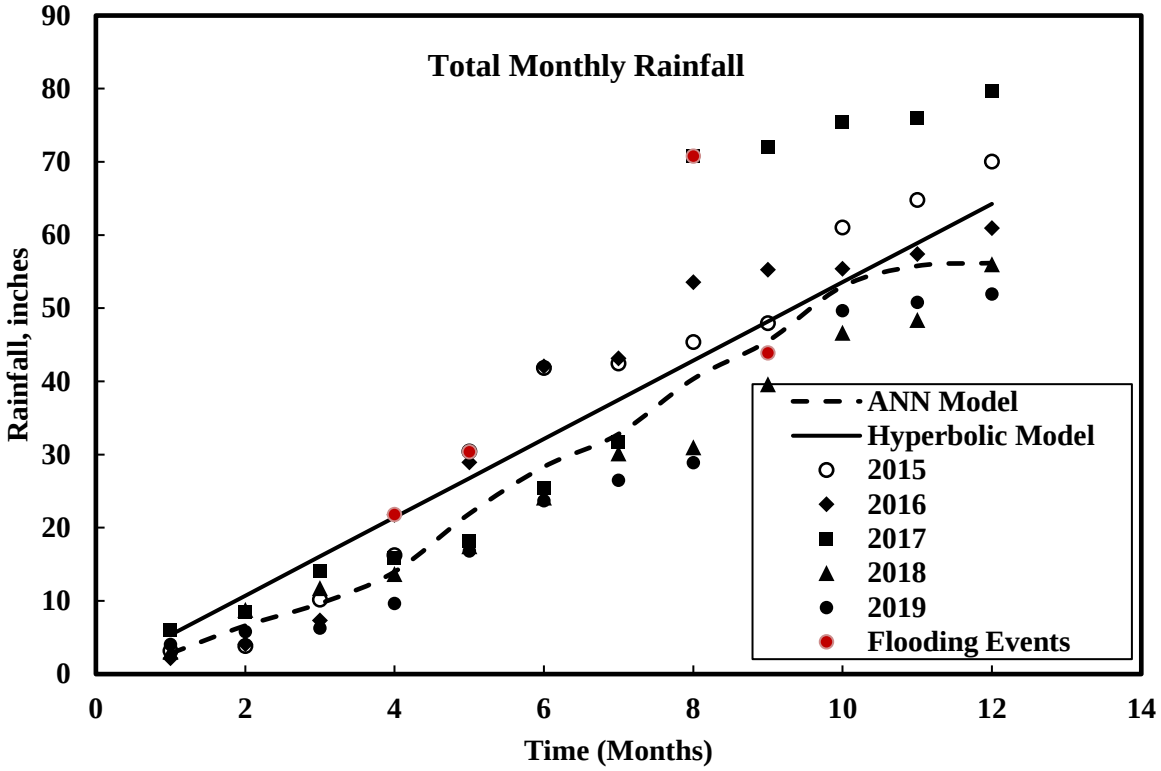


**Figure 5-47:Comparing the Cumulative Monthly Rainfall Predictions from 2015 to 2020.**

Vipulanandan Rainfall Model parameters C and D are 0.24 (month/inch) and -5.2 x$10^{-3}$ /inch respectively. The coefficient of determination ($R^2$) was 0.74 and the RMSE (root mean square error) was 9.29 inches (Table 5-13). Both the AI model and Vipulanandan Rainfall Model predicted are compared with the data in Figure 5-47.

**Table 5-13:Model correlation parameters for temperature and rainfall.**

| | ANN Model | | Temperature/Rainfall Model | |
|---|---|---|---|---|
| Parameter | $R^2$ | RMSE | $R^2$ | RMSE |
| Temperature | 0.94 | 2.75 | 0.91 | 3.48 |
| Rainfall | 0.86 | 9.22 | 0.74 | 9.29 |

### 5.4.6 Cement Curing

The Field model measurements were carried out for a period of about 1600 days. The measurements represent the vertical readings taken between two probes, for example 1-2, 2-3.

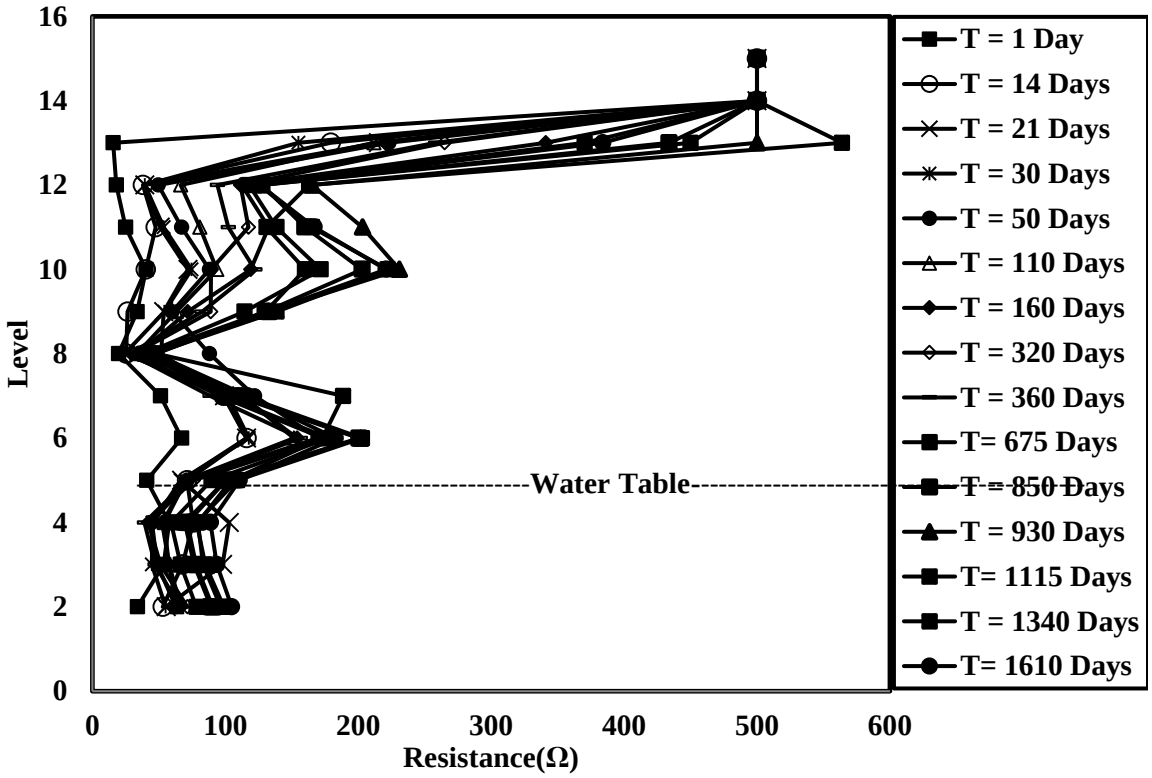


**Figure 5-48:Variation of vertical resistances in field model.**

The spacing of the vertical readings varied from about 0.5 inch to 4 feet. The bottom levels had a higher spacing of about 4 feet while the spacing reduces to 6 inches at the top. The resistance at all the levels was found to increase with the curing period as observed in the lab model (Figure 5-48). The resistance was influenced by temperature, curing conditions and stresses coming on to the cement sheath. The maximum resistance change was found to be seen at level 12-13 from about 15.6 Ω to 384 Ω in 1610 days due to curing of cement in air.

Because of stress from the self-weight of the cement, the level just above the water table experiences maximum change in the resistance. The effective stress increases with the depth while its slope is reduced below water table due to pore water stress. Above the water table, the resistances at all the levels increase with depth due to stress. In the levels below the water table, the resistance is reduced by 60% due to ground water effect (Figure 5-48). The Resistance was expected to increase but due to hot temperatures the resistance is equalized with increase and decrease. The

model had resistance values from about 100 Ω at bottom to about 180 Ω maximum at the level just above the ground water table. The value of the imaginary part was found to change from negative to positive but was very close to zero compared to resistance.

### 5.4.7 Electrical Resistance

The smart cement was mixed in the field and used for cementing the field well. It is important to identify the measurable parameters in the cement sheath and determine the changes with time and depth. Fiber optics are used for monitoring and it depends in the changes in the strain in the cement sheath. The strain in the cement will be influenced by the cement curing, stress and temperature in the cement sheath. Over the past 4.5 years (over 1600 days) thousands of data has been collected on the monitoring parameters. It is important to quantify the changes in the measuring parameters with important variable such as depth. In order to investigate the changes with depth, top level (CH soil), middle level (above the water table, CH soil) and the bottom level (below the water table, CL soil) were selected for investigation.

**Top Level**

***Resistance (R):*** The top level was about 1 ft. below the ground surface. The initial resistivity of the smart cement measured using the two probes was 1.03 Ω.m comparable to the laboratory mixed cement of 1.05 Ω.m. The resistance in the top level changed from 22 Ω to 221 Ω, about 9.05 times (905%) change in the resistance (Figure 5-49). The changes in the cement sheath resistance were not uniform but overall showed continuous increase. The rapid increase in the cement resistance was due to the lowering of the environmental temperature and losing of moisture in the cement. The rapid decrease in the cement resistance was due to increase in the environmental temperature and saturation of the cement due to flooding.

***Temperature (T):*** The temperature continuously fluctuated with time with no clear trend. Over the 4.5 years the minimum and maximum measured temperature in the cement sheath was 68$^{o}$F (20.1$^{o}$C) and 97.2$^{o}$F(36.2$^{o}$C), maximum change of 42.8% (Figure 5-49). The average temperature

at the top level was about 77.7°F (25.4 °C), a 14% decrease from initial temperature of 90.3°F (32.4°C) which would have been influenced by cement hydration.

***Strain (S):*** The strain gauge resistance increased from 123 Ω to 133 Ω during the period of 4.5 years with some fluctuations. The change in strain gage resistance was about 8.1%. The tensile strain at the top level was about 3.3xE-6.

Based on the measured monitoring parameters in the cement sheath, change in electrical resistance showed the largest change compared to the changes in temperature and strain. Hence it is important to develop models to predict this change with time for monitoring the well.

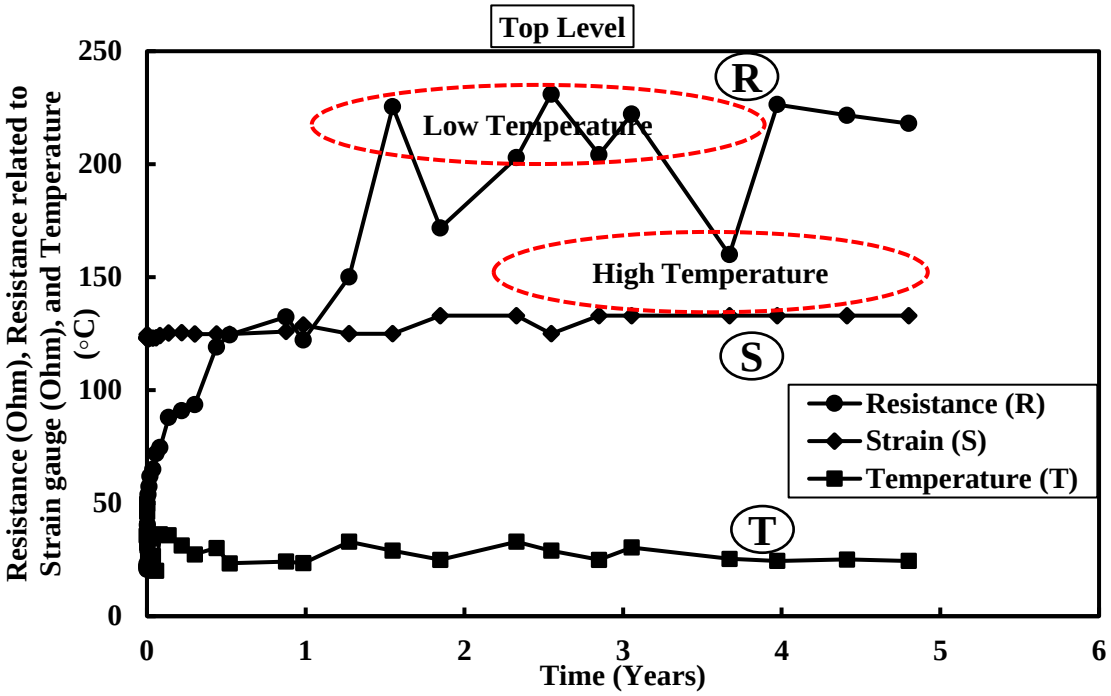


**Figure 5-49:Electrical Resistance, Strain and Temperature variation in top level after 4.5 years.**

**Middle Level**

***Resistance (R):*** The middle level was about 15 ft. below the ground level and above the water table. The initial resistivity of the smart cement measured using the two probes was 1.24 Ω.m higher than top level of 1.03 Ω.m and the laboratory mixed cement of 1.05 Ω.m. The resistance in the top level changed from 26.5 Ω to 182.9 Ω, about 5.90 times (590%) change in the resistance (Figure

5-50). The changes in the cement sheath resistance were not uniform but overall showed continuous increase. The rapid increase in the cement resistance was due to the lowering of the environmental temperature and losing of moisture in the cement. The rapid decrease in the cement resistance was due to increase in the environmental temperature and saturation of the cement due to rising of the water table because of flooding.

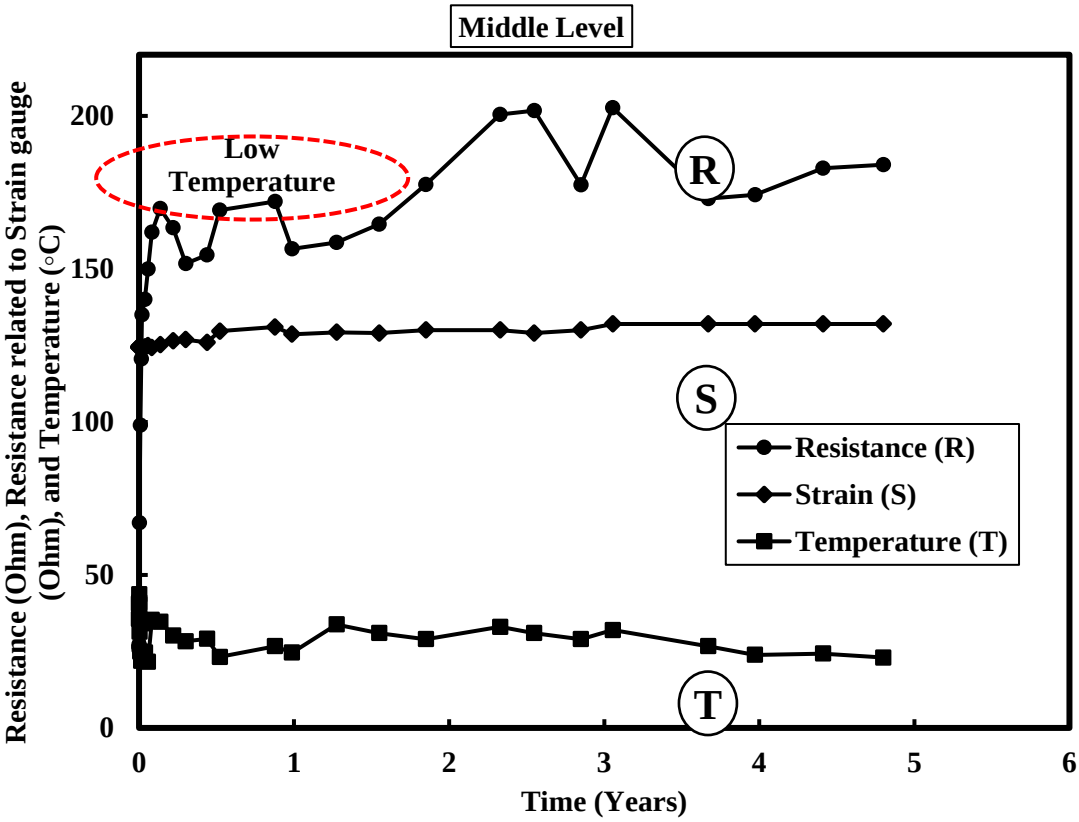


**Figure 5-50:Electrical Resistance, Strain and Temperature variation in middle level after 4.5 years.**

***Temperature (T):*** The temperature continuously fluctuated with time with no clear trend. Over the 4.5 years the minimum and maximum measured temperature in the cement sheath was 70.9°F (21.6°C) and 95.5°F(34.7°C), maximum change of 34.7% (Figure 5-50). The average temperature at the middle level was about 78.8°F (26 °C), a 18% decrease from initial temperature of 96.4°F (35.8°C) which would have been influenced by cement hydration.

***Strain (S):*** The strain gage resistance increased from 124 Ω to 132 Ω during the period of 4.5 years with some fluctuations. The change in strain gage resistance was about 6.5%. The tensile strain in the middle level was 3.65xE-6.

Based on the measured monitoring parameters in the cement sheath, change in electrical resistance showed the largest change compared to the changes in temperature and strain. Hence it is important to develop models to predict this change with time for monitoring the well.

**Bottom Level**

***Resistance (R):*** The bottom level was at 36 ft. below the ground and was under the water table. The initial resistivity of the smart cement measured using the two probes was 1.32 Ω.m higher than top level of 1.03 Ω.m and the laboratory mixed cement of 1.05 Ω.m. The resistance in the bottom level changed from 28.2 Ω to 104.9 Ω, about 2.72 times (272%) change in the resistance (Figure 5-51). The changes in the cement sheath resistances were uniform and overall showed continuous increase. The minor fluctuations are due to changes in water table level due to flooding.

***Temperature (T):*** The temperature fluctuated with time but was much less than the middle and top levels. Over the 4.5 years the minimum and maximum measured temperature in the cement sheath was 71.1°F (21.7°C) and 91.4°F(33°C), maximum change of 28.6% (Figure 5-51). The average temperature at the bottom level was about 77°F (25°C), a 15.8% decrease from initial temperature of 91.4°F (33°C) which would have been influenced by cement hydration.

***Strain (S):*** The strain gage resistance increased from 124 Ω to 133 Ω during the period of 4.5 years with some fluctuations. The change in strain gage resistance was about 8.6%. The tensile strain at the bottom level was 4.8xE-6.

Based on the measured monitoring parameters in the cement sheath, change in electrical resistance showed the largest change compared to the changes in temperature and strain. Hence it is important to develop models to predict this change with time for monitoring the well.

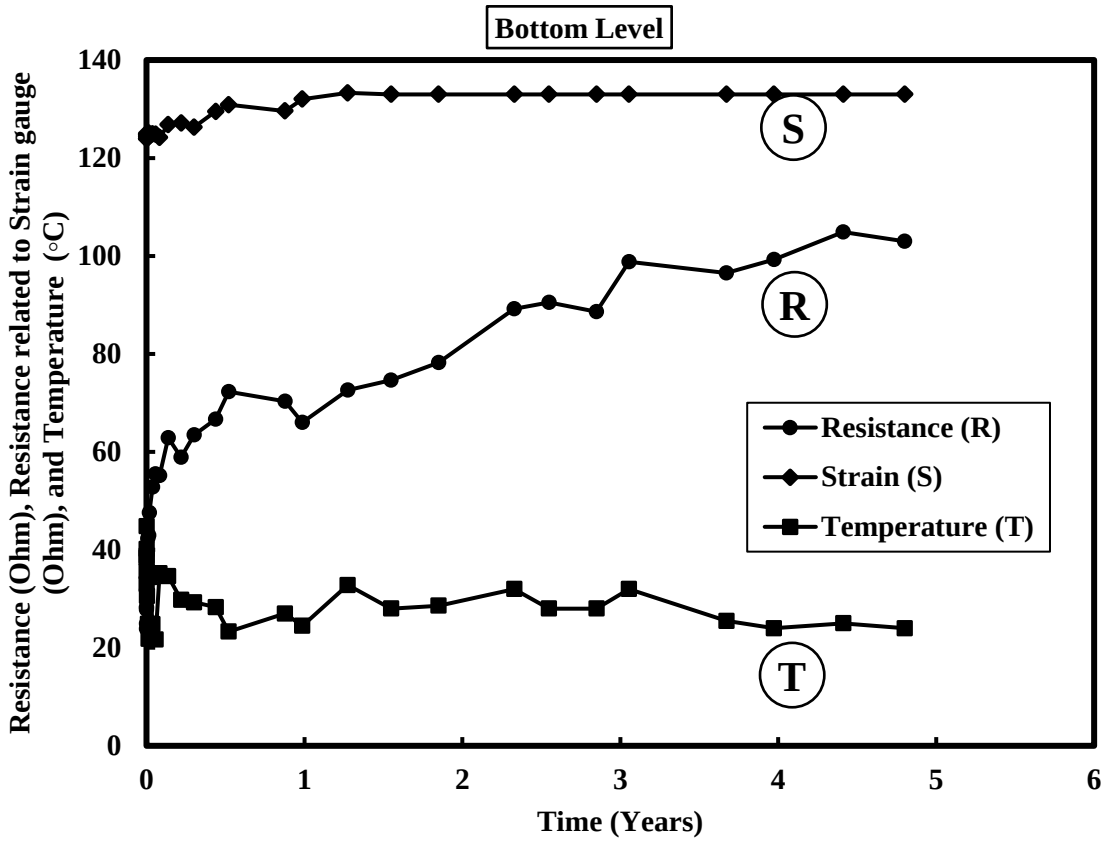


**Figure 5-51:Electrical Resistance, Strain and Temperature variation in bottom level after 4.5 years.**

**Comparing Resistance Change**

From the measurements made at all levels, clearly the electrical resistance change was the highest. Hence it is of interest compare the changes and trends in the electrical resistance with the depth. The electrical resistance change was not uniform in the top and middle levels in the field well. The electrical resistance changed by 905% in the top level close to the surface. The top level also showed the largest fluctuation in the resistance changes based on the weather patterns.

Both the environmental temperature and rainfall influenced the fluctuation in the resistance at the top level (Figure 5-52) The electrical resistance changed by 590% in middle level (15 feet below the ground) with much less in fluctuation compare to the top level. The electrical resistance change at the bottom level, below the water table, was 272% (Figure 5-52). Also, the difference in the electrical resistance changes was due to difference in cement curing conditions of the field well.

The top level was exposed to outside temperature and had air curing, while the middle level was under moisture curing and bottom level was cured under water.

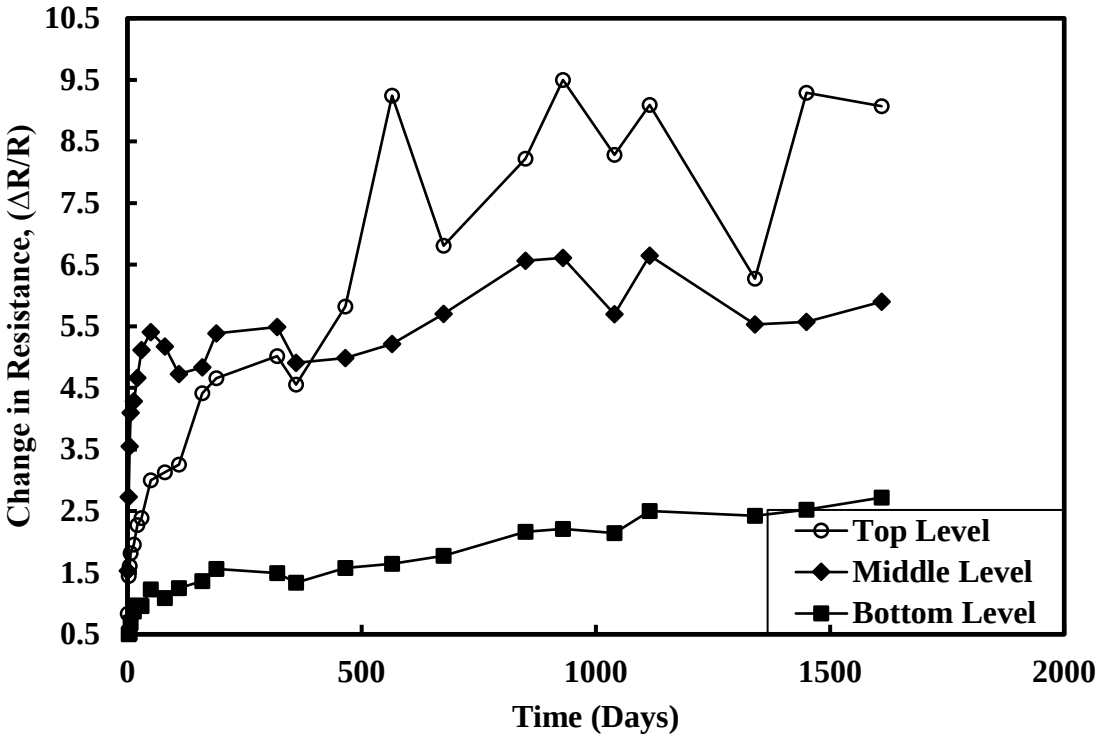


**Figure 5-52:Change in Electrical Resistance data for top, middle and bottom levels in field well for 4.5 years.**

### 5.4.8 Electrical Resistivity of Field Oil Well Model

**Top Level**

The value of initial resistivity of smart cement was 1.03 Ω.m. immediately after mixing. The electrical resistivity of smart cement was 10.4 Ω.m. after 4.5 years of curing (Figure 5-53). The time for minimum resistivity was 195 minutes after mixing (Table 5-14). Based on the preliminary analyses, AI model with for layers of ANN was selected predict the resistivity change with time. Over 30 data was used perform the BPNN and also predict the experimental trend. Curing Model parameters $p_1$ and $q_1$ were 0.76 and 0.24 respectively after 4.5 years of curing (Table 5-14). Also, the other curing model parameters are summarized in Table 5-14.

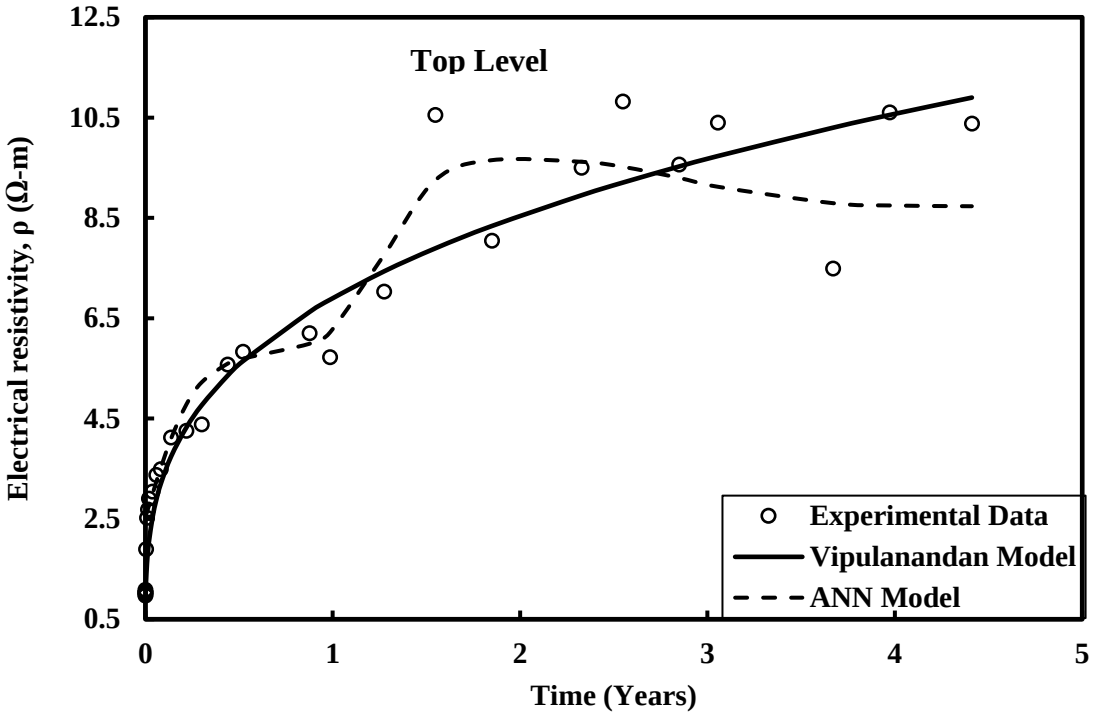


**Figure 5-53:Comparing the Prediction of Electrical Resistivity at the Top Level Using the AI Model and Vipulanandan Curing Model up to 4.5 years.**

The value of RMSE (root mean square error) for curing model was 0.86 Ω.m, while it was 1.02 Ω.m for the AI model. The value of $R^2$ for curing model was 0.97 while it was 0.91 for the AI model (Table 5-15). Thus, Vipulanandan curing model had comparatively better prediction for long term compared to AI model.

**Middle Level**

The value of initial resistivity of smart cement was 1.24 Ω.m. immediately after mixing. The electrical resistivity of smart cement was 8.5 Ω.m. after 4.5 years of curing (Figure 5-54). The time for minimum resistivity was 195 minutes after mixing (Table 5-14). Based on the preliminary analyses, AI model with for layers of ANN was selected predict the resistivity change with time. Over 30 data was used perform the BPNN and also predict the experimental trend. Curing Model parameters $p_1$ and $q_1$ were 0.78 and 0.22 respectively after 4.5 years of curing (Table 5-14). Also, the other curing model parameters are summarized in Table 5-14.

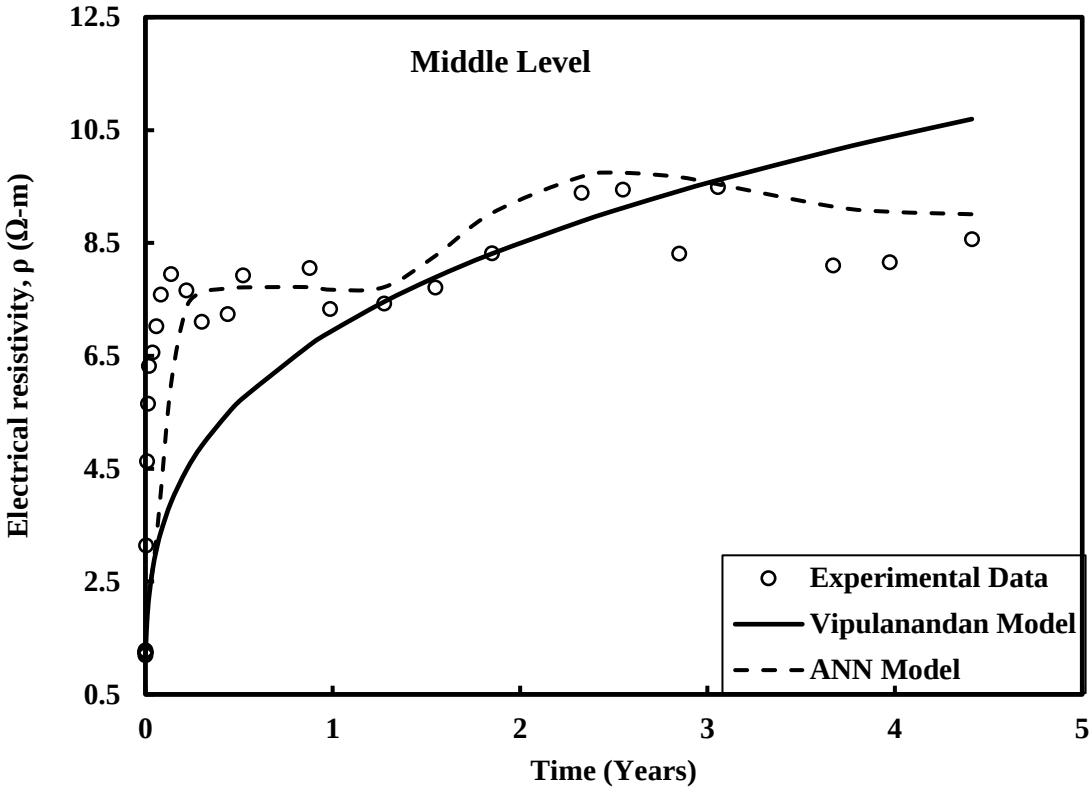


**Figure 5-54:Comparing the Prediction of Electrical Resistivity at the Middle Level Using the AI Model and Vipulanandan Curing Model up to 4.5 years.**

The value of RMSE (root mean square error) for electrical resistivity model was 1.44 Ω.m while it was 1.73 Ω.m for AI model. The value of $R^2$ for electrical resistivity model was 0.91 while it was 0.61 for AI model (Table 5-15). Thus, Vipulanandan curing model had comparatively better prediction for long term compared to AI model.

**Bottom Level**

The value of initial resistivity of smart cement was 1.32 Ω.m immediately after mixing. The electrical resistivity of smart cement was 4.91 Ω.m. after 4.5 years of curing (Figure 5-55). The time for minimum resistivity was 288 minutes after mixing (Table 5-14). Based on the preliminary analyses, AI model with for layers of ANN was selected predict the resistivity change with time. Over 30 data was used perform the BPNN and predict the experimental trend. Curing Model parameters $p_1$ and $q_1$ were 0.84 and 0.15 respectively after 4.5 years of curing (Table 5-14).

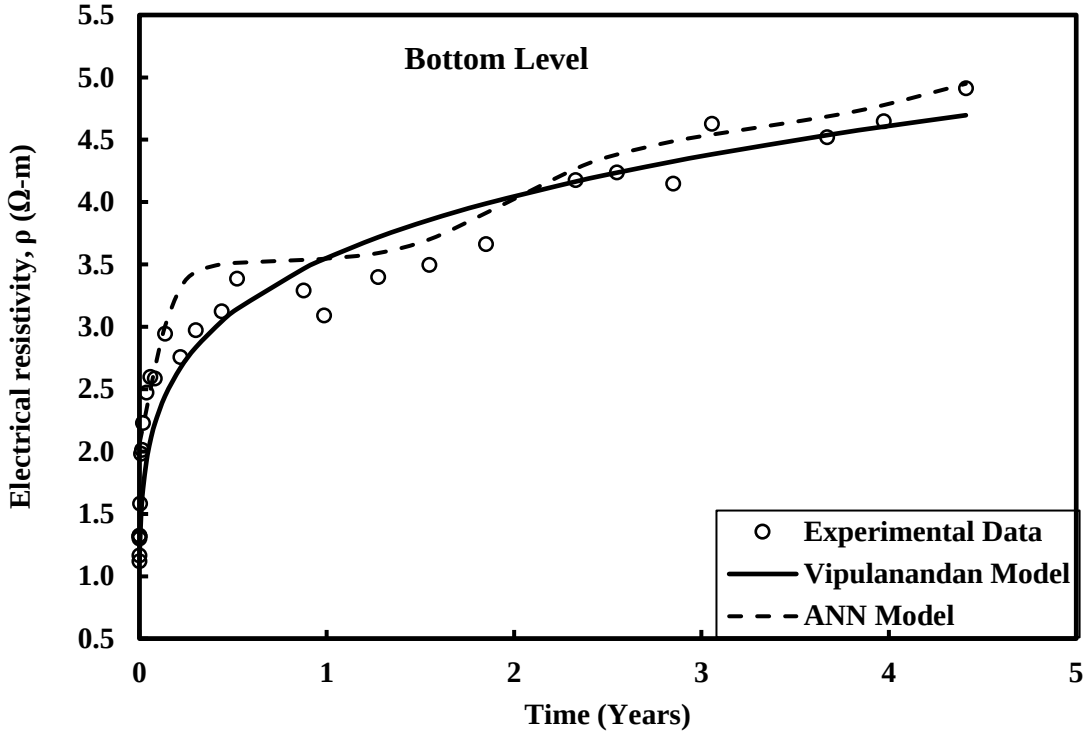


**Figure 5-55:Comparing the Prediction of the Electrical Resistivity at the Bottom Level Using the AI Model and Vipulanandan Curing Model up to 4.5 years.**

Also, the other curing model parameters are summarized in Table 5-14. The value of RMSE (root mean square error) for electrical resistivity model was 0.25 Ω.m while it was 0.43 Ω.m for AI model. The value of $R^2$ for electrical resistivity model was 0.95 while it was 0.86 for AI model (Table 5-15). Thus, Vipulanandan curing model had comparatively better prediction for long term compared to the AI model.

**Table 5-14:Electrical resistivity model parameters for smart cement in field for 4.5 years.**

| | Curing Model | | | | |
|---|---|---|---|---|---|
| Level | $\rho_o$ (Ω.m.) | $t_{min}$ (min) | $t_o$ (min) | $p_1$ | $q_1$ |
| Top | 1.03 | 195 | 250 | 0.76 | 0.24 |
| Middle | 1.24 | 195 | 300 | 0.78 | 0.22 |
| Bottom | 1.32 | 288 | 136 | 0.84 | 0.15 |

**Table 5-15:Correlation parameters for ANN Model and Resistivity model for smart cement in field after 4.5 years.**

| | ANN Model | | Curing Model | |
|---|---|---|---|---|
| Level | $R^2$ | RMSE (Ω.m.) | $R^2$ | RMSE (Ω.m.) |
| Top | 0.91 | 1.02 | 0.97 | 0.86 |
| Middle | 0.61 | 1.73 | 0.91 | 1.44 |
| Bottom | 0.86 | 0.43 | 0.95 | 0.25 |

### 5.4.9 Pressure Test

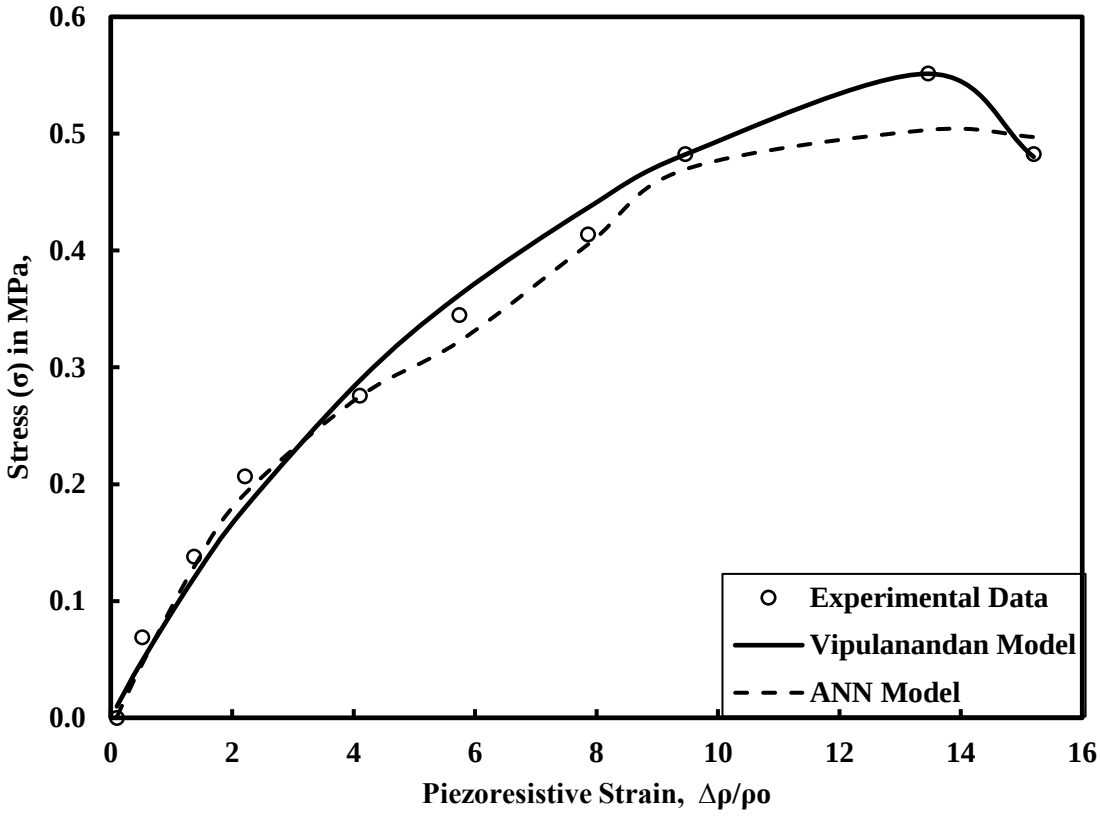


**Figure 5-56:Piezoresistive Strain for smart cement in the field after 4.5 years of curing.**

It is important to demonstrate the piezoresistivity of smart cement in the field. Also, it is important to show the sensitivity of smart cement for small pressure changes. Hence the test was performed at 10 psi (0.07 MPa) increments up to 80 psi (0.55 MPa). The maximum value of piezoresistive strain for smart cement after 4.5 years of curing was 13.5% at a stress of 0.55 MPa

(Figure 5-56). This is a clear demonstration of sensitivity of the smart cement. The piezoresistivity per unit stress was 0.17%/psi for field model after 1600 days of field curing. Also, by measuring the piezoresistive strain in the smart cement it will be possible predict the pressure in the casing using the models. The value of model parameters $p_2$ and $q_2$ for piezoresistivity model are 0.025 and 0.417. AI model had a RMSE of 0.015 Ω-m. value compared to piezoresistivity model RMSE of 0.02 Ω-m. with a coefficient of determination of 0.99 (Table 5-16). Hence both models predicted the piezoresistive behavior of the smart cement.

**Table 5-16:Correlation parameters for ANN Model and piezoresistivity model for smart cement in field after 4.5 years.**

| Pressure Test on Smart Cement | | | |
|---|---|---|---|
| ANN Model | | Piezoresistivity Model | |
| $R^2$ | RMSE (MPa) | $R^2$ | RMSE (MPa) |
| 0.99 | 0.015 | 0.99 | 0.02 |

## 5.5 Summary

Based on the resistivity monitoring of the field test following conclusions are advanced.

i) The two-probe method was effective in measuring the bulk resistance of the drilling fluid, and smart cement slurries. Based on the changes in resistance measurements it will be possible to identify the fluid rise in the well borehole.

ii) Field test demonstrate the real-time monitoring of the well bore with drilling fluid and smart cement slurries. During the installation of the field well

iii) The smart cement used to cement the field well was very sensitive to the applied pressure, piezoresistive cement. Using a nonlinear p-q model the change in electrical resistivity of smart cement was related to the applied pressure in the casing.

iv) The smart cement used to cement the field well was very sensitive to the applied pressure, piezoresistive cement. The piezoresistivity per unit stress was 0.178%/psi for lab model and 0.17%/psi for field model.

v) AI models with one, two, three and four layers of artificial neural networks were evaluated using the laboratory and field data with the statistical parameter coefficient of determination ($R^2$) and root mean square error (RMSE). Based on the type of available data both Generalized Regression Neural Networks (GRNN) and Back Propagation Neural Network (BPNN) were used to train the AI models.

vi) Based on the laboratory data and field data, electrical resistivity showed the largest variation compared to strain and temperature changes. Hence electrical resistivity was selected as the monitoring parameter for the smart cement.

vii) AI model predicted the long-term smart cement curing with the resistivity parameter very well and was comparable to the Vipulanandan Curing Model.AI model did not predict the short-term cuing well compared to the Vipulanandan Curing Model.

viii) AI model predicted the smart cement piezoresistive behavior in the laboratory and field very well. Vipulanandan p-q piezoresistive model predicted the behavior well.

ix) There is a need to further improve the AI perditions of resistivity change in the field. Vipulanandan curing model predicted the behavior very well.

# CHAPTER 6 SMART ORTHOPEDIC CAST MATERIAL CHARACTERIZATION

## 6.1 Introduction

Orthopedic cast material monitoring is of prime importance because of potential problems during ans after casting. In this study, orthopedic cast material was modified using conductive fillers to make it sensitive and investigate the effect of temperature, mechanical stresses and setting times.

## 6.2 Results

### 6.2.1 Density

The density of the orthopedic cast samples with and without conductive fillers was 1.71 g/cc at the time of mixing, 1.27 g/cc after 7 days of curing and 1.1 g/cc after 28 days of curing, indicating increase in the porosity over time due to loss of moisture during curing. The orthopedic cast samples showed a moisture loss of 30.4 % after 28 days of curing.

### 6.2.2 K Value Characterization

The electrical resistance (R) of the smart orthopedic cast samples were measured using LCR and the electrical resistivity (ρ) of the smart orthopedic cast was measured using both digital resistivity meter and conductivity meter for 35 mins to calculate the K value at room temperature. The electrical resistivity was measured for a shorter time 35 mis due to early setting of the orthopedic cast material. The relation between electrical resistance, electrical resistivity and K value is given by eqn. 3-1. The constants K and G are 61.9 $m^{-1}$ and 0 (Figure 6-1). This showed that the electrical resistance and resistivity had linear relationship for smart cement. The electrical resistance and electrical resistivity increased with time under moisture control curing conditions. The average value of K was 61.9 $m^{-1}$ for a curing period of 35 mins and hence it is assumed to constant (Figure 6-3). Investigation of the impedance versus frequency relationship showed that the smart orthopedic cast sample followed case 2 behavior as in Figure 3-13, indicating that the bulk material can be represented by resistance at high frequency impedance measurement.

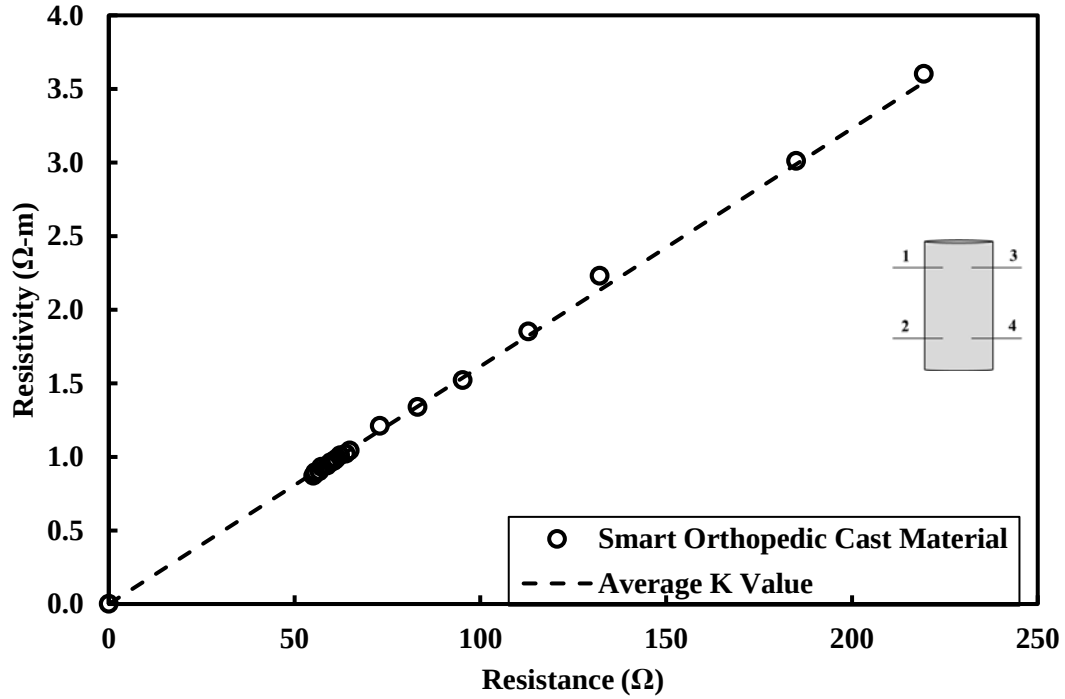


**Figure 6-1:Electrical Resistance vs Electrical Resistivity Plots for Smart Orthopedic Cast Material (1-2).**

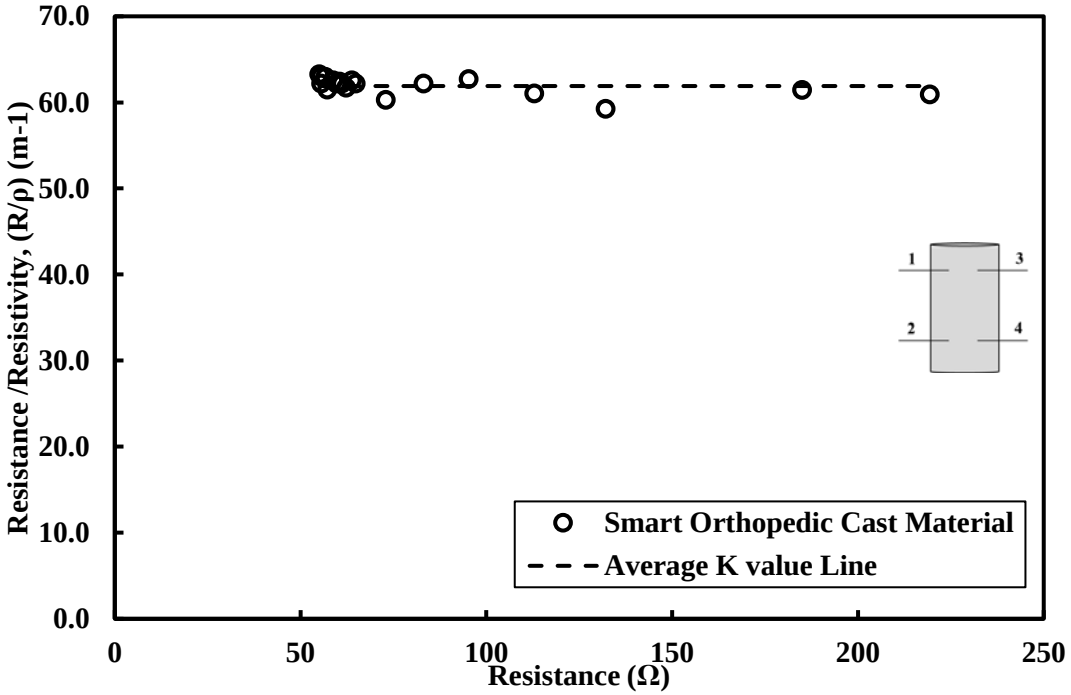


**Figure 6-2:Electrical Resistance/Electrical Resistivity (R/ρ) vs Electrical Resistivity plot for Smart Orthopedic Cast Material (1-2).**

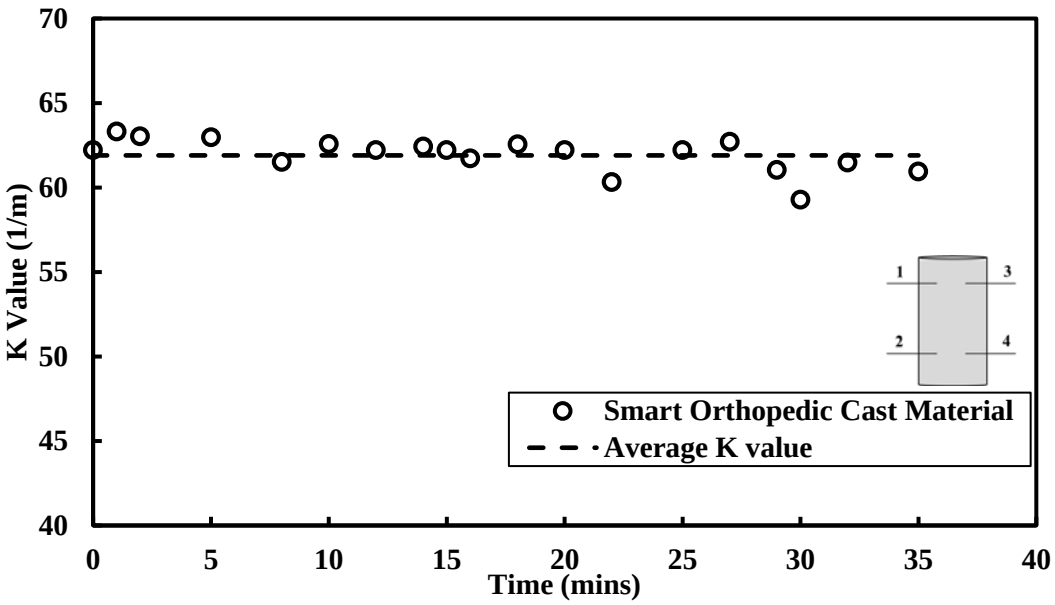


**Figure 6-3:K Value (1-2) for Smart Orthopedic Cast Material for curing time of 35 minutes.**

### 6.2.3 Impedance Vs Frequency Curves

The following are the impedance curve for smart orthopedic cast material immediately after mixing and for a curing time of 1, 7 and 28 days (Figure 6-4).

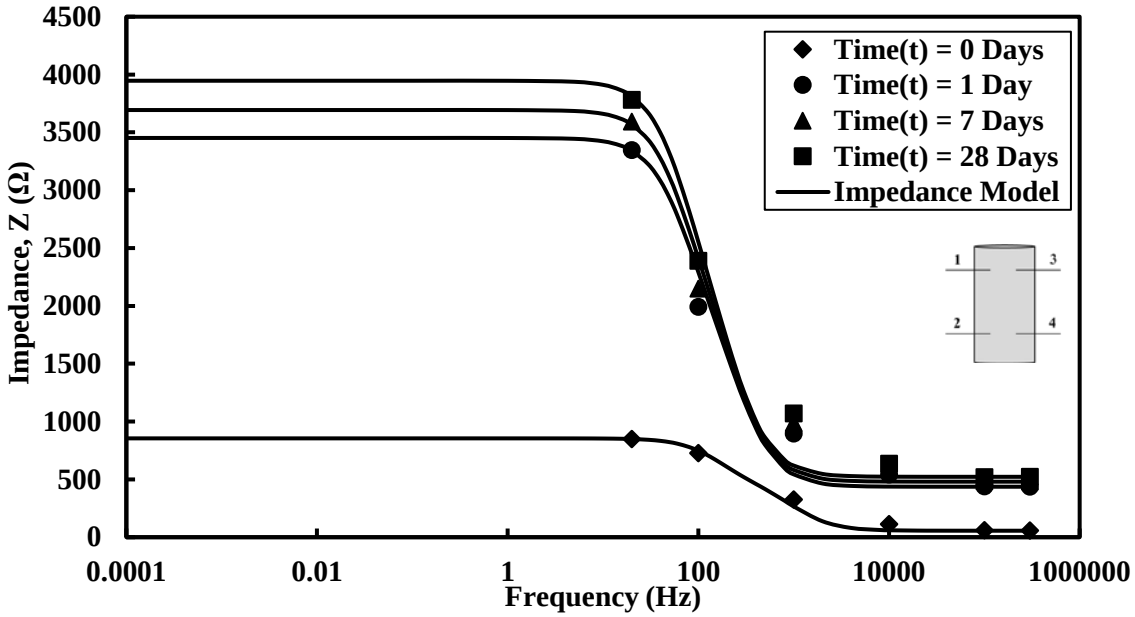


**Figure 6-4:Impedance (1-2) vs frequency for smart orthopedic cast material upto 28 days curing time.**

### 6.2.4 Bulk Resistance, Contact Resistance and Capacitance

The contact resistances and capacitances for smart orthopedic cast material for curing time of 28 days are obtained using impedance model given by eqn. 3-5.

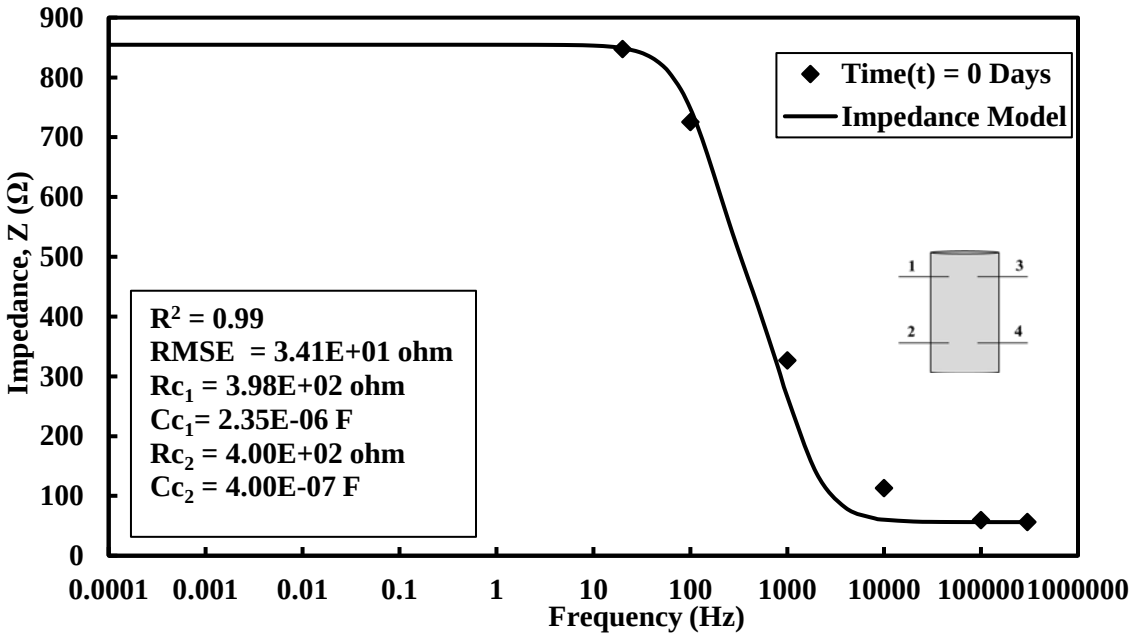


**Figure 6-5:Electrical Impedance (1-2) for smart orthopedic cast material at time (t) = 0 Days.**

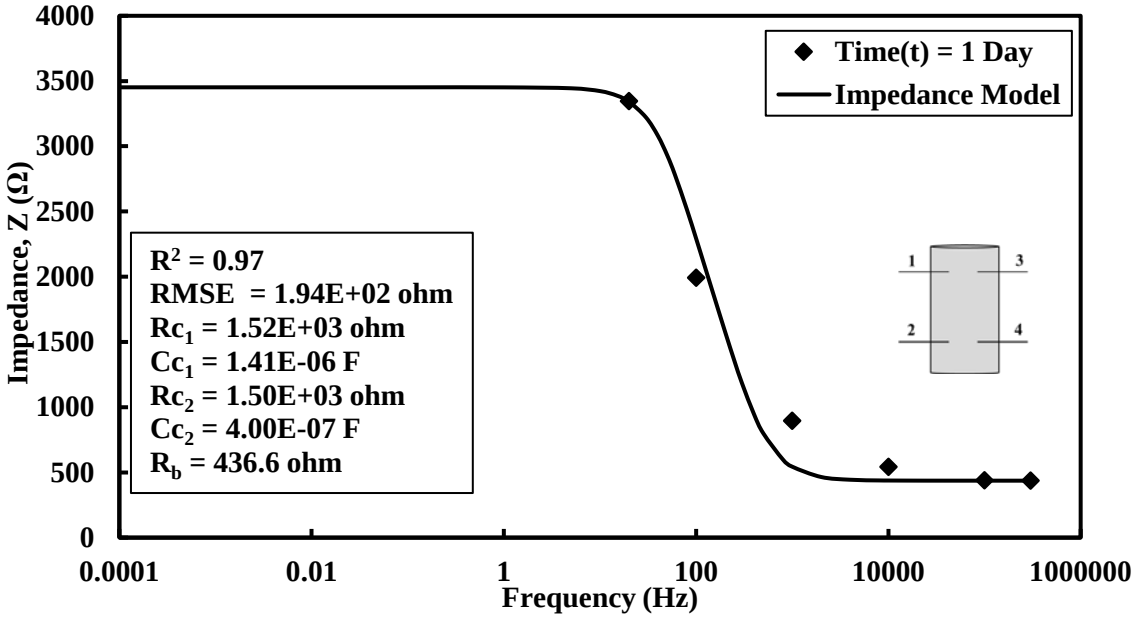


**Figure 6-6:Electrical Impedance (1-2) for smart orthopedic cast material at time (t) = 1 Day.**

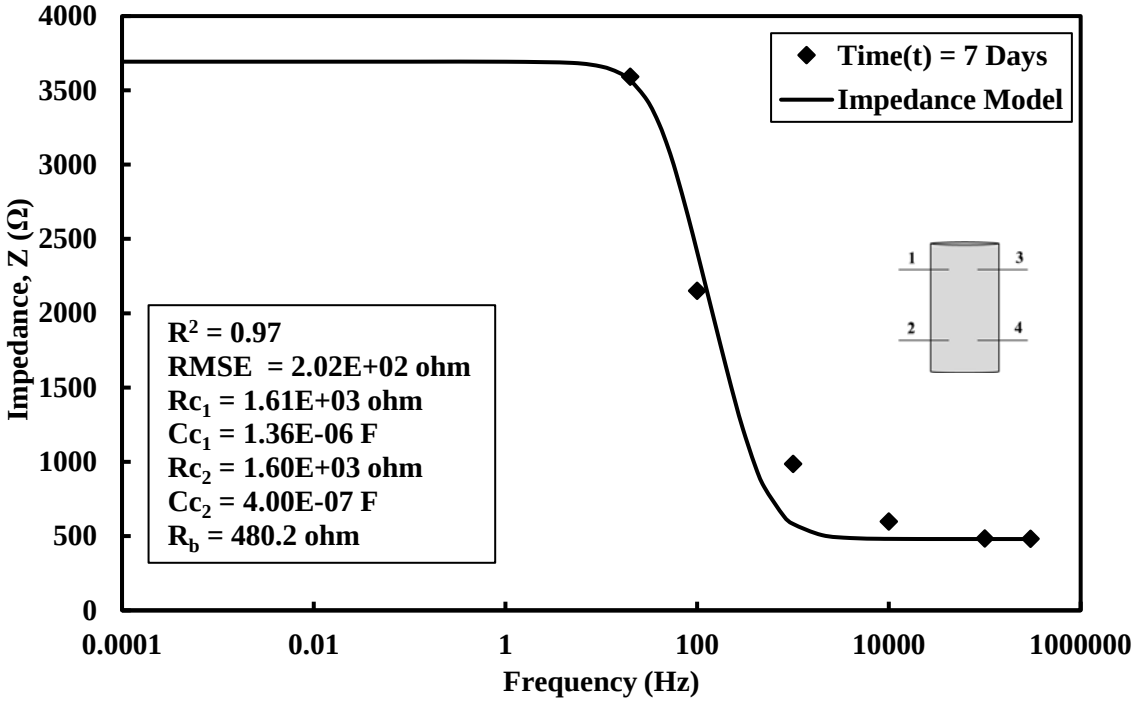


**Figure 6-7:Electrical Impedance (1-2) for smart orthopedic cast material at time (t) = 7 Days.**

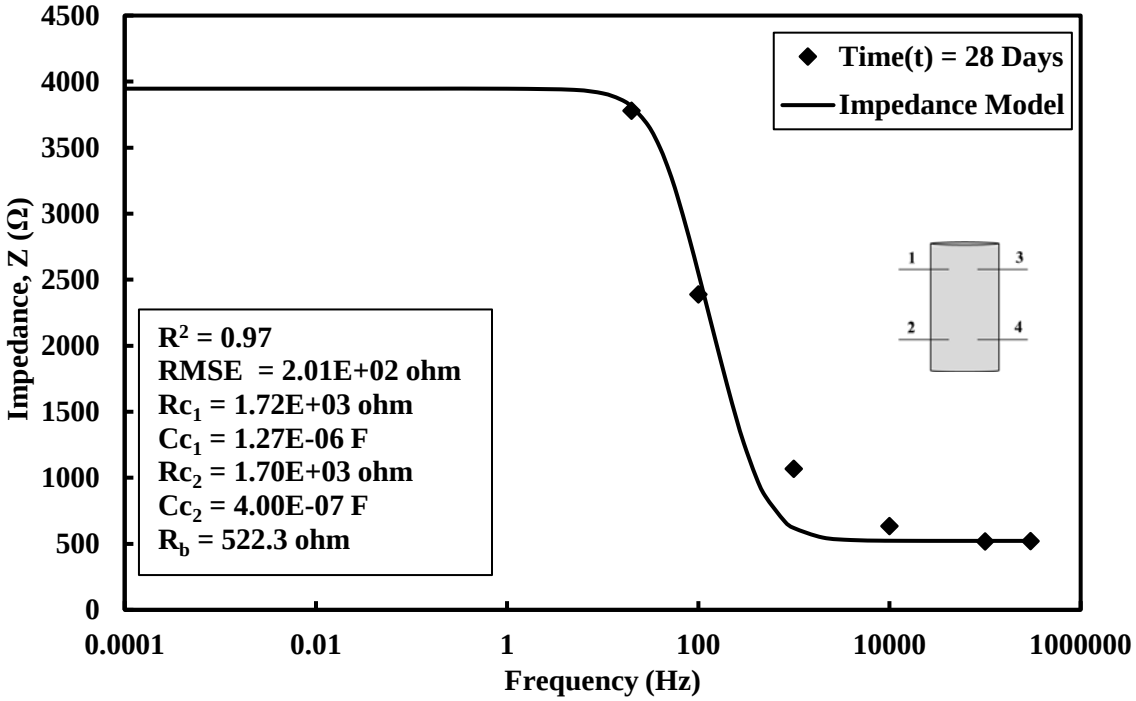


**Figure 6-8:Electrical Impedance (1-2) for smart orthopedic cast material at time (t) = 28 Days.**

The Bulk resistance of the smart orthopedic cast material increased from 56.2 Ω to 522.3 Ω (Figure 6-5 & Figure 6-8), 829% increase in 28 days when cured at room temperature of 25 °C. The contact resistance ($Rc_1$) increased from 398 Ω to 1720 Ω, 332% increase in 28 days of room temperature curing. The contact capacitance ($Cc_1$) varied from 2.35E-06 F to 1.27E-06 F, a 46% decrease over 28 days curing period. The product ($Rc_1$*$Cc_1$) of contact resistance and contact capacitance varied from 9.35E-04 Ω-F to 2.18E-03 Ω-F, a 133% increase during 28 days of curing (Figure 6-9).

Similarly, the contact resistance ($Rc_2$) increased from 400 Ω to 1700 Ω, 325% increase in 28 days of room temperature curing. The contact capacitance ($Cc_2$) varied from remained constant at 4.00E-07 F, over 28 days curing period. The product ($Rc_2$*$Cc_2$) of contact resistance and contact capacitance varied from 1.60E-04 Ω-F to 6.80E-4 Ω-F, a 325% increase during 28 days of curing (Figure 6-9).

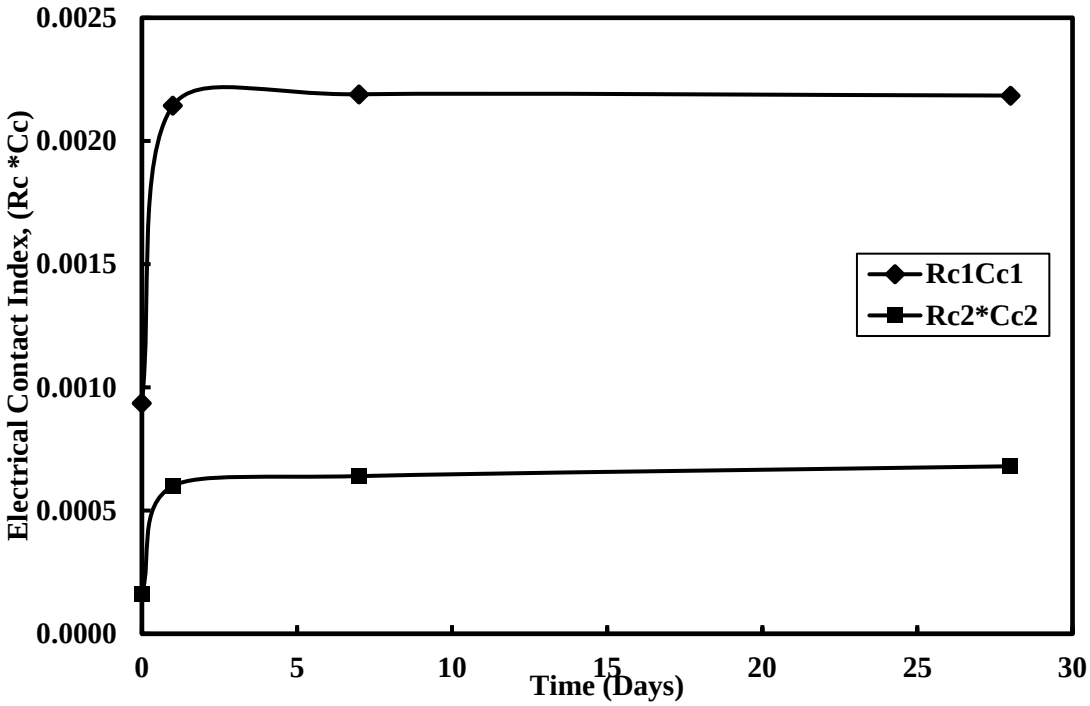


**Figure 6-9:Contact Resistance and Capacitance product variation over 28 days of time.**

### 6.2.5 Electrical Resistivity

**Curing of Orthopedic Cast Material (Plaster of Paris - POP)**

Initial resistivity was measured immediately after mixing the smart orthopedic cast material. During the curing process under room condition (relative humidity of 50% and temperature of 72$^{o}$F (22$^{o}$C)), the resistivity rapidly changed with the time as shown in Figure 6-10. Hence, there are several parameters that can be used in monitoring the curing (hardening process) of the orthopedic cast material. The parameters are initial resistivity ($\rho_o$), minimum resistivity ($\rho_{min}$), time to reach the minimum resistivity ($t_{min}$) and resistivity after 24 hours of curing ($\rho_{24}$). After initial mixing, the electrical resistivity reduced to a minimum value ($\rho_{min}$), and then it gradually increased with time. Time to reach minimum resistivity, $t_{min}$, can be used as an index of speed of chemical reactions and orthopedic cast material set times. With the formation of resistive solid hydration products which block the conduction path, resistivity increased sharply with curing time. The following increase in electrical resistivity was caused by the formation of large amounts of gypsum products in the orthopedic cast material matrix. Finally, a relatively stable increase in trend was reached by the ions diffusion control of hydration process, and resistivity increased steadily with the curing time. The electrical resistivity was modeled using Vipulanandan curing model (Eqn. 3-18).

The electrical resistivity of the orthopedic cast material slurry was found to vary between 3.3 to 0.89 Ω-m based on the quantity of conductive filler added (Figure 6-10). Initial Resistivity of orthopedic cast material without CF was 3.3 Ω-m right after the mixing. Initial Resistivity of orthopedic cast material with 0.02% and 0.05% percentages of conductive filler were 1.47 Ω-m and 0.89 Ω-m right after the mixing. Change resistivity for 24 hours of curing was in the range of 577 to 688 % for orthopedic cast material with and without CF (Table 6-1).

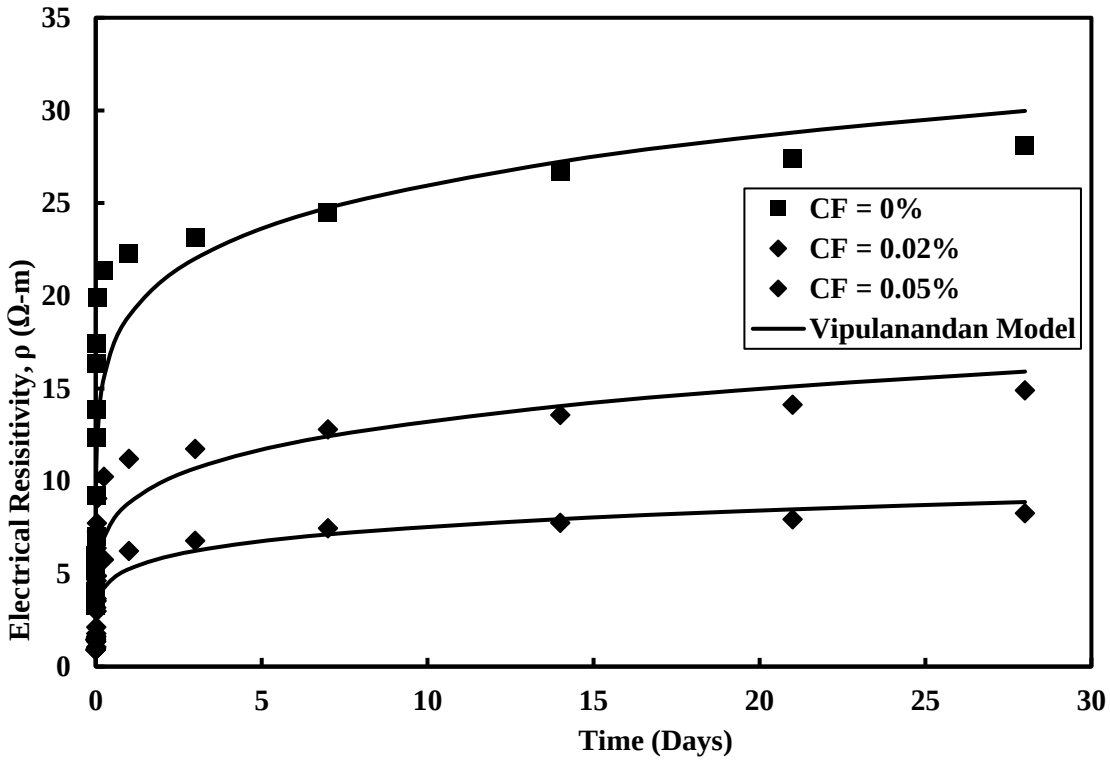


**Figure 6-10:Electrical Resistivity of smart orthopedic cast material during 28 days of curing.**

**Table 6-1:Electrical Resistivity model parameters for smart orthopedic cast material for 28 days of curing.**

| Orthopedic Cast Material | Initial Resistivity, $\rho_o$ (Ω-m) | $\rho_{min}$ (Ω-m) | $t_{min}$ (min) | $t_o$ (min) | $\rho_{24\,h}$ (Ω-m) | $RI_{24}$ (%) | $p_1$ | $q_1$ |
|---|---|---|---|---|---|---|---|---|
| CF = 0% | 3.29 | 3.29 | 0 | 0.001 | 22.3 | 577 | 0.878 | 0.121 |
| CF = 0.02% | 1.47 | 1.42 | 2 | 0.001 | 11.2 | 688 | 0.456 | 0.085 |
| CF = 0.05% | 0.89 | 0.89 | 0 | 0.001 | 6.23 | 600 | 0.624 | 0.101 |

The resistivity after 28 days of curing was 28.12 Ω.m for the orthopedic cast material without conductive filler, more than 754% increase compared to the initial resistivity. For orthopedic cast material with 0.02 % conductive filler, the resistivity after 28 days of curing was 14.89 Ω.m, a 913% increase. For orthopedic cast material with 0.05 % conductive filler, the resistivity after 28 days of curing was 8.27 Ω.m, an 829% increase. Vipulanandan Model parameters $p_1$ and $q_1$ decreased with the addition of conductive fillers for the orthopedic cast material. The model parameter $p_1$ varied from 0.456 to 0.878, while parameter $q_1$ varied from 0.085

to 0.121 (Table 6-1). This model predicted the curing trend very well (Figure 6-10). The coefficient of determination ($R^2$) varied was 0.99 and the RMSE (root mean square error) varied in the range of was 1.17 to 1.9 Ω.m.

### 6.2.6 Piezoresistivity

#### Uniaxial Compression Test

It is important to quantify the piezoresistive behavior of the smart orthopedic cast material. The specimens were cured under room condition and the stress- piezoresistive strain response was non-linear.

#### 1 Day of Curing

The piezoresistive strain for orthopedic cast material was 0.76% at a peak compressive stress of 2.14 MPa after 1 day of curing. This demonstrated that the orthopedic cast material was not sensitive to application of stress.

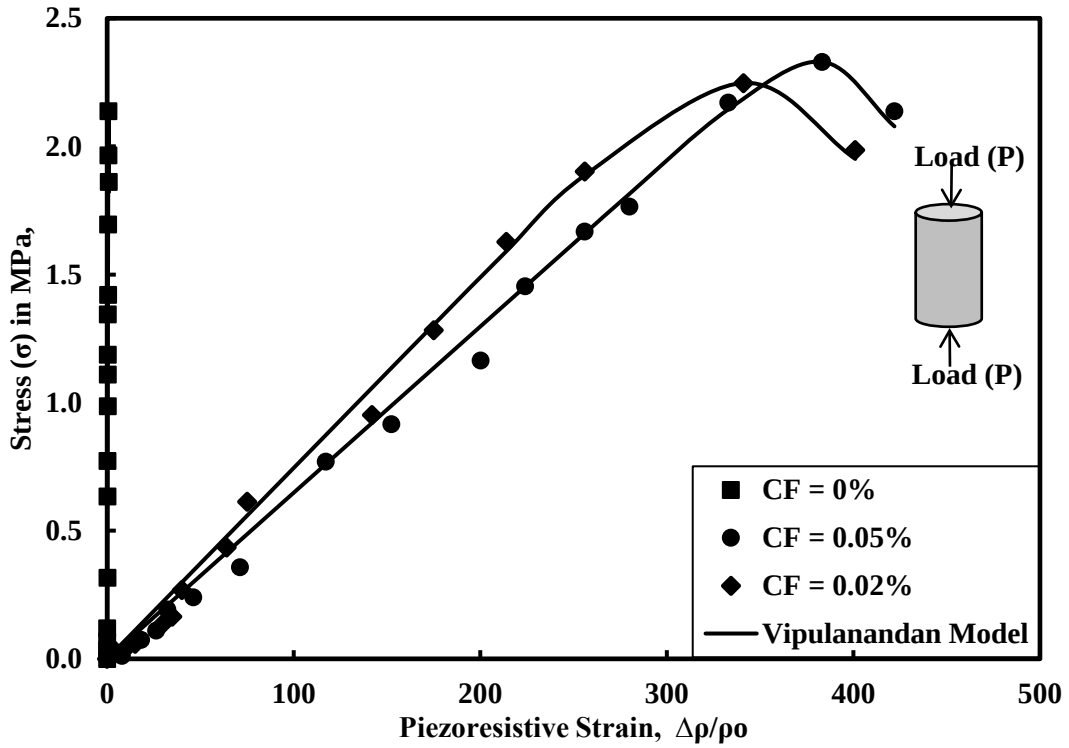


**Figure 6-11:Piezoresistive behavior of smart orthopedic cast material for 1 day of curing.**

With addition of 0.02% conductive filler, the piezoresistive strain for orthopedic cast material was 341% at a peak compressive stress of 2.25 MPa after 1 day of curing (Figure 6-11). Hence, the piezoresistivity per unit stress was 151%/MPa in the lab samples after 1 day of curing. Addition of 0.05% conductive filler further increased the piezoresistive strain of orthopedic cast material to 383.2% at a peak compressive stress of 2.33 MPa, showing piezoresistivity per unit stress was 164%/MPa after 1 day of curing (Figure 6-11). The piezoresistivity of smart orthopedic cast material was modeled using Vipulanandan piezoresistivity model (Eqn. 3-19). The model parameter $p_2$ decreased from 0.12 to 0.06 while the model parameter $q_2$ increased from 0.855 to 0.93 after 1 day of curing with varying conductive filler contents (Table 6-2). Vipulanandan piezoresistivity predicted the piezoresistivity trend very well (Figure 6-11). The coefficient of determination ($R^2$) was 0.99 and the RMSE (root mean square error) varied in the range of 0.05 to 0.056 MPa (Table 6-2).

**Table 6-2:Correlation and model parameters for Piezoresistivity model for smart orthopedic cast material for 1 day of curing.**

| 1 Day Piezoresistivity Model | | | | | | |
|---|---|---|---|---|---|---|
| Orthopedic Cast Material | $p_2$ | $q_2$ | $\sigma c_{max}$ (MPa) | $\Delta\rho/\rho_o$ (%) | $R^2$ | RMSE (MPa) |
| CF = 0% | 0.12 | 0.855 | 2.14 | 0.76 | 0.99 | 0.055 |
| CF = 0.02% | 0.115 | 0.885 | 2.25 | 341 | 0.99 | 0.05 |
| CF = 0.05% | 0.06 | 0.93 | 2.33 | 383.2 | 0.99 | 0.056 |

**7 Days of Curing**

The piezoresistive strain for orthopedic cast material was 0.72 % at a peak compressive stress of 4.32 MPa after 7 days of curing. This demonstrated that the orthopedic cast material was not sensitive to application of stress. With addition of 0.02% conductive filler, the piezoresistive strain for orthopedic cast material was 328% at a peak compressive stress of 4.49 MPa after 7 days of curing. Hence, the piezoresistivity per unit stress was 73%/MPa in the lab samples after 7 days of curing. Addition of 0.05% conductive filler further increased the piezoresistive strain of orthopedic cast material to 370% at a peak compressive stress of 4.61 MPa, showing

piezoresistivity per unit stress was 80.3%/MPa after 7 days of curing (Figure 6-12). The piezoresistivity of smart orthopedic cast material was modeled using Vipulanandan piezoresistivity model for 7 days curing (Eqn. 3-19).

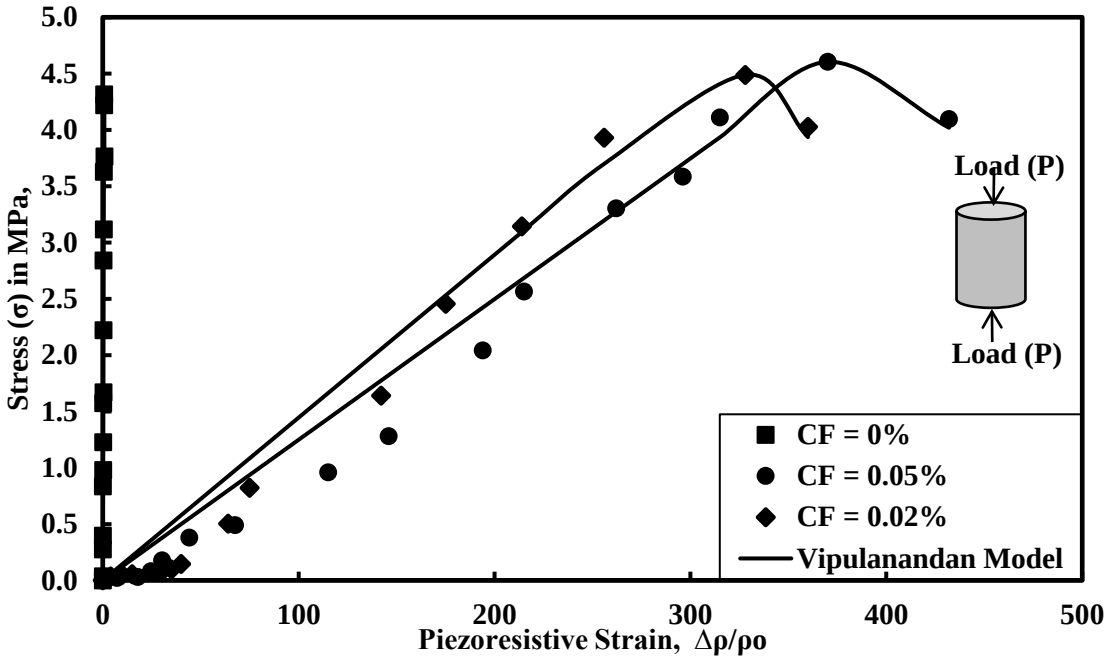


**Figure 6-12:Piezoresistive behavior of smart orthopedic cast material for 7 days of curing.**

The model parameter $p_2$ decreased from 0.065 to 0.033 while the model parameter $q_2$ increased from 0.935 to 0.966 after 7 days of curing with varying conductive filler contents (Table 6-3). Vipulanandan piezoresistivity predicted the piezoresistivity trend very well (Figure 6-12). The coefficient of determination ($R^2$) varied from 0.97 to 0.99 and the RMSE (root mean square error) varied in the range of 0.157 to 0.252 MPa (Table 6-3).

**Table 6-3:Correlation and model parameters for Piezoresistivity model for smart orthopedic cast material for 7 days of curing.**

| 7 Day Piezoresistivity Model | | | | | | |
|---|---|---|---|---|---|---|
| Orthopedic Cast Material | $p_2$ | $q_2$ | $\sigma c_{max}$ (MPa) | $\Delta\rho/\rho_o$ (%) | $R^2$ | RMSE (MPa) |
| CF = 0% | 0.065 | 0.935 | 4.32 | 0.72 | 0.99 | 0.157 |
| CF = 0.02% | 0.054 | 0.945 | 4.49 | 328 | 0.97 | 0.25 |
| CF = 0.05% | 0.033 | 0.966 | 4.61 | 370 | 0.97 | 0.252 |

**28 Days of Curing**

The piezoresistive strain for orthopedic cast material was 0.68 % at a peak compressive stress of 6.04 MPa after 28 days of curing. This demonstrated that the orthopedic cast material was not sensitive to application of stress. With addition of 0.02% conductive filler, the piezoresistive strain for orthopedic cast material was 311% at a peak compressive stress of 6.15 MPa after 28 days of curing. Hence, the piezoresistivity per unit stress was 50.5 %/MPa in the lab samples after 28 days of curing. Addition of 0.05% conductive filler further increased the piezoresistive strain of orthopedic cast material to 345% at a peak compressive stress of 6.28 MPa, showing piezoresistivity per unit stress was 54.9 %/MPa after 28 days of curing (Figure 6-13). The piezoresistivity of smart orthopedic cast material was modeled using Vipulanandan piezoresistivity model for 28 days curing (Eqn. 3-19).

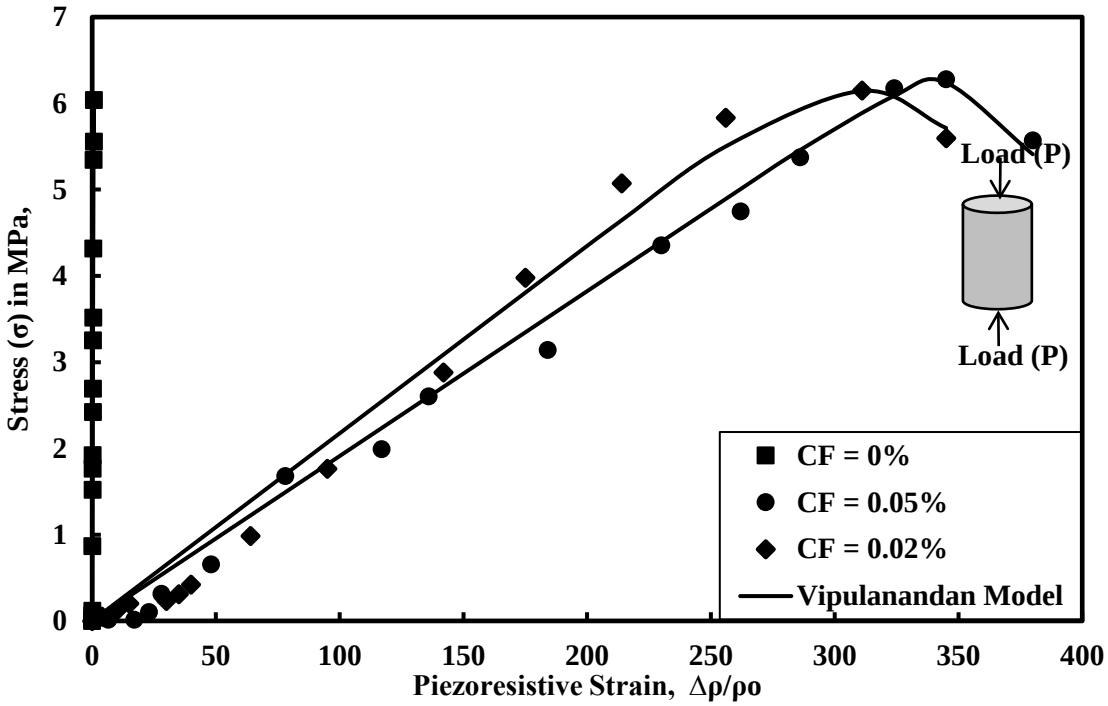


**Figure 6-13:Piezoresistive behavior of smart orthopedic cast material for 28 days of curing.**

The model parameter $p_2$ varied from 0.053 to 0.091 while the model parameter $q_2$ varied from 0.908 to 0.946 after 28 days of curing with varying conductive filler contents (Table 6-4).

Vipulanandan piezoresistivity predicted the piezoresistivity trend very well (Figure 6-13). The coefficient of determination ($R^2$) varied from 0.98 to 0.99 and the RMSE (root mean square error) varied in the range of 0.179 to 0.206 MPa (Table 6-4).

**Table 6-4: Correlation and model parameters for Piezoresistivity model for smart orthopedic cast material for 28 days of curing.**

| 28 Day Piezoresistivity Model | | | | | | |
|---|---|---|---|---|---|---|
| Orthopedic Cast Material | $p_2$ | $q_2$ | $\sigma c_{max}$ (MPa) | $\Delta\rho/\rho_o$ (%) | $R^2$ | RMSE (MPa) |
| CF = 0% | 0.06 | 0.94 | 6.04 | 0.68 | 0.99 | 0.179 |
| CF = 0.02% | 0.091 | 0.908 | 6.15 | 311 | 0.98 | 0.278 |
| CF = 0.05% | 0.053 | 0.946 | 6.28 | 345 | 0.99 | 0.206 |

Overall, addition of 0.05% conductive filler showed maximum piezoresistive strain of 164 %/MPa after 1 day of curing, 80.3 %/MPa after 7 days of curing and 54.9 %/MPa after 28 days of curing. For further characterization of smart orthopedic cast material, conductive filler content of 0.05% was used due to its high piezoresistive strain.

**Bending Test for Plates**

Circular plates of 3.65 inch diameter with thickness of 0.47 inch and 0.32 inch were prepared for bending test after 7 and 28 days of curing. The plates were prepared by addition of 0.05% conductive filler to orthopedic cast material.

**7 Days of Curing**

With addition of 0.05% conductive filler, the piezoresistive strain for orthopedic cast material was 17.56% at a peak bending stress of 1.04 MPa after 7 days of curing for thick plate samples. Hence, the piezoresistivity per unit stress in bending was 16.88 %/MPa in the thick plate samples after 7 days of curing. Addition of 0.05% conductive filler to thin plates showed a piezoresistive strain of 12.46% at a peak bending stress of 0.8 MPa, showing piezoresistivity per unit stress was 15.6 %/MPa after 7 days of curing (Figure 6-14). The piezoresistivity of smart orthopedic cast material was modeled using Vipulanandan piezoresistivity model for 7 days curing (Eqn. 3-19).

The model parameter $p_2$ varied from 0.02 to 0.108 while the model parameter $q_2$ varied from 0.35 to 0.98 after 7 days of curing with conductive filler content of 0.05% in thick and thin plates (Table 6-5). Vipulanandan piezoresistivity model predicted the piezoresistivity trend very well (Figure 6-14). The coefficient of determination ($R^2$) varied from 0.98 to 0.99 and the RMSE (root mean square error) varied in the range of 0.031 to 0.041 MPa (Table 6-5).

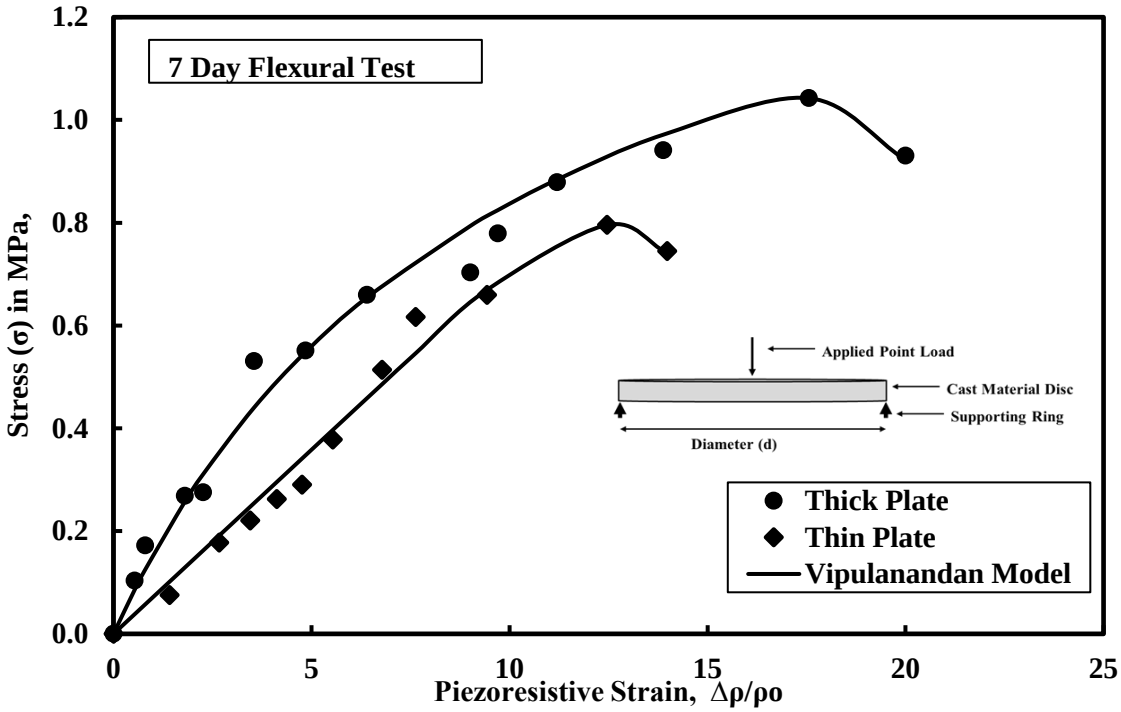


**Figure 6-14:Piezoresistive behavior of smart orthopedic cast material under bending stress for 7 days of curing.**

**Table 6-5:Correlation and model parameters for Piezoresistivity model for smart orthopedic cast material under bending stress for 7 days of curing.**

| 7 Day Piezoresistivity Model | | | | | | |
|---|---|---|---|---|---|---|
| Orthopedic Cast Material | $p_2$ | $q_2$ | $\sigma_{max}$ (MPa) | $\Delta\rho/\rho_o$ (%) | $R^2$ | RMSE (MPa) |
| Thick Plate | 0.02 | 0.35 | 1.04 | 17.56 | 0.99 | 0.041 |
| Thin Plate | 0.108 | 0.89 | 0.8 | 12.46 | 0.98 | 0.031 |

**28 Days of Curing**

With addition of 0.02% conductive filler, the piezoresistive strain for orthopedic cast material was 16.52% at a peak bending stress of 1.33 MPa after 28 days of curing for thick plate

samples. Hence, the piezoresistivity per unit stress in bending was 12.42 %/MPa in the thick plate samples after 28 days of curing. Addition of 0.05% conductive filler to thin plates showed a piezoresistive strain of 11.52% at a peak bending stress of 0.85 MPa, showing piezoresistivity per unit stress was 13.55 %/MPa after 28 days of curing (Figure 6-15). The piezoresistivity of smart orthopedic cast material was modeled using Vipulanandan piezoresistivity model for 28 days curing (Eqn. 3-19). The model parameter $p_2$ varied from 0.061 to 0.16 while the model parameter $q_2$ varied from 0.34 to 0.83 after 28 days of curing with conductive filler content of 0.05% in thick and thin plates (Table 6-6). Vipulanandan piezoresistivity predicted the piezoresistivity trend very well (Figure 6-15). The coefficient of determination ($R^2$) varied from 0.97 to 0.99 and the RMSE (root mean square error) varied in the range of 0.038 to 0.051 MPa (Table 6-6).

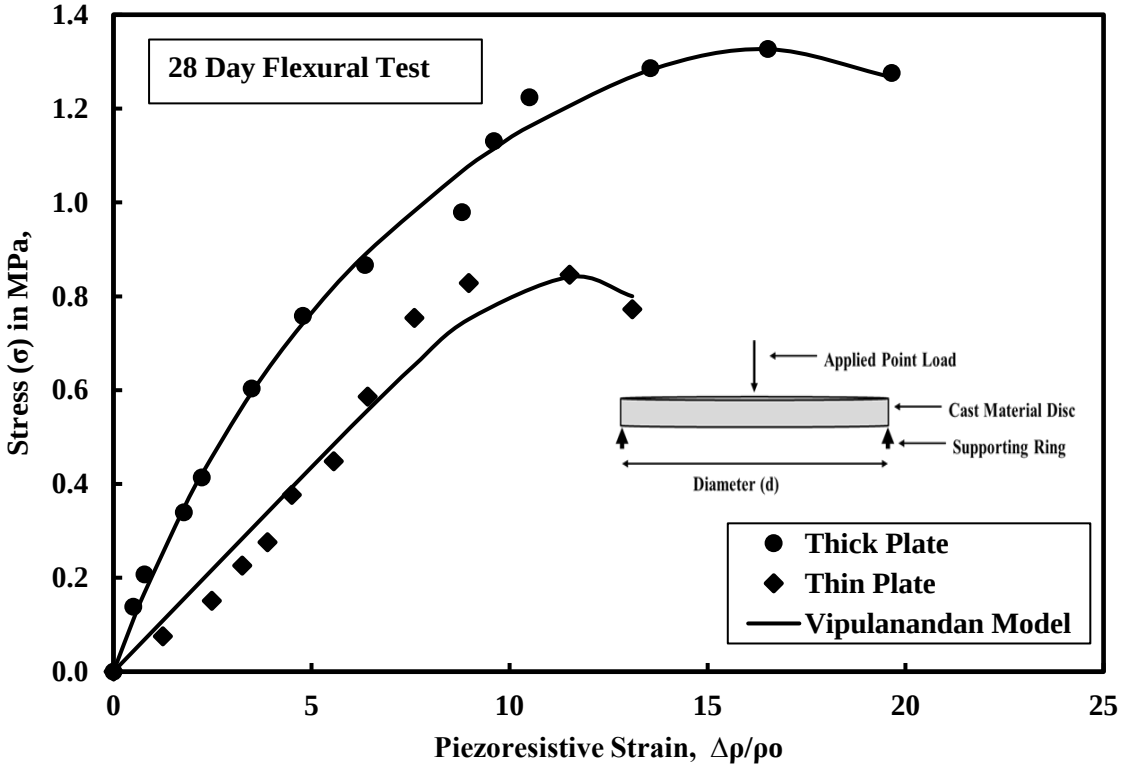


**Figure 6-15:Piezoresistive behavior of smart orthopedic cast material under bending stress for 28 days of curing.**

**Table 6-6: Correlation and model parameters for Piezoresistivity model for smart orthopedic cast material under bending stress for 28 days of curing.**

| 28 Day Piezoresistivity Model | | | | | | |
|---|---|---|---|---|---|---|
| Orthopedic Cast Material | $p_2$ | $q_2$ | $\sigma_{max}$ (MPa) | $\Delta\rho/\rho_o$ (%) | $R^2$ | RMSE (MPa) |
| Thick Plate | 0.061 | 0.345 | 1.33 | 16.52 | 0.99 | 0.038 |
| Thin Plate | 0.16 | 0.834 | 0.85 | 11.52 | 0.97 | 0.051 |

**Compression Test for Hollow Cylinders**

Hollow cylindrical molds were prepared to replicate the application around a broken hand. The Cylindrical hollow molds have internal diameter of 0.79 inch, outer diameter of 2 inches and a height of 4 inches. The compression and tensile tests were performed using universal compression testing machine. The compression tests were performed according to ASTM C39 while for tensile test, the procedure of Brazilian tensile testing (splitting tensioning test) was used according to ASTM C496.

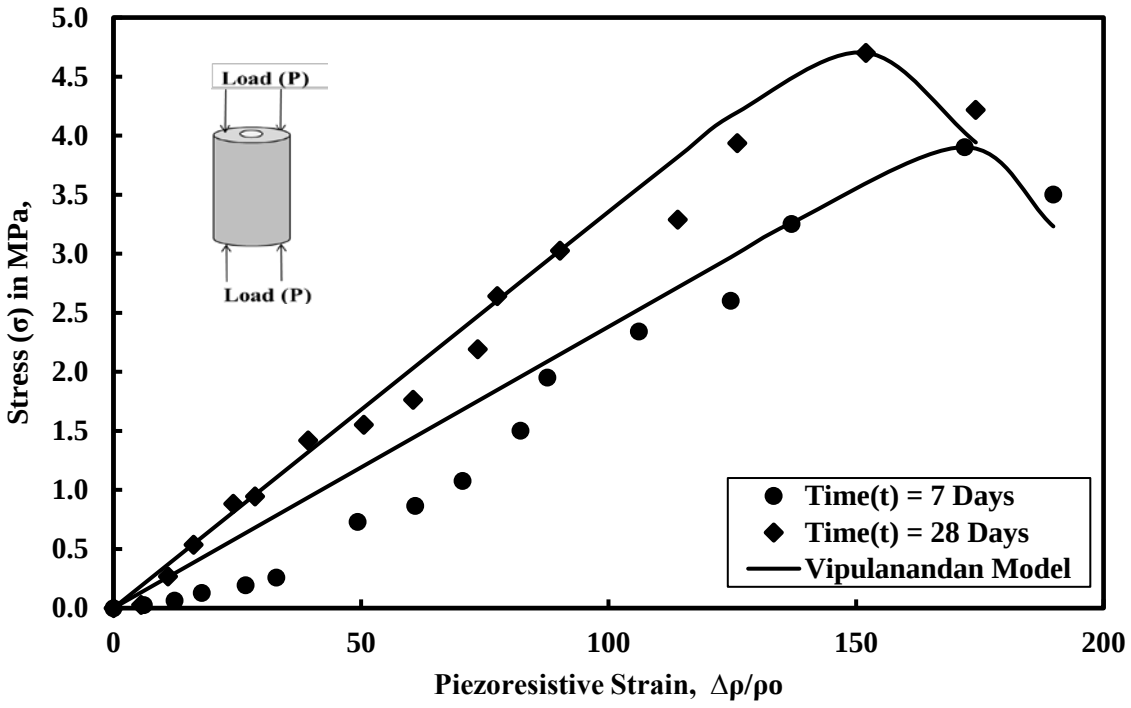


**Figure 6-16: Piezoresistive behavior of smart orthopedic cast material for 7 days of curing in hollow samples.**

The piezoresistive strain for smart orthopedic cast material hollow specimen with 0.05% conductive filler was 172 % at a peak compressive stress of 3.9 MPa after 7 days of curing. Hence, the piezoresistivity per unit stress was 44.1%/MPa in the lab samples after 7 days of curing. After 28 days of curing, piezoresistive strain for smart orthopedic cast material hollow specimen with 0.05% conductive filler was 152 % at a peak compressive stress of 4.7 MPa, showed piezoresistivity per unit stress was 32.3%/MPa after 28 days of curing (Figure 6-13). The piezoresistivity of smart orthopedic cast material was modeled using the Vipulanandan piezoresistivity model for 28 days curing (Eqn. 3-19).

The model parameter $p_2$ increased from 0.047 to 0.0785 while the model parameter $q_2$ decreased from 0.952 to 0.921 over 28 days of curing with conductive filler content of 0.05% (Table 6-7). Vipulanandan piezoresistivity predicted the piezoresistivity trend very well (Figure 6-13). The coefficient of determination ($R^2$) varied from 0.92 to 0.98 and the RMSE (root mean square error) varied in the range of 0.201 to 0.353 MPa (Table 6-7).

**Table 6-7:Correlation and model parameters for Piezoresistivity model for smart orthopedic cast material for 7 and 28 days of curing.**

| Hollow Cylindrical Smart Cast Samples | | | | | | |
|---|---|---|---|---|---|---|
| Compression Test | $p_2$ | $q_2$ | $\sigma_{max}$(MPa) | $\Delta\rho/\rho_o$(%) | $R^2$ | RMSE(MPa) |
| 7 Days | 0.047 | 0.952 | 3.9 | 172 | 0.92 | 0.353 |
| 28 Days | 0.0785 | 0.921 | 4.7 | 152 | 0.98 | 0.201 |

**Splitting Test for Hollow Cylinders**

Hollow cylindrical molds were prepared to replicate the application around a broken hand. The Cylindrical hollow molds have internal diameter of 0.79 inch, outer diameter of 2 inches and a height of 4 inches. The compression and tensile tests were performed using universal compression testing machine. The compression tests were performed according to ASTM C39 while for tensile test, the procedure of Brazilian tensile testing (splitting tensioning test) was used according to ASTM C496.

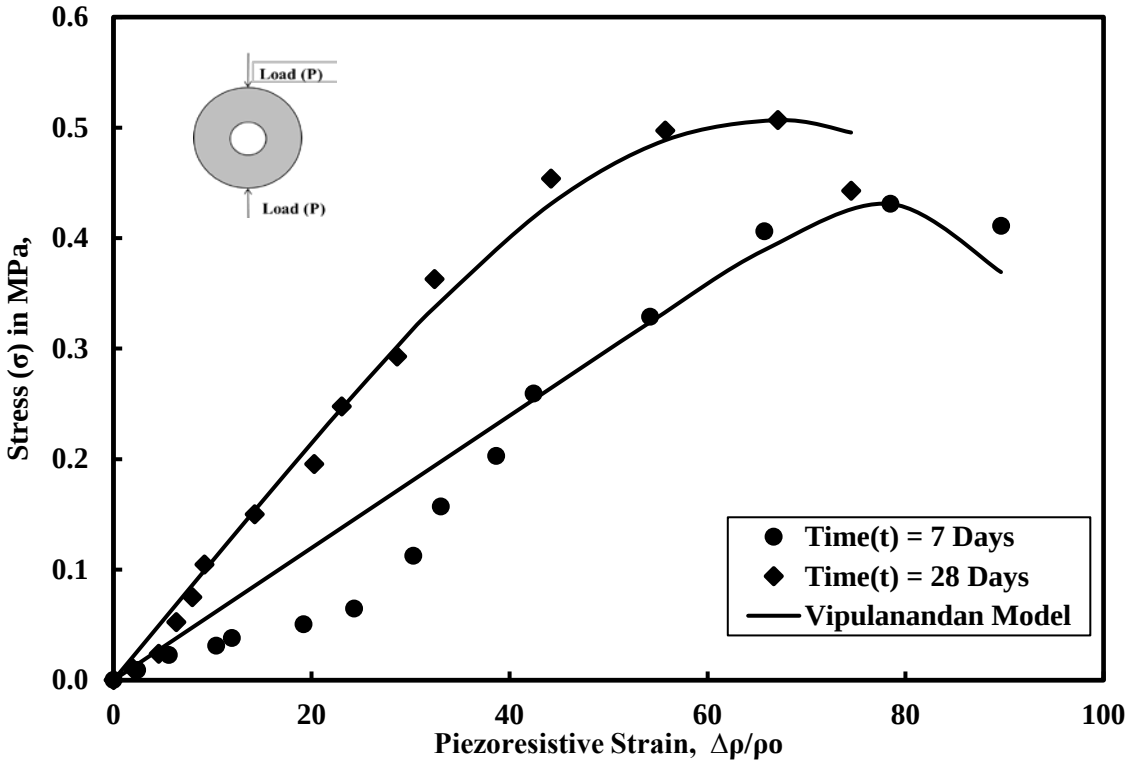


**Figure 6-17:Piezoresistive behavior of smart orthopedic cast material hollow samples under splitting tension after 7 days of curing.**

The piezoresistive strain for smart orthopedic cast material hollow specimen with 0.05% conductive filler under splitting tension was 78.5 % at a peak compressive stress of 0.43 MPa after 7 days of curing. Hence, the piezoresistivity per unit stress was 182.5%/MPa in the lab samples after 7 days of curing. After 28 days of curing, piezoresistive strain for smart orthopedic cast material hollow specimen with 0.05% conductive filler under splitting tension was 73.5 % at a peak compressive stress of 0.51 MPa, showing piezoresistivity per unit stress was 144.1%/MPa after 28 days of curing (Figure 6-17). The piezoresistivity of smart orthopedic cast material was modeled using Vipulanandan piezoresistivity model for 28 days curing (Eqn. 3-19).

The model parameter $p_2$ increased from 0.082 to 0.3 while the model parameter $q_2$ decreased from 0.917 to 0.699 over 28 days of curing with conductive filler content of 0.05% (Table 6-8). Vipulanandan piezoresistivity predicted the piezoresistivity trend very well (Figure 6-17). The

coefficient of determination ($R^2$) varied from 0.92 to 0.99 and the RMSE (root mean square error) varied in the range of 0.014 to 0.038 MPa (Table 6-8).

**Table 6-8:Correlation and model parameters for Piezoresistivity model for smart orthopedic cast material hollow samples under splitting tension after 7 and 28 days of curing.**

| Hollow Cylindrical Smart Cast Samples | | | | | | |
|---|---|---|---|---|---|---|
| Splitting Tension | $p_2$ | $q_2$ | $\sigma_{max}$(MPa) | $\Delta\rho/\rho_o$(%) | $R^2$ | RMSE(MPa) |
| 7 Days | 0.082 | 0.917 | 0.43 | 78.5 | 0.92 | 0.038 |
| 28 Days | 0.3 | 0.699 | 0.51 | 73.5 | 0.99 | 0.014 |

**Compressive Strain**

The stress strain behavior of hollow smart orthopedic cast material samples is monitored and modelled using Vipulanandan Piezoresistivity model after 28 days of curing. The compressive strength of hollow samples after 28 days of curing was 4.7 MPa at a failure strain of 3.2%. The young's modulus was 0.146 GPa for hollow samples (Figure 6-18).

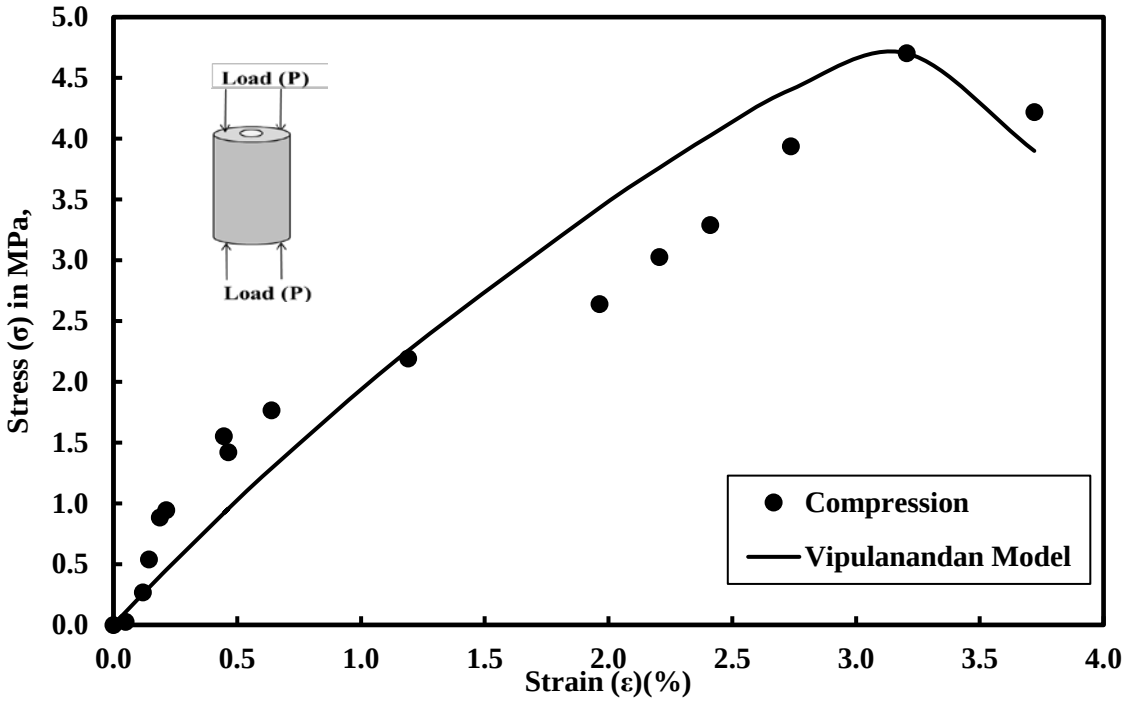


**Figure 6-18:Stress Strain behavior of smart orthopedic cast material hollow samples under compression after 7 days of curing.**

The model parameter $p_2$ was 0.053 while the model parameter $q_2$ was 0.674 for 28 days of curing with conductive filler content of 0.05% (Table 6-9). Vipulanandan piezoresistivity predicted the piezoresistivity trend very well (Figure 6-18). The coefficient of determination ($R^2$) was 0.93 and the RMSE (root mean square error) was 0.462 MPa (Table 6-9).

**Tensile Strain**

The stress strain behavior of hollow smart orthopedic cast material samples is monitored and modelled using Vipulanandan Piezoresistivity model after 28 days of curing. The splitting tensile strength of hollow samples after 28 days of curing was 0.51 MPa at a failure strain of 0.44%. The young's modulus was 0.116 GPa in splitting tension for hollow samples (Figure 6-19). The model parameter $p_2$ was 0.027 while the model parameter $q_2$ was 0.478 for 28 days of curing with conductive filler content of 0.05% (Table 6-9).

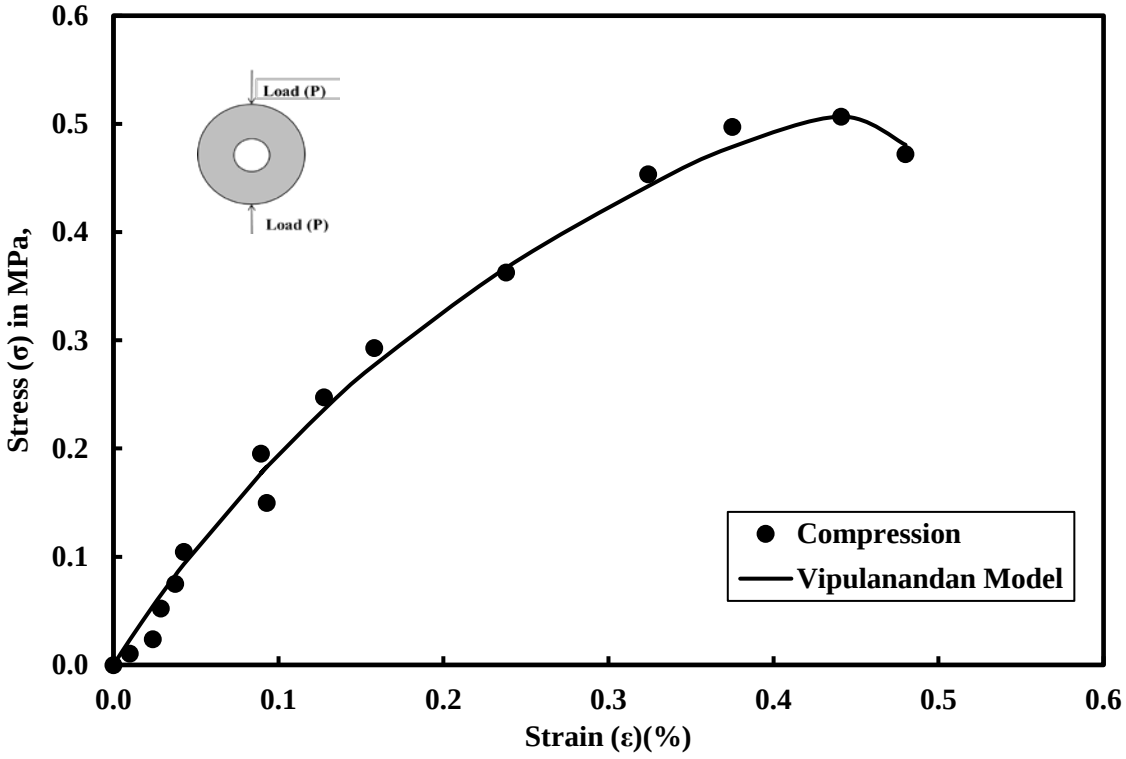


**Figure 6-19:Stress strain behavior of smart orthopedic cast material hollow samples under splitting tension after 28 days of curing.**

Vipulanandan piezoresistivity predicted the piezoresistivity trend very well (Figure 6-19). The coefficient of determination ($R^2$) was 0.99 and the RMSE (root mean square error) was 0.016 MPa (Table 6-9).

**Table 6-9: Correlation and model parameters for Piezoresistivity model for smart orthopedic cast material hollow samples under compression and splitting tension after 28 days of curing.**

| Hollow Cylindrical Smart Cast Samples | | | | | | | |
|---|---|---|---|---|---|---|---|
| Stress | $p_2$ | $q_2$ | $\sigma_{max}$ (MPa) | Strain, ε (%) | Modulus (E) GPa | $R^2$ | RMSE (MPa) |
| Compression | 0.053 | 0.674 | 4.7 | 3.2 | 0.146 | 0.93 | 0.462 |
| Tension | 0.027 | 0.478 | 0.51 | 0.44 | 0.116 | 0.99 | 0.016 |

### 6.2.7 Internal Pressure Test

Hollow smart orthopedic cast samples were applied with internal pressure of upto 40 psi using pressure tube and the change in resistivity was monitored. This internal pressure test represents pressure applied on orthopedic cast due to swelling. The pressure test was performed on the hollow cast specimens after 7 and 28 days of curing.

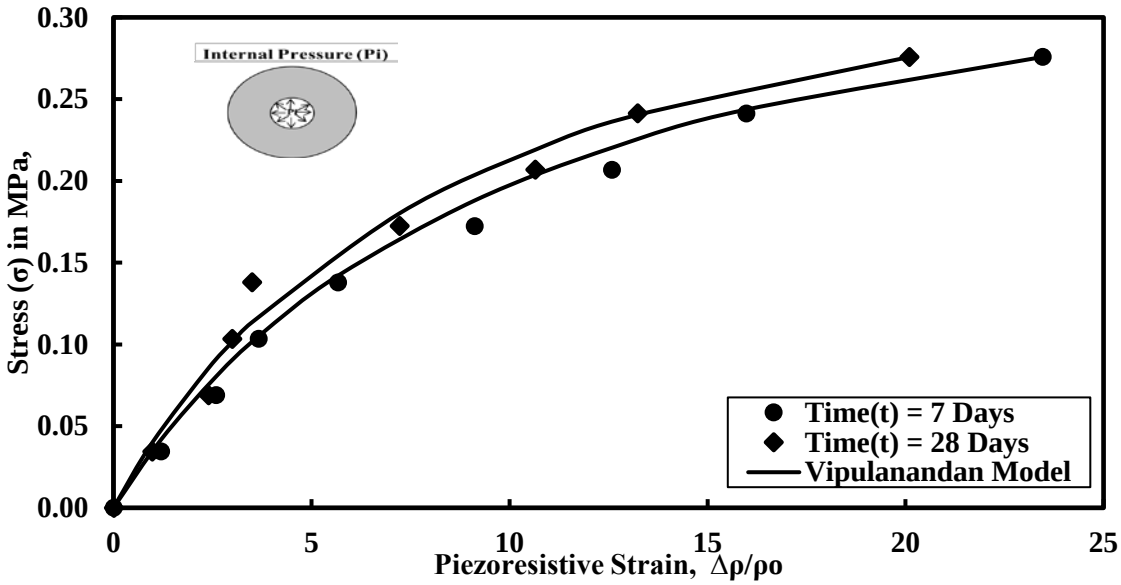


**Figure 6-20: Piezoresistive behavior of smart orthopedic cast material hollow samples under internal pressure after 7 and 28 days of curing.**

The piezoresistive strain for smart orthopedic cast material hollow specimen with 0.05% conductive filler under internal pressure of 0.28 MPa (40 psi) was 23.46 % after 7 days of curing. Hence, the piezoresistivity per unit stress was 83.7%/MPa in the lab samples after 7 days of curing. After 28 days of curing, piezoresistive strain for smart orthopedic cast material hollow specimen with 0.05% conductive filler under internal pressure of 0.28 MPa (40 psi) was 20.1 %, showing piezoresistivity per unit stress was 71.7%/MPa after 28 days of curing (Figure 6-20). The piezoresistivity of smart orthopedic cast material was modeled using Vipulanandan piezoresistivity model for 28 days curing (Eqn. 3-19).

The model parameter $p_2$ and $q_2$ were 0.01 and 0.303 over 28 days of curing with conductive filler content of 0.05% (Table 6-10). Vipulanandan piezoresistivity predicted the piezoresistivity trend very well (Figure 6-20). The coefficient of determination ($R^2$) varied from 0.98 to 0.99 and the RMSE (root mean square error) varied in the range of 0.0084 to 0.011 MPa (Table 6-10).

**Table 6-10:Correlation and model parameters for Piezoresistivity model for smart orthopedic cast material hollow samples under internal pressure after 7 and 28 days of curing.**

| Hollow Cylindrical Smart Cast Samples | | | | | | |
|---|---|---|---|---|---|---|
| Internal Pressure Test | $p_2$ | $q_2$ | $\sigma_{max}$ (MPa) | $\Delta\rho/\rho_o$ (%) | $R^2$ | RMSE (MPa) |
| 7 Days | 0.01 | 0.303 | 0.28 | 23.46 | 0.99 | 0.0084 |
| 28 Days | 0.01 | 0.304 | 0.28 | 20.1 | 0.98 | 0.011 |

### 6.2.8 Water Seepage Test

Smart orthopedic cast material samples cured for 28 days were placed in water to observe the change in resistivity within the first one hour. Electrical resistivity of the samples was monitored in real time to calculate the change in electrical resistivity with time. It was observed that with time, there is decrease in electrical resistivity due to ingress of water into the samples. The maximum change in resistivity was about 54% for a 60-minute submersion (Figure 6-21). The change in resistivity was modelled using water seepage model (Eqn. 3-25). The model parameter A, B and

$t_o$ were 7.68, 1.93 and 0. The model predicted the change trend very well. The coefficient of determination ($R^2$) was 0.99 and the RMSE (root mean square error) was 0.59 %.

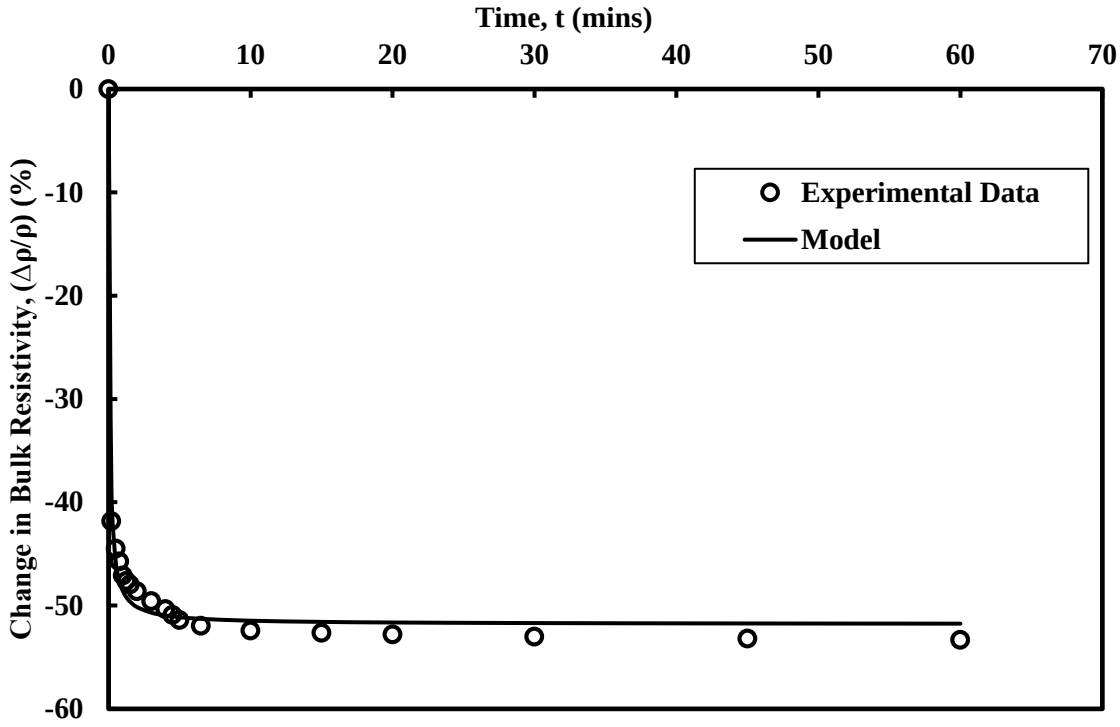


**Figure 6-21:Change in electrical resistivity with time for smart orthopedic cast material submerged in water.**

### 6.2.9 Temperature Effect

Smart orthopedic cast material samples cured for 28 days were placed in the oven for a temperature cycle of 60 °F to 170 °F. Electrical resistivity of the samples were monitored in real time to calculate the change in electrical resistivity with increase in the temperature. It was observed that with the increase in temperature, there is decrease in electrical resistivity. The maximum change in resistivity was about 10.4% for a change in temperature from 60 °F to 170 °F (Figure 6-22). The temperature and change in resistivity are modelled using temperature model (Eqn. 3-25). The model parameter A, B and $T_o$ were -0.083, 0.0025 and 74.56 °F. The temperature model predicted the temperature change trend very well. The coefficient of determination ($R^2$) was 0.99 and the RMSE (root mean square error) was 3.78 °F.

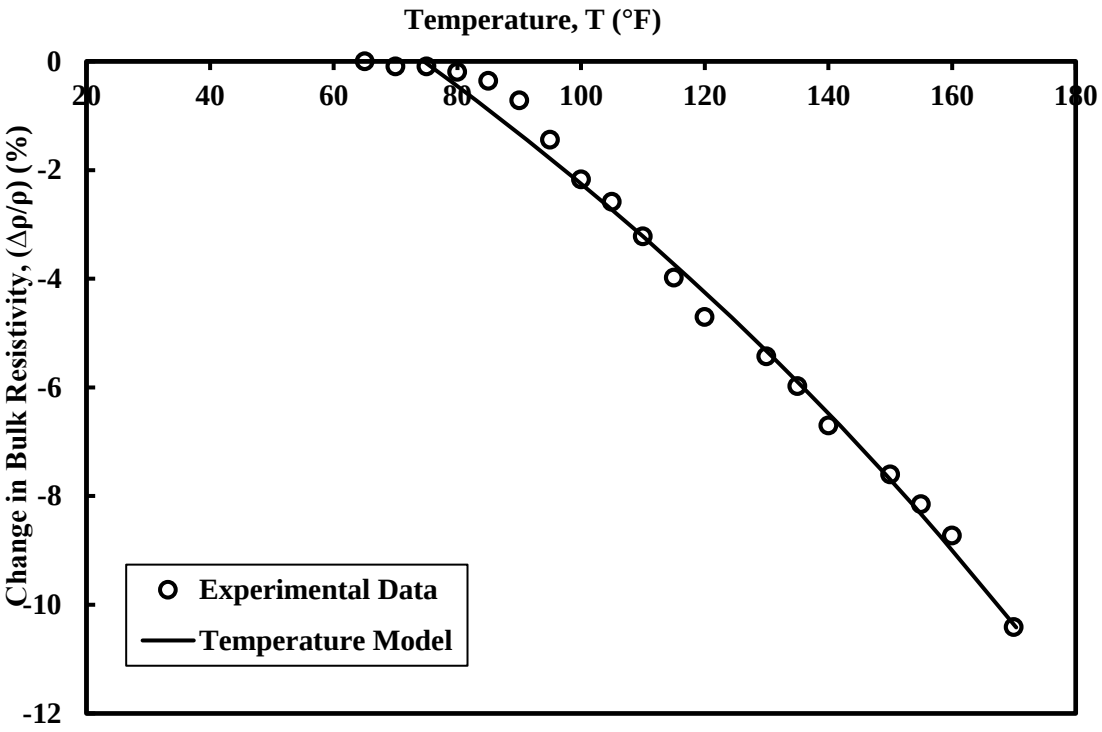


**Figure 6-22:Change in electrical resistivity with change in temperature for smart orthopedic cast material.**

## 6.3 Summary

In this study total of 260 samples were tested for electrical resistivity, setting time and piezoresistivity behavior. In this study, effects of the water seepage, temperatures on the electrical resistivity were investigated. Based on the experimental study and analytical modeling following conclusions are advanced:

- Orthopedic Cast material had very good sensing properties with the addition of conductive filler of 0.05%. Using this sensitivity, orthopedic cast material can be monitored during and after the process of casting, until it gains complete strength.
- Addition of 0.05% conductive filler further increased the piezoresistive strain of orthopedic cast material to 345% at a peak compressive stress of 6.28 MPa, showing piezoresistivity per unit stress was 54.9 %/MPa after 28 days of curing.
- With addition of 0.05% conductive filler, the piezoresistive strain for orthopedic cast material was 16.52% at a peak bending stress of 1.33 MPa after 28 days of curing for thick plate samples. Hence, the piezoresistivity per unit stress in bending was 12.42 %/MPa in the thick plate samples after 28 days of curing.
- After 28 days of curing, piezoresistive strain for smart orthopedic cast material hollow specimen with 0.05% conductive filler was 152 % at a peak compressive stress of 4.7 MPa, showing piezoresistivity per unit stress was 32.3%/MPa after 28 days of curing.
- After 28 days of curing, piezoresistive strain for smart orthopedic cast material hollow specimen with 0.05% conductive filler under splitting tension was 73.5 % at a peak compressive stress of 0.51 MPa, showing piezoresistivity per unit stress was 144.1%/MPa after 28 days of curing.
- The compressive strength of hollow samples after 28 days of curing was 4.7 MPa at a failure strain of 3.2%. The splitting tensile strength of hollow samples after 28 days of curing was 0.51 MPa at a failure strain of 0.44%.

- After 28 days of curing, piezoresistive strain for smart orthopedic cast material hollow specimen with 0.05% conductive filler under internal pressure of 0.28 MPa (40 psi) was 20.1 %, showing piezoresistivity per unit stress was 71.7%/MPa after 28 days of curing.
- The smart orthopedic cast material was highly sensitive to water seepage and temperature changes

# CHAPTER 7 ANALYTICAL AND FINITE ELEMENT MODELING

Modeling the flow of fluids is important to quantify the cleaning ability and analyzing the stresses in casing – cement – formation inside well bore enables to understand the performance of well bore. The stress distribution inside orthopedic cast material enables correlation to real time monitoring. In this study, analytical flow modeling of smart spacer fluid is performed quantify velocity profiles predicted by Bingham Plastic and Vipulanandan rheological models. Analytical and finite element modeling of casing - cement – formation system and orthopedic cast material are performed and compared to experimental results.

## 7.1 Analytical Flow Modeling of Smart Spacer Fluid

Azar and Samuel in 1937 proposed the analytical model for determination of the velocity generated by Newtonian, Power law (1906) and Bingham model (1922) for the fluid flow. In this study a new rheological model, Vipulanandan Rheological (2014) model is proposed to evaluate the rheological properties of the drilling and spacer fluids.

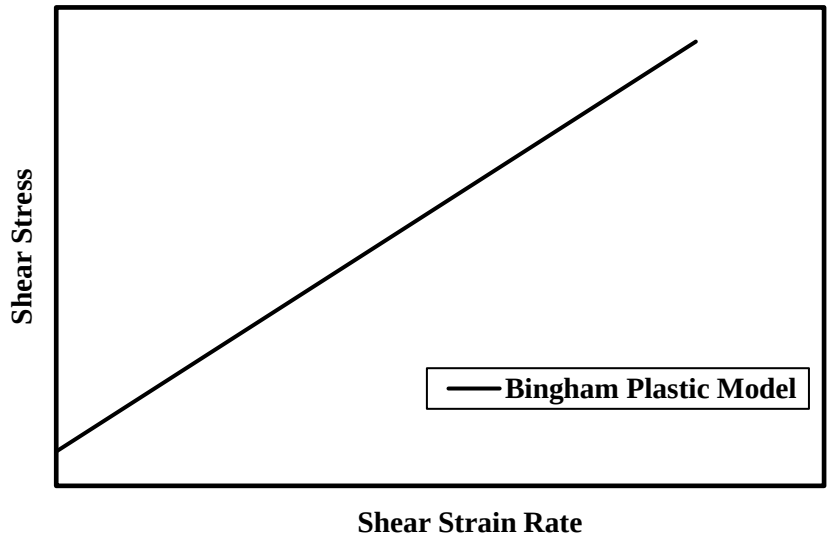


**Figure 7-1:Shear Stress Vs Shear Strain Rate behavior for Bingham Plastic model.**

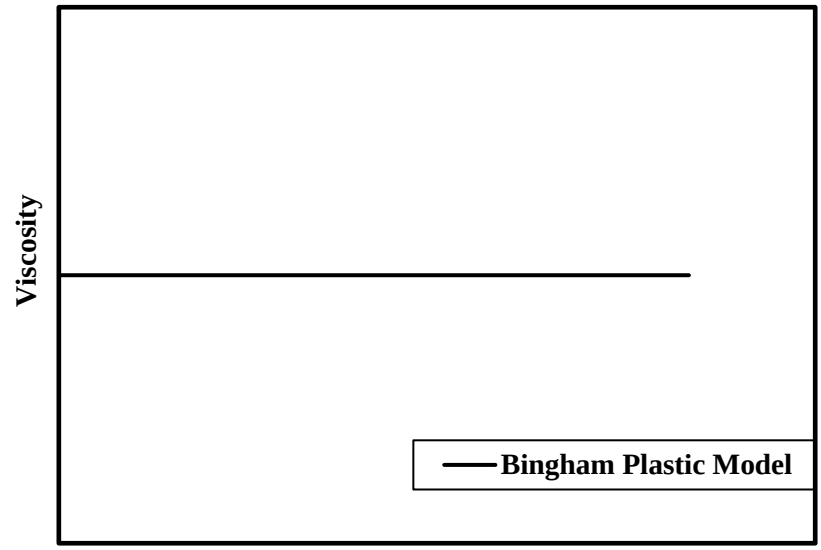


**Figure 7-2: Viscosity Vs Shear Strain Rate behavior for Bingham Plastic model.**

For shear thinning fluids, the Newtonian, Power law and Bingham models will predict the shear stress to reach infinity, when the strain rate reaches infinity. This behavior of fluids is not the case in reality (Figure 7-1 & Figure 7-2).

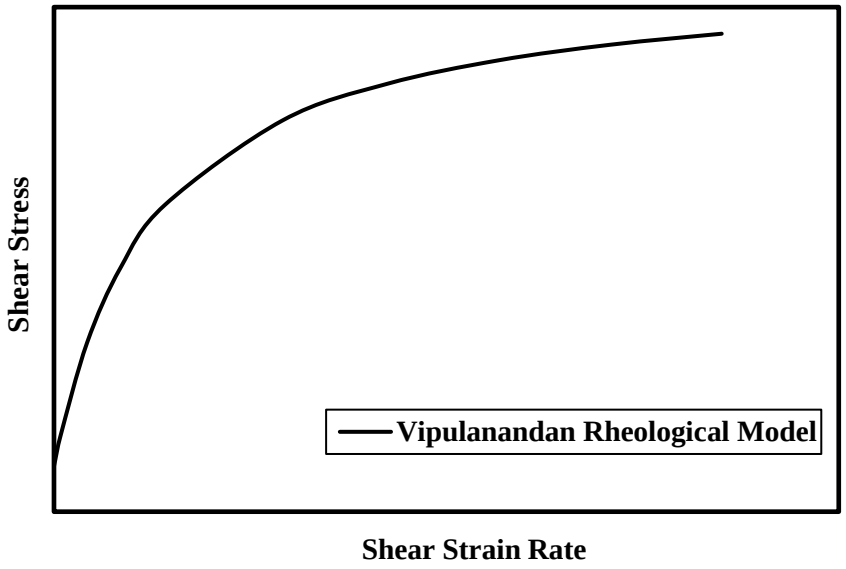


**Figure 7-3: Shear Stress Vs Shear Strain Rate behavior for Vipulanandan rheological model.**

The Vipulanandan rheological model eliminates this problem by limiting the shear stress in the fluid to a maximum value which is much close to the reality (Figure 7-3 & Figure 7-4). In this study, the analytical modeling of the axial fluid flow is investigated for the Smart Spacer fluid. The Bingham Plastic model analytical solution is shown and the Vipulanandan rheological model is proposed and compared to Bingham Plastic model.

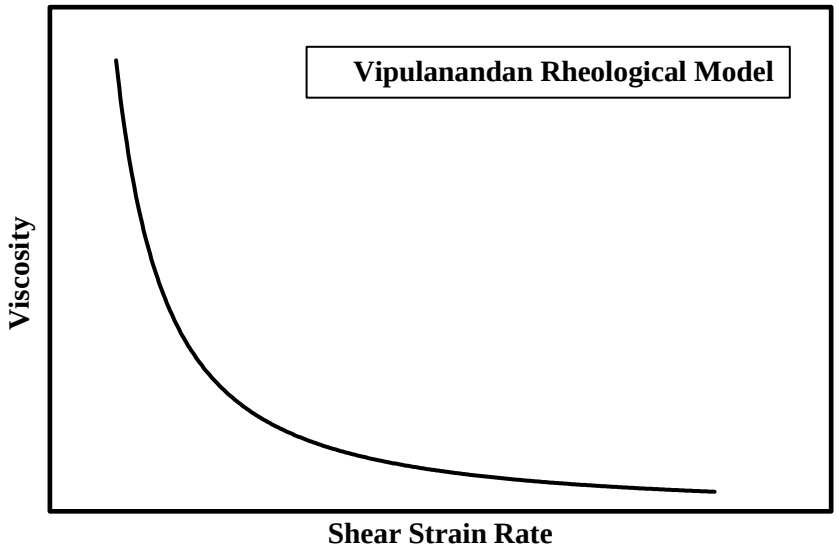


**Figure 7-4:Viscosity Vs Shear Strain Rate behavior for Vipulanandan rheological model.**

### 7.1.1 Equilibrium in Cylindrical Coordinate System

The velocity at some arbitrary point inside well bore is defined as

$$V = \nu_r e_r + \nu_\theta e_\theta + \nu_z e_z \,, \tag{7-1}$$

where $\nu_r$, $\nu_\theta$ and $\nu_z$ are the velocity of the flow in r, ɵ and z directions.

The relationship between the velocity and the strain rate in a cylindrical coordinate system is defined as follows:

$$\dot{\varepsilon_r} = \frac{\partial v_r}{\partial r}, \tag{7-2}$$

$$\dot{\varepsilon_\theta} = \frac{v_r}{r} + \frac{1}{r}.\frac{\partial v_\theta}{\partial \theta}, \tag{7-3}$$

$$\dot{\varepsilon}_z = \frac{\partial v_z}{\partial z}, \tag{7-4}$$

$$\dot{\gamma}_{r\theta} = \frac{1}{2}\left(\frac{\partial v_\theta}{\partial r} + \frac{1}{r}.\frac{\partial v_r}{\partial \theta}\right) - \frac{v_\theta}{r}, \tag{7-5}$$

$$\dot{\gamma}_{z\theta} = \frac{1}{2}\left(\frac{1}{r}.\frac{\partial v_z}{\partial \theta} + \frac{\partial v_\theta}{\partial z}\right), \tag{7-6}$$

$$\text{and} \quad \dot{\gamma}_{zr} = \frac{1}{2}\left(\frac{\partial v_r}{\partial z} + \frac{\partial v_z}{\partial r}\right). \tag{7-7}$$

In the axisymmetric condition the velocity in circumferential direction and the derivative of this direction is zero and are given by

$$v_\theta = 0, \frac{\partial v_\theta}{\partial \theta} = 0. \tag{7-8}$$

Therefore, the strain rates will be simplified as follows:

$$\dot{\varepsilon_r} = \frac{\partial v_r}{\partial r}, \tag{7-9}$$

$$\dot{\varepsilon_\theta} = \frac{v_r}{r}, \tag{7-10}$$

$$\dot{\varepsilon_z} = \frac{\partial v_z}{\partial z}, \tag{7-11}$$

$$\dot{\gamma}_{r\theta} = 0, \tag{7-12}$$

$$\dot{\gamma}_{z\theta} = 0, \tag{7-13}$$

$$\text{and} \quad \dot{\gamma}_{zr} = \frac{1}{2}\left(\frac{\partial v_r}{\partial z} + \frac{\partial v_z}{\partial r}\right). \tag{7-14}$$

The assumptions are made as following:

- Axisymmetric condition and no swirl, $v_\theta = 0, \frac{\partial v_\theta}{\partial \theta} = 0.$
- Flow is laminar and parallel to the wall, $v_r = 0, \frac{\partial v_r}{\partial r} = 0.$
- Steady Flow, $\frac{\partial Q}{\partial t} = 0.$
- Fully developed Flow, $\frac{\partial v_z}{\partial z} = 0.$

Therefore,

$$\dot{\varepsilon_r} = \dot{\varepsilon_\theta} = \dot{\varepsilon_z} = 0, \tag{7-15}$$

$$\dot{\gamma}_{r\theta} = \dot{\gamma}_{z\theta} = 0, \tag{7-16}$$

and $$\dot{\gamma}_{zr} = \frac{1}{2}\left(\frac{dv_z}{dr}\right). \tag{7-17}$$

The equilibrium equation in cylindrical coordinate system was studied for the spacer fluid with axial flow for an element shown in Figure 7-5. The following flow diagram represents flow of spacer fluid from bottom to top in the annulus. The shear stress in outer side and inner side of the element is calculated as dFs. The force due to piezo head and due to gravity is dFp and dFg, respectively. The forces are given as follows:

$$dF_S = [(\tau + \Delta\tau).2\pi(r + \Delta r) - \tau.2\pi(r)].\Delta l = (\tau.\Delta r + \Delta\tau.r).2\pi\Delta l, \tag{7-18}$$

$$dF_p = [(p + \Delta p).2\pi(r + \Delta r) - \tau.2\pi(r)].\Delta l = 2\pi r\,\Delta p\,\Delta r, \tag{7-19}$$

and $$dF_g = \rho g.2\pi r.\Delta r\Delta l. \tag{7-20}$$

The equilibrium for upward flow is given by

$$dF_p = dF_s + dF_g\,. \tag{7-21}$$

By substituting the Eqns. (7-18, 7-19, & 7-20) into eqn. (7-21),

$$2\pi r\,\Delta p\,\Delta r = (\tau.\Delta r + \Delta\tau.r).2\pi\Delta l + \rho g.2\pi r.\Delta r\,\Delta l. \tag{7-22}$$

Rearranging the terms and dividing by $2\pi r$ we have

$$\frac{\tau}{r} + \frac{\Delta\tau}{\Delta r} = \left(\frac{\Delta p}{\Delta z} - \rho g\right). \tag{7-23}$$

Integrating eqn. (7-23) we have,

$$\int(\tau.\Delta r + \Delta\tau.r) = \int\left(\frac{\Delta p}{\Delta z} - \rho g\right)r.\Delta r. \tag{7-24}$$

Eqn. (7-24) is a first order differential equation which can be solved as

$$\tau = \frac{r}{2}.\left(\frac{\Delta p}{\Delta z} - \rho g\right) + \frac{C_1}{\mathrm{r}}. \tag{7-25}$$

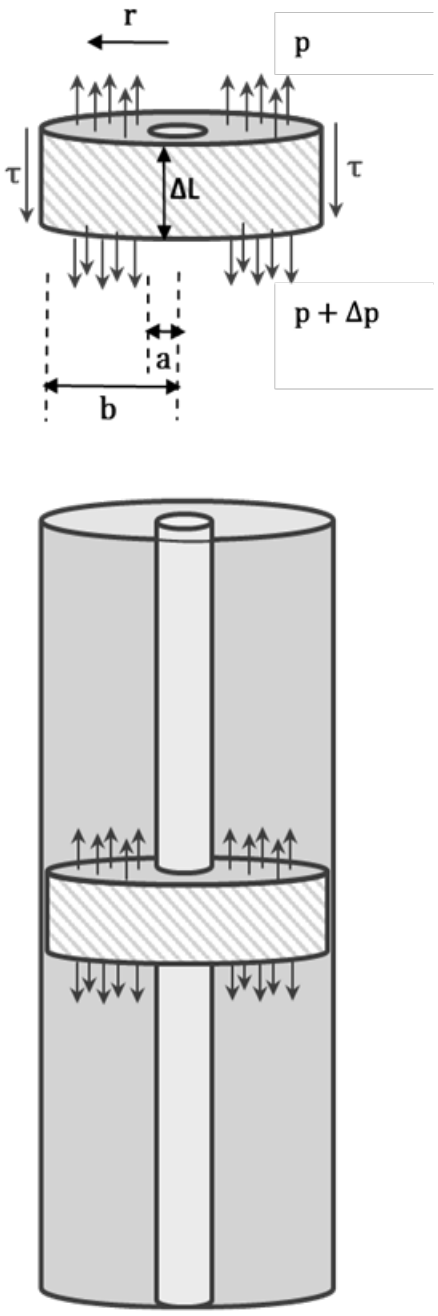


**Figure 7-5:Axial upward flow equilibrium diagram in a wellbore.**

### 7.1.2 Bingham Plastic Model

For a Bingham Plastic fluid flow, the constitutive model is a linear relationship between the shear stress and strain rate.

Two parameters model which can be presented as

$$\tau = \tau_y + \mu\dot{\gamma}, \tag{7 - 26}$$

in which $\tau_y$ is yield stress and $\eta_p$ is plastic viscosity of the fluid.

Substituting back in equilibrium eqn. (7-25), we have

$$\tau_y + \mu\dot{\gamma} = \frac{r}{2}.\left(\frac{\Delta p}{\Delta z} - \rho g\right) + \frac{C_1}{\mathrm{r}}. \tag{7 - 27}$$

By rearranging the terms, shear strain rate is given by

$$\dot{\gamma} \;=\; k_1 r + \frac{k_2}{r} - k_3\,, \tag{7 - 28}$$

where,

$$k_1 = \frac{P_Z}{2\mu}, \tag{7 - 29}$$

$$k_2 = \frac{C_1}{\mu}, \tag{7 - 30}$$

and

$$k_3 = \frac{\tau_y}{\mu}. \tag{7 - 31}$$

The velocity profile is given by eqn. (7-17). Substituting eqn. (7-28) in eqn.(7-17) and integrating, we get the velocity profile for Bingham Plastic Model as

$$V_z = \; 2\int \dot{\gamma}\, dr = \; 2\int (k_1\, r + \tfrac{k_2}{r} - k_3)\, dr. \tag{7 - 32}$$

Solving eqn. (7-32), we have velocity given by

$$V_z = \; 2\,(V_1 r^2 + V_2 \log(r) - V_3 r + V_4), \tag{7 - 33}$$

where

$$V_1 = \frac{P_z}{4\mu}, \tag{7 - 34}$$

$$V_2 = \frac{C_1}{\mu}, \tag{7 - 35}$$

$$V_3 = \frac{\tau_y}{\mu}, \tag{7 - 36}$$

and $V_4 = C_2$. (7 -37)

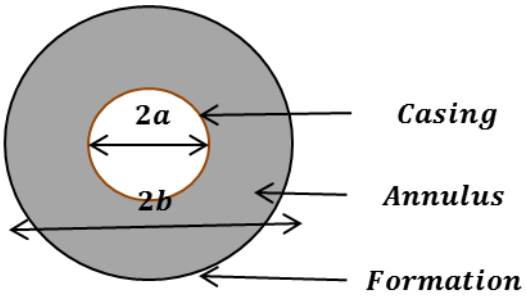


**Figure 7-6:Cross Sectional Diagram of the Well bore.**

Now by applying the boundary conditions,

Boundary Condition 1: $V_z = 0$ at radius (r) = a = 0.122 m. (4.8125 inch)

Boundary Condition 2: $V_z = 0$ at radius (r) = b = 0.1785 m. (7.0275 inch).

The two integration constants ($C_1$ *and* $C_2$) will be given as

$$C_1 = \frac{\tau_y(b-a)}{log\,(\frac{b}{a})} - \frac{P_z(b^2-a^2))}{4\log\left(\frac{b}{a}\right)}, \quad (7 - 38)$$

$$\text{and } C_2 = -(\frac{P_z * a^2}{4\mu} + \frac{C_1 * \log(a)}{\mu} - \frac{\tau_y * a}{\mu}) \ . \quad (7 - 39)$$

where $P_z = \left(\frac{\Delta p}{\Delta z} - \rho g\right)$, is the piezo head difference which is assumed to be 400 N/m³. The wellbore inner radius (a) and outer radius (b) are assumed to be 0.122 m and 0.1785 m. The fluid properties as follows: specific weight of $\gamma$ = 1000 N/m³, a constant viscosity of 0.0112 Pa.s. and yield stress of 48.5 Pa (Table 7-1). By applying the boundary conditions, the constant $C_1$ and $C_2$ can be derived as -1.56 and -48.09 (Table 7-2), respectively from eqns. (7-38 & 7-39). The constitutive model (shear stress and strain rate relationship) for the spacer fluid using Bingham Plastic model is a linear relationship shown in Figure 7-7 . The velocity and strain rate are shown along the radius in Figure 7-8 and Figure 7-9, respectively.

**Table 7-1:Input parameters for velocity profile, shear strain rate and shear stress calculation.**

| Inputs | | |
|---|---|---|
| Inner Radius (m) | $r_1$ | 0.122 |
| Outer Radius (m) | $r_2$ | 0.1785 |
| Density of Fluid (kg/m3) | ρ | 1000 |
| Acceleration due to gravity (m2/sec) | g | 9.8 |
| Unit (ρ*g) (N/m3) | | 9800 |
| Pressure Gradient (N/m3) | (ΔP/ΔZ) | 10200 |
| Pz (N/m3) | (ΔP/ΔZ) - ρg | 400 |
| Viscosity of Fluid (Pa.s) | μ | 0.0112 |
| Yield Stress (Pa) | $\tau_y$ | 48.5 |

**Table 7-2:Calculation of integration constants for Bingham Plastic model.**

| C1 | | | C2 | | |
|---|---|---|---|---|---|
| **m1** | $\frac{\tau_y(b-a)}{\log(\frac{b}{a})}$ | 2.90 | **n1** | $\frac{P_z * a^2}{4\mu}$ | 29.77 |
| **m2** | $\frac{P_z(b^2-a^2))}{4\log(\frac{b}{a})}$ | 4.461 | **n2** | $\frac{C_1 * \log(a)}{\mu}$ | 65.9 |
| **C1** | $(m_1 - m_2)$ | **-1.566** | **n3** | $\frac{\tau_y * a}{\mu}$ | 47.58 |
| | | | **C2** | $-(n_1 + n_2 - n_3)$ | **-48.09** |

**Table 7-3: Shear Strain Rate and Velocity constants calculation.**

| Shear Rate Calculation ($\dot{\gamma}$) | | | Velocity Calculation (V)- (m/sec) | | |
|---|---|---|---|---|---|
| **k1** | $\frac{P_Z}{2\mu}$ | **4000** | **V1** | $\frac{P_z}{4\mu}$ | 2000 |
| **k2** | $\frac{C_1}{\mu}$ | **-31.33** | **V2** | $\frac{C_1}{\mu}$ | -31.33 |
| **k3** | $\frac{\tau_y}{\mu}$ | **390** | **V3** | $\frac{\tau_y}{\mu}$ | 390 |
| | | | **V4** | C2 | -48.09 |

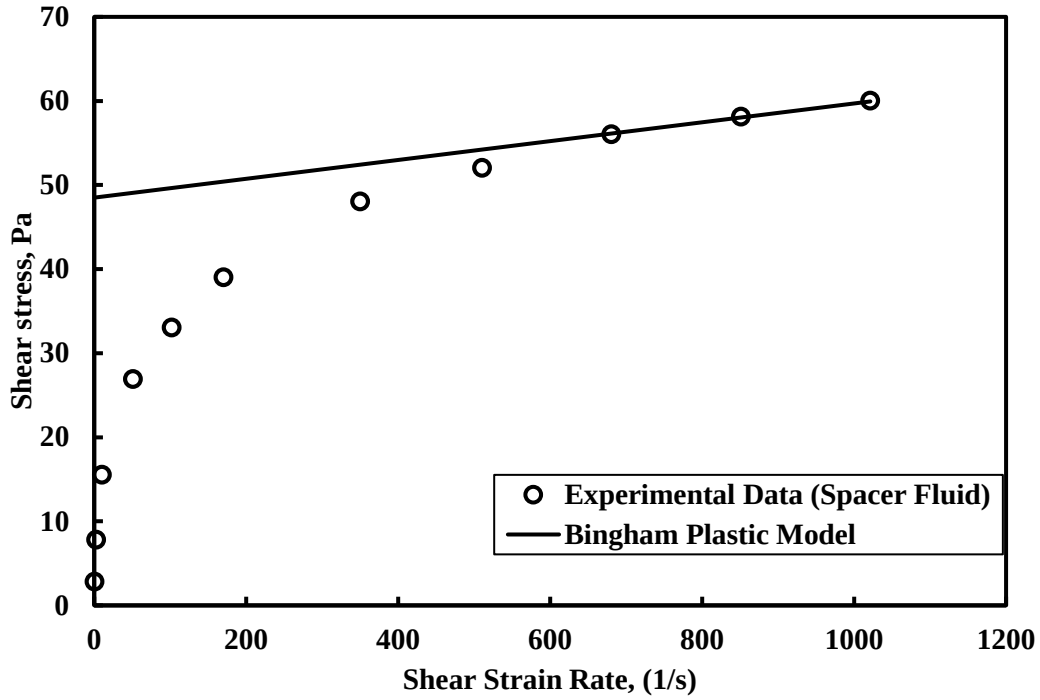


**Figure 7-7:Shear stress – shear strain rate relationship using Bingham Plastic model for spacer fluid.**

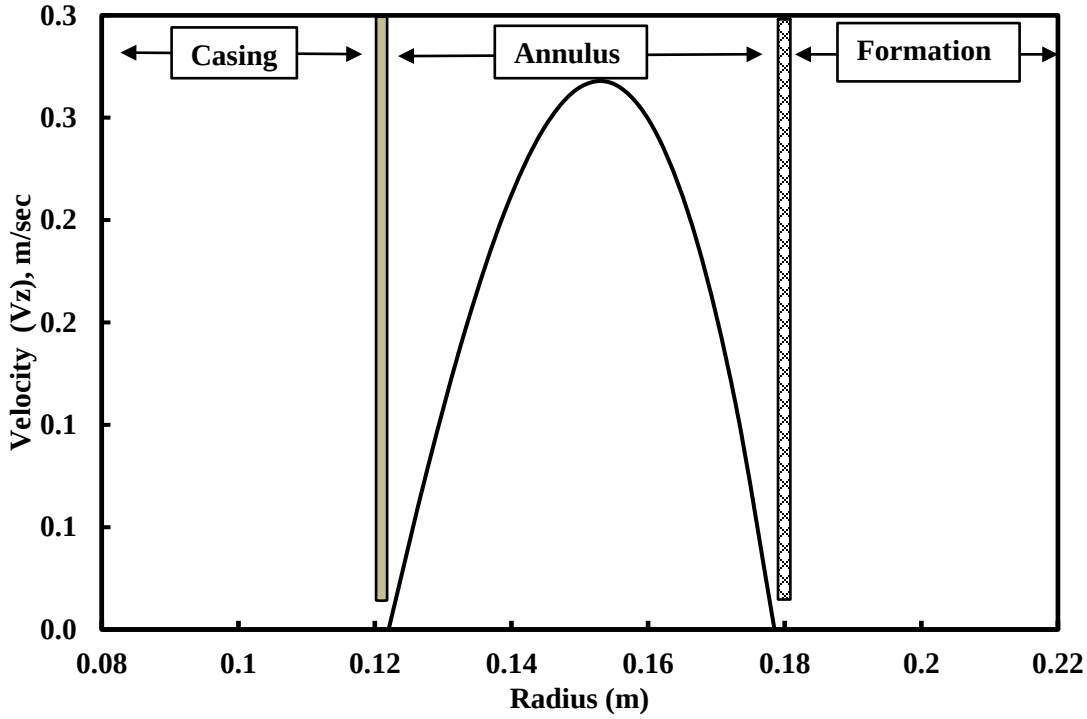


**Figure 7-8:Velocity profile along the radius for Bingham Plastic fluid flow.**

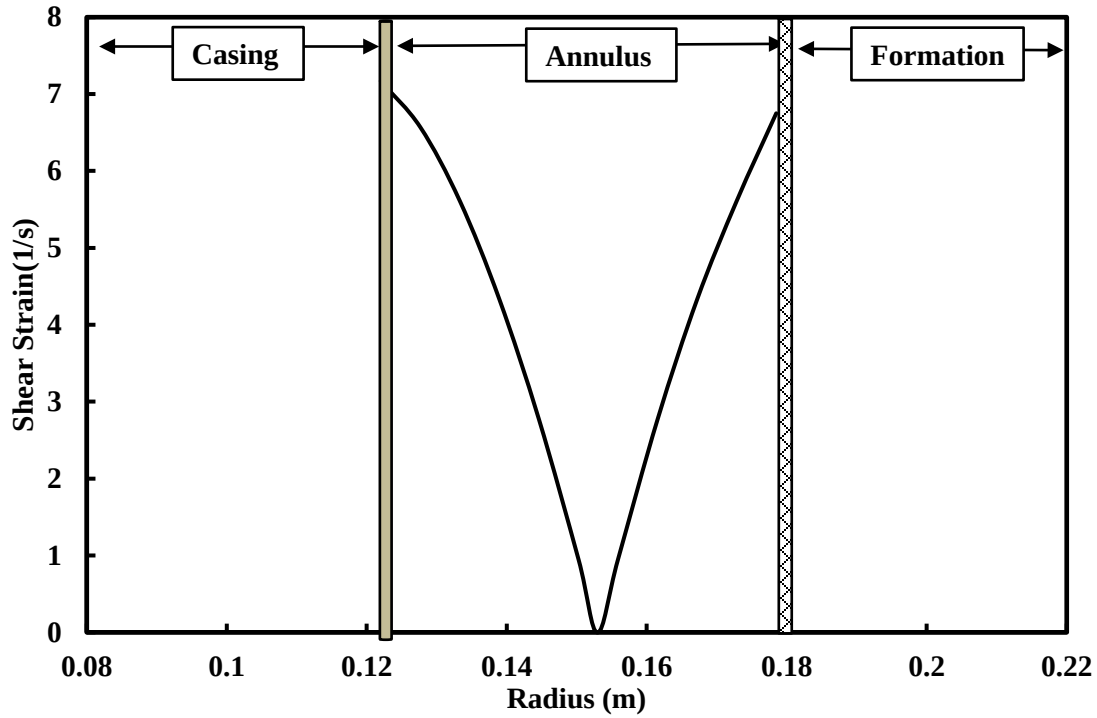


**Figure 7-9: Shear Strain rate profile along the radius for Bingham Plastic fluid flow.**

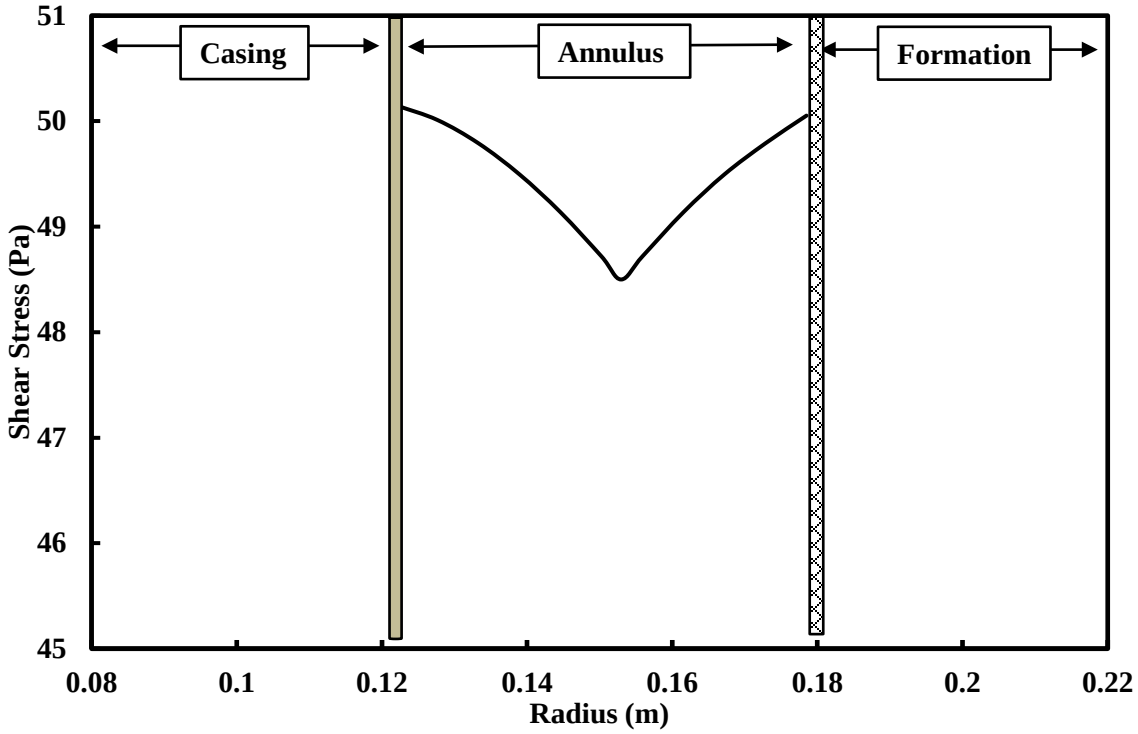


**Figure 7-10: Shear Stress profile along the radius for Bingham Plastic fluid flow.**

**Shear Stress – Shear Strain Rate**

The shear stress to shear strain rate relationship for spacer fluid using Bingham Plastic model showed linear behavior as shown in Figure 7-7. The yield stress and plastic viscosity using Bingham Plastic model for spacer fluid were 48.5 Pa and 11.2 cP. The coefficient of determination ($R^2$) was 0.52 and the RMSE (Root Mean Square Error) value was 22 Pa.

**Velocity Profile**

The spacing of the annulus varied from radius (a) = 0.122 m (casing annulus interface) to radius (b) = 0.1785 m (annulus formation interface) with radius (r) = 0 m representing casing center. The velocity profile of the spacer fluid varied from 0 m/sec at the interfaces (radius (r) = 0.122 & 0.1785 m) to maximum of 0.268 m/sec (48.2 ft/min) at a radius (r) equal to 0.15296 m (Close to the center) as shown in Figure 7-8. The velocity profile showed nonlinear variation with the radius.

**Shear Strain Rate – Radius**

The shear strain rate varied from 0 $s^{-1}$ to 7.17 $s^{-1}$ (4.2 rpm) in the annulus using Bingham Plastic constitutive model. The shear strain rate varied linearly across the radius with zero shear strain rate close to the center at radius = 0.15296 m for Bingham plastic constitutive model (Figure 7-9). The shear strain rate was maximum at the interfaces and minimum close to center inside annulus.

**Shear Stress - Radius**

The shear stress varied from 48.5 Pa to 51.05 Pa in the annulus using Bingham Plastic constitutive model. The shear stress varied linearly across the radius with shear stress equal to yield stress, 48.5 Pa of the spacer fluid close to the center at radius = 0.15296 m for Bingham plastic constitutive model (Figure 7-10). The shear stress was maximum at the interfaces and minimum close to center for spacer fluid flow inside annulus.

**Viscosity**

The viscosity of spacer fluid was constant at 11.2 cP. using Bingham Plastic model in the annulus (Figure 7-11 & Figure 7-12).

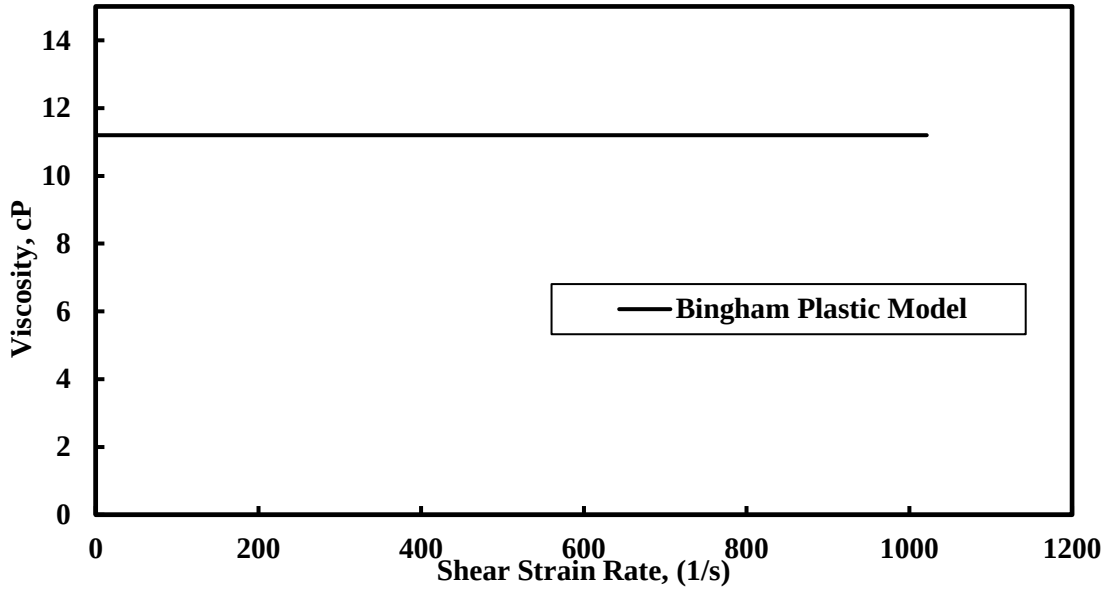


**Figure 7-11:Viscosity of spacer fluid using Bingham Plastic model.**

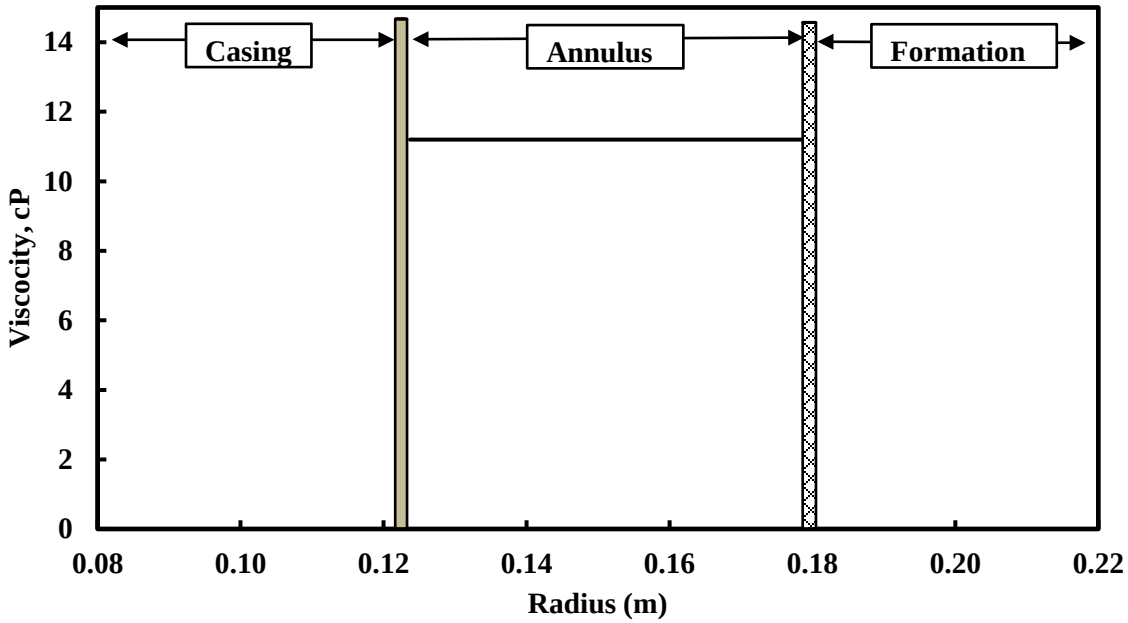


**Figure 7-12: Viscosity profile of spacer fluid in the annulus.**

### 7.1.3 Vipulanandan Rheological Model

The relationship between shear stress and shear strain rate for the smart spacer fluids was investigated (Vipulanandan and Mohammed 2014) and is given by

$$\tau - \tau_0 = \frac{\dot{\gamma}}{A + B\dot{\gamma}}. \tag{7 - 40}$$

Substituting the constitutive model in equilibrium equation (7- 25), we have

$$\tau_0 + \frac{\dot{\gamma}}{A + B\dot{\gamma}} = \frac{r}{2}.\left(\frac{\Delta p}{\Delta z} - \rho g\right) + \frac{C_1}{\mathrm{r}}. \tag{7 - 41}$$

So, the shear strain rate is given by

$$\dot{\gamma} = \frac{A(P_Z r^2 + 2C_1 - 2\tau_o r)}{(2r - Bkr^2 - 2BC_1 + 2B\tau_o r)} = \frac{l_1}{l_2}. \tag{7 - 42}$$

The velocity profile is obtained by integration of shear strain rate over the radius as given by eqn. (7-17). Substituting eqn. (7-42) in eqn. (7-17) and integrating, we get the velocity profile for Vipulanandan Rheological Model as

$$V_z = 2\int \dot{\gamma}\, dr = 2\int \frac{l_1}{l_2}\, dr. \tag{7 - 43}$$

The velocity profile for Vipulanandan Rheological Model is given by

$$V_z = 2\,(V_1 + V_2 + V_3 + V_4), \tag{7 - 44}$$

where,

$$V_1 = \frac{A_1 r}{A_2} - \frac{A_1 A_3 \ln\,(A_2 r^2 + A_3 r + A_4)}{2{A_2}^2} + \frac{A_1 V_4\left({A_3}^2 - 2A_2 A_4\right)}{2{A_2}^2}, \tag{7 - 45}$$

$$V_2 = \frac{A_5 ln(A_2 r^2 + A_3 r + A_4)}{2A_2} - \frac{A_5 A_3}{2A_2} V_4\,, \tag{7 - 46}$$

$$V_3 = A_6 V_4 \tag{7 - 47}$$

and $$V_4 = \frac{\ln\,(2A_2 r + A_3 - A_7/2A_2 r + A_3 + A_7)}{\sqrt{{C_1}^2 - 4B_1 D_1}}. \tag{7 - 48}$$

Constants are as follows:

$$A_1 = -AP_Z\,, \tag{7 - 49}$$

$$A_2 = BP_Z\,, \tag{7 - 50}$$

$$A_3 = -2(1 + B\tau_o), \quad (7 - 51)$$

$$A_4 = 2BC_1\,, \quad (7 - 52)$$

$$A_5 = 2A\tau_o, \quad (7 - 53)$$

$$A_6 = -2AC_1, \quad (7 - 54)$$

where $P_z$ = ($\Delta p/\Delta z$ - $\rho g$), is the piezo head difference which is assumed to be 400 N/m³. The wellbore inner radius (a) and outer radius (b) are assumed to be 0.122 m and 0.1785 m. The fluid properties as follows: specific weight of $\gamma$ = 1000 N/m³, yield stress of 6.63 Pa, model constant A and B equal to 2 and 0.0175 (Table 7-4).

**Table 7-4:Input parameters for velocity profile, shear strain rate and shear stress calculation using Vipulanandan Rheological model.**

| Inputs | | |
|---|---|---|
| Inner Radius (m) -a | $r_1$ | 0.122 |
| Outer Radius (m) -b | $r_2$ | 0.1785 |
| Density of Fluid (Kg/m3) | $\rho$ | 1000 |
| Acceleration due to gravity (m2/sec) | g | 9.8 |
| Unit ($\rho$*g) (N/m3) | | 9800 |
| Pressure Gradient (N/m3) | ($\Delta P/\Delta Z$) | 10200 |
| Pz (N/m3) | ($\Delta P/\Delta Z$) - $\rho g$ | 400 |
| Viscosity of Fluid (Pa.s) | $\mu$ | Variable |
| Yield Stress (Pa) | $\tau_y$ | 6.63 |
| Constant A | A | 2 |
| Constant B | B | 0.0175 |

**Table 7-5:Integration Constants for a sample input values.**

| **Integration Constants** | | |
|---|---|---|
| **A1** | $-AP_Z$ | **-799.2** |
| **A2** | $BP_Z$ | **7** |
| **A3** | $-2(1 + B\tau_o)$ | **-2.23** |
| **A4** | $2BC_1$ | **-0.12** |
| **A5** | $2A\tau_o$ | **26.49** |
| **A6** | $-2AC_1$ | **14.27** |
| **A7** | $\sqrt{{C_1}^2 - 4B_1D_1}$ | **2.91** |

By applying the boundary conditions, the constant $C_1$ and $C_2$ can be derived as -3.57 and -1.54, respectively (Table 7-5). The constitutive model (shear stress and strain rate relationship) for the

Vipulanandan rheological model is a non - linear relationship shown in Figure 7-13. The velocity and strain rate are shown along the radius in Figure 7-14 and Figure 7-15 , respectively.

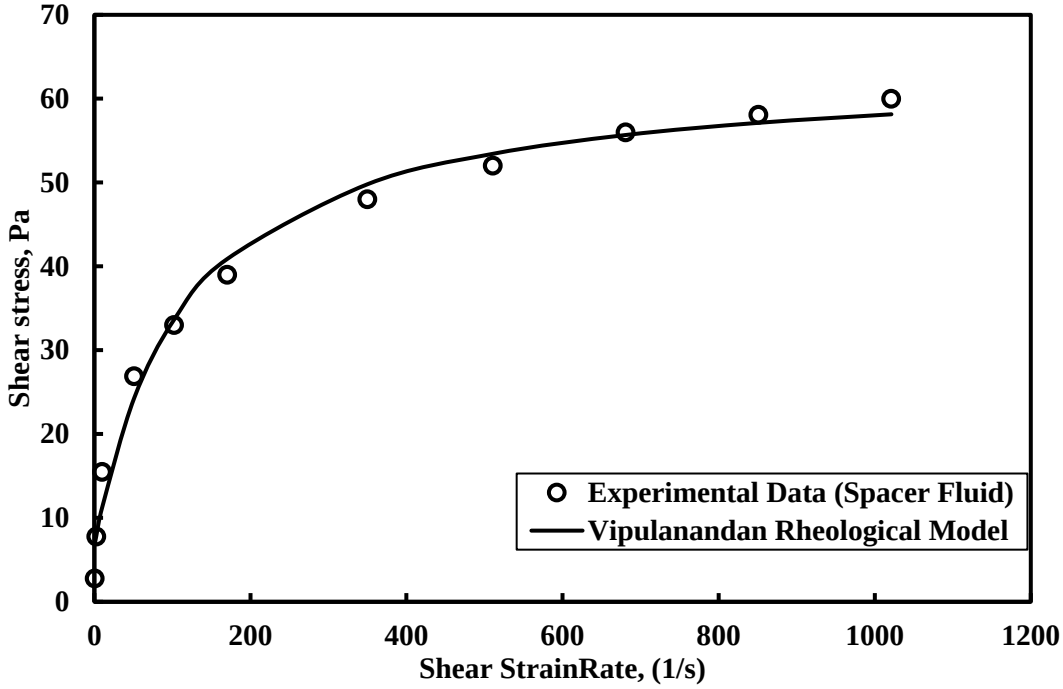


**Figure 7-13:Shear stress – shear strain rate relationship using Vipulanandan rheological model for spacer fluid.**

**Shear Stress – Shear Strain Rate**

The shear stress to shear strain rate relationship for spacer fluid using Vipulanandan rheological model showed nonlinear behavior as shown in Figure 7-13.The yield stress is equal to 6.63 Pa, model constants A and B equal to 2 and 0.0175. The coefficient of determination ($R^2$) was 0.99 and the RMSE (Root Mean Square Error) value was 2.13 Pa. The Vipulanandan model showed better correlation compared Bingham Plastic model.

**Velocity Profile**

The spacing of the annulus varied from radius (a) = 0.122 m (casing annulus interface) to radius (b) = 0.1785 m (annulus formation interface) with radius (r) = 0 m representing center of the casing. The velocity profile of the spacer fluid varied from 0 m/sec at the interfaces (radius (r) = 0.122 & 0.1785 m) to maximum of 0.57 m/sec (102 ft/min) at a radius (r) equal to 0.1512 m (Close

to the center) as shown in Figure 7-14. The velocity profile showed nonlinear variation with the radius.

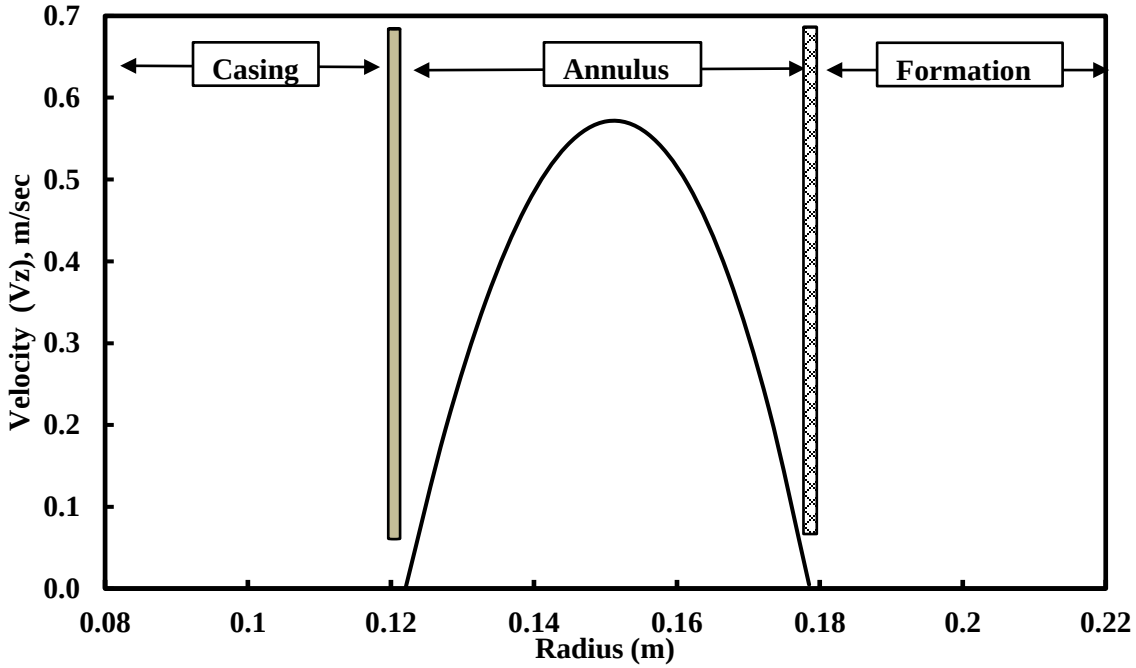


**Figure 7-14:Velocity profile along the radius for Vipulanandan rheological model fluid flow.**

**Shear Strain Rate – Radius**

The shear strain rate varied from 0 $s^{-1}$ to 21.5 $s^{-1}$ (13 rpm) in the annulus using Vipulanandan rheological model. The shear strain rate varied nonlinearly across the radius with zero shear strain rate close to the center at radius = 0.1512 m for Vipulanandan rheological model (Figure 7-15). The shear strain rate was maximum at the interfaces and minimum close to center inside annulus.

**Shear Stress - Radius**

The shear stress varied from 6.6 Pa to 15.7 Pa in the annulus using Vipulanandan rheological constitutive model. The shear stress varied nonlinearly across the radius with shear stress equal to yield stress, 6.6 Pa of the spacer fluid close to the center at radius = 0.1512 m for Vipulanandan rheological model (Figure 7-16). The shear stress was maximum at the interfaces and minimum close to center for spacer fluid flow inside annulus.

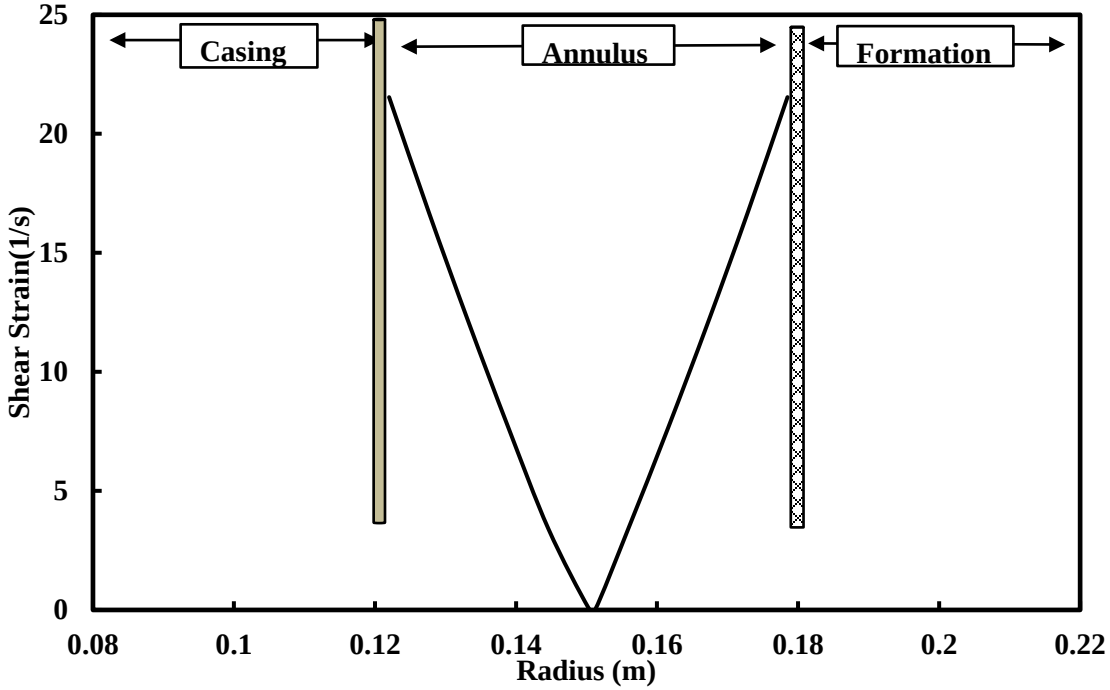


**Figure 7-15:Strain rate along the radius for Vipulanandan rheological model fluid flow.**

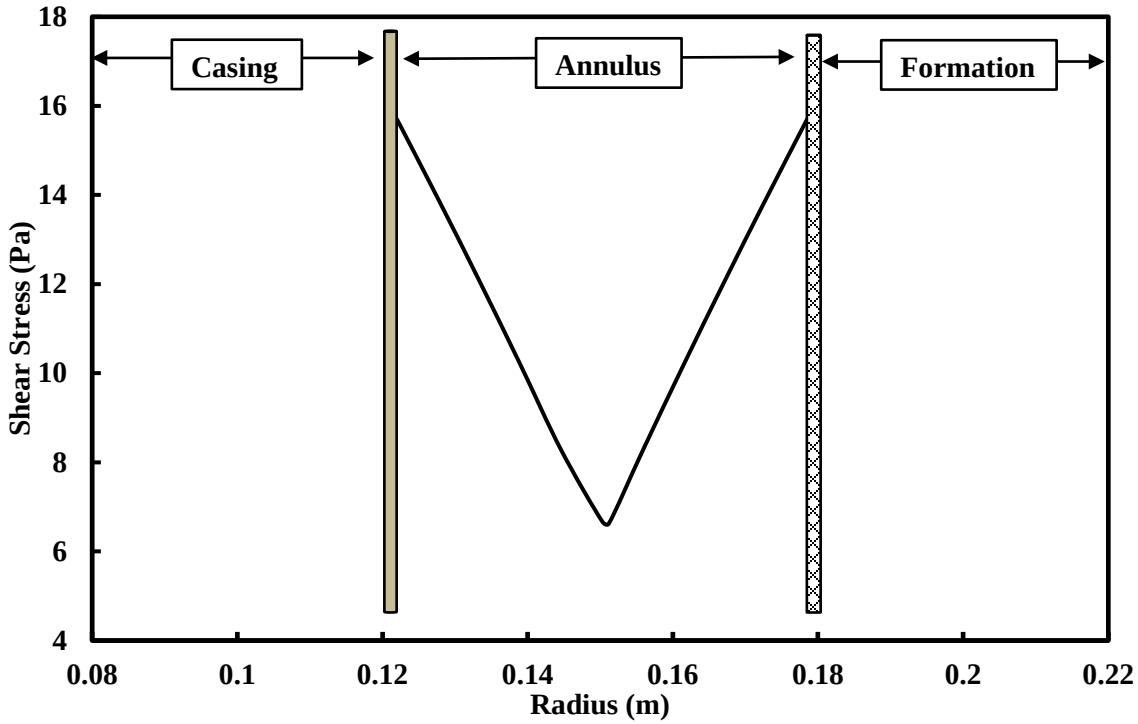


**Figure 7-16:Shear stress along the radius for Vipulanandan rheological model fluid flow.**

**Viscosity**

The viscosity of spacer fluid varied from at 360 cP to 600 cP. using Vipulanandan rheological model in the annulus (Figure 7-17 & Figure 7-18).

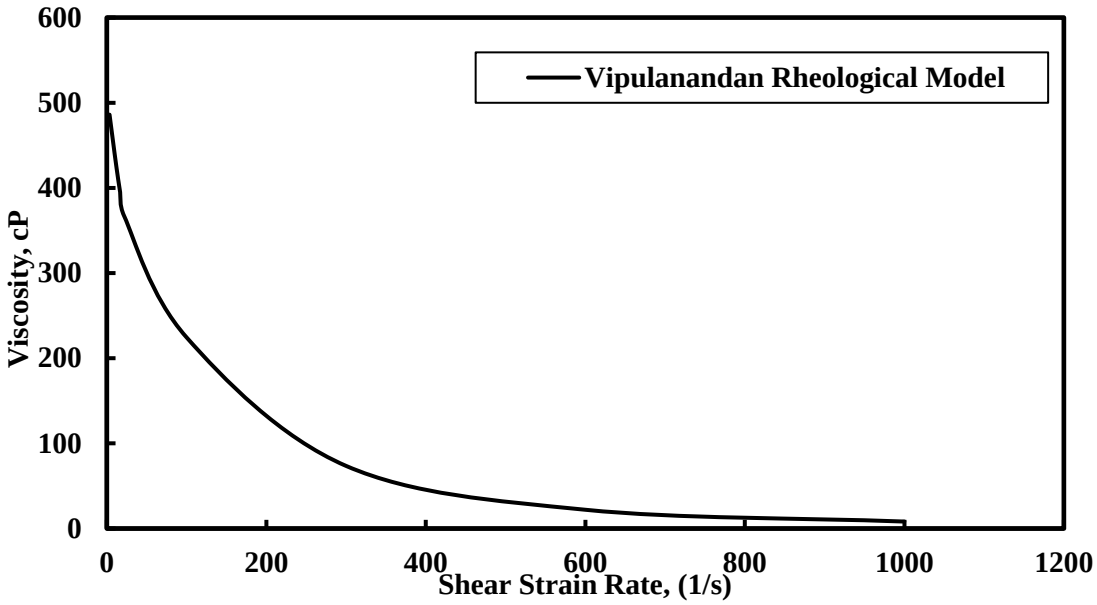


**Figure 7-17:Viscosity of spacer fluid using Vipulanandan rheological model.**

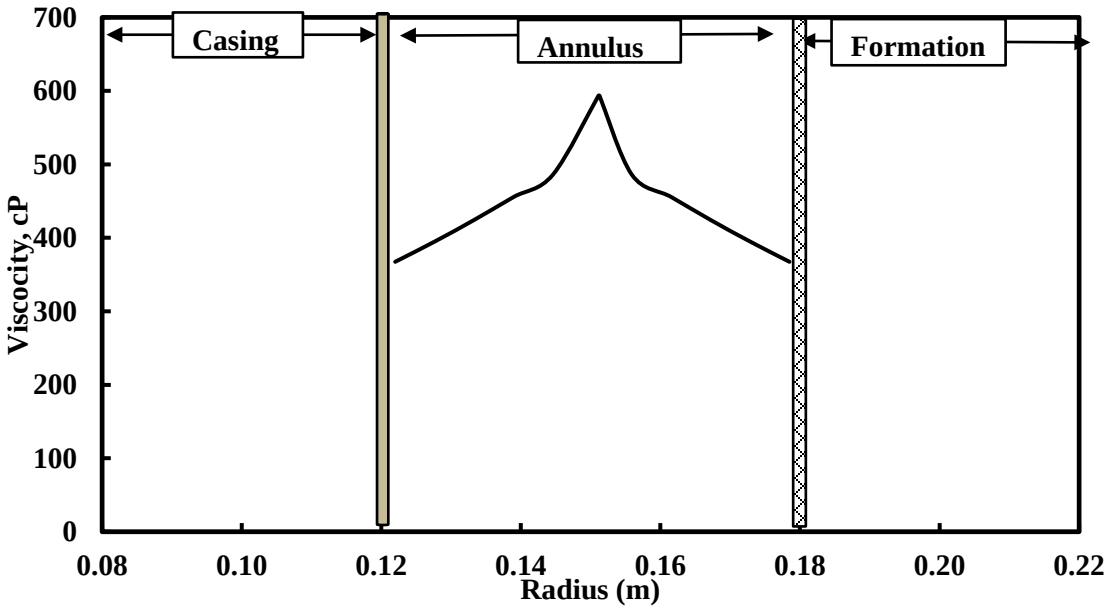


**Figure 7-18: Viscosity profile of spacer fluid in the annulus using Vipulanandan model.**

### 7.1.4 Comparison between Constitutive Models

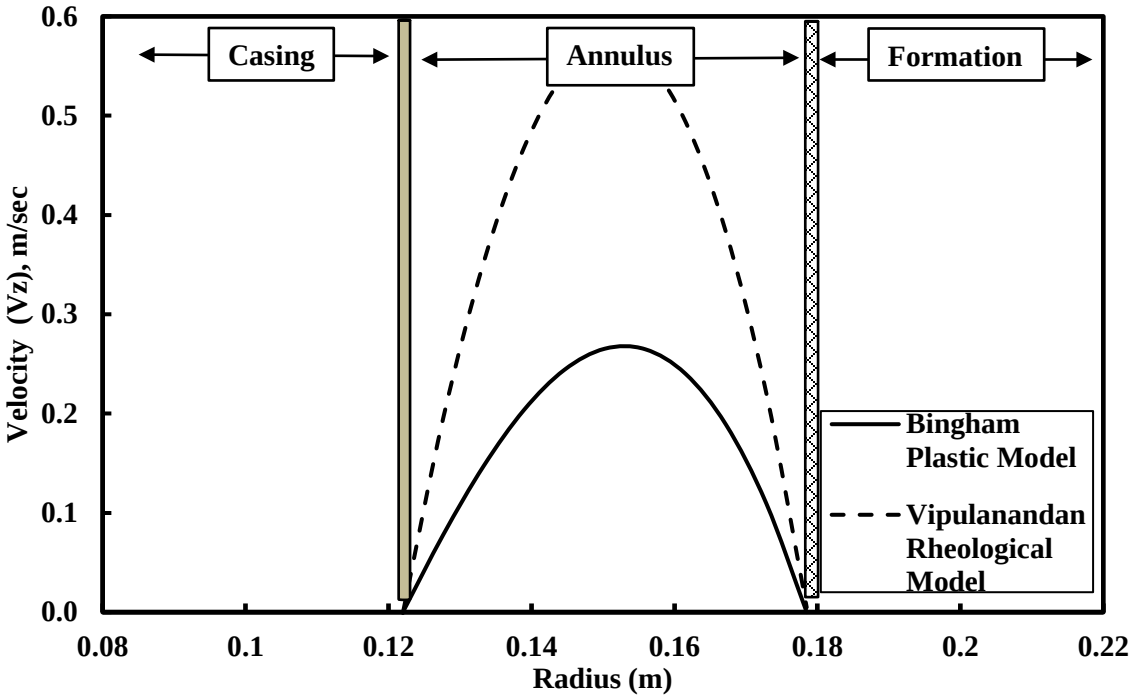


**Figure 7-19:Velocity profile along the radius for Bingham Plastic and Vipulanandan model.**

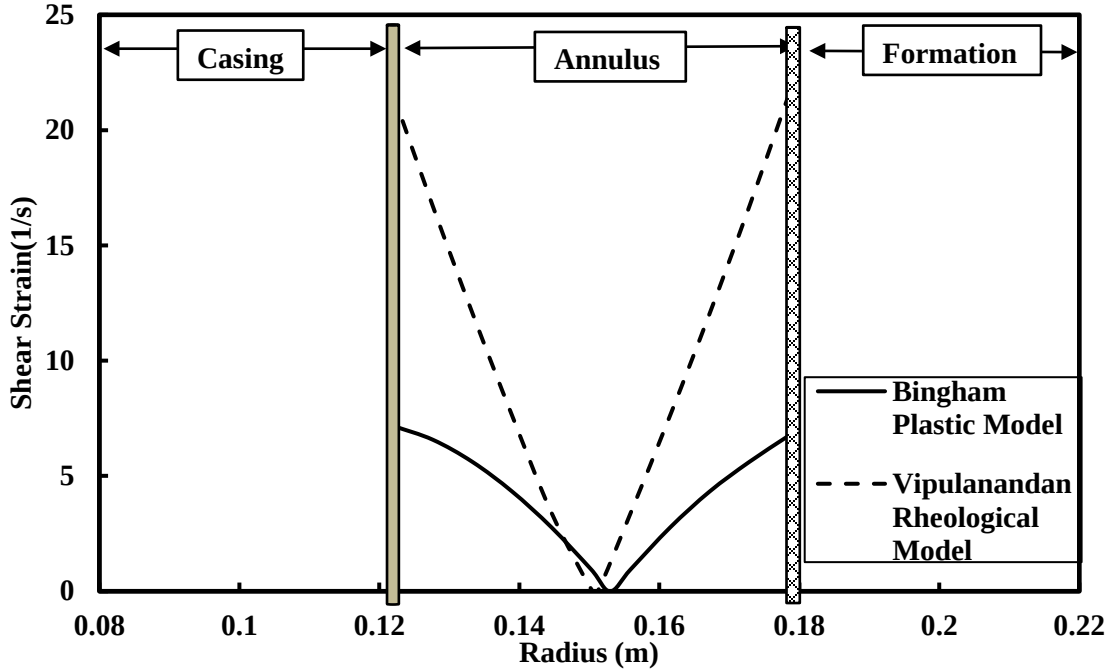


**Figure 7-20: Shear Strain rate profile along the radius for Bingham Plastic and Vipulanandan model.**

**Velocity profile**

The spacing of the annulus varied from radius (a) = 0.122 m (casing annulus interface) to radius (b) = 0.1785 m (annulus formation interface) with radius (r) = 0 m representing casing center. The velocity profile of the spacer fluid varied from 0 m/sec at the interfaces (radius (r) = 0.122 & 0.1785 m) to maximum of 0.268 m/sec (48.2 ft/min) at a radius (r) equal to 0.15296 m (Close to the center) for Bingham Plastic Model as shown in Figure 7-19. The velocity profile of the spacer fluid varied from 0 m/sec at the interfaces (radius (r) = 0.122 & 0.1785 m) to maximum of 0.57 m/sec (102 ft/min) at a radius (r) equal to 0.1512 m (Close to the center) for Vipulanandan rheological model as shown in Figure 7-19. The velocity in the annulus space comparison showed that Vipulanandan model is about 112.6 % greater than that predicted by Bingham plastic model.

**Shear Strain**

The shear strain rate varied from 0 $s^{-1}$ to 7.17 $s^{-1}$ (4.2 rpm) in the annulus using Bingham Plastic constitutive model. The shear strain rate varied from 0 $s^{-1}$ to 21.5 $s^{-1}$ (13 rpm) in the annulus using Vipulanandan rheological model. The shear strain rate for Vipulanandan model prediction was 199% greater than Bingham Plastic model (Figure 7-20).

**Shear Stress**

The shear stress varied from 48.5 Pa to 51.05 Pa in the annulus using Bingham Plastic constitutive model. The shear stress varied from 6.6 Pa to 15.7 Pa in the annulus using Vipulanandan rheological constitutive model. The shear stress for Vipulanandan model prediction was 77% lower than Bingham Plastic model (Figure 7-21). The Bingham Plastic model over predicted the shear stress in the annulus, thus leading to lower velocities.

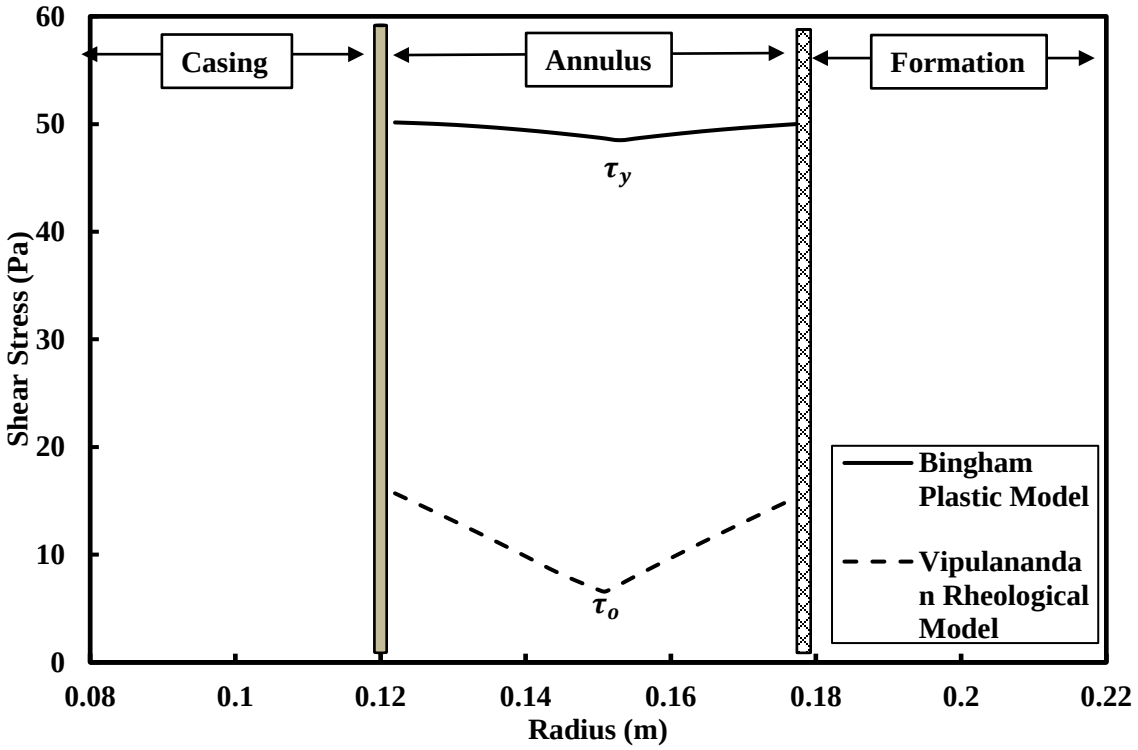


**Figure 7-21:Shear stress profile along the radius for Bingham Plastic and Vipulanandan model.**

**Spacer Fluid Discharge**

The volumetric discharge was calculated by integrating the velocity curve and multiplying with the area of the annulus. For Bingham Plastic model, the volumetric discharge was 0.0046 $m^3$/ sec (2.335 bbl./min) while for Vipulanandan model, the volumetric discharge was 0.001 $m^3$/sec (5.07 bbl./min). This demonstrated that the amount of volumetric discharge is underpredicted by Bingham Plastic model by 117% when compared to Vipulanandan model. This shows that use of efficient rheological models can help improve the efficiency of the drilling operations.

## 7.2 Smart Cement Modeling

In this section, finite element modeling of smart cemented well with and without internal pressures is compared to experimental piezoresistivity and stress values.

### 7.2.1 Problem Identification

Casing cement formation system in the field model was replicated in ANSYS for finite element modeling and comparison of stresses inside the cement layer with experimental values. The following were the properties of casing, cement and formation inputs in the ANSYS program obtained experimental results.

**Cement Properties**

Brittle cement system with compressive strength of 3,500 psi, tensile strength of 400 psi, a Young's modulus of 2.4 x $10^6$ psi and a Poisson's ratio of 0.15;

**Casing Properties**

Casing Young's modulus, Es, and Poisson's ratio: 2.9 x 107 psi and 0.3.

Casing outer diameter, *b*: 9.625 in

Casing wall thickness, *ts*: 0.545 in

Casing inner diameter, *a*: 8.535 in

Cement wall thickness: 2.125 in

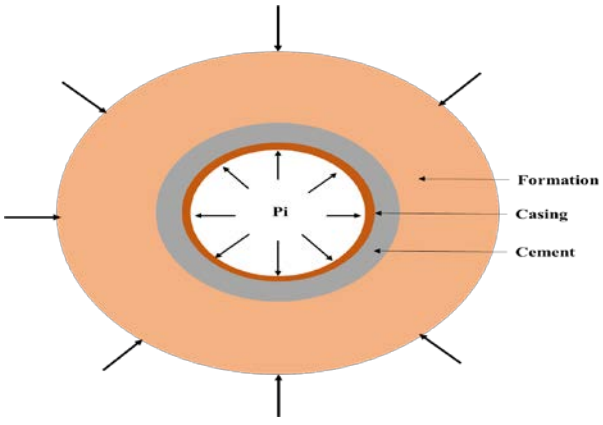


**Figure 7-22:Casing - Cement - Formation System.**

**Formation Properties**

Formation outer diameter, $d$: 20 in

Formation Young's modulus, $E_f$, and Poisson ratio, $v_f$: 3 x 106 psi and 0.42

Density of cement mix: 16.2 lb/gal

The finite element analysis was done with ANSYS workbench 11.0 and casing–cement–formation was used for the 2D modeling with plain strain condition. The casing–cement–formation model was also assumed fully bonded with no separation at the boundaries. The casing – cement – formation system is shown in the Figure 7-22.

**Well Pressures**

Internal well pressure (Pi): 80 psi,

Formation pressure (Po): -2.9 psi.

The formation pressure was calculated by using vertical effective stress in the top level 8-9, which is 5 ft below the ground surface. The effective vertical stress 5 ft below the surface was 4 psi. Using coefficient of earth pressure ($k_o$) of 0.724, the horizontal effective stress on the cement layer was 2.9 psi at 5 ft below the ground surface.

### 7.2.2 Casing – Cement – Formation System Mesh

The casing – cement – formation system developed using ANSYS modeler was meshed using quadrilateral elements. A total of 8071 nodes and 7501 elements were present in the meshed system model (Figure 7-23). The outer surface of the formation was assumed to a fixed surface and formation pressure of 2.9 psi was applied from outward to inward on the outer surface. An internal pressure of 80 psi was applied to replicate the field-testing condition.

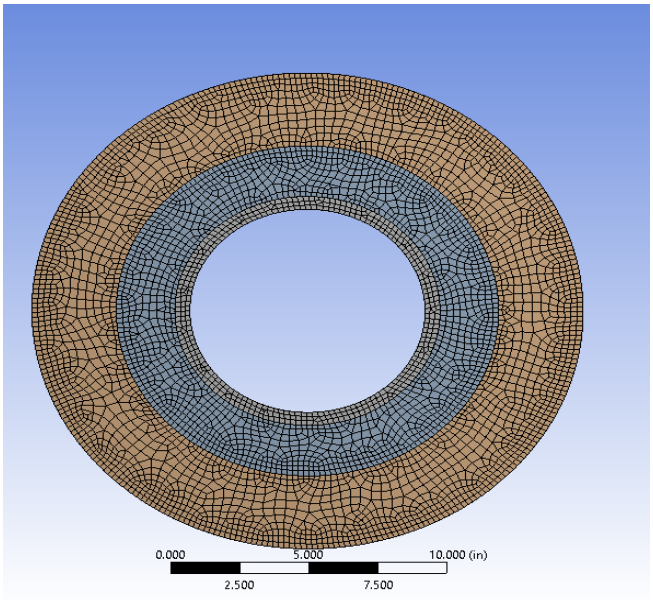


**Figure 7-23:Casing - Cement - Formation system mesh model.**

### 7.2.3 FEM Analysis Results

**Total Deformation**

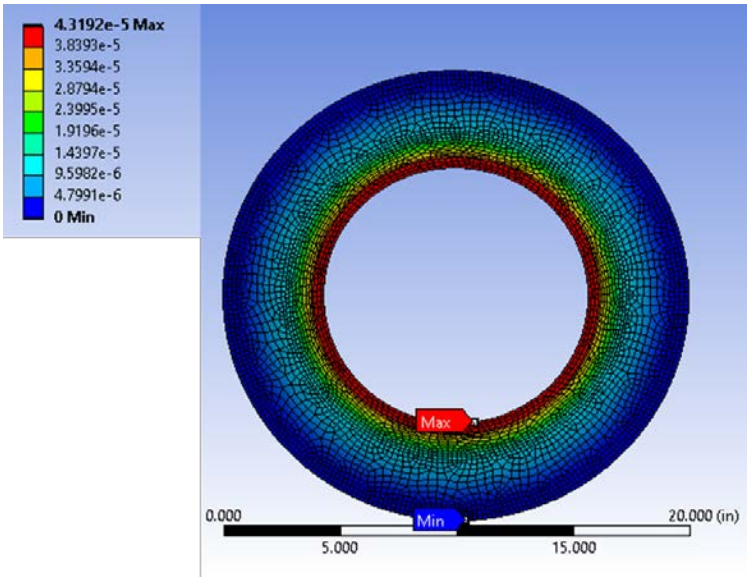


**Figure 7-24:Casing - Cement - Formation system total deformation in the FEM Model.**

The total deformation in the casing – cement – formation system varied from 0 to 4.31 x E-05 inch. The maximum deformation occurred in the casing while minimum deformation occurred in the formation (Figure 7-24).

**Equivalent Elastic Strain**

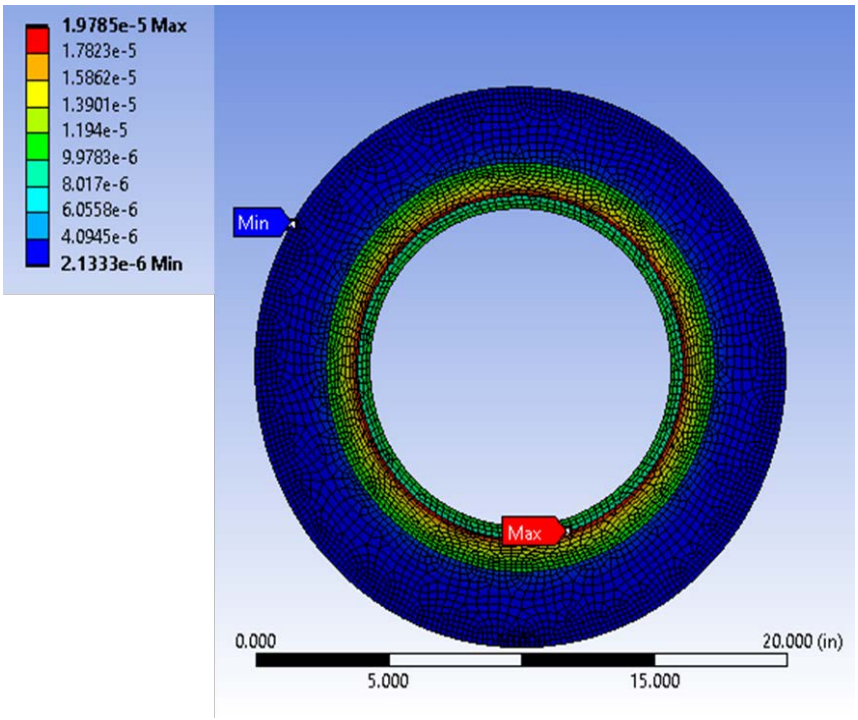


**Figure 7-25:Casing - Cement - Formation system equivalent elastic strain in the FEM Model.**

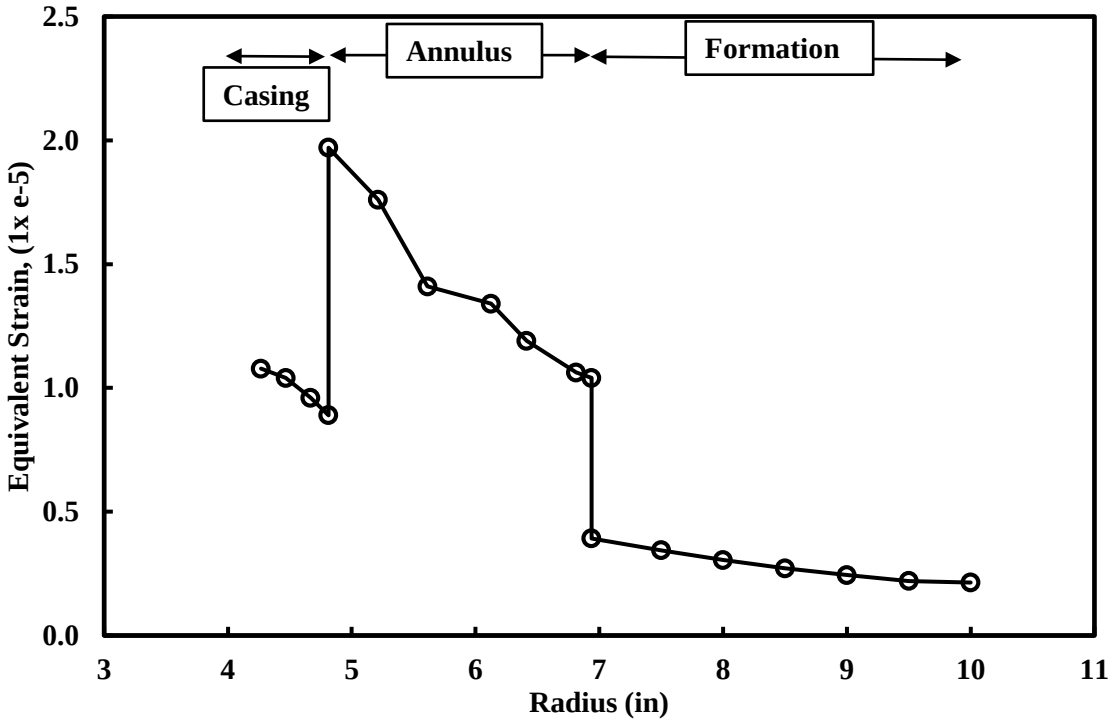


**Figure 7-26:Equivalent Elastic Strain variation across the radius.**

The equivalent elastic strain varied from 2.133 x E-6 to 1.97 x E-05. The value of minimum strain occurred in the formation due to lower stresses in the formation. The value of equivalent strains in the soil varied from 2.133 x E-06 to 3.9 x E-06. The equivalent elastic strains were maximum in the cement sheath layer varying from 1.04 x E-05 to 1.97 x E-05. The value of elastic stains in the casing ranged from 1.08 x E-05 to 8.9 x E-06.

The equivalent stress varied from 6.4 to 320.74 psi. The value of equivalent stress in casing varied from 258 to 320.74 psi. The maximum value of equivalent stress was in the casing. The equivalent stress inside the cement from 24.9 psi to 47.3 psi. The value of stress transfer decreased from casing to cement at the interface. The equivalent stress inside the formation varied from 5.95 psi to 6.02 psi.

**Equivalent (Von Mises) Stress**

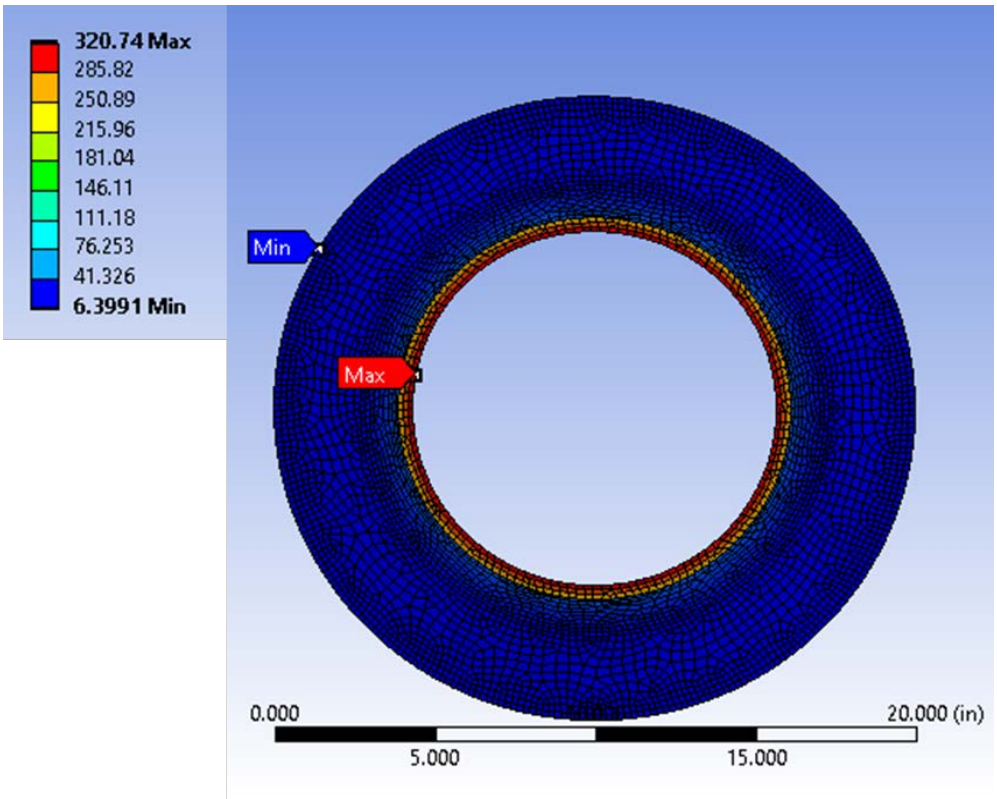


**Figure 7-27:Casing - Cement - Formation system equivalent stresses in the FEM Model.**

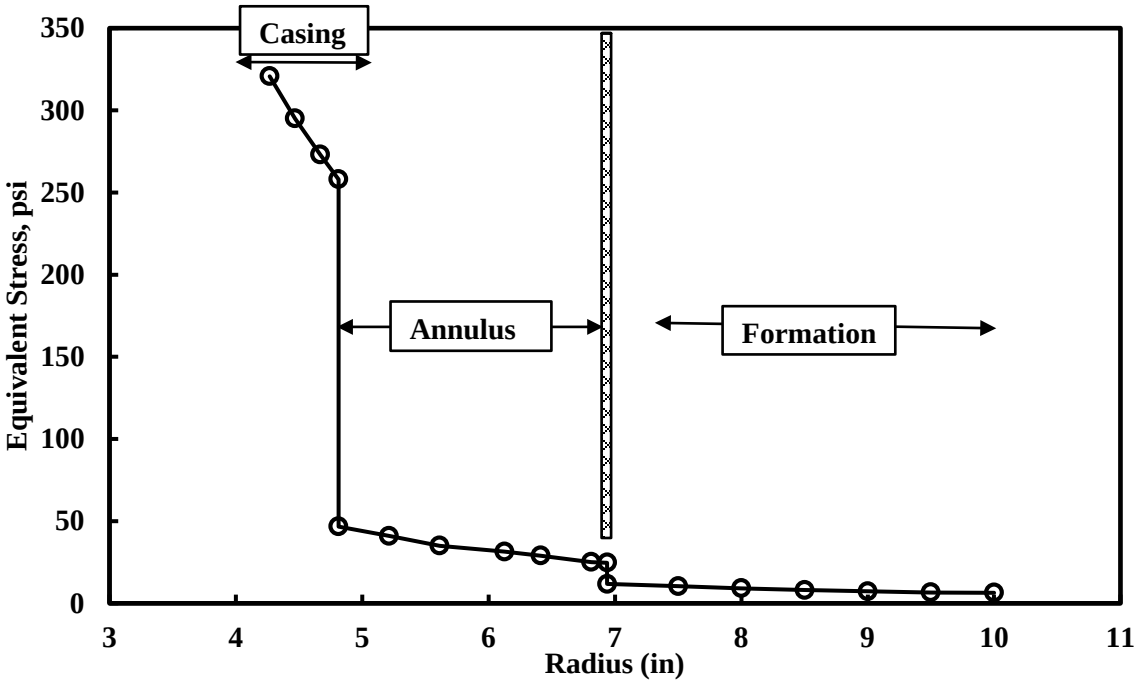


**Figure 7-28:Equivalent stress variation across the radius.**

**Shear Stress**

The value of shear stresses varied from -182.07 to 182.07 psi with maximum in the casing and minimum in the formation.

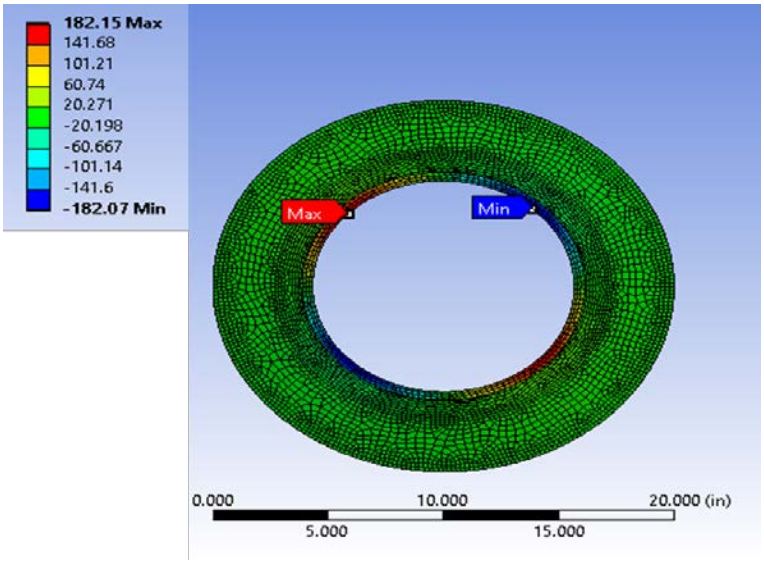


**Figure 7-29:Casing - Cement - Formation system shear stresses in the FEM Model.**

### 7.2.4 Experimental and FEM Analysis Comparison

Smart cement samples taken from the field while cementing various levels were tested for piezoresistivity after 45 days. The piezoresistive strain for smart cement sample taken for top level was 165% at a peak compressive stress of 2100 psi. Based on this, the smart cement in the field at top level showed piezoresistive strain of 0.08%/psi of stress. The value of piezoresistive strain observed with application of 80 psi stress at top level (8-9) in field model pressure test was 3.15%. Based on the piezoresistive value in the field and lab piezoresistive strain to stress ratio, the stress inside the cement can be calculated to be 39 psi. The value of equivalent stress in the cement varied from 25 to 47 psi, with an average of 36 psi. This showed that the finite element prediction was very close to the experimental prediction with a convergence of 92%.

## 7.3 Summary

In this study, analytical fluid flow modeling of smart spacer fluid was performed to analyze the velocity profiles, shear stresses and shear strain rates using Bingham Plastic model and Vipulanandan rheological model. This study also includes finite element analysis of smart cement well to verify experimental pressure tests on field model predictions.

- The velocity in the annulus space comparison showed that Vipulanandan model is about 87% lower than that predicted by Bingham plastic model.
- The shear strain prediction using Vipulanandan model was 85.5% lower than Bingham Plastic model prediction in the annulus space for smart spacer fluid.
- The shear stress prediction using the Vipulanandan model was 42% lower than Bingham Plastic model showing lower resistance in the annular space.
- The equivalent stress varied from 6.4 to 320.74 psi in the finite element casing cement formation system. The maximum value of equivalent stress was on the inner interface of the casing and minimum value was in the formation.
- The Elastic strain was maximum inside the cement sheath followed by casing and the formation respectively in the finite element model.
- The finite element prediction of equivalent stress inside the cement was very close to the experimental prediction with a convergence of 92%.

# CHAPTER 8 CONCLUSIONS AND RECOMMENDATIONS

This study focused on sensing, characterizing, testing and modelling of fluids and solid cementitious materials for multiple applications. The investigation of the behavior of oil well spacer fluid modified with nano$Fe_2O_3$ for in – situ sensing, property modifications and to investigate the effect of magnetic field and temperature on the sensing property has been studied for oil well cementing applications. This study also involves laboratory and field model wells installation and cementing using the smart cement with enhanced piezoresistive properties. The laboratory and field model wells were designed, built and used to demonstrate the concept of real time monitoring of the flow of drilling mud, smart cement and hardening of the cement paste in place for a period of over five years. In this study, orthopedic cast material was modified by conductive fillers to make it sensitive and investigate the efect of temperature, stresses and setting times for applications in the medical industry.

The analytical fluid flow modeling of smart spacer fluid was also performed to analyze the velocity profiles, shear stresses and shear strain rates using Bingham Plastic model and Vipulanandan rheological model. This study also includes finite element analysis of smart cement well to verify experimental pressure tests on field model predictions.

## 8.1 Conclusions

Based on this study the following conclusions are advanced:

1. The electrical resistivity of the spacer fluid decreased with increasing temperature and it was a good sensing parameter for real-time monitoring to predict the rheological properties of spacer fluid in the field.
2. The addition of nanoFe2O3 up to 1% modified the yield stress, shear thinning behavior, and ultimate shear stress limit of the spacer fluid. The amounts of changes in the properties were influenced by the temperature, nanoFe2O3 content, and magnetic field strength in the spacer fluid and have been quantified using a nonlinear model.

3. The most appropriate equivalent circuit for characterizing smart cement was identified as Case 2. It was proved that smart cement can be represented as a pure resistor and the embedded wire (contact) used for measurement and its interface with cement can be represented by a parallel combination of resistor and capacitor.
4. The smart cement used to cement the field well was very sensitive to the applied pressure, piezoresistive cement. The piezoresistivity per unit stress was 0.178%/psi for lab model and 0.17%/psi for field model.
5. Successful demonstration of smart cement application in oil well has been performed by investigation of long-term testing in both lab and field environments.
6. Orthopedic Cast material had very good sensing properties with the addition of conductive filler of 0.05%. Using this sensitivity, orthopedic cast material can be monitored during and after the process of casting, until it gains complete strength.
7. Addition of 0.05% conductive filler further increased the piezoresistive strain of orthopedic cast material to 345% at a peak compressive stress of 6.28 MPa, showing piezoresistivity per unit stress was 54.9 %/MPa after 28 days of curing.
8. With addition of 0.05% conductive filler, the piezoresistive strain for orthopedic cast material was 16.52% at a peak bending stress of 1.33 MPa after 28 days of curing for thick plate samples. Hence, the piezoresistivity per unit stress in bending was 12.42 %/MPa in the thick plate samples after 28 days of curing.
9. Smart Orthopedic cast material sensitivity was demonstrated for various mechanical stresses, temperature effects and water seepage effects.
10. Analytical fluid flow modeling of smart spacer fluid to analyze the velocity profiles, shear stresses and shear strain rates using Bingham Plastic model and Vipulanandan rheological model showed that Bingham Plastic model underpredicted the velocity profile inside the annulus.

11. Finite element analysis of smart cement well to verify experimental pressure tests on field model predictions showed very good convergence of 92%.

## 8.2 Recommendations

Based on the findings in this study, the following suggestions are offered with reference to future research:

1. In this study, a new insitu method for characterizing smart spacer fluid is presented apart from regular laboratory tests. The electrical resistivity was found to be the sensitive property for monitoring the behavior of smart spacer fluid and hence can be used for future applications in the oil well industry.
2. Instrumentation feasible to monitor the changes in the electrical resistance during the installation and after cementing of the well was developed in lab. Development of new instrumentation applicable for different fields can prove the effectiveness of electrical characterization.
3. Highly sensing orthopedic cast material was developed by addition of conductive fillers and a real time monitoring technique has been demonstrated. This method of monitoring has capable functionality to be used in medical industry for real time monitoring of orthopedic treatments with further enhancement.
4. In the present study piezoresistive behavior was characterized with the change in resistivity along the stress axis only. It is suggested that the material should also be characterized with change in resistivity perpendicular to the stress axis to get more understanding of its behavior as 3D sensor.
5. New analytical modeling of fluid flow inside well bore has been presented. This method optimizes the drilling performance by providing highly accurate velocity profiles. Comparison of this new rheological model prediction should also be compared with other models currently being used in the industry.

6. Integration of real time monitoring capability and finite element prediction enhances the accuracy and extent of smart cement application for prediction of internal stresses and in situ conditions of the cement sheath. Further advancement in the data acquisition system can enable smart cement to be used commercially.

# REFERENCES


Ahmad, R., Ha, J.H. and Song, I.H. (2015). “Fabrication of Self-Setting Aluminium Trioxide Foams for Potential Fire Retarding Applications.” *Material Letters*.

Ahmadi, A., Sakib, T., Ghaderi, A. and Beirami, A. (2013). “The Performance of Foam Cement in Iran Oil Wells and Comparison of the Bentonite Light Cement with Foam Cement.” *Australian Journal of Basic and Applied Sciences.*

Ahmed, R. M., Takach, N. E., Khan, U. M. and Godoy, R., (2009). “Rheology of Foam Cement.” *Cement and Concrete Research.*

Akthar, F. K. and Evans, J. R. G. (2010). “High Porosity Cementitious Foams.” *Cement and Concrete Research.*

Alan, R., Coventry, K., Edmondson, V. and Dias, E. (2015). “Crumb Rubber used in Concrete to Provide Freeze Thaw Resistance.” *Journal of Cleaner Production.*

Aldrich, C. A. and Mitchell, B. J. “Strength, Permeability and Porosity of Oilwell Foamed Cement.” *Journal of Engineering for Industry.*

Alex, George. “ Application of Foamed Cement and the Stringent Quality Control Techniques Basic to use this New Oil Field System.” *Indonesian Petroleum Association*.

Alonge, O. R. and Ramli, M. (2013). “Experimental Production of Sustainable Light Weight Foamed Concrete.” *British Journal of Applied Science.*

Al-Sarraf, A. and Hazel, R. A., “The Drilling Optimization Performance in Kuwait's High-Pressured Wells,” SPE/IADC paper 39270, presented at the SPE/IADC Middle East Drilling Technology Conference, Manama, Nov. 23-25, 1997.

API Recommended Practice 10B (1997). “Recommended practice for testing well cements.” Exploration and Production Department, 22nd Edition.

API recommended Practice 65 (2002). “Cementing shallow water flow zones in Deepwater wells.”

ASTM Standard - C267 . “Standard Test Method for Chemical Resistance of Mortars Grouts Monolithic Surfacings, Polymer Concretes.”

Atahan, H. N., Carlos, C. and Chae, S. (2008). “Morphology of Entrained Air Voids in Hardened Cement Paste Generated with Different Anionic Surfactants.” *Cement and Concrete Composites*.

Azhari, F. and Banthia, N. (2012). “Cement-based sensors with carbon fibers and carbon nanotubes for piezoresistive sensing, cement and concrete composites.” Vol. 34, pp. 866–873.

Bozich, M. P., Montman, R. C and Harms,W. M. “Application of Foamed Portland Cement to Deep Well Conditions in West Texas.” *SPE Deep Drilling and Production Symposium*.

Browner, B. D., Jupiter, J. B., Levine, A. M., Trafton, P. G., Krettek, C. and Green, N. E. (2008). “The history of fracture treatment.” Skeletal Trauma. pp. 1–32.

Bundar, B. (2015). “Ferron Bio mineralized Cement Based Materials: Impact of Inoculating Bacteria on Hydration and Strength.” *Cement and Concrete Research*.

Carney, L. (1974). “Cement Spacer Fluid.” Journal of Petroleum technology, Society of Petroleum Engineers, Vol. 26, pp 856-859.

Caroma, F., Canet, R. and Delhaes, P. (1987) “Piezoresistivity of Heterogeneous Solids,” *Journal of Applied Physics*, Vol.61, No.7, pp. 2550-2557.

Chung, D. D. L (1995), "Strain Sensors Based on Electrical Resistance Change,” Smart Materials Structures, No. 4, pp. 59-61.

Chung, D. D. L (2001), “Functional Properties of cement-Matrix Composites,” Journal of Material Science, Vol. 36, pp. 1315-1324.

Chung, D. D. L. (2001). “Functional properties of cement-matrix composites.” Journal of Material Science, Vol. 36, pp. 1315-1324.

Clarke, K. C. (1986). “Advances in geographic information systems, computers, environment and urban systems,” Vol. 10, pp. 175–184.

Cobb, S., Maki, V. and Sabins, F. (2002). “Method Predicts Foamed Cement Compressive Strength Under Temperature and Pressure.” *Oil and Gas Journal*.

Cristou, M. and Konstantinidou, M. “Safety of offshore oil and gas operations: Lessons from past accident analysis.” Joint Research Centre of the European Commission, 2012.

Daniel, Cesar, Jorge (2015). “Compressive Strength Study of Cement Mortars Lightened with Foamed HDPE Nanocomposites.”

Daniel, E. R. A., Nadia, B., Rosa, C. S. and Ortiz, J. (2015). “Compressive Strength Study of Cement Mortars Lightened with Foamed HDPE Composites.” *Materials and Design*.

Darbe, R., Gordon, C. and Morgan, R. (2008). “Slurry Design Considerations for Mechanically Enhanced Cement Systems.” *AADE.*

Demiral, B. (2015). “Effect of Metakaolin on Corrosion Resistance.” Construction and Building Materials.

Dinesh, K., Irawan, S. and Ridha, S. (2018). “The suitability of fly ash based geopolymer cement for oil well cementing applications: A review.” ARPN Journal of Engineering and Applied Sciences, Vol. 13. No. 20, pp 8296 – 8315.

Dooply, M. and DeBruin, G. (2014). “Evaluating Foamed Cement Slurry Stability in Laboratory Measurement.” *AADE Fluids Technical Conference and Exhibition.*

Dunn, C. and Hess, T. (2018). “The United States is now the largest global crude oil producer.” Today in Energy, U.S. Energy Information Administration.

Dusterhoft, D. M. (2003). “A Comparison between Foamed and Light Weight Cement.” *Petroleum Society’s Canadian International Petroleum Conference*.

Dzigita. (2014). “Cement Freezing Thawing Resistance of Hardened Cement Paste.” *Construction and Building Materials.*

Fan, Y., Zhang, S. and Wang, Q. (2015). “Effect of Nano Kaolinite Clay on the Freeze Thaw Resistance of Concrete.” *Cement and Concrete Composites*.

Fang, Y. and Shah, S. (2015). “Effects of Nano Kaolinite Clay on the Freeze Thaw Resistance of Concrete.” *Cement and Concrete Composites*.

Farouk, S. (2014). “An Overview of Integrated Remote Sensing and GIS for Ground Water Mapping in Egypt.”

Foote, K. E. and Lynch, M. “Geographic Information Systems as an Integrating Technology: Context, Concepts, and Definitions.” *The Geographer's Craft Project, Department of Geography, The University of Colorado at Boulder*. 2015.

Franklin, D. S. and Christopher, M. (2013). “Skin Temperatures Generated Following Plaster Splint Application.” Orthopedics Journal, Vol. 34, pp. 364-367.

Fuller, G., Souza, P., Ferreira, L. and Rouat, D. (2002). “High-Strength Lightweight Blend Improves Deepwater Cementing,” Oil & Gas Journal, Vol. 100, No.8, pp. 86-95.

Gaddy, D. E. (1998). “KOC increases rig fleet, prepares for future.” *Oil and Gas Journal.*

Gadea, J., Rodriquez, A. and Campus, P. L. (2010). “Light Weight Mortar Made with Recycled Polyurethane Foam.” *Cement and Concrete Composites.*

Gauckler, L. J. and Gonzenbach. (2012). “Tailoring the Hierarchical Pore Structures in Self Setting Particle Stabilized Foams made from Calcium Aluminate Cement.” *Material letters*.

Goodchild, M. F, (2010). “Twenty years of progress: GIScience in 2010.” *Journal of Spatial Information Science.*

Greeener, J. (2006). “Foamed Cement Successfully Applied in Shallow Water Environment in Caspian Sea.” *Article*.

Griffith, J. and Faul, R. (1997). “Mud Management Special Slurries Improve Deepwater Cementing Operations,” Oil and Gas Journal, Vol. 95, No. 42, pp. 49-51.

Guillot, D. (1990). “Rheology of well cement slurries.” In: E.B. Nelson and Guillot, D. (Eds.), Well Cementing, Schlumberger, Texas, pp. 93-142.

Harms, W. M, Febus, J. S. (1985). “Cementing of Fragile Formations Wells with Foamed Cement Slurries.” *Society of Petroleum Engineers*.

Harness, P. E. and Sabins, F. L. (1992). “New Technique Provides Better Low-Density Cement Evaluation.” *Society of Petroleum Engineers.*

Hasan, N. (2013). “Low Frequency Soundproof Cement based Syntactic Foam.” *International Journal of Materials*.

Heng, K. and Loon. (2006). “Compressive Strength and Shrinkage of Foamed Concrete Containing Pulverized Fly Ash.” *CONCET.*

Hengst, R. R. and Tressler, R. E. “Fracture of Foamed Portland Cement.” Cement *and Concrete Research.*

Hill, A. D. (1990). “Cement-Quality Logging. Production Logging—Theoretical and Interpretative Elements,” Vol. 14, 123-140. Richardson, Texas: Monograph Series, SPE.

Huang, J., Zhang, (2015). “Proportioning and Characterization of Portland Cement Based Ultra-Light Weight Foam Concrete.” *Construction and Building Materials.*

Irawan, S. and Sum, C. W. “Foamed Cement Properties for Zonal Isolation in Coal Bed Methane Wells.” *International Journal of Applied Science and Technology*.

Izon, D., Mayes, M. (2007). “Absence of fatalities in blowouts encouraging in MMS study of OCS incidents 1992-2006.” Well Control, pp. 86-90.

Jalali. “Sulphuric acid resistance of plain polymer modified concrete.” *Construction and Building Materials.*

Jiegiong. (2013). “Antibacterial and Physical Properties of EGCG Containing Glass Ionomer Cements.” *Journal of dentistry*.

Johannes, F. (2015). “Petroleum Engineer's Guide to Oil Field Chemicals and Fluids,” Second Edition, Gulf Professional Publishing.

John, B. (1992). “Class G and H Basic Oil Well Cements,” World Cement.

Jong. (2001). “Mechanical Properties of Cement Foams in Shear.” *Journal of Material Science.*

Katrin, O., Krause, C. and Willers, T. (2014). “Temperature Effect on Foamability, Foam Stability, and Foam Structure of Milk.” *Colloids and Surfaces.*

Kim, J. and Vipulanandan, C. (2003) "Effect of pH, Sulfate and Sodium on the EDTA titration of Calcium," Cement and Concrete Research, Vol. 33(5), pp. 621-627.

Kim, J. and Vipulanandan, C. (2006)"Removal of Lead from Contaminated Water and Clay Soil Using a Biosurfactant," Journal of Environmental Engineering, Vol. 132, No. 7, pp.857-865.

King, G. E. (2012). “Cement Evaluation Methods to Prove Isolation of Barriers in Oil and Gas Wells: Should a Cement Bond Log (CBL) Be Run or Required in Every Well?,” *Apache Corporation.*

Kolawale, Chad, (2010). “Techniques for the Study of Foamed Cement Rheology.” *SPE Conference.*

Kopko, V. M. (2002). “Heat network pipe heat insulation: Study Guide.” Techno print.

Kromer, Kowald, (2015). “Pozzolanic Hardened Three Phase Foams.” *Cement and Concrete Composites.*

Kyle, M. and Eric, O. (2014). “Improved regulatory oversight using real- time data monitoring technologies in the Wake of Mocondo.” SPE 170323, pp. 1-51.

Labibzadeh, M., Zhhabizadeh, B. and Khajehdezfuly, A., (2010) "Early Age Compressive Strength Assessment of Oil Well Class G Cement Due to Borehole Pressure and Temperature Changes, Journal of American Science, Vol. 6, No.7, pp.38-47.

Lesley, N., Eric, k. and Shawn, A. (2014). “Deepwater Gulf of Mexico”. OCS Report, Bureau of Ocean Energy Management.

Lewry, A. J. and Williamson, J. (1994). “The setting of gypsum plaster: Part II – The development of microstructure and strength,” Journal of Material Science, Vol. 29, pp. 5524-5528.

Lhusier, P. (2014). “Structural Properties of Solid Foams.” *Comptes Rendus Physique*.

Li, G and Muthyala, V.D. (2008). “Cement Based Syntactic Foam.” *Material Science and Engineering.*

Liao, Y. and Wei, X. (2014). "Relationship between chemical shrinkage and electrical resistivity for cement pastes at early age.” Journal of Materials in Civil Engineering, Vol. 26, pp. 384–387.

Lijju, W. (2011). “Preparation and Properties of Alkali Activated Foam Cement Reinforced with Polypropylene Fibers.” *Journal of Wuhan University of Technology.*

Loeffler, N. R. (1984). “Foamed Cement; a Second Generation.” *Society of Petroleum Engineers Conference.*

Lu, B., Y. (2013). “Improvement of Al Powder Application Measure Based 0n the Influence of Strength Properties.” *Construction and Building Materials*.

Maliene, V., Grigonis, V., Palevičius, V. and Griffiths, S. (2011). “Geographic information system: Old principles with new capabilities,” *Urban Design International*.

Mamun, M. and Bindiganavile, V. (2011). “Sulphate Resistance of Fibre Reinforced Cement Based Foams.” *Construction and Building Materials.*

Mamun, M. and Bindiganaville, V. (2014). “Specimen Size Effects and Dynamic Fracture Toughness of Cement Based Foams.” *Journal of Materials in Civil Engineering.*

Mamun, M. and Bindiganaville, V. (2014). “Thermo Mechanical Properties of Fibre Reinforced Cement Based Foam Exposed to Sulphate.” *Construction and Building Materials*.

Mangadlao, J., Cao, P. and Advincula, R. (2015).” Smart cements and cement additives for oil and gas operations.” Petroleum Science and Engineering.

Mariott, T. and Griffith, J. (2005). “Foamed Conventional Light Weight Cement Slurry for Ultra Low Density.” *SPE Annual Technical Conference*.

Marriot, T. (2005). “Foamed Conventional Light Weight Cement Slurry for Ultra-Low Density Solves Lost Circulation Problem.” *SPE Annual Conference*.

McCarter, W. J., Starrs, G., and Chrisp, T. M. (2000). “Electrical conductivity, diffusion, and permeability of Portland cement-based mortars.” Journal of Cement and Concrete Research, Vol. 30, pp. 1395–1400.

Mckenna, K., Heerchap, S. and Caran, K. L. (2015). “Foam Stabilized by Tricationic Amphiphilic Surfactants.” *Colloids and surfactants.*

Mebarkia, S. and Vipulanandan, C. (1992). “Compressive behavior of glass-fiber-reinforced polymer concrete.” Journal of Materials in Civil Engineering, Vol. 4, pp. 91–105.

Mehmet, (2014). “Abrasion and Freezing Thawing Resistance of Pervious Concrete Containing Waste Rubbers.” *Construction and Building Materials*.

Mirza, J, Mirza, M. S. and Saleh, K. (2002). “Basic Rheological and mechanical properties of High-Volume Fly Ash Grouts,” Construction and Building Materials, Vol. 16, pp.353-363.

Mohammed, A. and Vipulanandan, C. (2013). “Compressive and tensile behavior of polymer treated sulfate contaminated CL soil.” Journal of Geotechnical and Geological Engineering, Vol. 32, pp. 71-83.

Moore, J. and Benge, G. “Assessment of Foamed Cement Used in Deep Offshore Wells.” *SPE Conference.*

Nagrokiene, (2014). “Cement Freeze Thawing Resistance of Hardened Cement Paste with Synthetic Zeolite.” *Construction and Building Materials*.

Naik, T. R., Kumar, R. and Ramme, B. W. (2010). “Effect of High Carbon Fly Ash on the Electrical Resistivity of Fly Ash Concrete Containing Carbon Fibers.” *Sustainable Construction Materials and Technologies.*

Niggeman, K. and Samuel, A. (2013). “Foamed Cementing Geothermal Intermediate Casing.” *Case Study.*

Pallardy, R. (2010). “Deepwater Horizon oil spill of 2010, Oil Spill, Gulf of Mexico.” *Encyclopedia Britannica*.

Pan, Z., Li, H. and Liu, W. “Preparation and Characterization of Super Foamed Low-Density Cement.” *Construction and Building Materials.*

Park, J, Vipulanandan, C., Kim, J. and Oh, M. H. (2006) “Effect of Surfactants and Electrolyte Solutions on the Properties of Soils,” Journal of Environmental Geology, Vol. 49, pp.977-989.

Parmar, A. J., Tyagi, S. K., Dabas, V. S., Mistry, J. N., Jhala, S. K., Suthar, D. N., Bhatt, R. H., Pansuria, R. H. and Bhatti, I. M. (2014). “Assessment of the physical and mechanical properties of plaster of Paris bandage cast used as a splinting and casting materials.” Veterinary World, pp. 1123-1126.

Qin, B. T. and Lu, Y. (2013). “Experimental Research on Inorganic Solidified Foam for Sealing Air Leakage in Coal Mines.” *International Journal of Mining Science and Technology.*

Rae, P. and Dilullo, G. “Light Weight Cement Formulations for Deep Water Cementing.” *SPE Annual Technical Conference and Exhibition held in Houston, Texas*

Ramachandran, V. S. (1984). Concrete Admixture Handbook, Noyes Publication, Park Ridge, New Jersey, 628 pp.

Ramamurthy, K., Nambiar, E. K. and Ranjani, I. “A Classification of Studies on Properties of Foam Concrete.” *Cement and Concrete Composites.*

Ramanan, K. (2015). “Extracting the Benefits of Nanotechnology for the Oil Industry.” Journal of Petroleum technology, Society of Petroleum Engineers, Vol. 5.

Ramazan, D., Polat, R. and Turkmen, I., (2010). “Influence of Light Weight Aggregate on the Physio Mechanical Properties of Concrete.” *Cold Regions Science and Technology* .

Ramlal, P. (2014). “Developing a GIS based Integrated Approach to Flood Management in Trinidad.” *Journal of Environmental Science*.

Ravi, B.R., Mcmenhan. (2007). “Comparative Study of mechanical Properties of Density-reduced Cement Compositions,” SPE Drilling & Completion, Vol. 22, No. 2, pp. 119-126.

Reddy, B.R. and Riley, W.D. (2004). “High temperature viscosifying and fluid loss controlling additives for well cements, well cement compositions and methods.” US Patent 6 770 604, Assigned to Halliburton Energy Services, Inc. (Duncan, OK).

Reid, W. M. (1973), “Active faults in Houston Area,” Texas, University of Texas at Austin, Ph.D. Dissertation.

Rickard, W. M. (1985). “Foam Cement for Geothermal Wells.” *Transactions*

Rizwan, H. (2015). “Fabrication of Self Setting Aluminum Hydroxide Foams for Potential Fire Retarding Applications.” *Materials letters*.

Rourke, T. J. O. (1999). “A Unique Solution to Zonal Isolation Utilizing Foam Cement and Coiled Tubing Technologies.” *SPE Conference*.

Salih, T. and Meyer, C. (2015). “Effects of Internal Curing on the Strength, Shrinkage and Freeze Thaw Resistance of Concrete.” *Construction and Building Materials*.

Salim, P. and Amani, M. “Special Considerations in Cementing HPHT Wells.” *International Journal of Engineering and Applied Science.*

Samsuri, A., Junin, R., Osman, A. M. (2001). The utilization of Malaysian local bentonite as an extender and free water controller in oil-well cement technology, Society of Petroleum Engineers.

Sang, G. “Preparation and Characterization of High Porosity Cement Based Foam Material.” *Construction and Building Materials*

Saxena, A. K. and Ojha, K. (2014). “Optimization of Characteristic Properties Of Foam Based Drilling Fluids.” *Brazilian Journal of Petroleum and Gas*.

Siclen, V. (1967), “The Houston fault problem: American institute of professional geologists, Texas section.”

Sirisawat. (2014). “Durability and Testing of Mortar with Interground Flyash and Limestone Cements in Sulfate Solutions.” *Construction and Building Materials*.

Smith, T. and Dolerey, J. (1984). “Foamed Cement Application in Canada.” *Journal of Canadian Petroleum Technology*.

Spoerker, H.F. and Doschek, M. (2002). “Field Experience with Applying Foamed Cement Slurries in Mature Depleted Formations.” *SPE Conference*.

Stefanie, A. S., Tommie, J. W. and Patterson, M. M. (2011). “Casting All Wrapped Up.” Orthopaedic Nursing Journal, Vol, 30, No. 1, pp 37-41.

Steven, T. D. (2013). “Oil and Gas Cementing.” EPA Technical Workshop on Well Construction /Operation and Subsurface Modeling Research Triangle Park, NC.

Subramaniam, K. V. L. and Yiannis. “Blast Response of Cellular Cement Foams: An Experimental Evaluation.” *ASCE*.

Sugama, T., Brothers, L. E. and Van D. P. T. R. (2005). “Air Foamed Calcium Aluminate Phosphate Cement for Geothermal Wells.” *Cement and Concrete Composites*.

Syed, T. (2017). “Wellbore Integrity of Gas Storage Wells – Current Perspectives.” UIC Conference, Austin, Texas, February 2017.

Szostakowski, B., Smitham, P. and Khan, W. S. (2017). “Plaster of Paris – Short History of Casting and injured limb immobilization.” The Open Orthopaedics Journal, vol. 11, pp. 291-296.

Tan, X. and Wang. (2014). “Experimental Study of Ultralight Foamed Concrete.” *Advances in Materials Science and Engineering.*

Tayun.M, Freeze.R, (2014). “Thaw Resistance, Mechanical and Transport Properties of Self Consolidating Concrete.” *Materials and Design.*

Teresa, O. (2007). “Fracture Properties of Modern Casts: Plaster of Paris versus Fiberglass”.

Thaemlitz, J. and Patel, A. D. (1999). “New environmentally safe high-temperature water-based drilling-fluid system.” SPE Drilling & Completion Vol. 14(3), 185-189.

Tirasat, S. and Chai, J. (2007). “Evaluation of Sulphate Resistance of Concrete Containing Palm Oil Fuel Ash.” *Construction and Building Materials*.

Tonyan, T. D. and Gibson, L. J. (1992). “Structure and Mechanics of Cement Foams.” *Journal of Material Science.*

Tsivillis. (2012). “Sulfate Resistance of Limestone Cement Concrete Exposed to Combined Chloride Attack.” *Cement and Concrete Composites*.

Usluogullari, O. and Vipulanandan, C. (2011). “Stress-strain behavior and California Bearing Ratio of artificially cemented sand.” Journal of Testing and Evaluation, Vol. 39, pp. 1-9.

Vadim, Y. (2013). “Research of Sulfate Resistance of Cement Containing Composition.” *Procedia Engineering*.

Vegas. (2009). “Freeze Thaw Resistance of Blended Cements Containing Calcinated Paper Sludge.” *Construction and Building Materials*.

Verdolotti, L. and Maio, E. D. (2012). “Hydration Induced Reinforcement of Rigid Polyurethane Cement Foams.” *Journal of Material Science.*

Verdolotti, Maio and Lavorgna. (2008). “Polyurethane- Cement Based Foams: Characterization and Potential Uses.” *Journal of Applied Polymer Science*.

Vinghua, Z., Lunan, Y. and Jianhao.Y. (2012). “Experimental Development of Foam Slurry Materials.” *Procedia Engineering.*

Vipulanandan, C. and Garas, V. (2008). “Electrical resistivity, pulse velocity and compressive properties of carbon fiber reinforced cement mortar.” Journal of Materials in Civil Engineering, Vol. 20, pp. 93-101.

Vipulanandan, C. and Mohammed, A. (2014). “Hyperbolic rheological model with shear stress limit for acrylamide polymer modified bentonite drilling muds.” Journal of Petroleum Science and Engineering, Vol. 122, pp. 38‑47.

Vipulanandan, C. and Prashanth, P. (2013). “Impedance spectroscopy characterization of a piezoresistive structural polymer composite bulk sensor.” Journal of Testing and Evaluation, Vol. 41, pp. 898-904.

Vipulanandan, C. and Prashanth, P. (2013). “Impedance Spectroscopy Characterization of a Piezoresistive Structural Polymer Composite Bulk Sensor.” *Journal of Testing and Evaluation*.

Vipulanandan, C., Ahossin, Y. J. and Bilgin, O. (2007). “Geotechnical properties of marine and deltaic soft clays.” GSP 173 Advances in Measurement and Modelling of Soil Behavior, pp. 1-13.

Vipulanandan, C., and Garas, V. (2006), “Piezoresistivity of Carbon Fiber Reinforced Cement Mortar.” Proceedings, Engineering, Construction and Operations in Challenging Environments, Earth & Space 2006, Proceedings ASCE Aerospace Division, League City, TX, CD-ROM.

Vipulanandan, C., and Liu, J. (2005) “Polyurethane Based Grouts for Deep Off-Shore Pipe-in-Pipe Application,” Proceedings, Pipelines 2005, ASCE, Houston, TX, pp. 216-227.

Vipulanandan, C., and Sett, K. (2004). “Development and Characterization of Piezoresistive Smart Structural Materials,” Proceedings, Engineering, Construction and Operations in Challenging Environments, Earth & Space 2004, ASCE Aerospace Division, League City, TX, pp. 656-663.

Vipulanandan, C., Heidari, M., Qu, Q., Farzam, H.and Pappas, J. M. (2014). “Behavior of piezoresistive smart cement contaminated with oil-based drilling mud.” Offshore Technology Conference, OTC 25200-MS, pp. 1-14.

Wahab, A. and Noor. (2013). “Effects of FlyAsh Addition on Compressive Strength and Flexural Strength of Foamed Cement.” *Advanced Materials Research*.

Waheed, A. “Deep Water Shallow Flow Controlled by Foamed Cement.” *Halliburton Services*.

Wang, S. Y. and Vipulanandan, C. (1996) “Leachability of Lead from Solidified Cement-Fly Ash Binders,” Cement and Concrete Research, Vol. 26, No. 6, pp. 895-905.

Wang, T. (2014). “Freeze Thawing Resistance Effects on Electromagnetic Wave Reflectivity.” *Construction and Building Materials*.

Wang, Yang, L. (2015). “Microstructure and Properties of Cement Foams Prepared by Magnesium Oxychloride Cement.” *Journal of Wuhan University*.

Wei, X., Lianzhen, X. and Li, Z. (2008). “Electrical measurement to assess hydration process and the porosity formation.” Journal of Wuhan University of Technology-Material Science. Ed., Vol. 23, pp. 761-766.

Williams, H. F. L. (2009). “GIS Based Analysis of Foundation Repairs and Soil Conditions in Dallas, Texas.” *Environ Geology*.

Wu, B. (2014). “Residual Compressive Strength and Freeze Thaw Resistance of Ordinary Concrete after High Temperature.” *Construction and Building Materials*.

Younsung, J. (2001). “Study of New Type of Light Magnesium Cement Foamed Material.” *Materials Letters.*

Zhang, J., Weissinger, E. A., Peethamparan, S. and Scherer, G. W. (2010). “Early hydration and setting of oil well cement.” Journal of Cement and Concrete Research, Vol. 40, pp. 1023-1033.

Zhang, M., Sisomphon, K., Nag, T. S, and Sun, D. J, (2010). “Effect of superplasticizers on workability retention and initial setting time of cement pastes,” Construction and Building Materials 24, 1700–1707.

Zhang, M., Reid, A. (2015). “Mechanical, Thermal Insulation, Thermal Resistance and Acoustic Absorption Properties of Foam Concrete.” *Cement and Concrete Composites.*

Zhao, X. and Lim, K. (2015). “Properties of Foamed Mortar Prepared with Granulated Blast Furnace Slag.” *Materials Journal*.

Zhihua, A. (2014). “Preparation and Characterization of Super Low-Density Foamed Concrete from Portland Cement.” *Construction and Building Materials.*

Zitha, P., Felder, R., Zornes, D., Brown, K. and Mohanty, K. (2011). “Increasing Hydrocarbon Recovery Factors.” Society of Petroleum Engineers Conference.

Zuo, Y., Zi, J. and Wei, X. (2014). “Hydration of cement with retarder characterized via electrical resistivity measurements and computer simulation.” Journal of Construction and Building Materials, Vol. 53, pp. 411–418.